

# Numerical modelling of pollutant formation and removal during fuel combustion

---

**Bešenić, Tibor**

**Doctoral thesis / Disertacija**

**2021**

*Degree Grantor / Ustanova koja je dodijelila akademski / stručni stupanj:* **University of Zagreb, Faculty of Mechanical Engineering and Naval Architecture / Sveučilište u Zagrebu, Fakultet strojarstva i brodogradnje**

*Permanent link / Trajna poveznica:* <https://urn.nsk.hr/urn:nbn:hr:235:463980>

*Rights / Prava:* [In copyright / Zaštićeno autorskim pravom.](#)

*Download date / Datum preuzimanja:* **2025-03-09**

*Repository / Repozitorij:*

[Repository of Faculty of Mechanical Engineering and Naval Architecture University of Zagreb](#)





University of Zagreb

FACULTY OF MECHANICAL ENGINEERING AND NAVAL  
ARCHITECTURE

Tibor Bešenić

**NUMERICAL MODELLING OF  
POLLUTANT FORMATION AND  
REMOVAL DURING FUEL COMBUSTION**

DOCTORAL THESIS

Zagreb, 2021



Sveučilište u Zagrebu

FAKULTET STROJARSTVA I BRODOGRADNJE

Tibor Bešenić

**NUMERIČKO MODELIRANJE  
NASTAJANJA I UKLANJANJA  
POLUTANATA PRI IZGARANJU GORIVA**

DOKTORSKI RAD

Zagreb, 2021.



University of Zagreb

FACULTY OF MECHANICAL ENGINEERING AND NAVAL  
ARCHITECTURE

Tibor Bešenić

**NUMERICAL MODELLING OF  
POLLUTANT FORMATION AND  
REMOVAL DURING FUEL COMBUSTION**

DOCTORAL THESIS

Supervisor:

Assoc. Prof. Milan Vujanović, PhD

Zagreb, 2021



Sveučilište u Zagrebu

FAKULTET STROJARSTVA I BRODOGRADNJE

Tibor Bešenić

**NUMERIČKO MODELIRANJE  
NASTAJANJA I UKLANJANJA  
POLUTANATA PRI IZGARANJU GORIVA**

DOKTORSKI RAD

Mentor:

Izv. prof. dr. sc. Milan Vujanović

Zagreb, 2021.

# Bibliography Data

**UDC:** 532.51

**Keywords:** flue gas desulfurisation; seawater desulfurisation; absorption modelling; mass transfer coefficient; droplet absorption; wall film absorption; spray scrubbers; SO<sub>x</sub>; pulverised fuel combustion; nitrogen oxides formation; fuel nitrogen; fuel nitrogen partitioning; NO<sub>x</sub>

**Scientific area:** Technical sciences

**Scientific field:** Mechanical engineering

**Institution:** Faculty of Mechanical Engineering and Naval Architecture

**Thesis supervisor:** Assoc. Prof. Milan Vujanović, PhD

**Number of pages:** 151

**Number of figures:** 50

**Number of tables:** 17

**Number of references:** 196

**Date of examination:** 31 March 2021

**Thesis defence commission:**

Prof. Neven Duić, PhD – Chairman of defence commission

Prof. Manolis Gavaises, PhD – member

Prof. Daniel Rolph Schneider, PhD – member

Klaus Pachler, PhD – member

Asst. Prof. Jakov Baleta, PhD – member

**Archive:** Faculty of Mechanical Engineering and Naval Architecture

# Acknowledgements

I hereby declare that this Thesis is entirely the result of my own work and knowledge obtained during my studies, except where otherwise indicated. I have fully cited all used sources and I have only used the ones given in the list of references.

I am extremely grateful to my supervisor, Prof. Milan Vujanović, for providing me the opportunity to work in the group, as well as for the advices regarding the research, and the willingness to work long hours with me to meet the deadlines.

I am also very grateful to Dr. Klaus Pachler, for guidance and valuable discussions regarding the research and the implementation of models in AVL FIRE™.

My sincere gratitude goes to Prof. Nebojša Manić and Miloš Radojević from the Faculty of Mechanical Engineering in Belgrade for their time, hospitality, and invaluable help with the experimental investigation.

My thanks go to my colleagues from *Powerlab*, especially Filip Jurić, Dr. Marko Ban, Dr. Hrvoje Mikulčić, Dr. Zvonimir Petranović, Ivan Pađen, and others, who helped me with the technical issues, but also made the work much more enjoyable. I would particularly like to express my gratitude to Dr. Jakov Baleta for the help he provided with the research and the writing of the Thesis.

Most importantly, I am immeasurably grateful to my family for the understanding, support, and opportunities they provided for me.

Finally, a huge thank you goes to my significant other, Jelena Jakuš, for her patience, love, and understanding, especially during my PhD studies.

---

## **SPECIAL ACKNOWLEDGEMENTS**

I wish to express my gratitude to the Croatian Science Foundation for supporting the research in this thesis through "Young researchers' career development project – training of doctoral students" with my mentor Assoc. Prof. Milan Vujanović, PhD.

Additionally, the research conducted in this thesis was supported under the auspice of the European Regional Development Fund, Operational Programme Competitiveness and Cohesion 2014-2020, KK.01.1.1.04.0070.

Finally, I am truly thankful to AVL List GmbH and AVL - AST d.o.o. for the opportunity to participate in an international collaboration and the support provided throughout this work.





# Abstract

Reduction of harmful impact on the environment caused by rapid development of a fossil fuel-powered society is one of the most significant global challenges. The combustion-related pollutants such as sulfur oxides and nitrogen oxides stand among the most harmful ones due to large amounts of emissions discharged globally. The advanced models that provide insight into pollutant production and removal processes can be useful in designing new, more sustainable technology. Numerical models presented in this work aim to improve the calculation accuracy and efficiency for complex physicochemical processes of nitrogen oxides formation during the combustion of pulverised fuels, as well as the calculation of sulfur dioxide removal from flue gases by seawater absorption in spray droplets and liquid wall film.

The chemical processes of absorption in droplets were modelled for pure water by a simplified chemical model accounting for the reactions in the aqueous phase, and additionally for seawater, by introducing the influence of alkalinity that increases the absorption potential. The second part of absorption modelling is the mass transfer dynamics, and it was described by two film theory. It separates the influence of resistances for the interface's liquid and gas side. For droplets falling in the stream of rising gases, determining the mass transfer can be an issue, and the penetration theory was selected as the most suitable among the implemented models for the dominant liquid side mass transfer coefficient. Furthermore, to account for all of the relevant processes, the absorption of sulfur dioxide in wetted walls was also modelled by adopting an analogous approach. The main difference is in the implementation of the mass transfer model, as the hydrodynamic processes influencing the liquid wall film are different. The used approach is based on dimensionless parameters and hydrodynamic characteristics of wall film. The developed and implemented models were validated against experimental data obtained in the literature for simplified geometries and industrial cases. The comparison showed that the model is capable of replicating experimental results for different geometries, range of sulfur dioxide concentrations and liquid-to-gas ratios.

Additionally, the nitrogen oxides' formation was modelled with the aim of accurately predicting their concentrations in pulverised solid fuel combustion systems. The Euler-Lagrangian approach was also used for describing the multiphase flow of fuel particles, and the combustion model was augmented by addition of a nitrogen oxides' production model. Thermal and fuel production pathways were included, but the fuel nitrogen pathway was modified by the addition of partitioning factor that accounted for changing influences of different pathways. Then, the

experimental analysis of bituminous coal was performed on a TG-MS system and by applying a derived method for quantifying the fuel nitrogen partitioning. Finally, the obtained experimental data was used in numerical simulations of a drop tube test, resulting in nitrogen oxides' concentrations comparable with the ones reported in the literature.

**Keywords:** flue gas desulfurisation; seawater desulfurisation; absorption modelling; mass transfer coefficient; droplet absorption; wall film absorption; spray scrubbers; SO<sub>x</sub>; pulverised fuel combustion; nitrogen oxides formation; fuel nitrogen; fuel nitrogen partitioning NO<sub>x</sub>

# Prošireni sažetak

Zaustavljanje štetnog utjecaja na okoliš i uklanjanje posljedica nastalih zbog neodrživog rasta ljudske civilizacije jedan je od najvažnijih ciljeva današnjice. To je razlog zašto se nameću sve stroža ograničenja po pitanju emisija polutanata ispuštenih u okoliš, a za poštivanje tih ograničenja bit će potrebno razviti i konstruirati nova i efikasnija tehnološka rješenja, a stara zamijeniti održivijima. Korištenje naprednih alata za razvoj proizvoda bit će neizostavno za postizanje tih održivih ciljeva, a jedan od alata jest i računalna dinamika fluida.

Plinovite emisije dušikovih i sumporovih oksida spadaju među najznačajnije polutante nastale izgaranjem fosilnih goriva zbog njihovog štetnog utjecaja na zdravlje ljudi, nastanak kiselih oborina i troposferskog smoga, ali i zbog – u apsolutnom mjerilu – značajnih količina ispuštenih u okoliš. Stoga su numerički modeli koji opisuju ponašanje tih onečišćujućih tvari važni za njihovo smanjenje i kontrolu. Dušikovi i sumporovi oksidi nastaju pri izgaranju fosilnog goriva zbog njegovog sastava ili parametara izgaranja, a pri njihovom nastanku, širenju ili uklanjanju odvijaju se kompleksni kemijski i fizikalni procesi.

Jedan od često korištenih pristupa za smanjenje emisija sumporovog dioksida u dimnim plinovima je mokro odsumporavanje, gdje se struja onečišćenih plinova dovodi u kontakt s kapljevnom s apsorbirajućim kapacitetom. *Scrubberi* su takvi kontaktori u kojima se ostvaruje velika specifična površina između faza, često ubrizgavanjem spreja apsorbirajuće kapljevine. I obična voda ima svojstvo apsorpcije sumporovog dioksida, ali lužnate otopine povećavaju kapacitet. Morska se voda, zbog blago lužnate pH vrijednosti i prirodnog alkaliteta, može koristiti kao apsorbirajuća kapljevina, što omogućava primjene u brodskim i priobalnim aplikacijama. Za opis ovog procesa bitno je točnim modelom obuhvatiti kemijske reakcije u vodenoj fazi, kao i fizikalni prijenos mase preko granice sustava.

Kemijske reakcije mogu biti opisane sustavom jednadžbi za sve reaktivne vrste, čije rješenje daje vrijednosti ravnotežnih koncentracija. One zapravo pokazuju potencijal za apsorpcijom, a da bismo izračunali dinamiku uklanjanja sumporovog dioksida, potrebno je modelom opisati prijelaz mase između faza. U okviru modela dvofaznog strujanja implementiran je model dvaju filmova, koji otpor prijelazu mase dijeli na utjecaj plinovite i kapljevite faze. Ispitani su i implementirani modeli za računanje koeficijenta prijelaza mase, a za kapljevitu stranu koja je dominantna korištena je penetracijska teorija. Predstavljeni model validiran je prvo za slučaj jedne kapljice, a zatim i prema eksperimentalnim podacima za pojednostavljenu geometriju *scrubbera*. Rezultati simulacija su pokazali veoma dobro slaganje s eksperimentom, kako za običnu, tako i za morsku vodu. Za slučaj industrijske geometrije s velikim omjerom toka kapljevine u odnosu

na dimne plinove, rezultati simulacija se nisu poklapali s eksperimentalnim rezultatima iznad 90%, što je objašnjeno značajnijim utjecajem filma kapljevine na stijenci. Stoga je implementiran i ispitan model analogan prijašnjem, samo prilagođen računanju prijelaza mase u film kapljevine prema drugačijim hidrodinamičkim parametrima. Kad je model apsorpcije u film bio uključen, rezultati su bili u boljem slaganju s eksperimentalnim podacima za slučaj industrijskog *scrubbera*.

S druge strane, smanjenje dušikovih oksida često se pokušava ostvariti modifikacijama sustava izgaranja, tako da se postignu uvjeti koji su nepovoljni za njihov nastanak. Zbog toga je detaljniji uvid u kemijske reakcije i puteve nastanka izuzetno koristan, jer omogućava smanjenje polutanata tijekom njihovog nastanka. U sustavima izgaranja praškastog goriva, čestice koje ulaze u komoru izgaranja prolaze kroz složene transformacije, ugrubo podijeljene na zagrijavanje, sušenje, devolatilizaciju, te zapaljenje hlapljivih kemijskih vrsta i preostale čađe. Njihovo gibanje opisuje se Euler-Lagrangeovim pristupom za dvofazno strujanje, a izgaranje čestica opisano je izmjenom mase i kinetikom kemijskih reakcija. Na taj numerički okvir za modeliranje izgaranja nadograđen je numerički model nastajanja dušikovih oksida.

Kemijske reakcije i mehanizmi nastanka dušikovih oksida kompleksni su i ne u potpunosti razjašnjeni procesi, a pokušaji predviđanja koncentracija polutanata na temelju sastava goriva ne daju zadovoljavajuće rezultate. Njihovo formiranje izrazito ovisi o uvjetima izgaranja kao što su temperatura, sastav plinovite faze i goriva, veličina čestica te pretičak zraka. Nastanak dušikovih oksida uglavnom se dijeli na tri mehanizma: termalni, promptni te NO iz goriva. Termalni NO nastaje pri visokim temperaturama uslijed disocijacije molekularnog dušika iz zraka te je značajan pri visokim temperaturama.

Produkcija i destrukcija dušikovih oksida iz goriva još uvijek nije u potpunosti shvaćen fenomen, unatoč većem broju provedenih istraživanja, a u sustavima izgaranja praškastog goriva ima dominantni utjecaj. Postojeći model nastanka NO iz goriva unaprijeđen je upotrebom faktora raspodjele dušika iz goriva prema načinu doprinosa sveukupnom NO. Tako imamo doprinos preko hlapljivih komponenata goriva ili preko oksidacije koksnoeg ostatka u heterogenim reakcijama na površini čestica. Također, dušik iz goriva dijeli se i prema posrednoj kemijskoj vrsti koja na kraju sudjeluje u nastanku NO, tako da su dvije najznačajnije posredne kemijske vrste HCN i NH<sub>3</sub>, a njihov omjer ovisi o parametrima poput temperature, vrste goriva i vrste komore izgaranja. Kako bi rezultati simulacija bili što točniji, napravljena su eksperimentalna istraživanja na ugljenu koja su pokazala da je omjer HCN i NH<sub>3</sub> pri pirolizi u TG-MS sustavu otprilike jednak, ali da je utjecaj oksidacije koksnoeg ostatka značajno jači od utjecaja hlapljivih tvari za HCN. Za potrebe pribavljanja ovih rezultata, modificirana je i upotrijebljena metoda kvantificiranja kvalitativnih podataka iz signala masene spektroskopije. Ovi rezultati su spojeni s modificiranim modelom nastanka dušikovih oksida iz goriva te uspoređeni s eksperimentalnim istraživanjima, što je pokazalo da je korištenjem faktora raspodjele dušika iz goriva model unaprijeđen te da sa zadovoljavajućom točnošću reproducira koncentracije NO u dimnim plinovima koji izlaze iz komore izgaranja.

## HIPOTEZE I CILJEVI

Hipoteza ovog rada je da će novi i unaprijeđeni matematički modeli omogućiti detaljan i numerički učinkovit izračun kompleksnih fizikalno-kemijskih procesa nastanka dušikovih oksida pri procesu izgaranja krutog goriva te uklanjanja sumporovog dioksida iz dimnih plinova apsorpcijom u kapljicama i filmu morske vode na stijenci.

Ciljevi istraživanja su unapređenje i implementacija novih modela za nastanak dušikovih oksida pri procesu izgaranja krutog praškastog goriva te razvoj matematičkog modela apsorpcije sumporovih oksida u vodene kapljice i film kapljevine na stijenci, s krajnjim ciljem dobivanja sveobuhvatnog alata za istraživanje uklanjanja polutanata u realnim sustavima izgaranja.

## METODE I PREGLED DISERTACIJE

Ovaj rad numerički opisuje fizikalne i kemijske procese vezane za nastanak dušikovih oksida pri izgaranju praškastog goriva, kao i modele uklanjanja sumporovih oksida iz dimnih plinova sustava za izgaranje apsorpcijom u kapljice spreja ili film kapljevine na stijenci. Matematičkom nadogradnjom postojećeg numeričkog okvira temeljenog na zakonima održanja fizikalnih veličina postignuto je unapređenje modela za opisivanje relevantnih procesa. Kapljice i čestice goriva su kao diskretna faza opisane korištenjem Lagrangeove formulacije, a plinovita se faza rješava Eulerovom formulacijom unutar komercijalnog programskog paketa za računalnu dinamiku fluida AVL FIRE<sup>TM</sup>, baziranom na metodi kontrolnih volumena. Razvijeni matematički modeli implementirani su u programskom jeziku FORTRAN upotrebom korisničkih funkcija povezanih s glavnim rješavačem. Poveznica s ostalim transportnim jednadžbama, modelom izgaranja i spreja ostvarena je modifikacijom izvora i ponora fizikalnih veličina.

Eksperimentalno istraživanje provedeno je s ciljem određivanja raspodjele dušika iz goriva na mehanizme nastajanja posrednih kemijskih vrsta i posljedično dušikovih oksida. Primijenjena je nova metoda kvantifikacije uzoraka prema kvalitativnim rezultatima simultane termogravimetrijske analize i masene spektrometrije, a navedeni modeli omogućuju detaljniji uvid u mehanizme nastanka dušikovih oksida i unapređenje numeričkih izračuna sustava za izgaranje.

Konačni cilj rada bio je dobivanje sveobuhvatnih numeričkih modela koji sa zadovoljavajućom točnošću reproduciraju eksperimentalne podatke.

U *poglavlju 1* dan je pregled literature i motivacija za izradu rada, kao i uvid u recentna znanstvena istraživanja vezana za modeliranje onečišćujućih tvari.

U *poglavlju 2* izloženi su matematički modeli računalne dinamike fluida primijenjeni u ovom istraživanju, dajući tako kratak opis numeričkog okvira korištenog za implementaciju modela. Posebno su obrađeni Euler-Lagrangeov pristup te metoda diskretnih kapljica koje služe za opisivanje dvofaznog toka. Također, obrazložena je prikladnost korištenja pristupa koncentriranih parametara za modeliranje spreja, kao i osnovne jednadžbe za modeliranje ponašanja kapljica.

*Poglavlje 3* usredotočeno je na razvoj modela apsorpcije sumporovog dioksida u običnoj i morskoj vodi, te izlaže temelje modeliranja kemijskih procesa u vodenim otopinama pod ravnotežnim uvjetima. Prikazani su sustavi kemijskih jednadžbi među kemijskim vrstama koje sadrže

sumpor, kao i posebnosti pri modeliranju kemijskih reakcija u morskoj vodi. Nakon toga, fokus je prebačen na problematiku modeliranja prijenosa mase preko granice između plinovite i kapljevite faze. Glavni fizikalni procesi koji utječu na prijenos mase su recirkulacija u kapljicama, turbulentno strujanje, oscilacije kapljica i rastezanje površine, što zajedno čini kompleksan skup faktora. Izloženi su pojednostavljeni modeli te su rezultati dobiveni njima uspoređeni na razini jedne kapljice. Kasnije su odabrani modeli za kapljevitu i plinovitu stranu primijenjeni na cijeli sprej te su validirani na pojednostavljenim i kompletnim trodimenzionalnim slučajevima s realnim graničnim uvjetima.

U *poglavlju 4* izložen je rad vezan za modeliranje nastanka polutanata pri izgaranju krutog goriva. Prikazan je pregled prijašnjih istraživanja i korištenih modela, kao i pregled uobičajenih pristupa modeliranju procesa nastanka dušikovih spojeva. Ovo poglavlje detaljno analizira mehanizam nastanka NO iz dušika sadržanog u gorivu te prikazuje kemijske reakcije i posredne vrste u kemijskom mehanizmu. Kako bi se zaobišla izrazita ovisnost mehanizma nastanka dušikovih oksida o vrsti izgaranja, temperaturi, vrsti ugljena i ostalim parametrima, napravljena je eksperimentalna analiza ugljena gdje su pribavljeni podaci o raspodjeli dušika sadržanog u gorivu na posredne kemijske vrste HCN i NH<sub>3</sub>, kao i na volatile i oksidaciju krutog ostatka. Primijenjena je nova metoda za kvantifikaciju raspodjele iz kvalitativnih rezultata pribavljenih vezanim sustavom simultane termogravimetrijske analize i masene spektrometrije (TG-MS). Konačno, ti eksperimentalni rezultati spojeni su s numeričkim modelom i iskorišteni pri provođenju numeričkih simulacija, a rezultati modela su validirani s eksperimentalnim rezultatima za koncentracije NO.

U *poglavlju 5* prikazan je zaključak na temelju dobivenih rezultata provedenog istraživanja, kao i smjernice te preporuke za daljnji rad.

### ZNANSTVENI DOPRINOS I ZAKLJUČAK

Znanstveni doprinos rada vidljiv je u unapređenju alata za modeliranje uklanjanja i nastajanja onečišćujućih tvari pri izgaranju goriva. Glavni dio istraživačkog rada fokusiran je na razvoj i unapređenje numeričkog modela odsumporavanja dimnih plinova i njegovu implementaciju u okvir računalne dinamike fluida, što će omogućiti lakši razvoj tehnoloških rješenja za uklanjanje sumporovog dioksida u brodskim i priobalnim primjenama. Drugi je dio rada usredotočen na modeliranje nastanka dušikovih oksida prilikom izgaranja praškastog goriva, gdje je mehanizam za opisivanje njihovog nastajanja unaprijeđen i modificiran ponderiranim faktorima prema eksperimentalnoj analizi goriva simultanom termogravimetrijskom analizom i masenom spektrometrijom. Pritom razvijeni model omogućuje detaljnije opisivanje nastanka dušikovih oksida i unapređenje sustava za izgaranje

Znanstveni doprinosi istraživanja su sljedeći:

- Razvoj i implementacija sveobuhvatnog modela apsorpcije sumporovog dioksida iz dimnih plinova u kapljice spreja i film kapljevine na stijenci za običnu i morsku vodu, upotrebljiv za unapređenje procesa odsumporavanja u industrijskim primjenama.

- Numerički model nastanka dušikovog monoksida pri izgaranju praškastog goriva prilagođen korištenjem ponderiranih faktora utjecaja posrednih kemijskih vrsta u mehanizmu nastanka polutanata, dobivenih primjenom nove metode kvantifikacije rezultata simultane termogravimetrijske analize i masene spektrometrije.

**Ključne riječi:** odsumporavanje dimnih plinova; odsumporavanje morskom vodom; modeliranje apsorpcije; koeficijent prijelaza mase; apsorpcija u kapljicu; apsorpcija u film kapljevine; *scrubberi* sa sprejom;  $SO_x$ ; izgaranje praškastog goriva; nastajanje dušikovih oksida; dušik iz goriva; raspodjela dušika iz goriva;  $NO_x$

# Contents

<b>List of figures</b>	<b>xiv</b>
<b>List of tables</b>	<b>xvi</b>
<b>Nomenclature</b>	<b>xvii</b>
<b>1 Introduction</b>	<b>1</b>
1.1 Motivation and General Overview . . . . .	1
1.2 Overview of the Pollutant Emissions . . . . .	3
1.2.1 Power Plant Emissions . . . . .	5
1.2.2 Maritime Emissions . . . . .	9
1.2.3 Pollutant Chemistry . . . . .	18
1.2.3.1 Nitrogen Oxides . . . . .	18
1.2.3.2 Sulfur Oxides . . . . .	22
1.3 Hypothesis and Work Outline . . . . .	24
1.4 Thesis Contribution . . . . .	25
<b>2 Numerical Modelling</b>	<b>26</b>
2.1 Conservation Equations . . . . .	26
2.2 General Transport Equation . . . . .	29
2.3 Turbulence Modelling . . . . .	29
2.3.1 Incompressible Flows . . . . .	31
2.3.2 Compressible Flows . . . . .	32
2.3.3 Closure Problem . . . . .	33
2.3.4 $k$ - $\epsilon$ Turbulence Model . . . . .	35
2.3.5 $k$ - $\zeta$ - $f$ Turbulence Model . . . . .	36
2.4 Spray Modelling . . . . .	38
<b>3 Sulfur Oxides Removal</b>	<b>41</b>
3.1 Technology Overview . . . . .	41
3.1.1 Flue Gas Desulfurisation . . . . .	41
3.1.2 Scrubbing Liquids . . . . .	44
3.1.3 Scrubber Design . . . . .	46



3.2	Desulfurisation Chemistry Modelling . . . . .	50
3.2.1	SO <sub>2</sub> Solubility . . . . .	51
3.2.2	Pure Water Chemical Model . . . . .	52
3.2.3	Seawater Modelling . . . . .	57
3.2.3.1	Seawater Composition . . . . .	57
3.2.3.2	Alkalinity . . . . .	59
3.2.4	Seawater Chemical Model . . . . .	61
3.2.4.1	Ionic Strength . . . . .	64
3.2.4.2	Rate-approach Model . . . . .	67
3.3	Mass Transfer Modelling for Flue Gas Desulfurisation . . . . .	69
3.3.1	Single Droplet Mass Transfer Modelling . . . . .	70
3.3.1.1	Two-film theory . . . . .	71
3.3.1.2	Film Theory . . . . .	73
3.3.1.3	Penetration Theory . . . . .	75
3.3.1.4	Surface Renewal Theory . . . . .	75
3.3.1.5	Additional Mass Transfer Coefficient Models . . . . .	77
3.3.2	Validation of Mass Transfer Coefficient Models . . . . .	78
3.3.2.1	Single Falling Droplet Test: Walcek et al. . . . .	79
3.3.2.2	Single Falling Droplet Tests: Saboni and Alexandrova . . . . .	79
3.3.2.3	Single Falling Droplet Tests: Kaji . . . . .	81
3.4	SO <sub>2</sub> Absorption Modelling Results . . . . .	82
3.4.1	1 <sup>st</sup> Validation Case: Caiazza et al. . . . .	84
3.4.2	2 <sup>nd</sup> Validation Case: Chen et al. . . . .	91
3.5	Wall Film Absorption . . . . .	97
3.5.1	Overview of wall film absorption modelling . . . . .	97
3.5.2	Wall Film Absorption Modelling . . . . .	99
3.5.3	Numerical Simulations . . . . .	101
3.5.3.1	Initial Verification . . . . .	101
3.5.4	Wall Film Absorption Results . . . . .	103
3.6	Conclusion . . . . .	109
<b>4</b>	<b>Nitrogen Oxides Formation</b>	<b>111</b>
4.1	Combustion systems overview . . . . .	111
4.2	Pulverised Fuel Combustion . . . . .	112
4.3	Formation Models . . . . .	113
4.3.1	Thermal NO Mechanism . . . . .	115
4.3.2	Fuel NO Mechanism . . . . .	115
4.3.3	Impact of Turbulence on Pollutant Production . . . . .	118
4.4	Fuel Nitrogen Partitioning . . . . .	118

---

4.4.1	Experimental Determination of Fuel Nitrogen Partitioning . . . . .	119
4.5	Numerical Simulations . . . . .	122
4.6	Conclusion . . . . .	127
<b>5</b>	<b>Conclusions and Future Work</b>	<b>129</b>
5.1	Conclusions . . . . .	129
5.2	Proposals for Future Work . . . . .	131
5.2.1	Future Work on Sulfur Dioxide Absorption Model . . . . .	131
5.2.2	Future Work on Nitrogen Oxides Formation Model . . . . .	131
	<b>Bibliography</b>	<b>132</b>

# List of Figures

1.1	Currently established SO <sub>x</sub> emission control areas . . . . .	11
1.2	International shipping emission trends, 2012-2018 . . . . .	13
1.3	Allowed SO <sub>x</sub> concentrations in fuel for marine engines . . . . .	14
1.4	Exhaust gas cleaning system's design types . . . . .	16
1.5	Interactions of NO <sub>x</sub> , ozone and VOCs in troposphere . . . . .	21
1.6	Nitrogen cycle in the atmosphere . . . . .	21
2.1	Decomposition of turbulent flow . . . . .	31
3.1	Packed bed scrubber . . . . .	48
3.2	Spray scrubber . . . . .	49
3.3	Chemical reactions in liquid phase . . . . .	54
3.4	SO <sub>2</sub> equilibrium concentrations in pure water - comparison with data by Andreassen and Mayer . . . . .	56
3.5	SO <sub>2</sub> equilibrium concentrations in pure water - comparison with data by Hocking and Lee . . . . .	57
3.6	Bjerrum plot of carbonate system . . . . .	60
3.7	Bjerrum plot of SO <sub>2</sub> and CO <sub>2</sub> in aqueous solutions. . . . .	62
3.8	SO <sub>2</sub> seawater equilibrium concentrations . . . . .	64
3.9	SO <sub>2</sub> seawater equilibrium concentrations with the ionic strength included . . . . .	66
3.10	Comparison of the pure and seawater chemical model to experimental data . . . . .	67
3.11	Comparison of the seawater rate-approach model to the literature data. . . . .	69
3.12	Illustration of the two film theory - concentrations at the gas-liquid interface . . . . .	72
3.13	Illustration of film theory model . . . . .	74
3.14	Illustration of penetration theory model . . . . .	76
3.15	Illustration of surface renewal theory model . . . . .	76
3.16	Comparison of film theory with literature data . . . . .	80
3.17	Comparison of mass transfer coefficient models with literature data - Saboni and Alexandrova, case 1 . . . . .	81
3.18	Comparison of mass transfer coefficient models with literature data - Saboni and Alexandrova, case 2 . . . . .	82
3.19	Comparison of mass transfer coefficient models with literature data - Kaji . . . . .	83

---

3.20	Particle size distribution for the injected droplets under different flow rates . . .	85
3.21	Fluid flow properties at cross-section, droplet properties: temperatures and velocities . . . . .	87
3.22	Physical values in spray droplets . . . . .	88
3.23	SO <sub>2</sub> concentration on the cross-section for pure water absorption . . . . .	89
3.24	Removal efficiency for pure water absorption, 500 ppm – comparison with literature data . . . . .	90
3.25	Removal efficiency for pure water absorption, 700 ppm – comparison with literature data . . . . .	91
3.26	Removal efficiency for pure water absorption, 900 ppm – comparison with literature data . . . . .	92
3.27	Removal efficiency for seawater absorption, 500 ppm – comparison with literature data . . . . .	93
3.28	Computational mesh for the Chen case; side view and top view of mesh and nozzle position . . . . .	95
3.29	Physical values along the open spray scrubber height: velocities for single and two-phase flow, and temperature . . . . .	96
3.30	Simulation results for the Chen case: SO <sub>2</sub> concentration and droplet properties	97
3.31	Comparison of liquid side mass transfer models with the experimental data . .	101
3.32	Used computational mesh for initial wall film absorption . . . . .	103
3.33	Concentrations of total sulfur absorbed in spray droplets and wall film . . . . .	106
3.34	Wall film Reynolds number, thickness and temperature values on a large scrubber geometry . . . . .	106
3.35	Comparison between the absorption in spray only, and the included wall film absorption . . . . .	107
4.1	Detailed NO reaction mechanism scheme . . . . .	114
4.2	Fuel NO reaction mechanism scheme . . . . .	117
4.3	Mass spectrometry signals for HCN in oxygen and argon . . . . .	120
4.4	Computational mesh for the NO simulations with the selections . . . . .	122
4.5	Temperatures and particle composition in drop tube simulations . . . . .	124
4.6	Intermediate species' concentrations depending on the partitioning factor used .	124
4.7	Pollutant mole fractions . . . . .	126
4.8	NO concentration profile along the drop tube axis . . . . .	127

# List of Tables

1.1	Emission limit values for large combustion power plants in EU under the Directive 2010/75/EU [14], mg/(Nm <sup>3</sup> ) . . . . .	7
1.2	Emission standards for coal-fired power plants in the United States and China, mg/m <sup>3</sup> . . . . .	9
1.3	NO <sub>x</sub> emission limits for different engine speeds . . . . .	12
1.4	Fuel oil sulfur content and the corresponding flue gas emission ratios . . . . .	16
2.1	k- $\epsilon$ model constants . . . . .	36
2.2	k- $\zeta$ - $f$ model constants . . . . .	37
3.1	Comparison of major scrubber technologies and designs . . . . .	47
3.2	Seawater composition . . . . .	58
3.3	Numerical settings for simulations of the Caiazzo et al. case. . . . .	86
3.4	Relative errors for pure water simulations . . . . .	92
3.5	Numerical settings for simulations of the Chen et al. case. . . . .	94
3.6	Wall film initialisation . . . . .	103
3.7	Initial wall film verification results . . . . .	104
3.8	Removal efficiencies comparison with and without wall film absorption model .	108
4.1	Fuel nitrogen partitioning between species and the pathway type . . . . .	121
4.2	Coal characteristics . . . . .	121
4.3	Coal combustion simulation inlet boundary conditions . . . . .	123

# Nomenclature

## Abbreviations

CFD	Computational fluid dynamics
DDM	Discrete droplet model
DNS	Direct numerical simulations
EGCS	Exhaust gas cleaning system
EL	Euler-Lagrangian
EU	European Union
FANS	Favre-averaged Navier Stokes equations
FGD	Flue gas desulfurisation
GHG	Greenhouse gas
HFO	Heavy fuel oil
IC	Internal combustion
IMO	International Maritime Organisation
LES	Large eddy simulation
LNG	Liquefied natural gas
NECD	National Emission Ceiling Directive
RANS	Reynolds-averaged Navier Stokes equations
TG-MS	Thermal Gravimetric Mass spectrometry
VOC	Volatile organic compounds

## Greek letters

$\delta_{ij}$	Kronecker delta function
---------------	--------------------------

$\varepsilon$	Dissipation rate of turbulent energy	$\text{m}^2/\text{s}^3$
$\Gamma$	Diffusion coefficient	$\text{m}^2/\text{s}$
$\gamma$	Activity coefficient	-
$\lambda$	Thermal conductivity	$\text{W}/(\text{m}\cdot\text{K})$
$\mu$	Dynamic viscosity	$\text{Pa}\cdot\text{s}$
$\mu_t$	Turbulent viscosity	$\text{kg}/(\text{m}\cdot\text{s})$
$\phi$	General intensive scalar property	
$\rho$	Density	$\text{kg}/\text{m}^3$
$\sigma_{ij}$	Stress tensor	$\text{N}/\text{m}^2$
$\tau_{ij}$	Viscous stress tensor	$\text{N}/\text{m}^2$
$C_{1,2,\mu}, \sigma k, \varepsilon$	$k - \varepsilon$ model constants	

### Dimensionless numbers

$Re$	Reynolds number	
$Sc$	Schmidt number	
$Sh$	Sherwood number	

### Physical values

$\alpha$	Partitioning factor	-
$\delta$	Thickness	$\text{m}$
$\Delta_{sol}$	Enthalpy of dissolution	$\text{J}/\text{mol}$
$a$	Thermodynamic activity	-
$A_T$	Alkalinity	$\text{mol}/\text{kg}$
$c$	Species concentration in aqueous solution	$\text{mol}/\text{kg}$
$c_{\text{SO}_2}$	$\text{SO}_2$ concentration in liquid phase	$\text{mol}/\text{L}$
$D$	Diffusivity, binary diffusion coefficient	$\text{m}^2/\text{s}$
$D_{ij}$	Strain rate tensor	$1/\text{s}$

---

$e$	Specific energy	J/kg
$f_i$	Body forces	m/s <sup>2</sup>
$H^{cp} \ominus$	Henry's constant at reference temperature	mol/(m <sup>3</sup> Pa)
$H_{SO_2}^{cp}$	Henry's constant for SO <sub>2</sub>	mol/(m <sup>3</sup> Pa)
$H_{SO_2}^{cp}$	SO <sub>2</sub> partial pressure	Pa
$I$	Ionic strength	mol/L
$K$	Equilibrium constants	-
$k$	Individual phase mass transfer coefficient	m/s
$k$	Turbulence kinetic energy	m <sup>2</sup> /s <sup>2</sup>
$l$	Length	m
$m$	Mass	kg
$N_A$	Molar flux between the phases	mol/(m <sup>2</sup> s)
$p$	Pressure	Pa
$r$	Reaction rate constant	-
$S$	Source	
$T$	Temperature	K
$t$	Time	s
$t_{con}$	Contact time	s
$TS$	Total sulfur - concentration of sulfur-containing species	mol/L
$u_i$	$i$ -th component of the velocity vector	m/s
$v$	Volume; atomic diffusion volumes	m <sup>3</sup>
$x_i$	$i$ -th component of the position vector	m
$Y$	Species mass fraction	kg/kg
$z$	Ion charge number	-



## CHAPTER 1

# Introduction

## 1.1 Motivation and General Overview

Climate change stands as one of the most significant challenges humanity has ever faced, and the response to its perils and the actions in the next decades have the potential to shape the future for the generations to come. The world is still mainly powered by fossil fuels – energy needs are being met primarily by utilising coal and natural gas in power plants, and oil is dominating the transport sector. Further extensive use of fossil fuels is not feasible due to harmful emissions of pollutants and greenhouse gases and their impact on the environment, and the transition towards more sustainable technologies and energy sources is already underway. The focus is divided into three main directions: increasing the share of renewable energy sources; reducing energy consumption by improving energy efficiency and improving the existing technologies to reduce their impact on the environment.

Although the transition to cleaner, more sustainable energy sources and technology is inevitable, there is still uncertainty regarding the dynamics of their adoption and implementation. Part of the insecurity lies in the unclear future of the best technologies, and some in within the unclear legal and financial frameworks of the future energy systems. Finally, a part of the conventional technologies will retain their current status in the nearby future for specific applications, such as baseload power plants or using oil-based fuels in heavy-duty maritime and air transport. Thus, besides the development of new technologies and ideas, additional effort will be needed for upgrading existing technologies, improving their efficiency and making them more sustainable.

During the last decades, along with the rise of available computational resources, computer-aided engineering became prevalent in research and development of new technologies. The usage of computational fluid dynamics (CFD) has outgrown its initial development for fluid flow simulations, as researchers are increasingly applying it for diverse applications. It is being used for modelling combustion phenomena, multiphase flows, spray and liquid film formation, heat and mass transfer modelling, biotechnology, complex chemical reactions and more. It has become ubiquitous in the development of new technologies, where it facilitates the design pro-

cess in synergy with experimental research, reducing the required time and number of costly experimental setups. Additionally, coupling of the CFD with experimental investigations offers the benefit of insight into conditions and processes not readily available via the experimental measurements, such as high temperatures, harmful atmospheres and chemical reactions. Just as well, the fast-occurring phenomena such as combustion and turbulence, or conditions inside particles and droplets which are delicate and hard to observe can be investigated into fine details. The CFD is especially useful in modelling the reactive and multiphase fluid flows, combustion processes and heat and mass transfer modelling, which are an integral part of the power engineering applications.

The main focus is on the reduction of pollutants originating from the combustion of fossil fuels, among which are carbon, nitrogen and sulfur oxides, together with a high number of other toxic substances. Two main approaches are used for pollutant reduction in practical applications. First one is focused on the formation side, where the efforts are made on prevention of pollutant formation. This is achieved either by using better fuels that burn more cleanly or by modifying the conditions in combustion chambers of boilers and furnaces to avoid the conditions suitable for chemical reactions producing the harmful reactant species. The second approach includes the pollutant removal processes and techniques that clean the flue gases exiting the combustion chamber, which vary depending on the pollutant that is being removed.

Formation and removal of pollutants depend on a wide range of phenomena and modelling both of the approaches encompasses a numerical description of intricate physical and chemical processes co-occurring and on small timescales. Numerical models used must be accurate, capture all the relevant mechanism, while keeping the computational intensity at the level low enough to allow for the use in research and development. In the CFD, fluid flow is the underlying process that influences pollutant formation, as it controls the spatial and temporal distribution of heat and mass. Transport of chemical species is required as the foundation for the modelling of chemical reactions governed by chemical kinetic mechanisms. Multiphase flow models enable coupling of the discrete phase with the fluid flow simulations, allowing for the accurate representation of the spray phenomena and the solid fuel particles in the computational domain.

Furthermore, the combustion of fuels is crucial for the power systems, where intensive and fast chemical reactions occur, consuming fossil fuel and producing energy and products. Due to impurities and chemical composition of the fuel, harmful pollutant species such as nitrogen and sulfur oxides are formed during combustion. Their formation and removal can be modelled by the homogeneous and heterogeneous chemical reactions and the interactions with the discrete phase – droplets and particles. The processes mentioned above encapsulate the majority of models needed for a complete description of the pollutant formation and removal. The coupling between models is crucial, since the phenomena influence one another. Thus, pollutant formation and removal are a combination of a complex and interdependent set of processes, and their modelling presents a difficult challenge.

Therefore, this work will focus on developing and improving mathematical models for

accurate and efficient calculation of the complex physical and chemical processes of pollutant formation and removal for fuel combustion. The goal of this thesis is twofold: to improve the nitrogen oxides formation model during the solid fuel combustion in practical combustion systems; and to develop and implement the sulfur dioxide removal model from flue gases by absorption in water droplets, applicable for the industrial desulfurisation processes.

## 1.2 Overview of the Pollutant Emissions

The modern world relies on vast amounts of energy for powering the growing industry, enabling trade across the globe, and for keeping the pace with improving the quality of living for an increasing number of people. Unfortunately, together with the increasing energy production, transport volume and number of people comes the pollution of the environment, and significant efforts are being made in a wide variety of fields to alleviate this impact.

The better part of human progress since the industrial revolution is owned to the presence of cheap and available fuel which has been a basis of heat and power generation. The initially unregulated use of fossil fuels — first coal and then also oil and gas — has led to the present situation where more than 80% of the world's 14 Gtoe total energy production is supplied from the fossil fuel sources whose exploitation negatively impacts the environment. However, it seems that the situation and the sentiment towards environment protection are slowly changing. Major movements for reducing the human-made impact on the environment were initiated by the scientific community and then accepted by the public during the last decades. Possibly the first such significant movement was the recognition of toxic effects of tetraethyllead used in gasoline engines, after which the chemical was gradually excluded from use in engines. Another example was the acknowledgement of ozone layer depletion due to emissions of chlorofluorocarbons used for refrigerants, propellants and solvents, which sensitized the public and resulted in a worldwide movement and ban of these harmful substances. More recently, the so-called *20-20-20* climate and energy targets in the European Union set the collective goals for the improvement of energy efficiency, the share of renewable energy sources and the reduction of greenhouse gases. The last one is a part of the probably most important objective, which is the mitigation of climate change and the global warming, that has a potential to increase the average global temperatures, significantly alter the global weather and drastically impact the future. Several other agendas for the reduction of impact on the environment will probably gain more attention in years to come, such as loss of biodiversity and species extinction, deforestation and depletion of natural resources, soil degradation, ocean acidification and the microplastics in water and environment. These issues impacting the environment will have to be tackled in a global pursuit of a sustainable future.

The 2016 Paris Agreement is a result of combined international efforts to combat the climate change and aims to limit the increase of average temperatures below 1.5 °C compared to the

pre-industrial levels while acknowledging the requirements of the less-developed countries [1]. Although the need for prompt actions is evident, the processes and the changes are still quite slow, and there exists significant inertia of existing systems and involved parties. Carbon dioxide (CO<sub>2</sub>) concentration in the air reached 410 ppm [2], the highest values since the industrial revolution, and the emissions in the environment peaked at the record-high values in 2018. This rising trend seems to be in contradiction with the proclaimed commitment to reduce the emissions. Although the renewable technologies — primarily wind and solar photovoltaics — have had a stellar increase in their installation capacities in last decade, renewable energy sources still account for less than 10% of world's primary energy demand [3]. Presently, it is impossible to predict the dynamics of energy transition, as the steep decline in the price of sustainable technologies will probably be opposed by the hesitancy for change, the need for reliable energy supply, and the uncertainty about technologies and the future. Even though various publications and studies forecast different fuel mixes, levels of penetration of renewable energy sources, adoption of novel technologies and different approaches to fossil fuel phase-out, a significant portion of the world will still be powered by fossil fuels in the future. Industry, transport and buildings each account for roughly a third of the 10 Gtoe final energy consumption, and stand as major targets for further improvements. In accessing the impact on the future, inaction and business as usual scenario can not lead to fulfilling the set targets. The adoption of the currently proposed environmental policies and their intensification could mitigate the climate change effects. The global energy demand is predicted to increase in decades to come, mostly due to emerging countries and markets closing the gap in the quality of living. In contrast, in developed countries, there will be a tendency for an increase in energy efficiency and demand reduction. The increase in energy efficiency will be preferred option for policy-makers in pursue of emission reductions due to simplicity and lower cost compared to the introduction of novel technology and increase of renewable energy sources in the energy mix. However, without the comprehensive changes, the energy policies and efficiency alone will not be enough for curtailing the global emissions, as the increased accessibility of modern technologies and decrease in energy poverty will increase the demand, especially in south-east Asia, India, and in sub-Saharan part of Africa.

The abovementioned indicates that pollution from traffic, industry and power generation will remain a significant issue in the following decades and that the implementation of novel technologies and increase of renewable energy sources will act favourably for the energy consumption and the pollutant emissions.

Among pollutants emitted in the environment, carbon dioxide is the prevalent one. It is the most significant greenhouse gas due to great amounts of fossil fuels burned, and the 33 Gt of CO<sub>2</sub> emissions from energy sector alone represent an immense addition to the atmosphere, leading to global warming and ocean acidification. Combating the CO<sub>2</sub> emissions will represent the major part of the path towards meeting the Paris Agreement objectives, and measures such as carbon taxation have already been put in place. Still, the carbon capture, utilisation and storage technologies will need to be developed and employed on a wider scale. The utilisation of fossil

fuels also produces other harmful pollutants that impact the environment and human health, such as nitrogen oxides ( $\text{NO}_x$ ), sulfur oxides ( $\text{SO}_x$ ), methane, heavy metals, volatile organic compounds (VOC) and particulate matter, to name a few. Air pollution has a significant and detrimental impact on human health; it is linked to respiratory issues and breathing diseases, and causes more than 5 million premature deaths annually [4]. Emission reduction from fossil fuel combustion, primarily  $\text{NO}_x$ ,  $\text{SO}_x$  and particulate matter from burning coal and fuel oil for energy production and transport have far-reaching potential for improving human health and lives.

Combating the emissions had different timelines and paths around the world. For example, emission trading schemes emerged as important mitigation factors, with 21 operating and 24 new systems under development across the globe. The first large greenhouse emission trading scheme, the European Union Emissions Trading System, has been introduced in 2005 and is still the biggest one [5], setting the allowed emission amounts for the participants. Subjects can meet them by improvements in technology, or by buying the unused allowances from others. The United States currently does not have a joint national  $\text{CO}_2$  cap-and-trade program, but there is an increasing number of federal states trading together in a Regional Greenhouse Gas Initiative. In 2010 China passed the United States as the biggest global  $\text{CO}_2$  emitter, which put additional focus on China's emissions and impact on the environment [6]. This fact, combined with the Paris Agreement goals, increased the need for sustainability, and China pledged to reduce the carbon emissions per unit of gross domestic product 60% to 65% by 2030. They are currently in the process of establishing the national carbon market via trial plans and pilot projects and cities based on European experiences, and their market has the potential to become the biggest one globally. In terms of emissions, a significant issue are the *locked-in* emissions in the coal-fired power generation. This is the truth, especially for China, as the majority of coal-fired power plants during the last two decades were installed in China and Asia. Although the rate of instalment has significantly declined, their global capacity still increases, and these potentially long-lived power plants lock the emissions for decades to come. Despite the overall increasing emissions and the fossil fuel-fired electricity generation capacities, these examples show that the regulations and emission trading schemes can lead to a lowered impact on the environment without sacrificing the economy.

## 1.2.1 Power Plant Emissions

Production of emissions is concentrated in specific locations, but their consequences have regional character. This was the motivation behind the 1979 Convention on Long-Range Transboundary Air Pollution which was signed by 51 countries including EU, Canada, the United States and several Asian countries. Since its inception, it has been expanded by several annexes, most notably and recently by the 1999 Gothenburg Protocol for stopping acidification, eutrophication and ground-level ozone. Although the nitrogen and sulfur oxides are not as prominent pollutants as carbon dioxide, their emissions are also significant and regulated by different

regulations. Similarly to CO<sub>2</sub>, NO<sub>x</sub> emissions have increased in previous decades, although some regions — mostly developed countries in the west — have implemented regulations and achieved reductions. Therefore, the nitrous oxide emissions were at 2.5 billion t in 1990, and in 2016 peaked globally at over 3 billion t of CO<sub>2</sub> equivalent, mostly due to increases in India and Brazil [7]. On the other hand, a positive example is the European Union, which has reduced its overall NO<sub>x</sub> emissions for 60% since 1990 [8]. Although no mandatory trading or *cap* schemes were introduced for power plants, the incentive caused the installation of low-NO<sub>x</sub> burners, abatement technology such as selective catalytic and non-catalytic reduction, or switching from coal to gas [9]. The previous EU regulations and global conventions for sulphur dioxide, nitrogen oxides, volatile organic compounds, ammonia and fine particulate matter have been incorporated in legislation for member states as policy instruments under the new National Emission Ceiling Directive from 2016. It did not introduce the emissions trading scheme as for carbon emissions, but introduced the total limits and mandated regular reporting, allowing EU States flexibility in ways to achieve these limits. For example, the new NECD imposed limits for NO<sub>x</sub> and SO<sub>x</sub> for the entire EU that will enable reduction of 42% and 59% up to 2029, respectively. After 2030 the limits will be lowered to 63% for NO<sub>x</sub> and 79% for SO<sub>x</sub> compared with 2005.

In the European Union, the majority of NO<sub>x</sub> emissions are currently emitted by road transport, and it represents the most significant potential for reduction at around 40% [8]. These emissions have been tackled by the introduction of increasingly stringent European emission standards that govern the acceptable emissions limits for vehicles' exhaust. They have forced the installation of catalytic converters to vehicles, reducing the road traffic NO<sub>x</sub> emissions by 60% [10]. The latest Euro 6 standard imposes strict limits to CO, NO<sub>x</sub> and particulate matter, and despite the recent findings of the systemic cheating on the emission tests by some car manufacturers, it has been a successful way of reducing the emissions. In the United States, similar legislature under the Clean Air Act and its amendments succeeded in reducing the transport section nitrogen oxides by 65% since 1990 [11].

In the last couple of years, the decline has somewhat decelerated, most likely due to the emergence of SUV vehicles and their increased fuel consumption. Still, the future with a high probability of hybrid, electric and hydrogen vehicles dominating the market combined with the strict and established regulations for ICE engines further reduces the significance of traffic NO<sub>x</sub> emissions.

In the United States, the Acid Rain Program has been implemented since the 1990s by the Environmental Protection Agency, aiming to reduce overall SO<sub>x</sub> and NO<sub>x</sub> emissions to 50% of 1980 levels. The program was deemed successful, and it implemented measures oriented primarily towards the coal-burning power plants. The approach for reducing NO<sub>x</sub> emissions was not as stringent, since it did not *cap* emissions or include allowances trading systems. Nonetheless, it achieved 85% reductions from the power plants compared to the 1995 values, according to the United States Environmental Protection Agency [12].

Although the industrial processes play an essential role in the economy, they account for

**Table 1.1**

Emission limit values for large combustion power plants in EU under the Directive 2010/75/EU [14], mg/(Nm<sup>3</sup>)

	<i>Thermal output, MW</i>	<i>Coal</i>	<i>Biomass</i>	<i>Peat</i>	<i>Liquid fuels</i>
SO <sub>x</sub>	50 to 100	400	200	300	350
	100 to 300	250	200	300	250
	>300	200	200	200	200
NO <sub>x</sub>	50 to 100	300	300		450
	100 to 300	200	250		200
	>300	200	200		150

a significant share of the emitted pollution due to discharge of air pollutants, wastewater and waste generation. Globally, 25% of NO<sub>x</sub> emissions in 2018 came from the industry sector, and the power production accounted for 16% [4]. As these facilities represent the large portion of the overall nitrogen oxides emissions, and due to being concentrated sources of pollution, the environmental focus on them is understandable. Among these concentrated sources, combustion power plants represent the largest individual facilities and have been subjected to a series of regulations. As a continuation of previous efforts to limit the pollution from industry and power generation in the EU, the Industrial Emissions Directive (2010/75/EU) from 2010 combined the regulations for large industrial emissions. The Directive introduced limitations for emissions of acidifying pollutants, ozone precursors and particles through the integrated approach to accessing the overall pollution of a facility; by incorporating the polluter pays principle; and by setting the limits according to the best available technologies.

Chapter III of Directive is focused on the emissions of combustion plants with thermal outputs larger than 50 MW, irrespective of the type of fuel used, of which there are more than 3500 in the EU. Although the installed capacity increased by 4% from 2004 to 2017, and the trend is declining, 141 plants emitted 50% of NO<sub>x</sub> emission, and just 61 of them were responsible for half of total large combustion plants SO<sub>x</sub> emissions [13].

In addition to the new industrial facilities, whose emission limits are set according to the best available technologies, the Directive also provides allowed emissions for large power plants granted permits before 2013 depending on the fuel used, as presented in Table 1.1. Adhering to the limits set for the existing power plants generally mandated installation of some kind of pollutant abatement system for NO<sub>x</sub> and SO<sub>x</sub>, depending on the fuel used. Additional directives are aimed at the medium and small-sized power plants, as they are more common in EU due to the greater significance of district heating systems.

Combined with Europe's shift towards renewable energy sources and the substantial emission reductions already made, the efficiency of implemented measures becomes clear. However, significant efforts are still needed in some parts of the world, since considerable amounts of

harmful emissions are still emitted. China, Asia and Africa are even more dependant on the fossil fuels, and the 90% of coal power plants installed during the last two decades were in Asia, providing flexible and affordable electricity for hundreds of millions of people [4]. Introduction of regulations on allowed emissions is inevitable for the rest of the world, especially with increased environmental pressures and adherence to the Paris agreement. Therefore, advanced technological solutions for emissions mitigation will be of crucial importance in the future, when the regulations force retrofitting of existing fossil fuel power plants and removal of *built-in* emissions. This will include addressing emissions from existing power plants and industrial facilities, cargo ships and infrastructure already in use. Besides the modifications on existing technology, designing new and more sustainable power plants with low emissions and abatement technologies will be needed.

China is presently experiencing severe air pollution, with high SO<sub>x</sub>, NO<sub>x</sub> and fine particulate matter emissions, causing 850 thousand premature deaths in 2017 [15]. As a part of China's three-year action plans, the 2013 Air Pollution Action Plan introduced stringent regulations on allowed emissions from fossil fuel power plants that aimed to reduce sulfur, nitrogen, and particulate matter emissions. To achieve the planned reductions, power plants required pollutant removal technology and nearly 70% of installed coal capacity has been retrofitted over the last decade to match the levels of gas-fired plants. Also, new power plants in some heavily polluted regions were prohibited, and at least 54 GW of smaller and sub-critical plants were prematurely shut down [4]. The results of the regulations confirmed the effectiveness of the measures and benefits of the focus on industry and power generation: China's overall man-produced emissions decreased from 2013 to 2017 by 59%, 21% and 33% for SO<sub>x</sub>, NO<sub>x</sub> and fine particulate matter, respectively [16]. Even greater success can be observed if only power generation emissions are considered. Then, reductions reach 65%, 60% and 72%, respectively. These reductions were enforced by implementing one of the world's strictest allowed limits for pollutants in industrial flue gases.

This progress represents notable achievements in the environment protection, even though some inconsistencies with reporting were present [16]. This is especially so if GDP per capita between 2010-2017 is considered, which was almost doubled in that period. However, although the achieved reductions are considerable, the absolute emission amounts are still significant, due to initially high values. Additionally, the 2018 Greenpeace ranking of Chinese cities showed that only 107 out of 338 reached World Health Organisation basic standard of 35 µg/m<sup>3</sup>, and neither reached recommended annual levels of 10 µg/m<sup>3</sup> [17].

In the latest plan, named *Action Plan for Winning the Blue Sky War*, the same approach was continued for the period 2017-2020. The plan puts more focus on particulate matter and imposes 18% reduction requirement compared to 2015, as well as a change of key polluted regions, responding to the real-world situation. The NO<sub>x</sub> and SO<sub>x</sub> emission targets are set to decrease by at least 15% from 2015 levels [18], which was a goal that was just a continuation of the previous period, lacked ambition, and took 2015 as the base year [19]. Although the



**Table 1.2**Emission standards for coal-fired power plants in the United States and China, mg/m<sup>3</sup>

		<i>China</i>	<i>United States</i>
NO <sub>x</sub>	existing	100	135
	new	50	95
SO <sub>x</sub>	existing	50/100/200	185
	new	35	136
Particulate matter	Existing	20/30	19
	new	10	12

reduction in pollutant emissions are impressive when considering that China is globally the greatest polluter and that just a couple of years ago did not have a systematic and ambitious pollutant reduction plan, there is still a long way ahead of achieving sustainability and mitigating the overall influence on the environment. However, once more, the increasingly strict regulations proved as a reliable pathway towards the emission reduction, and as a good set of measures for achieving sustainability without crippling impacts on the economy.

The trends and the reduction legislature laid out for NO<sub>x</sub> mostly stand for SO<sub>x</sub> as well. On a global scale, the emissions from industry, power and transport sectors account for over 90% of anthropogenic SO<sub>x</sub> pollution, and coal and oil are the sources of almost all of the emissions. Similarly, the SO<sub>x</sub> emission reductions were imposed in several big markets around the world. The EU achieved 92% reductions in 2018 compared to 1990 [8], and the United States and China also reported significant reductions. The success is mostly owed to the combination of measures aimed to remove pollutants from main emitting sources. Energy-related facilities with high contents of sulfur in fuels, such as coal or heavy fuel oil, were replaced with low-sulfur fuel such as gas or replaced by renewable energy sources. Additionally, SO<sub>x</sub> abatement technology was mandated for cleaning flue gases after the combustion.

## 1.2.2 Maritime Emissions

Besides the industrial facilities and fossil-fuelled power plants that were the initial targets for emissions reduction due to their sizes, spatially concentrated character and ability to reduce large amounts of emissions by focused measures, emissions from transport sector have also been targeted with the aim of reducing the impact on the environment. The already-mentioned Euro standards for vehicles with internal combustion (IC) engines imposed restrictions on pollutants such as NO<sub>x</sub>, CO, particulate matter and others, and the similar regulations are in place in the other parts of the world. However, the fossil fuel utilisation in maritime transport represents significant distributed sources of pollutants that has considerable negative impact on the environ-

ment, both locally and globally. Maritime trade accounts for 80% to 90% of global trade [20], and represents the most important mode for transporting the goods. Although the growth recently lost the momentum it had during last decades, it has peaked at 11 billion t of cargo annually [21]. Cumulative emissions from marine transport represent 3% of overall CO<sub>2</sub> emissions, which would position marine transport above Germany at 6<sup>th</sup> place, if it were taken as country [22]. However, despite the often-copied information about just the few of the world's biggest ships emitting more SO<sub>x</sub> than all the cars combined, transport by ships is the most energy-efficient mode of transport when the distance and the total volume of goods and people are considered. Its energy intensity has been declining, as the more efficient engines, designs and solutions are being investigated under the pressure for increased sustainability. However, the efficiency improvements were more than outweighed by gains in activity and the transport volume, thus increasing the overall emissions [22].

Ships are mainly powered by heavy fuel oil — the heavy residual of crude oil distillation. Heavy fuel oil (HFO) has tar-like consistency and is contaminated with high concentrations of sulfur, nitrogen and aromatics. This is the reason why it produces significantly more pollutants during combustion compared to other, lighter and higher distillation fractions. Nevertheless, it has been historically widely used in marine applications, due to lax regulations concerning the impact on the environment, and it is now a dominant fuel in international shipping, accounting for 79% of total fuel energy consumption [23].

Another reason is its price, which is 30% lower than the cleaner fuels, and has facilitated expansion of maritime transport. Usage of HFO for powering ships has stayed out of focus for long time, partly due to vastness of seas and oceans, but increasing evidences of global impacts of emitted pollutants and the growing amount of traffic through the most delicate areas such as Arctic, has forced imposing the control over emissions.

The maritime and air traffic were not included in the Paris Agreement, and no limits or the outlook were brought up. Therefore, the regulations by other governing bodies were needed to prevent the emissions acceleration. Moreover, with the other sectors on the way to emissions reduction, this could have led to marine transport being responsible for even higher portions of global emissions.

The International Maritime Organisation (IMO) is the United Nations agency responsible for introduction and maintaining the shipping regulations, safety, legal matters and environmental concerns. The most notable regulation for regulating pollution from ships is the 1973 International Convention for the Prevention of Pollution from Ships (MARPOL 73/78). With it and its Annexes, pollution by oil, harmful noxious liquid substances in bulk, garbage and sewage from ships is regulated. The last one is Annex VI [24], was brought up in 2005 and sets the requirements aimed for regulation of air pollution being emitted by ships. This includes the emission of ozone-depleting substances, NO<sub>x</sub>, SO<sub>x</sub> and volatile organic compounds from shipboard incineration. These regulations are mandatory for all ships sailing under flags of MARPOL parties, which accounts for more than 99% of global shipping tonnage. Besides the global limits

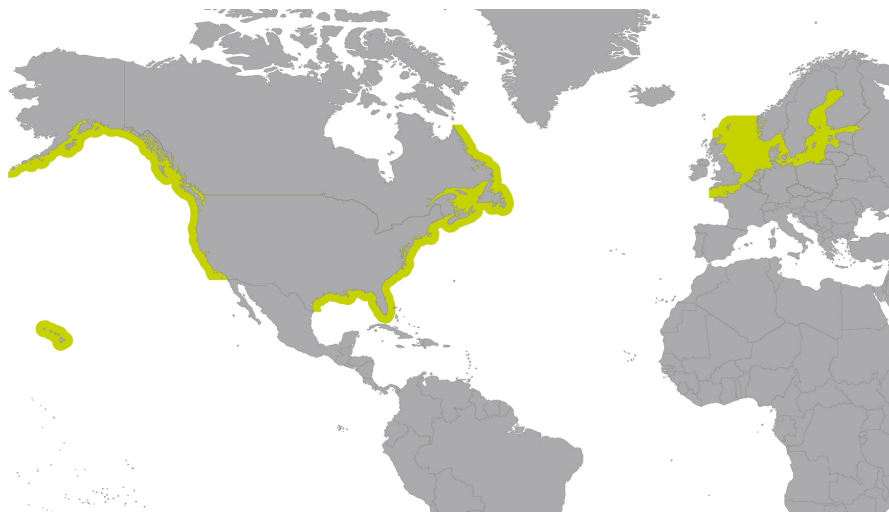


**Figure 1.1:** Currently established SO<sub>x</sub> emission control areas [25].

for pollutant emissions, several areas have been defined that fell under tighter regulations. Thus the Baltic Sea, North Sea, North American shores including most of Canada, the US, Caribbean and Hawaiian coasts are included in *Emission Control Areas* under the MARPOL convention, but additional restrictions have been imposed in several countries.

Ship-generated emissions into air can be significant in areas subject to heavy marine traffic, so many actions have been undertaken in recent years to significantly reduce them. Most of these actions have been imposed by the Annex VI of MARPOL, a treaty developed through the International Maritime Organization that establishes legally-binding international standards to regulate specific emissions and discharges generated by ships.

Nitrogen oxides released into air with flue gases from ships do not represent the most pressing issues, as their impact is smaller compared to carbon or sulfur emissions. Nonetheless, their allowed concentrations are regulated most recently in Tier III of the Annex VI, and concern ships with an engine output  $>130$  kW. Table 1.3 lays out the emission values for NO<sub>x</sub> allowed by the Annex VI, depending on the maximum engine speed. Tier III is prescribed for the control areas around North America, while Tier II is currently valid for the whole world. Since the introduction of these limits, shipowners have adapted either by altering the fuels used or using dual fuel systems, or by implementing technologies such as selective catalytic reduction or exhaust gas recirculation. However, the changes and limitations pertaining to the nitrogen emissions did not stand out as insurmountable issues and did not introduce large turmoil into the shipping sector, as is currently the situation with complying to new SO<sub>x</sub> regulations.

On the other hand, the limits imposed on SO<sub>x</sub> emissions from maritime sector during recent years led to bigger turmoil and uncertainties in shipping sector. Gradual tightening of the allowed emissions had forced shipowners to adapt and improve their fleets. Regulation 14 of Annex VI states the allowed sulfur quantities in fuels used in maritime applications — for main, auxiliary engines, and for all on-board devices such as boilers or gas generators — and regulates reduction

**Table 1.3**  
NO<sub>x</sub> emission limits for different engine speeds

	Year	NO <sub>x</sub> limit, g/(kWh)		
		$n < 130$	$130 \leq n < 2000$	$n \geq 2000$
Tier I	2000	17.0	$45 \cdot n^{-0.2}$	9.8
Tier II	2011	14.4	$44 \cdot n^{-0.22}$	7.7
Tier III	2016	3.4	$9 \cdot n^{-0.2}$	1.96

of these limits Fig. 1.3. The latest change occurred at the beginning of 2020, when a significant reduction of global limits decreased the sulfur mass fraction in fuels from 3.5% to only 0.5%. This reduction had a potential to severely impact the shipping industry and the global trade, as it is pertinent for all of the vessels globally. By limiting the amount of allowed sulfur in the fuel used to 0.5%, the aim was to reduce the emissions from shipping sector, while the time between the limit's affirmation in 2016 and its the start in 2020 provided sufficient time for adoption. In the meantime, the IMO brought up several reports, analyses and instructions helping the easier implementation of new limits.

Besides the newly-imposed global limits and the stricter regulations in IMO's emission control areas, another significant regions with restricted SO<sub>x</sub> emissions is the China's ECA. The sulfur content in fuel used in Chinese coastal waters 12 nautical miles from the coast and major river deltas is limited to 0.5%. The European Union has adopted the MARPOL convention and the global limits through its legislative, but has also introduced additional limitations. The Directive 2016/802 defines the maximum allowed sulfur content in fuel for ships at berth in European ports at 0.1% [26].

Despite the increased concern and stricter regulations on pollutant emissions, SO<sub>x</sub> and particulate matter emissions have actually increased during the recent years [23]. Even though the use of HFO has decreased, and the share of cleaner fuels such as liquefied natural gas or distillate fuels has increased — especially due to expansion of emission control areas in 2015 — the increase of average sulfur concentration in HFO and the rise in volume of maritime traffic have negated the benefits, as seen in Fig. 1.2. The IMO figures show that the global HFO yearly average sulfur content in 2018 was 2.6%, while the average for distillate fuel was 0.07% [27]. Additionally, in Fig. 1.2, the already-mentioned increase of carbon emissions can be noted, despite the less energy intensive engines, as well as slight increases in nitrogen-containing emissions.

Generally, the sulfurous emissions can be avoided either by primary measures, where the formation of pollutants is avoided altogether, or by secondary measures that remove the pollutants prior to discharge in the environment. The regulations are primarily aimed at the reduction of sulfur in fuel, which produces less SO<sub>x</sub> when burned in marine engines. The greater quality fuels stand as the obvious choice for complying with the new rules, but the change is not so

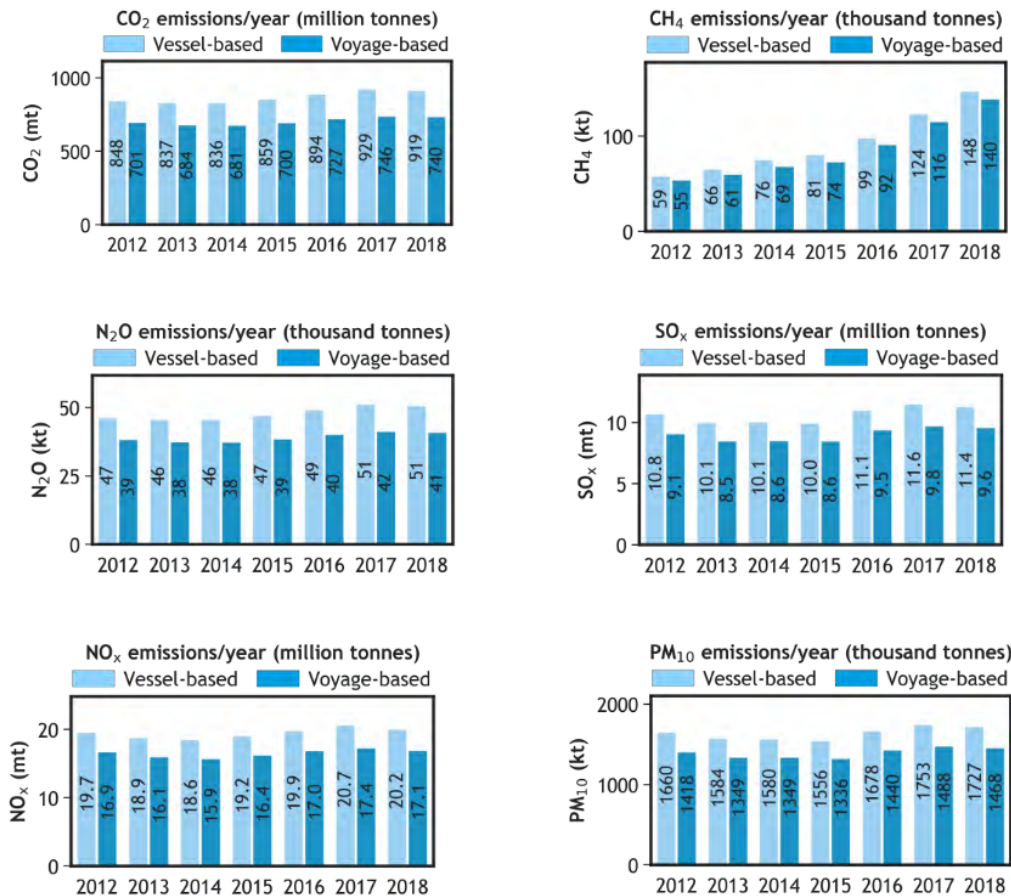


**Figure 1.2:** International shipping emission trends, 2012-2018 [23].

straightforward. Besides increased price of the low-sulphur compliant fuel oil, the fuel supply poses as a problem, since the refineries must adapt to the increased demand of the higher-quality fuel. However, it seems that the change transpired without the major hold-ups, mostly due to IMO's *Assessment of fuel oil availability* study [28] that correctly assessed the feasibility of the 2020 implementation, and the close collaboration between the institutions, shipowners and the refineries in preparing the transition. The fuel switch is the most commonly chosen way for adhering to the limits, and additional technical obstacle with new fuels can cause issues, as fuels have different physical and chemical properties. Ships can use either very- or ultra-low sulfur fuel oils which comply to the limits, or lower the overall sulfur concentrations by blending of additional distillates with existing heavy fuel oil. However, lower viscosity and density of new fuels can cause internal leakages in engines and machinery, they can have different handling temperatures and combustion characteristics. Furthermore, due to lack of standardisation for fuel blends, their quality can vary significantly, and the mixing of different fuels can cause issues, as some blends are incompatible and can lead to instabilities, which requires additional testing procedures and on-board fuel separation.

The above-stated, when coupled with the instability of the higher-quality fuels supply chain,

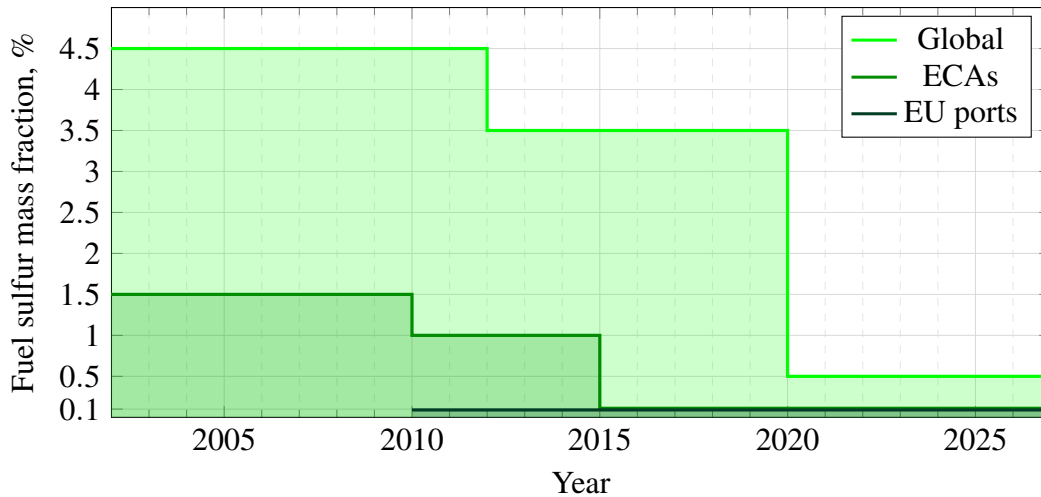


**Figure 1.3:** Allowed  $\text{SO}_x$  concentrations in fuel for marine engines.

pushed some of the shipowners in alternative direction, which is using the liquefied natural gas (LNG) as a marine fuel. LNG is cost-competitive fuel that can be used for powering ships and offers air pollution benefits. When combusted, it produces no sulfur-containing emissions, while its  $\text{NO}_x$  and particulate matter emissions are significantly lower. The use of LNG as fuel in ships has increased considerably in previous years, partly as a preparation for the IMO regulation change, and partly led by LNG's more affordable prices and diversified supply on the market. Retrofitting of the existing ships fuelled by heavy fuel oil to use LNG has proven to be economically infeasible as the capital investments are very high, and therefore most of the demand for LNG-powered vessels is driven by newly-built ships. Their numbers and demand has increased, raising from 77 in operation and 85 ships under construction in 2016 to 122 and 132 in operation and under construction in 2018, respectively [29]. Additionally, the orders for new LNG ships increased in 2019, in preparation for new limits starting in 2020. Although the LNG will have a more prominent position as a fuel for marine applications in the future, following its increasingly significant role in the global fuel mix, it is unlikely that the majority of ships will be powered by it. Although the changes are visible, the accompanying infrastructure required for fuelling, especially for smaller vessels, is still not developed, as the majority of terminals and storage facilities are designed for less frequent servicing of full-sized LNG carriers. Furthermore, the use of LNG as fuel, although highly beneficial when  $\text{SO}_x$  and  $\text{NO}_x$  emissions are concerned, seems to have detrimental consequences for greenhouse gases emissions. The increase of LNG is associated with significantly higher methane emissions due to *methane slip* during handling and incomplete combustion of fuel. The *Fourth IMO GHG Study* from 2020 determined that the methane emissions grew for 150% from 2012 to 2018 (see Fig. 1.2), and since methane is a greenhouse gas with significantly higher global warming potential, this increased emissions might negate the reduction in  $\text{CO}_2$  gained by using the LNG fuel [23].

Even though the LNG has seen a major increase in demand as a fuel for maritime applications, it is not predicted to dominate the market in future, but rather to take a place as one of the ways

of diversification in fuel mix, while complying with the stricter regulations concerning  $\text{SO}_x$ . Additionally, although the pipeline gas price is currently low, the LNG's cost highly depends on the liquefaction and bunkering costs, along with the availability of infrastructure [30]. When taken together with additional methane emissions (Fig. 1.2), and the waiting period for building or retrofitting of the LNG ship, many shipowners have turned to another way of adhering to the  $\text{SO}_x$  regulations, applying the secondary measures for removing the emissions.

The Regulation 4 of the Annex VI introduces an additional possibility for ships to satisfy the regulations. Alternative compliance method for new sulfur limits can be an *exhaust gas cleaning system* (EGCS). They should achieve at least the same efficiency at pollutant removal from flue gases as is required by the Annex. The IMO has released guidelines for EGCS [31], where details and requirements are stated, along with the detailed regulations concerning testing, survey certification and verification of these systems. The EGCS in ships is almost synonymous to the scrubbers — the gas–liquid contactors designed for increasing mass transfer between the phases. One of the several designs are the spray towers, commonly used in maritime applications, but more pertinent for the regulatory framework are the fluid used and the washwater design. Several alkaline chemicals are usually used in scrubbers, namely lime, limestone or sodium hydroxide solutions, but for maritime applications, using the seawater as a scrubbing agent has obvious benefit of availability. This is related to another choice, which is either closed- or open-loop design. With the open-loop design, water is taken from the surrounding sea and used in scrubber due to its natural alkalinity.

Scrubber effluent is then moderately processed, removing sludge, oils and particles, and then diluted with additional seawater before returning back into the environment. On the other hand, the closed-loop design features the closed system where the fluid is used for scrubbing, and repeatedly treated for re-use. The alkalinity is maintained by addition of alkaline chemical, but still some processed effluent remains unsuitable for re-use and it needs to be replenished with fresh seawater. Both options offer some benefits and downsides in their technical implementations, but the main ones are that the first one comes with the uncertainty about the washwater impact on the environment, while the second one entails additional storage and the more complex processing procedures. The Fig. 1.4 shows the schematics of both types of scrubbers on a ship. The increased complexity of the closed-loop scrubber can be noted, as the holding tank, water processing unit, tank for alkaline chemicals and more complex operation are required. Additionally, a hybrid design that is a combination of the two is possible, and its benefit is the ability to comply with the no-discharge rules in some locations, while also allowing for the easier operation when at other times.

The regulations for the EGCS are formulated regardless of the type of the scrubber, as they simply prescribe the required emission values. Table 1.4 lists the limits from the Regulation 4, which are based on the corresponding emissions between the fuel oil and its sulfur content and the required  $\text{SO}_2/\text{CO}_2$  ratio. The Guidelines provide more detailed insight on the rationale behind using the emissions ratio, but basically, it relates  $\text{SO}_2$  concentrations in flue gases to the

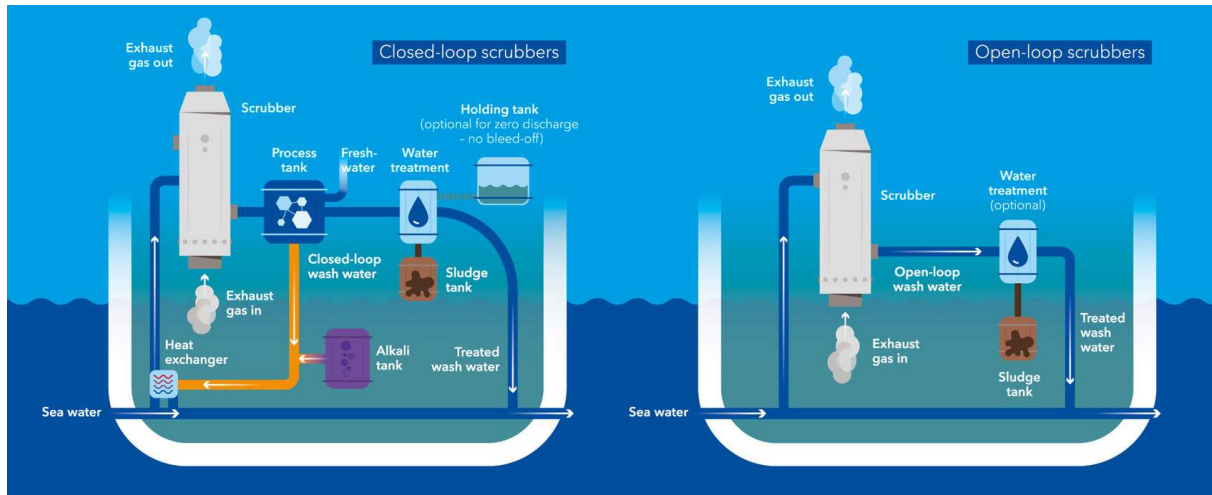


**Figure 1.4:** Exhaust gas cleaning system's design types [32].

**Table 1.4**

Fuel oil sulfur content and the corresponding flue gas emission ratios

Fuel oil S content, % m/m	Flue gas $\text{SO}_2/\text{CO}_2$ ratio, % %v
4.50	195.0
3.50	151.7
1.50	65.0
1.00	43.3
0.50	21.7
0.10	4.3

corresponding sulfur concentration in fuel. This method is quite universal, and with acceptable accuracy applicable to different engines at different speeds and power outputs and exhaust flows. No fuel properties are required, besides that the fuel is heavy fuel oil, or a petroleum-based fuel. Additionally, the only two measurements needed are the gas concentrations of  $\text{SO}_2$  in ppm<sup>1</sup>, and the  $\text{CO}_2$  as volume percentage (% %v). This method utilises the constant ratio between the carbon and sulfur independent of the fuel-to-air ratio, and simplifies the correspondence between required limits of sulfur in fuel with the required efficiencies of the scrubber systems.

Open loop scrubbers release their washwater while operating, and in order to prevent the harmful impact on the seas, the quality of effluent needs to be recorded and controlled. The Regulation prescribes that the monitored values should include pH, polycyclic aromatic hydrocarbons, turbidity and temperature. The washwater is acidic after the scrubbing process, and the effluent pH values are especially problematic when viewed in the broader picture. Although globally the influence of ocean acidification due to rising  $\text{CO}_2$  emissions has significantly more severe impact, local effects due to releasing the acidic effluent into mildly basic seawater might

<sup>1</sup>When using the *parts per* notation, the molar concentrations are tacitly assumed.



be significant [33]. Therefore, the acidity is prescribed not to decrease below 6.5 at the point of discharge, or not to cross the limit of 2 pH units between the intake and discharge during manoeuvring and transit.

The IMO published a study on environmental impact of scrubbers in 2019, which analyses the available literature and investigations of scrubber systems on marine life and biogeochemical processes [34]. The study displays the results of a comprehensive literature review, and finds two causes for concern, namely the scrubbers' efficiency for removal of other pollutants than SO<sub>x</sub>, and the impact of effluent discharge on the environment. The EGCS systems have been proven effective in removal of the sulfur-containing pollutants from flue gases to levels equivalent to using low sulfur fuel, but data indicates that the removal of particulate matter might be worse than compared to vessels powered by low-sulfur fuel. The second issue revolves around the acidic washwater resulting from the scrubbing process. This is a greater problem for open-loop scrubbers, as they need to neutralise the effluent which has significantly increased acidity, either by additional chemicals, or more commonly by dilution in seawater before being discharged. The available monitoring data shows that neutralisation is possible and effective, but the open-loop scrubbers require significant amounts of water, ranging roughly to 45 m<sup>3</sup> of washwater per MWh. The reviewed studies are divided about the long-term consequences of the acidification, stating that it is manageable and might not present a problem, but as not enough data is available, also call for more conservative approach and stricter IMO guidelines. This is the reason that, although the scrubbers are allowed by the IMO, some ports have restricted the overboard discharges from open-loop scrubbers, permitting only closed-loop or hybrid designs the method of compliance. For example, discharge of the open-loop type scrubbers is currently prohibited in Chinese ECAs, as well as in several European and other ports around the globe, with the remark for some of them that the ban is valid until the environmental standards are developed.

The uncertain situation in the global shipping sector and market introduced by the new regulations for SO<sub>x</sub> emissions makes it difficult to predict future trends and development. Although the measures were announced with enough time for preparation, the shipowners were not incentivised to make early adoptions, and the insecurity about the best strategies lead to delays in decisions. Additionally, the unforeseen disruptions caused by COVID-19 pandemic introduced additional uncertainties, delays, and decrease in market volume, reinforcing the conservative mindset. From the low numbers of approximately 350 installed scrubber units in 2016 [35], accounting for 1% of global vessels and mainly for use in the ECAs, the IMO's report forecasted the rise to 3000 to 4000 in 2020 [28]. Although the number of initial orders were low and mainly oriented on retrofits, they significantly increased during 2019 in preparation for new measures, although mostly for new builds. The official and exact numbers are hard to obtain, but it is estimated that approximately 3800 ships sailing globally will have installed scrubbers on-board, with additional ships on order [36]. On the other hand, some sources estimate the number to be lower, with 2815, 3169 and 3221 ships equipped with scrubbing systems reported or anticipated in 2019, 2020 and 2021, respectively [11].

The issues discussed above indicate that there are significant questions regarding the scrubber development for maritime applications. Besides the need for investigating the impact of pollutants and acidification on marine life and ocean chemical processes, additional optimisation of the scrubber design, chemistry and operation will be useful for complying with the regulations. Currently, without stricter environmental standards for control of seawater discharge and with the uncertainties about the long-term impacts of current scrubbers, the EGCS technology does not represent the ultimate solution for  $\text{SO}_x$  emission abatement. However, the spread of emission control areas and additional strictening of the allowed sulfur limits are to be expected in the future. The investigations of chemical and physical processes in scrubbers are therefore required for the improvement of their design and operation, as EGCS systems will be one of the crucial technologies for complying with the regulations concerning the  $\text{SO}_x$  emissions.

## 1.2.3 Pollutant Chemistry

### 1.2.3.1 Nitrogen Oxides

Nitrogen oxides, or  $\text{NO}_x$ , is a collective term for a family of chemical compounds containing nitrogen and oxygen. Among them, nitric oxide (NO), nitrogen dioxide ( $\text{NO}_2$ ), and nitrous oxide ( $\text{N}_2\text{O}$ ) are the most prevalent ones, formed by the anthropogenic activity. Nitrogen oxides emitted in the environment by human-generated sources have significant and harmful effect on health and environment, contributing in the formation of smog and acid rain, and some of them are greenhouse gases as well.

Elemental nitrogen present in atmosphere with almost 80% is exceptionally stable due to strong triple bond. High activation energy is required for breaking the bond and for nitrogen to participate in chemical reactions. This also means that the atomic nitrogen is highly reactive with three unpaired electrons, and that it can produce several nitrogen oxides.

Nitrous oxide  $\text{N}_2\text{O}$  is a chemical compound better known for its use as an anaesthetic, but it is a potent ozone-depleting substance and has been identified as a major culprit for the thinning of the ozone layer. It is also a greenhouse gas, having approximately 300 times higher global warming potential than  $\text{CO}_2$ . It is a non-reactive and long-lived pollutant with the half-life of more than 100 years, making it a considerable global pollutant despite its localised sources. Although  $\text{N}_2\text{O}$  is mainly produced by biogenic sources and nitrogen-based fertilizers, with comparatively smaller amounts originating from fossil fuel combustion, its role in greenhouse effect and ozone layer depletion is still significantly high.

Nitrogen dioxide  $\text{NO}_2$  is another major pollutant in the  $\text{NO}_x$  group. It is a reddish-brown gas mostly used in production of fertilizers, but otherwise significant as a pollutant.  $\text{NO}_2$  is produced by natural causes, such as the lightning, volcanic activity and bacterial respiration, however it is emitted mainly as a consequence of fossil fuels combustion in power plants and internal combustion engines.  $\text{NO}_2$  is a gas toxic to humans, and short exposures to air with

high concentrations of it can lead to lung injury and irritation, and can enhance respiratory diseases, while long term exposures can lead to development of chronic illnesses such as asthma, bronchitis or pneumonia. Additionally, its concentrations in residential areas have been linked to increased cardiovascular and respiratory diseases mortality. Although the  $\text{NO}_2$  is a primary pollutant, it also leads to formation of secondary pollutants such as ozone responsible for the photochemical smog.

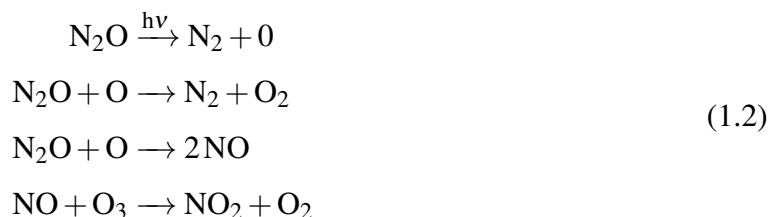
Nitrogen-containing emissions from fossil fuels combustion are released mainly as  $\text{NO}$ . It is a reactive species with one unpaired electron, and it rapidly converts into  $\text{NO}_2$ .  $\text{NO}$  is emitted mainly by combustion and human activities, and in lesser extent by the biogenic production, natural fires and lightning in thunderstorms. Nitrogen oxides are generally represented by nitrogen dioxide  $\text{NO}_2$ , as  $\text{NO}$  rapidly converts into it, and  $\text{N}_2\text{O}$  is not highly reactive. This makes  $\text{NO}_2$  the most common form of  $\text{NO}_x$  in the atmosphere that is generated by anthropogenic activities. Several pathways for formation of  $\text{NO}$  during fuel combustion have been identified. It can be produced by oxidation of atmospheric nitrogen at increased temperatures above  $1500^\circ\text{C}$  via *thermal* mechanism; by oxidation of nitrogen contained in heavier solid and fuels, dubbed *fuel* mechanism; and by *prompt* mechanism in reaction of atmospheric nitrogen with fuel radicals at the initial stages of combustion in fuel-rich mixtures (see Section 3.2).

Ultraviolet radiation hitting the oxygen molecules in the stratosphere photolytically breaks their bonds and forms atomic oxygen. These radicals then recombines with additional oxygen molecules, producing ozone molecules  $\text{O}_3$ . This naturally-occurring ozone in stratosphere absorbs ultraviolet light from roughly 200 nm to 315 nm wavelength while being destroyed, forming the *ozone layer* and protecting the Earth's surface from the majority of harmful radiation. The unpaired oxygen radical then reacts with the ozone molecule and forms regular oxygen molecules. This rapidly-occurring cycle of formation and destruction, equation (1.1), exhibits daily and seasonal variations, and is in equilibrium without external influences upon it.

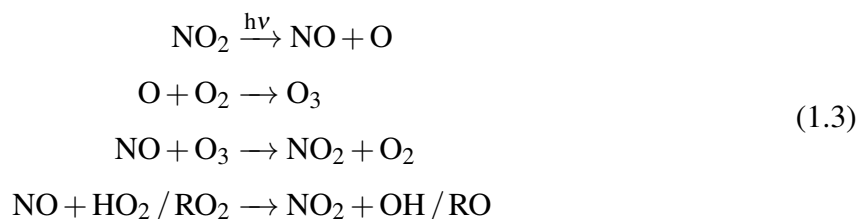


The anthropogenic pollutant emissions present a danger for the ozone layer. Besides the chlorofluorocarbons, which are the best known and most harmful ozone-depletion chemicals due to their amounts, the aforementioned  $\text{N}_2\text{O}$  plays significant role in destruction of ozone [37]. Usually non-reactive, the  $\text{N}_2\text{O}$  slowly reduced by the photolytic effects in atmosphere, seen in the first reaction in equation (1.2). However, in larger quantities it interferes with the regular ozone cycle, reacting with the atomic oxygen and forming nitric oxide  $\text{NO}$ . Additionally, the  $\text{NO}$  reacts with the ozone molecule, further reducing its concentration. The role of nitrous oxide

$\text{N}_2\text{O}$  is especially detrimental, as it both reacts in the ozone cycle and produces nitric oxide in the stratosphere, where it ordinarily does not reach due to its reactivity.



When ultraviolet radiation passes through the ozone layer, it leads to photolysis of nitrogen dioxide in the troposphere. In regular conditions and concentrations, this is a natural process because  $\text{NO}_2$  is present in the atmosphere in small quantities, but depleted ozone layer, increased ultraviolet radiation and  $\text{NO}_x$  exacerbates the effect. Photons excite  $\text{NO}_2$  molecule in troposphere, destroy its bonds and form  $\text{NO}$  and atomic oxygen radical. This process occurs during the day and, together with the emissions from fossil fuel combustion, represents the sources of  $\text{NO}$  and  $\text{O}_3$  via first two reactions in equation (1.3). During the night this process is ordinarily reversed by the third reaction, which consumes the ozone formed in the troposphere [38], regulating the process in equilibrium without net gain of  $\text{O}_3$ .



However, in the presence of volatile organic compounds — another group of harmful, human-produced chemicals — this cycle is also interrupted [39]. Therefore, the  $\text{NO}$  molecules no longer recombine with the ozone, but rather with the VOCs, namely  $\text{HO}_2$  and  $\text{RO}_2$  radicals. This way the additional  $\text{O}_3$  molecule is produced in the chemical balance and the ground-level ozone is formed in increasing quantities during the day, contributing to smog and other harmful impacts on health. This difference can be seen in Fig. 1.5, where the regular cycle is displayed on the left, compared with the impact of VOCs on the tropospheric nitrogen-ozone cycle on the right.

For completing the picture about atmospheric cycle of nitrogen oxides, additional pathway must be mentioned. The nitrogen dioxide  $\text{NO}_2$  can also react with ozone, forming  $\text{NO}_3$ , as can be seen in Fig. 1.6. This additional cycle can produce  $\text{N}_2\text{O}_5$  molecule, which can be photolysed back into  $\text{NO}_2$ , but more importantly, it creates a path for deposition from the atmosphere. This can occur either dry absorption into the ground, or by reaction with water and formation of nitric acid  $\text{HNO}_3$ . The overview of the whole nitrogen cycle in the atmosphere can be seen in Fig. 1.6.

Besides the direct harm on human health, ozone layer depletion and formation of tropo-

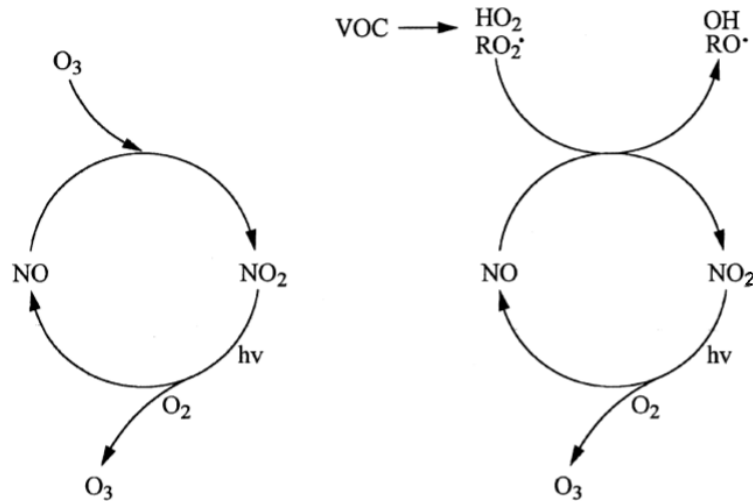


**Figure 1.5:** Interactions of  $\text{NO}_x$ , ozone and VOCs in troposphere [40].

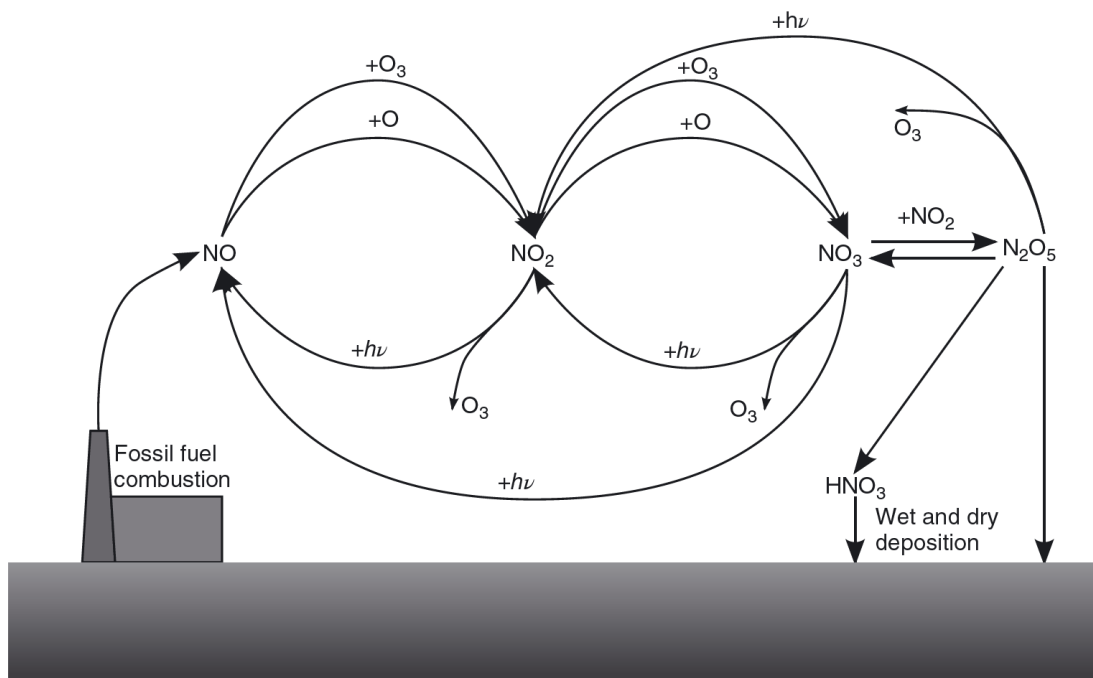
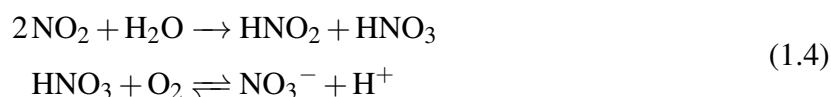


**Figure 1.6:** Nitrogen cycle in the atmosphere [41].

spheric ozone, nitrogen oxides impact the environment in another significant way. The unpolluted rainwater has a pH of about 5.6. The reason for it being slightly acidic is the natural presence of chemicals that form acids in reactions with water molecules in the atmosphere. The most important chemicals are  $\text{CO}_2$ ,  $\text{NO}$  and  $\text{SO}_2$ , which had been emitted from biological sources, microbial decay of organic material, volcanic eruptions, lightning and forest fires, but have always been integral parts of their respective atmospheric cycles. However, with the increased emissions from anthropogenic sources, their concentrations have risen, especially around

large industrial and highly populated regions. This has led to increased acidity of precipitation, either rain or snow, measuring the pH of around 4, with values as low as pH 2 reported in some cases. The acid rain causes the acidification of water surfaces, and although it has smaller effect on oceans compared to the acidification due to dissolved  $\text{CO}_2$ , it decreases the pH levels of lakes and coastal seas, significantly impacting the aquatic life-forms. Although the acid rainfall does not directly impact the human health, it damages the soil biology and chemistry and damages buildings by reacting with limestone and marble, or by increasing the corrosion rate of metals.



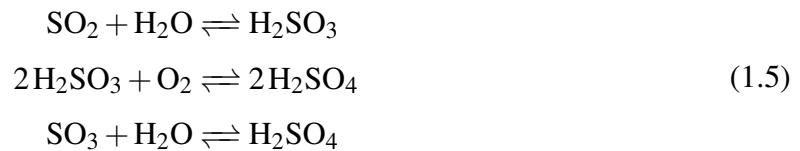
Besides the already mentioned pathway to nitric acid, additional reactions lead to acidification of rainwater. Nitrogen dioxide emitted from the combustion sources dissolves in water, forming nitrous and nitric acids, and the nitric acid dissociates in water and yields the nitrate ion  $\text{NO}_3^-$  and hydrogen ion  $\text{H}^+$  which increases the pH level and acidifies the solution, equation (1.4).

### 1.2.3.2 Sulfur Oxides

Sulfur oxides, generically termed  $\text{SO}_x$ , are another group of chemicals known for their contribution as pollutants. They are naturally present in atmosphere but their concentrations have been rising due to human activity. Volcanic eruptions can represent significant sources of sulfur oxides and severely impact the environment, but the increased anthropogenic emissions lasting for more than a century increased  $\text{SO}_x$  concentrations and have disturbed the global sulfur chemical cycle. They are emitted into the air mostly as a byproduct of fossil fuel combustion, especially in coal and fuel oil, as they can contain up to 5% of sulfur. Additionally, metal smelting and other industrial processes are also known as excessive  $\text{SO}_x$  sources. During the pyrolyzation of sulfur-containing compounds in the devolatilization phase of combustion, they react with the oxygen in the gas phase and produce sulfur oxides. Majority of fuel sulfur — up to 95% — is thus converted to the  $\text{SO}_2$ ,  $\text{SO}_3$  accounts for 1% to 4% of the sulfur, and  $\text{H}_2\text{SO}_4$  is usually emitted in even smaller amounts [42]. Brief exposures to  $\text{SO}_2$  can affect human breathing and be especially harmful for children, elderly and those who suffer from respiratory diseases, but it has greater consequences to the environment as well. Sulfur oxides reacting in the atmosphere promote formation of particulate matter, which present an additional impact on health. This way,  $\text{SO}_x$  is a secondary source to tropospheric smog, although they also have a minor influence in ozone production cycle [43].

Sulfur oxides are the main causes for the acid rain formation, accounting for approximately 75% of acidity in rainwater. This is because  $\text{SO}_x$  in atmosphere form the strong sulfuric acid in reactions with water, which readily dissociates and releases  $\text{H}^+$  ions, similarly to the reaction

of nitrogen oxides with moisture to form nitric acid [44]. The sulfur dioxide dissolves in water, forming sulfurous acid, which is subsequently slowly oxidised to sulfuric acid, equation (1.5). Another reaction path towards sulfuric acid is the hydration of sulfur trioxide with water in the atmosphere. In the aqueous phase, the sulfuric acid dissociates in two stages and significantly increases  $H^+$  ion concentration, and lowers the rainwater pH to dangerous levels, equation (1.6).



Dry and wet deposition of  $SO_x$  into the soil also affects the environment, modifying the chemistry of aquatic and terrestrial ecosystems, as well as causing excessive exfoliation in forests and vegetation.

The issue with listed effects of  $SO_x$  and  $NO_x$  pollutants is that besides the effects on the neighbouring areas around the industrial sources of pollution, their influences can be felt over the large distances. The pollutants can be distributed by air currents and diffusion to unindustrialised areas or to locations with delicate ecosystems, making the pollutants a global, cross-border problem. This was the motivation behind the legislature introduced during the last decades regulating the emissions, and it continues to be a problem in today's interconnected, highly-industrialised society. From the information presented insofar, it can be concluded that the environment protection has become increasingly important, but significant efforts will be needed in the future to reduce and reverse the impact that we have done. In battling the pollutant emissions, *business as usual* scenarios will not lead to the needed changes, but to uncertain future and possible ecological disasters. Only by improving the current technological solutions, increasing their efficiency and reducing negative effects on the environment will we be able to get closer to the sustainable future, clean nature and improved quality of living for all mankind. There is a great potential in designing better equipment for cleaner utilisation of solid fuels, as well as for improving the technology of pollutant abatement from flue gases, and this Thesis hopefully represents a small step towards that direction.

## 1.3 Hypothesis and Work Outline

The research hypothesis of this study is that newly-developed and upgraded mathematical models will enable the physically accurate and numerically efficient calculation of the complex physicochemical processes of nitrogen oxides formation during the combustion of pulverised solid fuels, as well as the calculation of sulfur dioxide removal from flue gases by seawater absorption in spray droplets and liquid wall film. Models will be developed within the commercial software for the CFD based on the control volume method and implemented in the code by the user functions and FORTRAN programming language. On the path towards the final models that describe pollutant behaviour in real industrial systems, a wide range of phenomena needs to be taken into account. Since the ultimate goal of this work is to develop comprehensive models that will capture the relevant physics and chemistry occurring in these processes, the structure of this thesis is divided into sections that follow the development of models and their validation.

Initially, the mathematical models used in this work are presented in Chapter 2, establishing the numerical framework of the approach. The essentials of the computational fluid dynamics are laid out, together with the basics of the finite volume method. Euler-Lagrange approach for modelling the two-phase flow is presented, as well as the discrete droplet model (DDM) that governs the dispersed phase behaviour. The rationale behind using the lumped-parameter approach for droplets and particles is given, with the basic equations governing the spray behaviour.

Chapter 3 focuses on the development of sulfur dioxide absorption model in pure and seawater, and lays out the physical and chemical background of the absorption process. Reactions in the liquid phase are presented, along with the modelling approaches. After that, the focus is shifted towards the issue of mass transfer across the phase boundary, and the intricate physics governing it. The used models are shown for individual absorbing droplets, and the verification of each section is presented. Subsequently, the model is expanded onto the whole spray in a three-dimensional environment and validated on available experimental cases. After that, development of SO<sub>2</sub> absorption model in wall film is presented, along with dimensionless and parametric analyses, the choice of suitable mass transfer modelling approaches, and the validation on simplified and real cases.

In Chapter 4, the nitrogen oxides formation modelling is presented. An overview of the previous research and approaches is provided, together with the common assumptions and issues with modelling. This section details the chemical pathways and reactions occurring during the combustion of solid fuel particle and provides detailed insight into the formation of nitrogen oxides, intermediate species, and the significant dependence on the fuel type and ambient conditions. Following is the overview of the experimental work done on examining the product species from the pyrolysis reactions, and integrating them into the simulation procedure.

Finally, Chapter 5 presents the conclusion based on the shown results, together with the guidelines and suggestions for further research.



## 1.4 Thesis Contribution

The expected contribution of this thesis is the enhancement of modelling tools for pollutant formation during the combustion of pulverised solid fuels and the pollutant removal from flue gases. A part of the presented work is focused on the development of flue gas desulfurisation model and its implementation in the CFD framework, which is expected to facilitate the research of technological solutions for sulfur dioxide removal in stationary and maritime applications. The adopted simulation approach integrates the relevant physical and chemical processes that govern the pollutant absorption in droplets and wall film, both for pure water and seawater. The model is the foundation for tools that will enable the design of highly efficient, energy-conserving and sustainable devices needed for the mitigation of the impact on the environment by the release of harmful sulfur oxides.

The presented work also augments the nitrogen oxides production model by integrating the experimental data into the chemical pathways model and can account for specifics of different solid fuel types. This approach simplifies the highly complex chemical processes during the fuel combustion, while maintaining the essential chemical background and taking into account all of the relevant physical processes.

Contributions of this research are:

- Development and implementation of sulfur dioxide removal model for the investigation of flue gases purification by absorption in droplets and wall film that could be used as a tool in industrial applications for desulfurisation process improvement.
- Improvement of the comprehensive numerical model for the formation of nitrogen oxides during combustion of pulverized solid fuels by using the weighted factors obtained by a novel method of quantification of coupled thermogravimetry and mass spectrometry.

## CHAPTER 2

# Numerical Modelling

The foundation of mathematical modelling is the computational fluid dynamics, which is an approach for numerical solving the fluid dynamics equations. The CFD is a widely used tool for scientific and industrial research, as it can be expanded to describe a broader range of phenomena than purely fluid flow. Within the CFD, the finite volume method is a discretisation method used for approximating the partial differential equations that describe the conservation laws as algebraic equations. It is conservative, which makes it especially suitable for simulations of fluid flows, ensuring the conservation of physical properties across the domain. The domain is spatially discretised into control volumes, connected elements over which the systems of algebraic equations are solved. The simulation is obtaining numerical solutions by marching through time-domain over discrete time steps, and different approaches for time and domain discretisation are available for different applications.

## 2.1 Conservation Equations

Beneath the CFD, which is just an approach for solving the equations, lie the physical laws that govern the processes. They are described by the conservation laws, stating that the particular property of an isolated system does not change over time. In their integral forms, and applied to the concept of control volumes, these laws account for the accumulation of the property in the volume, the net rate of flow across the boundaries, and for the sources or sinks in the volume.

Mass conservation is one of the fundamental law that ensures that inflow and outflow from the cell are balanced by the rate of change inside the cell. It is described by the continuity equation, which further states that there are no mass sources or sinks in the differential element of the volume; or rather that the mass flow is continuous.

$$\frac{\partial \rho}{\partial t} + \frac{\partial (\rho u_j)}{\partial x_j} = 0 \quad (2.1)$$

In the equation above,  $\rho$  is the fluid density,  $t$  is time,  $u_j$  are velocity vector components, and  $x_j$  represents coordinates. The first term describes the density change in the volume cell, while

the second one is the difference between the inlet and the outlet flux. For the incompressible fluid, density is constant, and there is no additional mass accumulation or loss in the cell.

For an infinitesimal fluid element, the momentum conservation stems from Newton's second law, which states that the rate of change equals the sum of surface and volume forces on the fluid particle.

$$\frac{\partial(\rho u_i)}{\partial t} + \frac{\partial(\rho u_j u_i)}{\partial x_j} = \rho f_i + \frac{\partial \sigma_{ji}}{\partial x_j} \quad (2.2)$$

Here, the momentum rate change is designated by the first term in the equation. The second term represents the net change of the momentum flux over the boundaries of the infinitesimal element. On the right side,  $f_i$  stands for the body forces acting on the element (gravity, electric and magnetic fields, centrifugal force), while the surface forces are represented by the fluid total stress tensor  $\sigma_{ji}$ . Since fluids do not exhibit static shear stress, total stress tensor  $\sigma_{ji}$  can be decomposed into two parts: the influence of fluid hydrostatic pressure  $p$  and the viscous stress tensor  $\tau_{ij}$ .

$$\sigma_{ji} = -p \delta_{ji} + \tau_{ji} \quad (2.3)$$

In the previous equation,  $\delta_{ji}$  is the Kronecker delta, a function of  $i$  and  $j$ , such that its value is 1 if  $i = j$ , and 0 if  $i \neq j$ . The viscous stress tensor displays the linear dependency on the rate of deformation, and under the assumption of isotropic fluid, it can be expressed as:

$$\tau_{ji} = \mu \left( \frac{\partial u_i}{\partial x_j} + \frac{\partial u_j}{\partial x_i} \right) - \frac{2}{3} \mu \delta_{ji} \frac{\partial u_k}{\partial x_k}, \quad (2.4)$$

where  $\mu$  denotes the fluid viscosity. By combining the previous equation with equation (2.3), the momentum conservation equation for the infinitesimal fluid element is obtained.

$$\frac{\partial(\rho u_i)}{\partial t} + \frac{\partial(\rho u_j u_i)}{\partial x_j} = \rho f_i - \frac{\partial p}{\partial x_i} + \frac{\partial}{\partial x_j} \left[ \mu \left( \frac{\partial u_i}{\partial x_j} + \frac{\partial u_j}{\partial x_i} \right) - \frac{2}{3} \mu \frac{\partial u_k}{\partial x_k} \delta_{ji} \right] \quad (2.5)$$

This equation represents momentum conservation in three Cartesian coordinates, and along with the continuity equation form the Navier-Stokes equations, which are the foundation of the fluid flow modelling and the CFD. Further, the angular momentum conservation for fluid is reduced to the symmetry of the stress tensor,  $\sigma_{ji} = \sigma_{ij}$ .

The energy conservation law states that the energy cannot be destroyed or created, but only transformed between the types, leaving the total energy of the isolated system unchanged. For the non-relativistic conditions, it is an additional law separated from the mass conservation, but it requires an additional constitutional equation for completion. The total energy is defined as the combination of the kinetic energy and the internal energy of fluid,  $e = \frac{1}{2} u_i u_j + i$ , and the

basic conservation equation is:

$$\frac{\partial(\rho e)}{\partial t} + \frac{\partial(\rho u_j e)}{\partial x_j} = \rho f_i u_i + \frac{\partial(\sigma_{ji} u_i)}{\partial x_j} - \frac{\partial q_j}{\partial x_j} + S_e. \quad (2.6)$$

Analogous to the previous examples, the first term on the left side represents the rate of change of total energy, the second represents convective fluxes across the boundaries. On the right-hand side, the first term is the power from the body forces, and the second is the influence of surface forces, divided further into pressure forces and the viscous stress:

$$\sigma_{ji} = -p \delta_{ji} + \tau_{ji}. \quad (2.7)$$

The third term in the equation (2.6) is the heat flux density vector  $q$ , representing the heat conduction, and the final term stands for energy sources due to radiation or exothermic chemical reactions.

The additional constitutional equations are required for completion, and it is defined by the Fourier's law of conduction. It relates the heat flux vector through the surface to the temperature gradient, with the assumption of isotropic fluid.

$$q_j = -\lambda \frac{\partial T}{\partial x_j} \quad (2.8)$$

The  $T$  in the equation (2.8) is temperature, and the  $\lambda$  is the thermal conductivity. By combining the previous equations, an expanded version of the conservation law can be obtained.

$$\frac{\partial(\rho e)}{\partial t} + \frac{\partial(\rho u_j e)}{\partial x_j} = -p \frac{\partial u_j}{\partial x_j} + \frac{\partial}{\partial x_j} \left( \lambda \frac{\partial T}{\partial x_j} \right) + \Phi + S_e \quad (2.9)$$

Additionally, for chemically reactive flows where species transport is relevant, an additional expression is used for describing the chemical species mass conservation. This is important for modelling of combustion processes, chemical reactions and species absorption. The mass fraction of chemical species  $Y_k$  is defined as the ratio between the mass of the species  $m_k$  and the total mass of the volume  $m$ .

$$Y_k = \frac{m_k}{m} \quad (2.10)$$

Analogous to the previous equations, the first term in Equation (2.11) is the accumulation, the second represents the net change of mass flux over the boundaries. The third one is the diffusion of species, commonly described by the Fick's law, stating that the mass flux is proportional to the species concentration gradient and the diffusivity coefficient. Chemical reactions are accounted

for by the last term, which represents sources or sinks of the reactants and products.

$$\frac{\partial(\rho Y_k)}{\partial t} + \frac{\partial(\rho Y_k u_j)}{\partial x_j} = \frac{\partial}{\partial x_j} \left( \rho \Gamma_k \frac{\partial Y_k}{\partial x_j} \right) + S_k \quad (2.11)$$

## 2.2 General Transport Equation

The analogy between the conservation laws mentioned in the previous chapter leads to the derivation of a general form of the conservation law, which can be applied to any physical property represented by a scalar or a vector. The transport equations are the building blocks of the CFD, as all the physical properties follow the identical procedure, and since developing new models, or including a description of a new property, follows the uniform approach.

$$\frac{\partial(\rho \phi)}{\partial t} + \frac{\partial(\rho \phi u_j)}{\partial x_j} = \frac{\partial}{\partial x_j} \left( \rho \Gamma_\phi \frac{\partial \phi}{\partial x_j} \right) + S_\phi \quad (2.12)$$

In a transport equation, the first term on the left side is the temporal rate of change of some scalar value  $\phi$  and represents the accumulation in the cell volume. The second one is the convective term, which describes the flux of the property  $\phi$  over the cell boundaries. The first term on the right side is the diffusive term that represents the flux over the volume boundaries due to the concentration gradient, with  $\Gamma$  being the diffusion coefficient. Finally, the last term represents the volumetric source or sink of the transported scalar value.

## 2.3 Turbulence Modelling

The conservation laws presented above were discussed without the regard for the regime of the flow they are describing. In nature, two types of fluid flows are encountered: laminar and turbulent. Laminar flows are stable and display orderly and smooth behaviour without disruptions between layers. Turbulent flows, on the other hand, are characterised by the intensive mixing, with fluid particles exhibiting chaotic movement between the layers. They are highly unstable, with three-dimensional vortices of different sizes mixing the flow, thus increasing diffusivity. The vortices manifest as pulsations in local pressure and velocity with different temporal and spatial frequencies. Turbulence depends on flow velocity, fluid viscosity and the characteristic length of the flow, and is more pronounced with the increase of non-dimensional Reynolds number ( $Re$ ) that is used for describing it.

Kolmogorov's concept of *energy cascade* is, at present, the most widely accepted theory describing turbulence [45]. It describes turbulence as eddies of decreasing sizes, each carrying energy corresponding to their length scale. The energy is transferred from the larger eddies

by their break-up to smaller ones until the energy of the smallest vortices is dissipated via molecular viscosity as heat. Based on this concept, the numerical solution of Navier-Stokes equations for fluid flow can be calculated, resolving the flow to the scale of the smallest eddies. This necessitates the use of very fine meshes, and a large number of cells, scaling with the  $Re^3$  [46]. Similarly, to capture high-frequency pulsations of fluid particles, the time discretisation also needs to be very fine, leading to significant requirements on computational power. This approach is referred to as Direct numerical simulations (DNS) and, although the present-day computational resources are increasing, it is still unfeasible to apply it on industrial applications [47].

To circumvent the prohibitive computational requirements of directly resolving turbulent flows, statistical analysis has been used to reduce the problem's complexity. Random flow fluctuations are statistically averaged, approximating their solution. Large eddy simulation (LES) is an approach that partially introduces the statistical modelling for turbulence on lower spatial scales, where it is assumed to be isotropic, but fully simulates large turbulent structures [48]. It is therefore computationally less demanding than the DNS, but its complexity depends on the limit below which the smaller vortices are filtered, and the sub-grid scale models are applied. The application of LES is rising along with the increase of available computational resources, but it still has not been widely applied for industrial applications.

Lastly, the whole turbulent field can be resolved by modelling. The results obtained by DNS provide information about the flow on a very fine scale and in a high number of time steps, which is preferable for the detailed analyses of fluid flow and the investigation of turbulence. However, for the majority of uses, and especially for engineering applications, averaged values of physical fields and their integral variables are of interest. Therefore, the approach that incorporates averaging of the physical variables before the Navier-Stokes equations is applied as a way of significantly simplifying numerical solving of the fluid flows. Averaging can be performed on time- and on space-basis, while the former is more widely used. One of the techniques available is the Reynolds decomposition, where the instantaneous variable of some physical quantity  $\phi$  is decomposed into the time-averaged component  $\bar{\phi}$  and its fluctuating value  $\phi'$  [49].

$$\phi(x_i, t) = \bar{\phi}(x_i) + \phi'(x_i, t) \quad (2.13)$$

The Figure 2.1 illustrates the decomposition and the background of the Reynolds-averaged Navier Stokes equations (RANS). It solves only the mean variables, and the details of turbulence are modelled. RANS approach utilises the time averaging for the mean value  $\bar{\phi}$  as described in Equation (2.14).

$$\bar{\phi}(x_i) = \lim_{T \rightarrow \infty} \frac{1}{T} \int_t^{t+T} \phi(x_i, t) dt \quad (2.14)$$

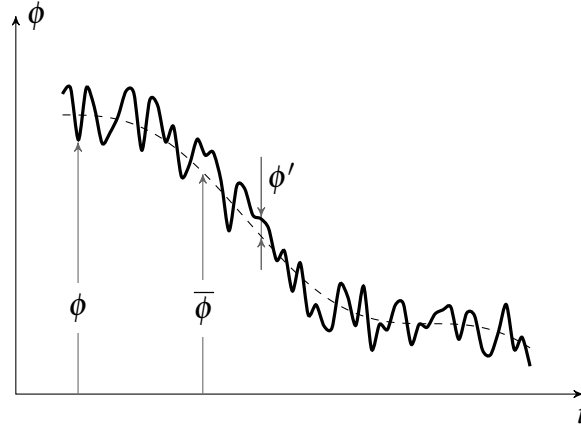


**Figure 2.1:** Decomposition of instantaneous turbulent flow into mean and fluctuating values.

### 2.3.1 Incompressible Flows

The incompressible formulation of the conservation laws is considered, as turbulence models have been developed initially for these flows [50]. In incompressible flows, the density is taken as constant, so the continuity equation from (2.1) reduces to

$$\frac{\partial u_j}{\partial x_j} = 0. \quad (2.15)$$

If Reynolds decomposition, equation (2.13), is applied to the continuity equation, along with the averaging rules ( $\overline{\overline{\phi}} = \overline{\phi}$ ;  $\overline{\phi'} = 0$ ), an averaged continuity equation is obtained:

$$\overline{\frac{\partial u_j}{\partial x_j}} = \frac{\overline{\partial \overline{u}_j + u'_j}}{\partial x_j} = \frac{\partial \overline{u}_j}{\partial x_j} = 0. \quad (2.16)$$

Analogously to the continuity, the momentum conservation equation for the averaged values is derived. The viscous stress tensor for incompressible flows is reduced to the first term in equation (2.4), as the divergence of the velocity field in the second term equals zero. After inserting velocity decomposed into the mean and pulsating part, the identity for viscous stress tensor for average velocity and incompressible flow is obtained.

$$\tau_{ji} = \mu \left( \frac{\partial \overline{u}_i}{\partial x_j} + \frac{\partial \overline{u}_j}{\partial x_i} \right) \quad (2.17)$$

When the expression above is applied to the momentum equation (2.2), along with the decomposition of velocity, and taking into account that the product of two fluctuating parts does not equal zero, the following form is obtained.

$$\frac{\partial (\rho \overline{u}_i)}{\partial t} + \frac{\partial \rho \left[ (\overline{u}_i \overline{u}_j) + \overline{u'_i u'_j} \right]}{\partial x_j} = -\frac{\partial \overline{p}}{\partial x_i} + \frac{\partial}{\partial x_j} \left[ \mu \left( \frac{\partial \overline{u}_i}{\partial x_j} + \frac{\partial \overline{u}_j}{\partial x_i} \right) \right] \quad (2.18)$$

This equation for averaged velocity is similar to the original incompressible conservation equation, except for the addition of the product of fluctuating velocities which are caused by the non-linear convective term. This new product is a symmetrical second-order tensor, which introduces six additional unknowns, and represents the turbulent diffusion of momentum. By rearranging the convecting term and grouping the new tensor with the molecular diffusion. The new term also acts as stress and is labelled Reynolds stress tensor  $\tau_{ij}^R$ .

$$\frac{\partial(\rho\bar{u}_i)}{\partial t} + \frac{\partial\rho(\bar{u}_i\bar{u}_j)}{\partial x_j} = -\frac{\partial\bar{p}}{\partial x_i} + \frac{\partial}{\partial x_j} \left[ \mu \left( \frac{\partial\bar{u}_i}{\partial x_j} + \frac{\partial\bar{u}_j}{\partial x_i} \right) - \rho\overline{u'_i u'_j} \right] \quad (2.19)$$

With the introduction of Reynolds stress tensor, the system contains more unknowns than the number of equations. Therefore, additional equations are needed for solving this *closure problem*, which is achieved by modelling the turbulence.

### 2.3.2 Compressible Flows

Compared to the incompressible flows, density changes due to pressure variations or combustion processes can be significant in compressible flows. Reynolds averaging can become complicated if used in compressible flows, as products of fluctuating density and velocity  $\overline{\rho' u'_i}$  and triple correlation with  $\rho', u'_i$  and  $u'_j$  appear in continuity and momentum equations, respectively [51]. Therefore, it is more convenient to use mass-based averaging, to simplify derivations and avoid additional terms. Favre averaging [52] decomposes the instantaneous variable to the average and fluctuating one, similarly to the Reynolds averaging:

$$\phi = \tilde{\phi} + \phi'' , \quad (2.20)$$

where  $\phi''$  represents the fluctuating value, and the averaged value  $\tilde{\phi}$  is defined as follows, with  $\bar{\rho}$  being the Reynolds-averaged value:

$$\tilde{\phi} = \frac{1}{\bar{\rho}} \lim_{T \rightarrow \infty} \frac{1}{T} \int_t^{t+T} \rho(x_i, t) \phi(x_i, t) dt . \quad (2.21)$$

Following are the continuity and momentum equations for compressible flow and Favre-averaged values. They are derived analogously to the RANS equations, and together comprise the Favre-averaged Navier-Stokes equations (FANS).

$$\frac{\partial\bar{\rho}}{\partial t} + \frac{\partial(\bar{\rho}\tilde{u}_j)}{\partial x_j} = 0 \quad (2.22)$$

$$\frac{\partial(\bar{\rho}\tilde{u}_i)}{\partial t} + \frac{\partial(\bar{\rho}\tilde{u}_i\tilde{u}_j)}{\partial x_j} = \bar{\rho}\bar{f}_i - \frac{\partial\bar{p}}{\partial x_i} + \frac{\partial\tau_{ji}}{\partial x_j} - \frac{\partial(\bar{\rho}\widetilde{u'_i u'_j})}{\partial x_j} \quad (2.23)$$

Here, as well as with the RANS equations, an additional term  $-\bar{\rho}\widetilde{u'_i u'_j}$  is introduced com-



pared to the regular Navier-Stokes equations. It is a consequence of non-linearity of convective terms: turbulence is highly sensitive to perturbations, and needs to be modelled with additional equations, since averaging does not reduce the order of the problem. This Reynolds stress tensor is, therefore, a central issue in turbulence modelling. It is a symmetrical second-order tensor with six unknowns, shown below, and it represents.

$$\tau_{ij}^R = \overline{\rho u_i'' u_j''} = -\overline{\rho} \begin{bmatrix} \overline{u_1''^2} & \overline{u_1'' u_2''} & \overline{u_1'' u_3''} \\ \overline{u_2'' u_1''} & \overline{u_2''^2} & \overline{u_2'' u_3''} \\ \overline{u_3'' u_1''} & \overline{u_3'' u_2''} & \overline{u_3''^2} \end{bmatrix} \quad (2.24)$$

The trace of the Reynolds stress tensor matrix represent the normal stresses, and is usually isolated to form the turbulent kinetic energy.

$$k = \frac{1}{2} \overline{u_i'' u_i''} = \frac{1}{2} \left( \overline{u_1''^2} + \overline{u_2''^2} + \overline{u_3''^2} \right) \quad (2.25)$$

### 2.3.3 Closure Problem

One of the most important ideas behind turbulence modelling is the Boussinesq hypothesis [53]. It is based on the idea that the momentum transfer in turbulent flows is predominantly influenced by the large and turbulent vortices that mix the flow. The hypothesis assumes that the turbulent stress tensor is linearly dependent on the mean velocity gradients, analogously to the laminar flows. The proportionality factor is called *turbulent* or *eddy viscosity*  $\mu_t$ . It is not related to any physical property of the fluid involved, but to the flow conditions[54]. Therefore, if we decompose the Reynolds stress tensor similarly to equation (2.4), we can obtain the Boussinesq hypothesis for the compressible flows as follows:

$$\tau_{ij}^R = 2\mu_t \widetilde{D}_{ij} - \frac{2}{3} \left( \mu_t \frac{\partial \widetilde{u}_k}{\partial x_k} \delta_{ij} + \overline{\rho} \widetilde{k} \delta_{ij} \right), \quad (2.26)$$

where  $\widetilde{D}_{ij}$  represents the Favre-averaged strain rate tensor. By removing the divergence term, one can obtain the incompressible form of the equation, while the last term on the right is often omitted in simpler turbulence models.

The eddy viscosity approach is interesting in engineering approaches to turbulence since modelling of turbulent viscosity  $\mu_t$  is sufficient for closing the system of equations. It has become the basis of simpler closure models for more straightforward applications

While the linear dependency of turbulent stress tensor on the velocity gradient made calculations simpler, the assumption of the equilibrium between the turbulence and the averaged strain is not always valid. For the flows with abrupt changes of strain, significant curvature of streamlines, flows in ducts and turbomachinery, an improved correlation was needed. By introducing the non-linear eddy diffusivity models, additional accuracy and applicability to wider range of

fluid flows can be achieved [55].

Based on the order of relations for velocity, actual turbulence models can be divided in several categories:

- Algebraic (zero-equation) models

In zero-equation models the turbulent viscosity is algebraically determined — the solution does not require additional equations as the turbulence is calculated just from the flow property. They are usually not detailed enough, as they do not account for the convection and former diffusion effects on the turbulent energy. Following the approach by Prandtl, the turbulent viscosity  $\mu_t$  is calculated through the turbulent velocity  $u_t$  from the turbulent length scale  $l_m$  [56]. The latter is the unknown dimension that is obtained based on the experimental measurements.

$$\bar{\mu}_t = \rho u_t l_m \quad (2.27)$$

- One-equation models

In one-equation models, rather than calculating the characteristic turbulent velocity algebraically, an assumption is made that connects the turbulent velocity with the turbulent kinetic energy  $k$ .

$$\mu_t = \rho \sqrt{\bar{k}} l_m = \rho \sqrt{\frac{1}{2} \overline{u_i'' u_i''}} l_m \quad (2.28)$$

One-equation models account for the past flow turbulence by solving a single transport equation for turbulent kinetic energy. These models introduced transport properties in the turbulence calculation, but due to need for algebraic formulation of turbulent length scale, the improvement compared to zero-equation models was not so significant.

- Two-equation models

In two-equation models an additional transport equation is calculated for resolving the turbulent length-scale issue. The choice of additional variable depends between the models, but the most commonly used ones are dissipation rate  $\varepsilon$  or the specific dissipation rate per turbulent kinetic energy  $\omega = \varepsilon/k$ . These models are commonly used in engineering applications, as they represent a compromise between speed and accuracy. Many variations have been developed, and the two-equation models are still actively researched. However, for more accurate results and turbulence-focused research, DNS and RANS are more relevant.

- Second-order closure models

Also called the Reynolds stress transport models, these represent the set of models that solve transport equations for each of the six unknown components of stress tensor. They

are computationally more demanding, and also include additional models for diffusion [46].

### 2.3.4 $k$ - $\varepsilon$ Turbulence Model

As was mentioned previously, the  $k$ - $\varepsilon$  model is a two-equation approach which introduces two additional transport equations to the Navier-Stokes equations to deal with the closure problem. The physical properties tracked are the turbulent kinetic energy  $k$  and turbulent dissipation rate  $\varepsilon$ . It is based on the linear Boussinesq approach and the assumption of turbulence being isotropic and is likely the most widely used turbulence model. It can be traced to the work by Chou [57], but a large number of model variations has been presented since, most notably by Launder and Spalding [58], who introduced so called *standard*  $k$ - $\varepsilon$  model.

From the dimensional analysis, the turbulent length scale proportionality to the turbulent kinetic energy and dissipation rate is obtained:

$$l_m \propto \frac{k^{3/2} \varepsilon}{\varepsilon}. \quad (2.29)$$

When the previous equations is applied to the  $\mu_t$  dependency to  $k$ , equation (2.28), the following expression for eddy viscosity is obtained, with the variable  $C_\mu$  being a model constant.

$$\mu_t = C_\mu \rho \frac{\bar{k}^2}{\bar{\varepsilon}} \quad (2.30)$$

Two additional transport equations are presented below, derived from the general transport equation equation (2.12).

$$\frac{\partial (\rho \bar{k})}{\partial t} + \frac{\partial (\rho \bar{u}_j \bar{k})}{\partial x_j} = \frac{\partial}{\partial x_j} \left[ \left( \mu + \frac{\mu_t}{\sigma_k} \right) \frac{\partial \bar{k}}{\partial x_j} \right] + G - \rho \bar{\varepsilon} \quad (2.31)$$

$$\frac{\partial (\rho \bar{\varepsilon})}{\partial t} + \frac{\partial (\rho \bar{u}_j \bar{\varepsilon})}{\partial x_j} = \frac{\partial}{\partial x_j} \left[ \left( \mu + \frac{\mu_t}{\sigma_\varepsilon} \right) \frac{\partial \bar{\varepsilon}}{\partial x_j} \right] + C_1 G \frac{\bar{\varepsilon}}{\bar{k}} - C_2 \rho \frac{\bar{\varepsilon}^2}{\bar{k}} \quad (2.32)$$

In the equations above,  $G$  represents the generation of turbulent kinetic energy:

$$G = \mu_t \left( \frac{\partial \bar{u}_i}{\partial x_j} + \frac{\partial \bar{u}_j}{\partial x_i} \right) \frac{\partial \bar{u}_i}{\partial x_j}. \quad (2.33)$$

The rest of the unknowns are the model parameters, or closure constants, which can be adjusted on a case-to-case basis. However, the set of values presented below covers a wide range of industrial applications can be found in Table 2.1.

The  $k$ - $\varepsilon$  model found its application in a wide range of engineering applications, but it has significant drawbacks that need to be taken into account.

Standard model  $k$ - $\varepsilon$  models degrade for flows with significant pressure gradients, and these

**Table 2.1**  
k- $\varepsilon$  model constants

$C_\mu$	$C_1$	$C_2$	$\sigma_k$	$\sigma_\varepsilon$
0.09	1.44	1.92	1.0	1.3

types of models can not correctly resolve the near-wall flows and turbulent variables, requiring high resolution of the grid in near walls. Further, k- $\varepsilon$  models tend to overestimate the kinetic energy production, which is commonly solved by implementing the damping functions for the near-wall behaviour.

### 2.3.5 $k$ - $\zeta$ - $f$ Turbulence Model

A large number of turbulence models has been developed since the initial ones, and different models, their variants and improvements are still being investigated. The basic two-equation k- $\varepsilon$  model does not produce correct results in the vicinity of the wall, as they assume isotropic turbulence, while it has strongly anisotropic character. The mentioned damping functions are an improvised solution since they essentially represent curve-fitting of the results in the near-wall region. Durbin [59] applied a different approach, by introducing an additional transport equation for the *velocity scale*  $\overline{v^2}$ , which represents the velocity fluctuations in the direction normal to the streamlines. Additionally, the elliptic relaxation concept that accounts for the anisotropic turbulence was introduced by the differential function  $f$ . Together, they form the  $\overline{v^2}$ - $f$  model, which is simple but physically based. It is suitable for use in industrial applications, as it represents a compromise between the robust, but simple two-equation models, and the physically more sound, but stiff models for full Reynolds stress tensor [60]. The stability of simulations with the original version of this model was sensitive to cell sizes near the wall, as function  $f$  was inversely proportional to the fourth power of the distance to the cells. This issue can be solved by using coupled solvers, but a different version of eddy-viscosity model, called the  $k$ - $\zeta$ - $f$  model, also aims to resolve these issues. It was presented by Hanjalić et al. [61], and it is an eddy-viscosity model-based Boussinesq hypothesis and the Durbin's concept of elliptic relaxation. Instead of  $\overline{v^2}$ , a transport equation for the *velocity scales ratio*  $\zeta$  is used. It is defined as the ratio  $\overline{v^2}/k$ . This formulation is significantly more robust and insensitive to grid issues.

This model retains the elliptic relaxation and the sensitivity to inviscid wall conditions, together with the relaxed stiffness of the function  $f$  [62]. Turbulent viscosity is similar to previous expressions:

$$\mu_t = C_\mu \rho \zeta \overline{k} \tau. \quad (2.34)$$

Turbulent time and length scales  $\tau$  and  $L$  are required as parts of the model. They are defined

**Table 2.2**  
k- $\zeta$ - $f$  model constants

$C_\mu$	$C_{\varepsilon 1}$	$C_{\varepsilon 2}$	$C_1$	$C'_2$	$\sigma^k$	$\sigma^\varepsilon$	$\sigma^\zeta$	$C_L$	$C_\mu$	$C_\tau$
0.22	$1.4(1 + 0.012/\zeta)$	1.9	0.4	0.65	1	1.3	1.2	0.36	85	6.0

below, bounded by the Kolmogorov scales on the lower end, and combined by the Durbin's realizability constraints [63].

$$\tau = \max \left[ \min \left( \frac{\bar{k}}{\bar{\varepsilon}}, \frac{a}{\sqrt{6}C_\mu |S| \zeta} \right), C_\tau \left( \frac{v}{\varepsilon} \right)^{\frac{1}{2}} \right] \quad (2.35)$$

$$L = C_L \max \left[ \min \left( \frac{\bar{k}^{\frac{3}{2}}}{\bar{\varepsilon}}, \frac{\bar{k}^{\frac{1}{2}}}{\sqrt{6}C_\mu |S| \zeta} \right), C_\mu \left( \frac{v^3}{\varepsilon} \right)^{\frac{1}{4}} \right] \quad (2.36)$$

In the equation above, the recommended value for  $a$  is 0.6, and the rest of the model parameters are given in Table 2.2 [64]. The variable  $S$  stands for mean strain rate.

$$\begin{aligned} |S| &= \sqrt{S_{ij}S_{ij}} \\ S_{ij} &= \frac{1}{2} \left( \frac{\partial u_i}{\partial x_j} + \frac{\partial u_j}{\partial x_i} \right) \end{aligned} \quad (2.37)$$

Finally, three transport equations are presented for the properties that are being tracked — turbulent kinetic energy  $k$ , turbulent energy dissipation  $\varepsilon$ , and the velocity scales ratio  $\zeta$ .

$$\frac{\partial}{\partial t} (\rho \bar{k}) + \frac{\partial}{\partial x_j} (\rho \bar{u}_j \bar{k}) = \frac{\partial}{\partial x_j} \left[ \left( \mu + \frac{\mu_t}{\sigma^k} \right) \frac{\partial \bar{k}}{\partial x_j} \right] + G - \rho \bar{\varepsilon} \quad (2.38)$$

$$\frac{\partial}{\partial t} (\rho \bar{\varepsilon}) + \frac{\partial}{\partial x_j} (\rho \bar{u}_j \bar{\varepsilon}) = \frac{\partial}{\partial x_j} \left[ \left( \mu + \frac{\mu_t}{\sigma^\varepsilon} \right) \frac{\partial \bar{\varepsilon}}{\partial x_j} \right] + \rho \frac{C_{\varepsilon 1} G - C_{\varepsilon 2} \bar{\varepsilon}}{\tau} \quad (2.39)$$

$$\frac{\partial}{\partial t} (\rho \zeta) + \frac{\partial}{\partial x_j} (\rho \bar{u}_j \zeta) = \frac{\partial}{\partial x_j} \left[ \left( \mu + \frac{\mu_t}{\sigma^\zeta} \right) \frac{\partial \zeta}{\partial x_j} \right] + \rho f - \rho \frac{\zeta}{k} G \quad (2.40)$$

The elliptic relaxation function  $f$  is defined as follows:

$$L^2 \frac{\partial^2 f}{\partial x_j^2} - f = \frac{1}{\tau} \left( C_1 + C'_2 \frac{G}{\bar{\varepsilon}} \right) \left( \zeta - \frac{2}{3} \right). \quad (2.41)$$

The mentioned advantages in physical accuracy and stability are complemented by additional numerical benefits. For example,  $\varepsilon$  does not appear in the  $\zeta$  equation, which is favourable since it is difficult to correctly reproduce near the wall. Instead, the turbulence kinetic energy production is present, and it is significantly easier to obtain. The additional fact that benefits the stability is the dependence of  $\zeta$  to distance to wall. Compared to the  $y^4$ , now it scales with  $y^2$ , which

improves stability of the computational schemes. Together with the use of hybrid wall treatment introduced by Popovac et al. [65], the  $k-\zeta-f$  stands as a universally applicable model for different applications and  $y^+$  values, with increased numerical robustness and more accurate results than the two-equation models [66].

## 2.4 Spray Modelling

So far, only the mathematical modelling of single-phase fluid flows has been discussed. However, the CFD spans into different areas and can be used in diverse applications, and modelling of multiphase flows is a crucial topic significant for many technical systems. Spray modelling is of particular interest for researchers, since spray processes lie as a foundation of many industrial applications, with combustion, gas turbines, IC engines, rocket propulsion, spray cooling and painting being just a few of them. Modelling of single-phase fluid flow is based on the fluid dynamics and the continuum assumption. Usually, the rate of change occurring in the fixed point of space is of greater interest than the behaviour or the shape of individual fluid segments at the referenced time. Therefore, the Eulerian approach is dominantly utilised in fluid flow modelling, together with the introduction of the *control volume* — a subdomain in which processes are investigated. Previously presented conservation laws were derived with the Eulerian approach, which is essentially a field specification.

In contrast to Eulerian, the Lagrangian approach represents discrete tracking of individual fluid segments in different time steps throughout the domain. Each of the approaches has its benefits for different applications: the Eulerian approach more naturally matches the fluid flow modelling, while the Lagrangian description is more suitable for solid mechanics since the ability to control the shape of the domain of interest is lost when applied to fluid flows. Nevertheless, the approaches are analogous, and their relation is expressed by the concept of *material derivative*. It describes the rate of change of some property for the fluid segment travelling along the pathline. In equation (2.42) the left side represents the material derivative, or the Lagrangian rate of change, while the first term on the right side stands for the Eulerian rate of change, and the last term represents the convective rate of change.

$$\frac{D\phi}{Dt} = \frac{\partial\phi}{\partial t} + u_i \frac{\partial\phi}{\partial x_i} \quad (2.42)$$

For multiphase modelling, both the continuous and discrete phases need to be described. As a continuation of single-phase modelling, the Eulerian description has been applied to the second phase as well. This is the *Euler-Eulerian* approach, where discrete particles are represented by one or more separate phases and additional sets of transport equations governing their behaviour. The Euler-Eulerian description is most suitable for the dense sprays and the locations near the nozzle, where the assumption that the discrete phase acts as homogeneous fluid is valid

[67]. Although the method has some drawbacks, such as losing the shape of liquid spray and unsuitability for the dilute spray regions, this approach gained popularity in recent years and is still being actively researched.

The more conventional concept for multiphase modelling is the Euler-Lagrangian approach (EL). The Eulerian description is still used for the continuous phase, but the discrete particles are tracked by the Lagrangian formulation. The initial research of the EL can be traced to the 1950s and is the prevailing numerical concept for multiphase modelling [68], capable of describing both liquid droplets and solid particles. The liquid sprays differ significantly in their characteristics and droplet sizes, depending on the applications. Aerosols and fine spray injections in internal combustion engines form droplets as small as  $10\mu\text{m}$ , while rain and low-pressure atomizer droplets are in the millimetre range. In addition to the significant size difference, the number of droplets that rises to  $1 \times 10^8$  makes tracking of every droplet computationally prohibitive [69].

A practical alternative to tracking absolutely every discrete particle is the *Discrete droplet method* proposed by Dukowicz [70]. It arranges the spray particles into statistical classes called *parcels*, which represent mutually non-interacting particles with identical properties that are being tracked through the domain by the Lagrangian approach. The DDM approach is suitable for high-pressure sprays in IC engines with high momentum and entrainment, reactive sprays in combustion applications and chemically reactive applications. The phases are fully coupled, and the interactions between them are accounted by the source terms in the continuity, momentum and the energy equations. This approach contrasts some atmospheric pollution approaches, which assume that the discrete phase does not influence the flow, and are reduced to tracking particles in the velocity field. The EL method avoids numerical diffusion, and represents the statistical approach to spray modelling, with the initial droplet velocities, positions, and particle size distributions individually assigned. The original method by Dukowicz was limited only to the constant-sized particles, but the present model in AVL FIRE<sup>TM</sup> accounts for evaporation and reactive sprays, together with other phenomena. However, there are several drawbacks of the EL and the DDM approaches, such as the computational intensity when dealing with large number of droplets. In contrast to Euler-Eulerian method, which is suitable for the dense spray region, assumptions for the EL methods are not valid for near-nozzle regions: liquid volume fraction is no longer low, and the parcels are not equally distributed across the domain [71]. Furthermore, to increase the numerical stability, the cell sizes around the nozzle need to be larger than the orifice dimensions. This ensures low volume fraction, but decreases the spray resolution. Another difficulty with the standard DDM method is the treatment of parcels as concentrated sources, which can lead to numerical instabilities unless interpolation is included [72].

By considering the forces acting on a parcel in a Lagrangian framework, one can obtain the ordinary differential equations describing motion and tracking the parcels in three-dimensional space.

$$m_d \frac{du_{id}}{dt} = \sum F_i \quad (2.43)$$

The force that needs to be taken into consideration is the drag on the particle travelling in the gas phase. The drag force  $F_{id}$  is given as:

$$F_{id} = D_d u_{irel} , \quad (2.44)$$

where  $D_d$  represents the velocity-dependent drag function, defined as:

$$D_d = \frac{1}{2} \rho_g A_d C_D u_{irel} . \quad (2.45)$$

In the equation above,  $\rho_g$  is the gas phase density, and  $A_d$  is the parcel cross-sectional area, and  $u_{irel}$  is the relative velocity between the fluid and dispersed droplet. Drag coefficient  $C_d$  is taken for a single sphere, and the expression depends on the droplet Reynolds number. To account for the reduced drag coefficient on small particles, the Cunningham correction factor  $C_p$  has been implemented in AVL FIRE™ software [73].

$$C_d = \begin{cases} \frac{24}{Re_d C_p} (1 + 0.15 Re_d^{0.687}) & Re_d < 10^3 \\ \frac{0.44}{C_p} & Re_d \geq 10^3 \end{cases} \quad (2.46)$$

The Reynolds number for particles is used in equation (2.46), where the physical properties are related to the gas phase, the velocity is relative between the phases, and the characteristic dimension used is droplet diameter:

$$Re_d = v_d \frac{\rho_g u_{abs} d_d}{\mu_g} . \quad (2.47)$$

Even though the drag is the dominant forces acting on the particle, the effects of gravity can also be significant. Gravity is taken into account together with the effects of buoyancy, as following:

$$F_{ig} = (\rho_p - \rho_g) g_i . \quad (2.48)$$

The instantaneous particle position is determined by integrating the velocity, so the position vector is obtained:

$$\frac{dx_{id}}{dt} = u_{id} . \quad (2.49)$$

During the years since the DDM approach was introduced, additional submodels were introduced to expand the physicality of the model. For example, interaction of discrete phase and turbulence was investigated by Gosman and Ionnides [74]. It includes the stochastic influence of turbulent dispersion by adding the fluctuating velocity  $u_{ig}$ .



## CHAPTER 3

# Sulfur Oxides Removal

## 3.1 Technology Overview

The  $\text{SO}_x$  or  $\text{NO}_x$  emissions from combustion sources can generally be avoided by couple of approaches: i) using the fuels with low sulfur or nitrogen contents chemically bound in them; ii) by implementing modifications during combustion, such as burner optimisation, altering the combustion parameters, or injection of chemicals into combustion chamber; iii) or by employing the post-combustion technologies for gas cleaning. For the part of this Thesis revolving around the controlling the sulfur oxides emissions, the focus will be placed on the latter approach. Technologies for  $\text{SO}_x$  removal from the combustion gases are collectively called *flue gas desulfurization*, FGD. Cleaning is generally achieved by scrubbing processes, which are used for removal of particulates and pollutant gases from exhaust streams.

### 3.1.1 Flue Gas Desulfurisation

Originally, the scrubbers were designed for carbon dioxide removal in first submarines, but have found more widespread application in industrial gas cleaning in 1930s and onwards. Due to increasing concern for the health and the environment, but certainly bolstered by the regulations forcing the reduced emissions, there has been a significant increase in the desulfurisation capacities in the previous decade. For example, just in the period between 2006 and 2009, China equipped 422 GW coal power plants with  $\text{SO}_x$  removal technologies, increasing the coal power capacities equipped with the  $\text{SO}_x$  scrubbers from 10% to 71% [75]. The installed capacities increased further, and Tang et al. claim that by the end of 2017 nearly all of the coal-fired power plants in China had installed  $\text{SO}_x$  removal equipment [18]. Wet limestone systems accounted for roughly 85% of installed stationary systems, while seawater was used as absorbent in approximately 2.5% systems in 2016. On the other hand, the United States had the 140 GW, or 42% of installed coal capacities, equipped with desulfurisation technologies prior to 2008 [75]. These numbers are in rough agreement with the US Energy Information Administration's data for 638 power plants with 151.5 GW of associated net summed capacity in 2008 [76]. The growth in

the United States has not been as outstanding as in China, as the number of power plants with desulfurisation capabilities rose to 661, accounting for the 214 GW of installed capacities.

The economics of desulfurisation system installation in power plants is difficult to discuss, as myriad of factors can influence costs and profitability. Additionally, different types of power plants are subject to different regulations in countries around the world, making the detailed comparison unfeasible. Besides being out of scope of present work, the analysis is further aggravated by the non-existence of the widely available data on the costs of equipment, as well as by the different financial penalties and benefits included in the choices around the desulfurisation systems. Nevertheless, the data for Chinese coal power plants report that the operation and maintenance costs of both new and retrofitted facilities ranged from 1.8 to 4.1 \$/MWh in 2008 [75]. For the United States, the reported figures are somewhat lower, but still in the similar range. The average operation and maintenance costs were at 1.44 \$/MWh in 2008 and increased to 2.08 \$/MWh in 2018 [76]. Additionally, the installed capital costs were reported from 158 \$/kW to 358 \$/kW, possibly ranging more due to particularities and sizes of installed equipment.

Exhaust gas cleaning systems on ships are comparatively new application and the data is not available for longer historical trends, but the more dynamic market with higher numbers of installed scrubbers in recent years allow for more information about the capital investments. However, since the optimal path and the ideal solution for complying with the IMO sulfur limits has not yet crystallised, capital costs still vary significantly with the scrubber type, ship design, configuration and performances. The estimations in 2012 placed the installation costs of 1 MW wet scrubber at around \$ 1 million, and the scrubber for 20 MW engine at \$ 2 to 5 million [77]. Total capital costs of a wet seawater scrubber installed in 2014 for cleaning the gases of a 3.5 MW engine were at \$ 3.2 million, with the scrubber system accounting for roughly the half of the price, while the rest of the amount was spent on designing, installation and retrofitting [78]. The numbers given by the EGCSA, the association for promoting the exhaust gas cleaning systems and associated supporting technologies, fall into this range, as they report \$ 1 million for 1 MW and \$ 3 million for 20 MW engines. The indicative price of 125 to 375 USD per kW can be used as an approximation for capital costs. On the other hand, annual operating costs are reported at \$ 43.5k for a 1 MW engine, and \$ 477k for a 20 MW engine, which can be approximated to 3% of the capital investments. Similarly, the reported power consumption for seawater scrubber is between 10 to 30 kWh/MW [77]. In the end, the overall profitability depends on larger number of factors, and is hard to be accessed unless examined on a case-to-case basis. Differences between the designs, ships, technology, as well as the volatile price of heavy fuel oil or low-sulfur alternatives can affect the best solution. Further, and as the number of installed scrubbers will grow, the technology will mature and the prices will drop as well.

Initially, scrubbers implied the *wet* design with liquid medium for cleaning pollutants from flue gases, but more recently, the *dry* approach is included as well, where dry reagents or slurry have been used to clean the exhaust gases. Wet scrubbing brings the liquid in contact with flue gases and the pollutants are absorbed or washed away, with some of the scrubbing agents being

lime and limestone suspensions, sodium hydroxide [79] and magnesium hydroxide solutions [80], or seawater. Wet process can remove soluble gases as well as solid particulates, but usually the scrubbers for coal power plants that emit increasing amounts of fly ash are coupled with electrostatic precipitator or a baghouse filters for better removal efficiencies and easier operation. Wet processes are a choice for the majority of applications, accounting for more than 85% of installed removal capacity [81], but dry scrubbing offers some benefits as well. Wet scrubbers achieve higher pollutant removal efficiencies — easily over 90% and for some designs even above 99%, while dry scrubber systems generally demonstrate lower efficiency [80]. Generally, the choice of the desulfurisation design depends on the plant size and the targeted emission removal, and the wet design is chosen for the large projects with higher removal requirements, while dry design is usually installed in smaller applications, power plants with sizes less than 200 MW. Additionally, it has been reported that dry scrubbers require more space and heavier equipment, while achieving lower efficiency levels at around 80%, making their implementation in ships prohibitive [82]. Scrubbing with liquid agents offers greater flexibility in operating conditions — flue gases with higher temperatures and high humidity can be treated without issue, and liquid surface area can be modified more easily compared to the injection of solids.

The main benefit of dry scrubbing is the reduced production of waste materials and its easier handling, as wet scrubbing can produce considerable amounts of slurry [83]. This can present a greater issue for the scrubbers installed on ships that require closed-loop operation in some ports, increasing the system's complexity and mass (Section 1.2.2). However, dry scrubbing using the solid alkaline sorbents can only be used for acid gases removal and suffers from issues with particle agglomeration. However, despite the mentioned lower efficiency, it found its way in limited number of applications [84]. The wet process offers better flexibility for possible operating conditions, offers greater choice of scrubbing chemical agents and are preferred when high  $\text{SO}_x$  removal efficiency and removal of particulate matter are needed, and is thus more represented in industrial applications [85].

Operational issues characteristic for wet scrubbers can cause issues: solids build-up and clogging — especially when the entering flue gases contain high levels of particulates; freezing of the piping and the equipment at low temperatures; corrosion occurring in system due to exposure to water and chemicals. Therefore, higher maintenance is required [86]. Care has to be taken when designing the hydrodynamics of wet scrubbers as well, since the pressure drop through the system can be considerable and affect the fluid flow. Similarly, the exhaust gases after the desulfurisation exit the scrubber with high humidity and lowered temperature, which can impact buoyancy, dispersion of gases, increase ground concentrations of pollutants or cause condensation in chimneys, sometimes leading to the need for reheating of gases [87], which likewise raises the temperature above the dew point, preventing condensation of sulfuric acid.

### 3.1.2 Scrubbing Liquids

In wet scrubbers, the exhaust gases are brought into contact with liquid medium, which absorbs pollutants into the liquid phase. The process can be divided into physical and chemical absorption, where the first part includes dissolution of the compound, while the second one occurs when the absorbed compound and the solvent react chemically. Depending on the application, different chemicals can be used as scrubbing liquids and chemical absorption may limit the process, but typically the rate limiting step is the physical absorption between the phases. Generally, the scrubbing liquids are alkaline solutions, and their use increases the capability for SO<sub>2</sub> absorption by additional neutralisation of the formed H<sub>3</sub>O<sup>+</sup> ions. Most widely used type of wet flue gas desulfurisation is scrubbing with lime or limestone, which are calcium-containing chemicals [88]. It is a mature technology, in development since the 1970s, and presently accounts for the great majority of the globally installed desulfurization capacity. It is characterised by high desulfurisation capacities and efficiencies, stable and simple operations. Both lime and limestone are only dispersed in water and pumped as slurry, since they do not readily dissolve in aqueous solutions. Sulfur dioxide is absorbed and reacts with limestone or lime, producing calcium sulfite CaSO<sub>3</sub>. The cost of materials is not prohibitive to their use as they are abundant, but still, the operating cost connected with their transport and preparation are not insignificant [89]. Limestone is preferred, since lime has higher price and requires more complex preparation, but it provides better pH stability due to faster dissolution. The process results in a slurry which can be dried and the solid residue is easier to transport and handle. Furthermore, by the oxidation of slurry, gypsum is obtained, which is then used as plaster in construction, allowing for some reduction of operating costs [90]. The main drawback of this process is a tendency for nozzles and pipes clogging and scaling over scrubber walls and packing material. The calcium compounds produced in the process accumulate in recirculation loops, and the clogged nozzles reduce efficiency by affecting the atomisation of spray droplets. This leads to operation issues and increased maintenance, and necessitates simpler geometries for the scrubbers.

Besides the widespread limestone process, technologies with other scrubbing agents have also been developed and implemented. Neutrality of the scrubbing liquid can be achieved by dissolving sodium hydroxide or magnesium hydroxide in water, usually in a closed-loop regenerative systems. Another example of the desulfurisation technology is the Wellman–Lord process, in which sulfur dioxide reversibly reacts with sodium sulfite, followed by the regeneration stripping process in an evaporator, producing the stream of SO<sub>2</sub> in steam. This approach is characterised by the low environmental impact, as it avoids the waste disposal and raw material supply, but its complexity is significantly higher, and the maintenance and capital costs are presently prohibitively high.

Additionally, alternative approaches that employ sodium bicarbonate [91] or hydrogen peroxide solutions [92], ozone oxidation systems [93] or the use of electrical discharges [94] have been developed, but despite offering some advantages over the more conventional processes

such as avoiding residual sludge, decreased fouling, requirement for large amounts of reactants and others, they still account only for a fragment of total installed scrubbing capacities due to their disadvantages or novelty.

On the other hand, utilisation of seawater in flue gas scrubbing stands as a promising alternative technology for pollutant removal that avoids using additional chemicals. This approach has been first proposed by Bromley [95] and has since been investigated and applied in industrial applications. The obvious benefit of seawater is its abundance and availability in locations near the sea, so the desulfurisation process is possible in the coastal power plants which already commonly use seawater for cooling purposes. Additionally, the previously discussed regulations and requirements concerning the emissions from maritime applications opened the way for increased application of the seawater desulfurisation processes in ships. The fresh seawater is generally alkaline, with the pH values slightly above neutral — from 7.9 to 8.4 — and fluctuating with the location and seasons [96]. Seawater has a complex and varying chemical composition with salts and ions such as sodium, chloride, magnesium, sulphate and calcium. The dissolved alkaline compounds in seawater — mainly carbonate and bicarbonate ions — contribute to its intrinsic alkalinity, which generates a buffering effect, conserving the pH values. This enables higher absorption capacities of seawater compared to the physical absorption in pure water and stands as a basis behind the seawater scrubbing process.

Seawater used as a scrubbing agent offers high removal efficiency — the literature sources somewhat disagree on the exact numbers, but the consensus is that the efficiency is similar to other wet scrubbing technologies. For example, Wang et al. state that the efficiency is about 90% [96], and the literature review by del Valle-Zermeño et al. found that the efficiency lies in the range of 92% to 97% [89]. These results are in agreement with the work by Oikawa et al., who reported measurements from the 600 MW power plant equipped with the seawater desulfurisation system. The removal efficiency was 90% to 98%, but with somewhat lower sulfur content in coal at 1%, which corresponded to SO<sub>2</sub> concentration of 500 ppm to 700 ppm in flue gases. This issue is connected to the reported lower capacity of seawater absorption compared to lime-based alkaline solutions. The alkalinity of seawater is regionally dependent and can vary considerably, which can lead to decreased capacity for absorption and lowered removal efficiency in presence of high-sulfur conditions [82]. Consequently, this can require increased amounts of seawater for desulfurisation and more careful design of systems. On the other hand, Pandey et al. [97] and Radojević [98] state in their works that the removal efficiency of seawater systems is 99%, which indicates dependency on seawater, scrubbing conditions, design solutions, as well as the need for further research.

Research and development of seawater systems has lead to the point that it is a technology competing with the more common alkaline systems. Its advantages over the lime and limestone systems are easier preparation and decreased cost of material procurement. Operating costs and maintenance are generally lower, as seawater does not cause clogging and scaling as limestone scrubbing. Still, due to larger flows of liquid medium required, seawater scrubbing consumes

more power for pumps, spraying and circulation. Capital investments are more favourable for seawater scrubbing as well, due to the easier preparation and treatment, and can account for as little as  $\frac{1}{3}$  of the conventional alkaline scrubbing facility [96]. Nevertheless, seawater systems presently do not take up a large share of land-based desulfurisation capacities, as they were implemented in approximately 1% of power plant FGD systems in 2000s [89]. However, seawater scrubbing has a different outlook in maritime applications, where it is a dominant technology for FGD, especially after the recently-imposed restrictions on  $\text{SO}_2$  emissions. In maritime transportation, diesel engines represent the majority of installed powering devices, with two-stroke, low-speed diesel engines being used almost exclusively for large ships due to high efficiency and ability to use cheap HFO. The cost of fuel comprises  $\frac{2}{3}$  of the total freight cost, according to some estimates [99], and this explains the need for fuel efficiency. This presents another obstacle for the change to low-sulfur fuels for avoiding the  $\text{SO}_x$  emissions. A study by Ma et al. [100] compared greenhouse gas emissions and total energy consumption on a well-to-wake bases, and concluded that installing the seawater after-treatment systems might be better and more economical than switching to more expensive low-sulfur fuels.

Besides the mentioned advantages and potentials of the seawater scrubbing, there are also some barriers that need to be overcome. Despite the benefits in operation, a drawback of using seawater is its increased corrosivity for piping and exposed equipment. Additionally, the regional variations in seawater properties can negatively impact the operation and desulfurisation process, as the removal efficiency depends on the alkalinity and chemical composition. Finally, there are the uncertainties with effluent discharge, already described for maritime applications in Section 1.2.2. A techno-economic analysis of the available desulfurisation technologies for the 2400 MW coastal power plant concluded that the seawater scrubbing is the preferred technology, and that the environmental impact is to be low, with just 1% increase of sulphate ions compared to the fresh seawater [90]. Although the research hitherto did not prove the harmful effects of acidified effluent discharge, caution and additional long-term studies are needed, as well as compliance to stricter rules and assessment of possible environmental impacts of new scrubbing capacities.

### 3.1.3 Scrubber Design

Flue gas desulfurisation units are the contactor devices used to absorb  $\text{SO}_2$  from flue gases. Besides the choice of scrubbing agent and the underlying chemical processes, another crucial part is the scrubber design, which dictates the interface area between phases and the overall mass transfer, and the Table 3.1 lists the characteristics of widely used scrubber technologies and types. The most common designs for the wet scrubbers are packed beds, tray scrubbers, bubbling reactors and spray scrubbers.

Packed beds employ the design where liquid flows over the packing inside the scrubber column, achieving high mass transfer, large contact area and residence time. The packing

**Table 3.1**  
Comparison of major scrubber technologies and designs.

<i>SCRUBBER TYPE</i>	<i>Dry</i>	<i>Wet</i>
efficiency	approx. 80% to 90%	90% to 99%
advantages	easier residue collection and handling; easier retrofit; smaller space requirements; cheap and available reagents that might be reused	flexible operation at wide range of conditions; applicable for high temperatures; removes particulates; smaller space required
disadvantages	suitable for smaller sizes; require more space and heavier equipment; only for acid gases removal; particle agglomeration issues	higher power requirements; clogging and corrosion; water pollution; issues with effluent disposal
<i>ABSORBENT</i>	<i>Lime / limestone</i>	<i>Seawater</i>
efficiency	up to 99%	90% to 99%
price	higher cost of reactants, but not expensive	higher capital cost of piping and pumps; higher energy consumption due to larger amounts of seawater; seawater is free
advantages	high removal efficiency not dependant on seawater; residue can be used for gypsum production	abundant and available liquid; high efficiency; no chemicals used
disadvantages	scaling and clogging; use of chemicals and absorbent preparation;	increased corrosion, higher amounts of seawater required; alkalinity varies
<i>SCRUBBER DESIGN</i>	<i>Packed bed</i>	<i>Spray</i>
advantages	high mass transfer rates; large interface; high residence time	simple design and operation; smaller pressure drop; high mass transfer
disadvantages	packing deterioration; higher pressure drop	mass transfer and interface area hard to determine; larger power consumption

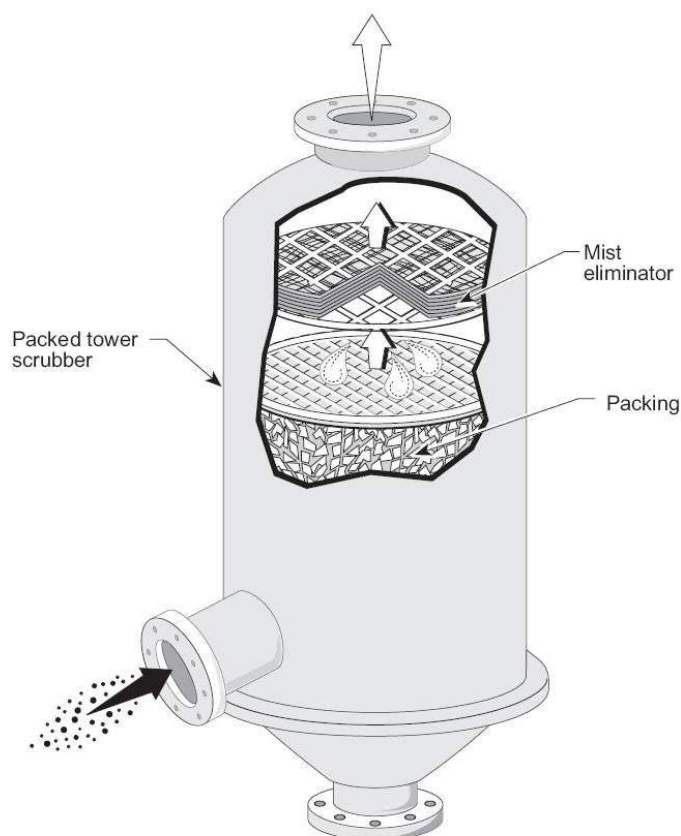


**Figure 3.1:** Packed bed scrubber [101].

material can be made of different sizes, shapes and materials, and the counter-current flow of gas and liquid is preferred. Although this is the most common design for stationary applications in chemical and process industry, it still has some drawbacks. The exposed packing material can corrode or degrade, and clogging and scaling represent issues for limestone scrubbing [102]. Depending on the packing material, pressure drop inside the scrubber can be significant, especially for the earlier generations of unstructured packing. Tray scrubbers achieve gas-liquid contact by directing the flows through the perforated tray, therefore mixing the phases [103]. Similarly to packed beds, they suffer from clogging and high pressure drop. On the other hand, bubbling reactors employ different approach, as flue gases are introduced in the liquid phase, forming rising bubbles that exchange mass [104].

Pressure drop and obstacles to flow in scrubber can cause excessive backpressure and impact the operation of system's boiler or engine. The increased backpressure may change the operating conditions and cause excessive pollutant formation. It presents greater issues when multiple engines or boilers are connected to single exhaust, which can mutually interact if resistance to flow inside scrubber is too high. This issue can be avoided by installation of a fan, but careful designing of scrubbers with low pressure drops can prevent issues as well.

The scrubber design of interest in this Thesis is the spray scrubber. They are commonly used counter-currently, with the liquid sprayed from nozzle arrays into a stream of rising flue



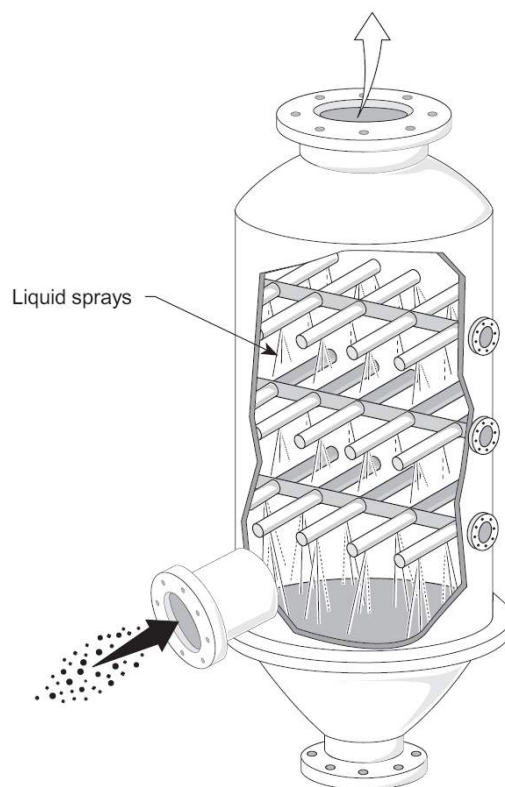


**Figure 3.2:** Spray scrubber [105].

gases. Their design and operation is more straightforward and they are less prone to clogging, which makes them more suitable for lime and limestone scrubbing. Compared to the packed bed scrubbing, they have smaller pressure drop, but are characterised by higher liquid flow rates and somewhat higher power consumption due to lower residence times. Spray scrubbing is widely spread technology capable of high mass transfer rates, but one of the main issues is the difficulty in predicting the surface area and the overall mass transfer. The mass transfer is highly dependant on droplet sizes and spray conditions so the exact interface area is hard to determine. Additionally, in stationary scrubbing, but especially in maritime applications, achieving high removal efficiency is a necessity. Reducing the required inflow of fresh seawater reduces the strain on the environment, the operational issues and the required size of the scrubber, so the high mass transfer rate is a requirement for the spread of seawater scrubbing spray scrubbers [106].

These issues indicate the need for further development of the spray scrubbing technology. There is a requirement for advanced tools capable of modelling the complex phenomena occurring in seawater spray scrubbing. During the past century, liquid-gas contactors have been a topic of investigation for numerous researches and scientists in different fields and applications. Theories and equations for mass transfer and absorption ranged from empirical to analytical and finally to adoption of numerical approach for modelling the scrubbers. Seawater scrubbing of  $\text{SO}_2$  pollutants in maritime and coastal operations represents only a niche application in the

overarching mass transfer processes. However, the combination of advanced numerical tools such as computational fluid dynamics with the use of seawater as an alternative scrubbing fluids, could lead to improved processes, lower impact on the environment and increased sustainability. Thus, further development of these tools is essential for deeper insights into processes and the ability to design better products. In the 1923 pioneering paper on inter-phase convective mass transfer, Whitman [107] states:

Few subjects are creating more interest both theoretically and practically than gas absorption. For years entirely empirical in its applications and even yet preponderantly so, there have been developed several theories that seem to shed some light on its mechanism. This paper clears up some of the fog around the potential factor. [...] One of the slogans should perhaps be, „No more monstrosities as absorption towers!“ No more of the old formula, „Let’s make it a foot bigger in diameter and 5 feet higher just for good luck“.

It seems that the design issues today are still not fully resolved, as the comprehensive numerical model for seawater absorption is not available for the industrial usage and research. With this in mind, this Thesis tries to contribute to mentioned issues.

## 3.2 Desulfurisation Chemistry Modelling

Desulfurisation lies at the interception of several physical and chemical phenomena, which complicates its modelling. First of all, the spray of liquid requires accurate description, which can represent an issue with large quantities of water injected in spray scrubbers. Although the gas flow on its own is not overly complicated, the spray-gas interaction can introduce complexities. Further, besides the sheer number of droplets needed tracking in the numerical domain, they can exhibit hydrodynamical phenomena that can be significant for absorption modelling, such as droplet oscillations and pulsations, internal circulation of fluid, collisions, droplets breakup and turbulence dissipation. On the other hand, chemical species in flue gases exiting the engine or combustion chamber need to be tracked, and the aqueous phase chemical reactions of absorbed  $\text{SO}_2$  require careful modelling approach. The interaction of mentioned phenomena needs to be accounted for and implemented in the numerical model for  $\text{SO}_2$  absorption.

Sulfur dioxide absorption in water droplets can be divided in two major sections. The first one covers the chemical processes of transferred  $\text{SO}_2$  in the liquid phase. In comparison to the pure absorption with no chemical reactions, the reactive process increases the absorbing potential and the  $\text{SO}_2$  removal efficiency. The second part entails the process of physical absorption of  $\text{SO}_2$  from the gas phase into the liquid, and it covers the influence of fluid flow, spray droplets’ characteristics and physical properties on the mass transfer across the gas-liquid interface. This way, the physical absorption controls the dynamics of mass transfer into the liquid phase, while

the chemical reactions hold the major influence on the maximum achievable SO<sub>2</sub> concentrations in droplets. This two-pronged approach divides the chemical and physical sections of the process, and presents the base of absorption modelling. It is commonly used in the available research on absorption processes, and in the subsequent sections the implementation from single droplet to the full spray will be presented.

### 3.2.1 SO<sub>2</sub> Solubility

When a gas mixture comes in contact with a liquid phase, its constituents dissolve into the liquid depending on their solubility. The total amount of individual gases that is dissolved is proportional to their partial pressures in the mixture, and the whole process is described by the Henry's law. Henry's law implies the equilibrium between the phases and is valid for describing sufficiently dilute solutions. On the other end of the spectrum is the Raoult's law, which correctly describes the behaviour of non-ideal solutions at high concentrations, closer to the pure substances. Since the concentrations encountered in scrubbing processes are quite low, the application of Henry's law is valid in desulfurisation modelling [108]. The proportionality constant that indicates the solubility of different chemical species is called Henry's law constant, and Sander [109] provided a comprehensive introduction, covering the physical background, variations of Henry's law and dimensions, temperature and solution composition dependence, as well as the detailed compilation of Henry's law constants for various chemical species dissolved in water. By using the Henry's law, partial pressure of SO<sub>2</sub> in flue gases can be related to the achievable equilibrium concentration of dissolved SO<sub>2</sub> in the liquid phase:

$$H_{\text{SO}_2}^{cp} = \frac{c_{\text{SO}_2}}{p_{\text{SO}_2}} = \frac{[\text{SO}_2]}{p_{\text{SO}_2}}. \quad (3.1)$$

The expression above connects the partial pressure  $p_{\text{SO}_2}$  to the concentration of *unreacted* dissolved SO<sub>2</sub> in the aqueous phase  $[\text{SO}_2]$ <sup>1</sup>.

Sulfur dioxide solubility in aqueous solutions varies with the temperature, and while the van 't Hoff equation can be generally used to describe the temperature dependency of equilibrium constants, it can also be applied to Henry's law constants. The first equation below represents the van 't Hoff equation modified for Henry's law constants and, when integrated, leads to the second expression with parameters  $A$  and  $B$  that can be tabulated.

$$\frac{d \ln H}{d(1/T)} = \frac{-\Delta_{\text{sol}}H}{R} \quad (3.2)$$

$$H(T) = A \cdot \exp\left(\frac{B}{T}\right)$$

<sup>1</sup>Square brackets around the chemical formula—conventionally representing concentrations in chemistry—are used onwards.

However, a more practical approach is to use an expression based on reference values. Equation (3.3) shows the temperature dependence of Henry's law constant with the reference temperature  $T^{\ominus} = 298.15K$ .

$$H^{cp}(T) = H^{cp\ominus} \cdot \exp\left(\frac{-\Delta_{sol}H}{R} \left(\frac{1}{T} - \frac{1}{T^{\ominus}}\right)\right) \quad (3.3)$$

$H^{cp\ominus}$  represents the value of the constant at the reference temperature, and in the expression  $-\Delta_{sol}H/R$ , the  $H$  represents the enthalpy at the reference temperature. Both of the values are tabulated and reported for different chemical species, and are valid for limited temperature range. The values used in this work for  $SO_2$  are  $1.2 \times 10^{-2} \text{ mol}/(\text{m}^3 \text{ Pa})$  and 2850 K for  $H^{cp\ominus}$  and  $-\Delta_{sol}H/R$ , respectively [109]. The Henry's law constant for  $SO_2$  is large compared to other atmospheric or exhaust gases, making it rather soluble in water and allowing for absorption from flue gases.

In equation (3.1),  $[SO_2]$  represents only the  $SO_2$  transferred through the interface and dissolved in water. This is purely physical process and for a given temperature provides a linear correlation between the pressure and dissolved concentrations. However,  $SO_2$  is reactive in aqueous phase and participates in chemical reactions that modify the final amount of dissolved  $SO_2$ .

### 3.2.2 Pure Water Chemical Model

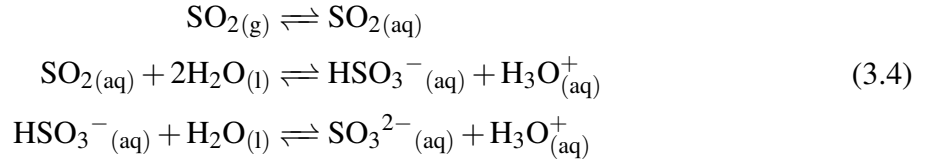
Chemical reactions in the aqueous phase are the foundation of the sulfur dioxide removal process. The unreacted  $SO_2$  that is absorbed through the gas-liquid interface and dissolved in the liquid phase can partake in chemical reactions in aqueous form. It is being spent in chemical reactions, a process that increases the available  $SO_2$  absorption capacity. Therefore, the accurate modelling of chemical reactions in aqueous phase is important for determining the possible  $SO_2$  uptake by water.

The initial investigations in sulfur absorption chemistry were focused on determining equilibrium conditions of gas and liquid phases for different parameters [110], but disregarded the influence of mass transfer dynamics between the phases. Subsequent research was done primarily as a part of atmospheric studies and focused on removal of pollutants in atmosphere by falling raindrops [111], while applying the improved chemical models for  $SO_2$  reactions in water to the experimental data obtained from tests in rain shafts [112].

Chemical models available in the literature on the subject of  $SO_2$  absorption in water range in complexity and applicability. The accuracy and computational requirements of the model vary depending on the application, thus either a comprehensive chemical system with a larger number of species and reactions can be used, or a reduced system with global reactions can be solved for.

The dissolved sulfur dioxide is surrounded by the water molecules and reacts, forming

sulfurous acid  $\text{H}_2\text{SO}_3$ , as per first reaction in equation (1.5). However, sulfurous acid has only been observed in gas phase and no evidence of the acid has been found in the solution, as it dissociates into conjugate bases which are common bisulfite and sulfite ions. These ions, together with the unreacted  $\text{SO}_{2(\text{aq})}$  comprise the *total*  $\text{SO}_2$ .



The first reaction in the chemical mechanism above is the dissolution of the gaseous  $\text{SO}_2$  into unreacted, aqueous form. As described earlier, this step is governed by the Henry's law. Next is the first dissociation step, where  $\text{SO}_2$  reacts with the water molecules forming bisulfite  $\text{HSO}_3^-$  and hydronium ion  $\text{H}_3\text{O}^+$ . The following step is the second dissociation of the diprotic sulfurous acid, where sulfite ion  $\text{SO}_3^{2-}$  and additional hydronium ion are formed. The presented system of equations relates the  $\text{SO}_2$  in gas to the liquid phase and its conjugate acids and bases. This creates an equilibrium system of connected reactions that influence one another, and creating a sink for one of the species shifts the balance of the equilibrium, allowing additional absorption from the gas phase. Dissociation reactions are sufficiently fast to assume the instantaneous reactions and to allow modelling with chemical equilibrium models [113].

The first dissociation is the dominating reaction and the equilibrium constant  $K_I$  is defined as:

$$K_I = \frac{[\text{HSO}_3^-][\text{H}_3\text{O}^+]}{[\text{SO}_{2(\text{aq})}]}. \quad (3.5)$$

The temperature dependence of the equilibrium constant is taken from work by Rabe and Harris, and defined by the equation (3.6) below [110].

$$K_I = \exp\left(\frac{1972.5}{T} - 10.967\right) \quad (3.6)$$

The dissociation of sulfur dioxide in water occurs in two stages, and the second dissociation is much slower than the first one at temperatures considered for absorption processes. The produced sulfite ions thus have significantly lower concentrations in the solution.

$$K_{II} = \frac{[\text{SO}_3^{2-}][\text{H}_3\text{O}^+]}{[\text{HSO}_3^-]} \quad (3.7)$$

The temperature dependence is similarly given by the equation (3.8), found in the work by Milerro et al. [114].

$$K_{II} = \exp\left(-358.57 + \frac{5477.1}{T} + 65.31 \cdot \log(T) - 0.1624T\right) \quad (3.8)$$

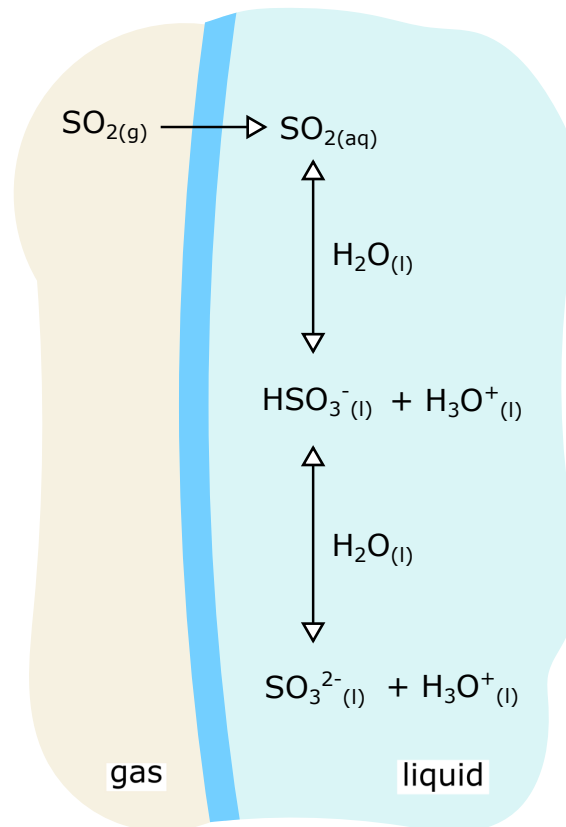


**Figure 3.3:** Chemical reactions in liquid phase.

Pure water has a neutral pH value of 7—a result of equal concentrations of  $\text{OH}^-$  and  $\text{H}^+$  ions. From the equations (3.5) and (3.7) it can be seen that the dissolved  $\text{SO}_2$  and the two dissociation steps produce two  $\text{H}_3\text{O}^+$  ions per single  $\text{SO}_2$  molecule absorbed in the liquid phase. The increase of  $\text{H}_3\text{O}^+$  concentration acidifies the solution and the resulting pH value is lowered. Although generally the pH values are not decreased enough, the reaction of autodissociation of water is also included in the system. This is the ionisation reaction where two water molecules produce one hydronium ion and one hydroxide ion.



As with previous equilibrium reactions, this one is also temperature-dependant, but as the equilibrium constant does not change significantly in the temperature range of interest, the constant value is adopted [115].

$$K_w = [\text{H}_3\text{O}^+] [\text{OH}^-] = 10^{-13.99} \quad (3.10)$$

The electroneutrality condition is commonly used in modelling chemical reactions of aqueous solutions. It ensures overall conservation of electric charge, since the aqueous solutions remain electrically neutral during the  $\text{SO}_2$  dissociation. In the available literature, electroneu-

trality condition is used for closing the system of equations [108].

$$[\text{H}_3\text{O}^+] = [\text{HSO}_3^-] + 2[\text{SO}_3^{2-}] + [\text{OH}^-] \quad (3.11)$$

The presented chemical system is analogous to the approaches that can be found in the literature on the topic, such as papers by Marocco and Insoli [116] and Darake et al. [117]. This system is applicable for calculation of concentrations of dissolved sulfur dioxide in water, regardless the type of water surface or form; the only condition are the equilibrium conditions. This *equilibrium concentration* is the maximum amount of  $\text{SO}_2$  that can be absorbed in the water under the set conditions.

The model is capable of correctly reproducing the equilibrium concentrations of dissolved  $\text{SO}_2$  in pure water over range of temperatures and partial pressures. In their 2007 paper, Andreassen and Mayer [118] presented the results of equilibrium concentrations for dissolution of  $\text{SO}_2$  in pure water and seawater under different conditions and model assumptions. In Fig. 3.4, the concentrations of absorbed sulfur species are given for water temperature range between 273 and 353 K, and gas phase  $\text{SO}_2$  partial pressures up to 50 Pa. For obtaining the total sulfur concentration, all of the sulfur-containing species are summed: unreacted  $\text{SO}_{2(\text{aq})}$ , bisulfite and sulfite ions. As can be seen, the equilibrium concentrations are reproduced, and small discrepancies can probably be contributed to differences in physical properties such as density. In the equilibrium curves in Fig. 3.4 the impact of chemical reactions on  $\text{SO}_2$  absorption can be noted. The Henry's law alone provides a linear dependency of unreacted  $\text{SO}_2$  concentrations to the partial pressure, while the inclusion of aqueous phase chemical system increases the achievable concentrations and modifies the behaviour compared to the linear profile with respect to the Henry's law alone. Further, as the solubility is temperature-dependant, it can be noted that the higher temperatures display lower  $\text{SO}_2$  solubility, which can have significant impact in real-world absorption processes, as temperature of ocean water differs with location, and the flue gases can heat it and further affect the solubility. Besides the impact on solubility, temperature increase also impacts the reaction rates. According to equations (3.6) and (3.8), higher liquid temperatures decrease dissociation constants and reactions are shifted to the left. This leads to the characteristic shapes of equilibrium concentrations curves and sets the ratio between first and second dissociation constants, the latter being roughly five orders of magnitude lower at 25 °C.

The data for equilibrium conditions are a good initial indicator for the maximum absorption capacity in water and for testing the dependency of chemical model on input parameters such as system temperature or  $\text{SO}_2$  concentration in gas phase, which is a force causing the mass transfer.

Another paper dealt with the sulfur dioxide equilibrium concentrations in air-water systems. Hocking and Lee [119] presented the results of their model for equilibrium chemical reactions in aqueous phase and compared it to experimental data with close agreement. The liquid phase temperatures ranged up to 60 °C and the investigated total  $\text{SO}_2$  concentrations were at the low

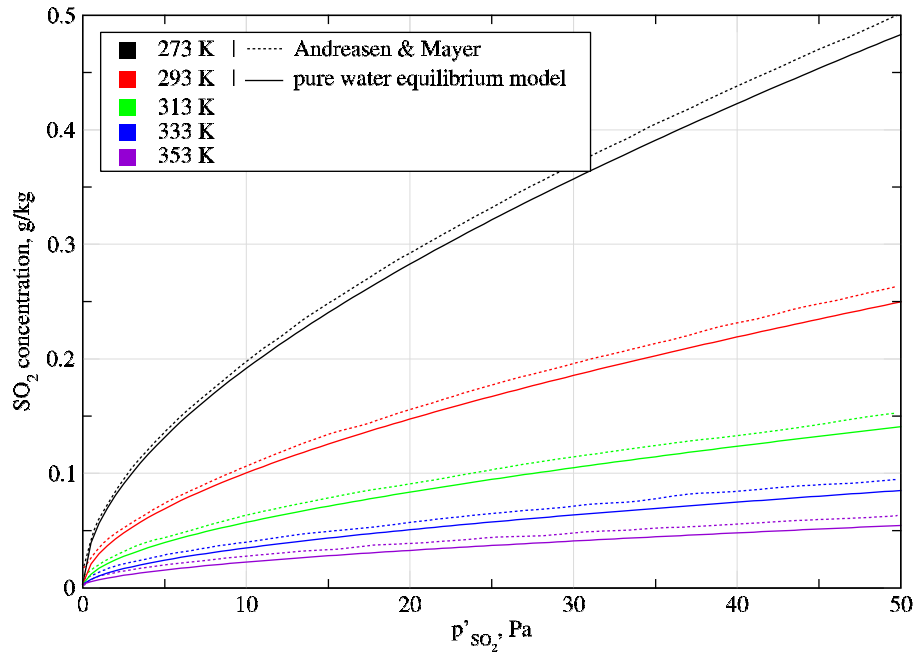


**Figure 3.4:**  $\text{SO}_2$  equilibrium concentrations in pure water - comparison with data by Andreasen and Mayer [118].

end of the range interesting for the industrial absorption application, up to 130 ppm. This corresponds to the partial pressure of around 13 Pa in the ambient air, and Fig. 3.5 shows the comparison between literature data and equilibrium chemical model for pure water presented above. Even for the low  $\text{SO}_2$  concentrations in gas phase, which result in weaker driving force and low amount of dissolved sulfur species, the reproduced equilibrium concentrations show good agreement with literature data.

Although the presented model and the results verified with the literature data show good agreement, the applicability of this chemical system on its own is of little practical use. Although the distilled water has absorbing capabilities—as shown in previous figures—it is not used as a absorbing medium in real-world industrial applications, and even natural water can contain composition significantly different to distilled water, which can affect the aqueous phase chemistry.



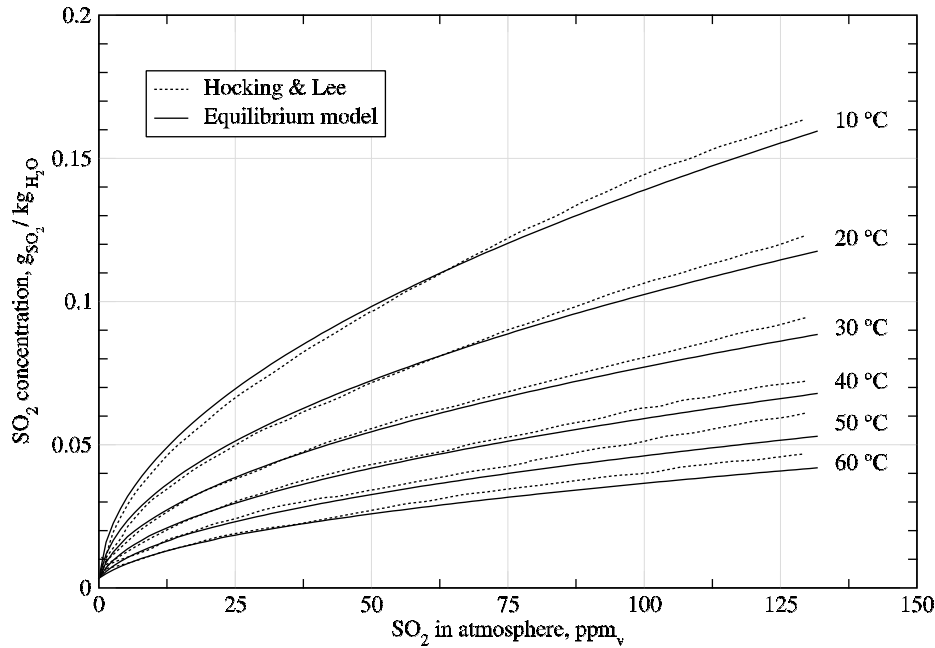


**Figure 3.5:**  $\text{SO}_2$  equilibrium concentrations in pure water - comparison with data by Hocking and Lee [119].

### 3.2.3 Seawater Modelling

#### 3.2.3.1 Seawater Composition

Compared to the pure water, seawater has a complex composition and contains dissolved salts, smaller amounts of sodium, chloride, magnesium and calcium ions, other organic material and particulates, dissolved atmospheric gases, and a large number of trace elements. By passing through the rocks, soil, and Earth's crust, minerals are dissolved in water and alter its composition. In addition, the seawater takes part in a complicated interplay between the atmosphere as it absorbs the atmospheric gases, out of which the carbon dioxide is probably most notable and significant in recent years. This is a connection to the carbon cycle in nature, and oceans and seas are accumulating larger concentrations of  $\text{CO}_2$ , leading to their acidification.

The salinity represents the amount of dissolved salts in water, and for the majority of oceans and seas its value ranges between 31 and 38 g/kg, but mostly it has value of 35 g/kg, or 35‰.

In Table 3.2 the major constituents of seawater obtained from literature are shown. The composition and the ratio of dissolved ions depends on temperature, pressure and location, and can vary annually. It can be seen that sodium and chlorine ions dominate the composition, with other chemicals present in varying concentrations. As the  $\text{H}^+$  concentration in seawater is lower

**Table 3.2**  
Seawater composition at salinity 35 ‰, g/kg.

<i>Chemical species</i>	<i>Harrison [121]</i>	<i>Dickson and Goyet [122]</i>	<i>Flagiello et al. [106]</i>
Na <sup>+</sup>	10.77	10.7837	9.3626
Mg <sup>2+</sup>	1.29	1.2837	0.0256
Ca <sup>2+</sup>	0.4123	0.4121	0.1074
K <sup>+</sup>	0.3991	0.3991	0.0023
Sr <sup>2+</sup>	0.008 14	0.0079	-
Cl <sup>-</sup>	19.353	19.3524	19.5551
SO <sub>4</sub> <sup>2-</sup>	0.905	2.7123	2.7434
HCO <sub>3</sub> <sup>-</sup>		0.108	0.6346
CO <sub>3</sub> <sup>2-</sup>	0.276	0.0156	0.0158
Br <sup>-</sup>	0.673	0.0673	0.000058
B(OH) <sub>3</sub> , B(OH) <sub>4</sub> <sup>-</sup>	0.0445	0.0277	-
F <sup>-</sup>	0.001 39	0.0013	0.000068

than the OH<sup>-</sup>, this makes it slightly basic.

The residence time of different chemical species also varies, as sodium or chlorine ions have long residence time, while calcium precipitates more rapidly. Another constituent with long residence is sulphate SO<sub>4</sub><sup>2-</sup>, which is found in seawater in significant amounts. Sulphates are naturally occurring in the seawater and rather insensitive to temperature or pH changes, making them a conservative compound. After the desulfurisation process by using seawater, the effluent can contain higher concentrations of sulphate ions. However, these concentrations are negligible compared to the already present amounts. This way, emissions of sulfur-containing species into the atmosphere are avoided, where it has greater harmful effect than sulphates directly deposited in the sea. By acid rain and deposition in soil, emissions to atmosphere eventually end up washed into the seas and the oceans, which makes desulfurisation process with seawater a shortcut that avoids environmental impact on the atmosphere. In the end, the negative effect of burning the fossil fuels can not be completely removed, but seawater scrubbing reduces its impact, and while it increases the issue of ocean acidification, the impact is minor compared to the influence of acidification due to rising carbon dioxide concentration in the atmosphere [120].

Although seawater composition and characteristics are complex and have an essential influence on marine life, climate and humans, the properties such as alkalinity, pH and hardness are used in typical water quality analyses, as they can be indicative of the water quality for engineering purposes. The hardness represents the mineral content and is more important for monitoring the drinking water. The pH scale is used to indicate acidity or basicity of an aqueous

solution, and it depends on the activity<sup>2</sup> of  $[H^+]$  ions.

$$pH = -\log(a_{H^+}) = -\log[H^+] \quad (3.12)$$

While salinity and hardness indicate the composition of the seawater, and the pH value, alkalinity is the property that shows how the seawater will react with the other bases or acids.

### 3.2.3.2 Alkalinity

The alkalinity is the measurement of the water's capacity to react with acids and neutralise them. It is determined by titration of water sample with a strong monoprotic acid such as HCl to the endpoint corresponding to equivalence point of carbonate or bicarbonate. This occurs when the pH value decreases enough to cause the change of pH indicator colour. When all of the added  $H^+$  ions have reacted, the spent amount of the acid shows the alkalinity, usually expressed as miliequivalents per litre, but mol/kg are sometimes more suitable for discussing the alkalinity of seawater.

Alkalinity is mostly composed out of weak acid salts dissolved in the seawater, but strong bases such as  $OH^-$  may also contribute in some extreme cases. For use in seawater and other groundwaters, total alkalinity  $A_T$  can be formulated as the sum of bases titrable with strong acid:

$$A_T = [HCO_3^-] + 2[CO_3^{2-}] + [B(OH)_4^-] + [OH^-] + 2[PO_4^{3-}] + [HPO_4^{2-}] + [SiO(OH)_3^-] - [H^+] \dots \quad (3.13)$$

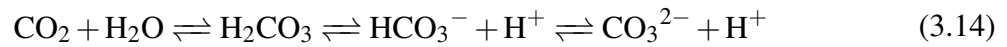
Total alkalinity is not strongly affected by the changes in seawater temperature, pressure, or pH, but the influence can be seen in the mutual conversions of the carbonate constituents.

Alkalinity can be also viewed as a strength of a buffer solution that contains weak acids and their conjugate bases to oppose the change of pH when strong acids or bases are added. Therefore, when adding the acid in the seawater, the alkalinity opposes the change of pH by reacting with the excess of  $H^+$  ions.

In seawater, the carbonate system is an important part of the aqueous chemistry, ensuring the balance between the carbon in the atmosphere and the oceans, and preventing the radical changes in the seawater pH values. The carbon dioxide present in the atmosphere is in balance with the dissolved  $CO_2$  in the seawater, while it forms the carbonic acid  $H_2CO_3$  in reaction with water molecules. Carbonic acid is a weak acid that dissociates in two stages, forming bicarbonate and carbonate ions,  $HCO_3^-$  and  $CO_3^{2-}$ , respectively [123]. The reactions are in equilibrium and

<sup>2</sup>Thermodynamic activity  $a$  is a measure of an effective concentration in solution (just as fugacity for gaseous mixtures), and it accounts for the difference between the ideal solution and the real one. The influence of temperature, pressure, solute-solute interactions and electrical fields can create a difference between the nominal concentration  $[c]$  and the effective concentration, but for dilute solutions and normal conditions, activity coefficient  $\gamma$  can be taken as unity:  $\lim_{\gamma \rightarrow 1} \gamma a = [c]$ .

there is a dynamic interaction between the dissolved carbonate forms, equation (3.14).



It can be noted that by reacting in water,  $\text{CO}_2$  produces  $\text{HCO}_3^-$  and  $\text{H}^+$  ions in equal amounts, and the influence of bicarbonate on alkalinity is counteracted by the hydrogen ion. Therefore, while the addition of carbon dioxide in the system increases the acidity by  $\text{H}^+$  ion production, it does not impact the alkalinity [124].

In the Fig. 3.6, the Bjerrum plot of the carbonate system shows the dependency of species' concentrations to pH values of the solution. Carbonic acid is a diprotic acid and dissociates in two stages. Due to low values of the equilibrium constants, there is an overlap in the concentrations of species. Additionally,  $\text{H}^+$  and  $\text{OH}^-$  concentrations are plotted as well. It can be seen that the hydrogen and hydroxide concentrations are not significant outside the extreme pH values, and that for the moderate acidity encountered in most cases, bicarbonate ion has the greatest influence.

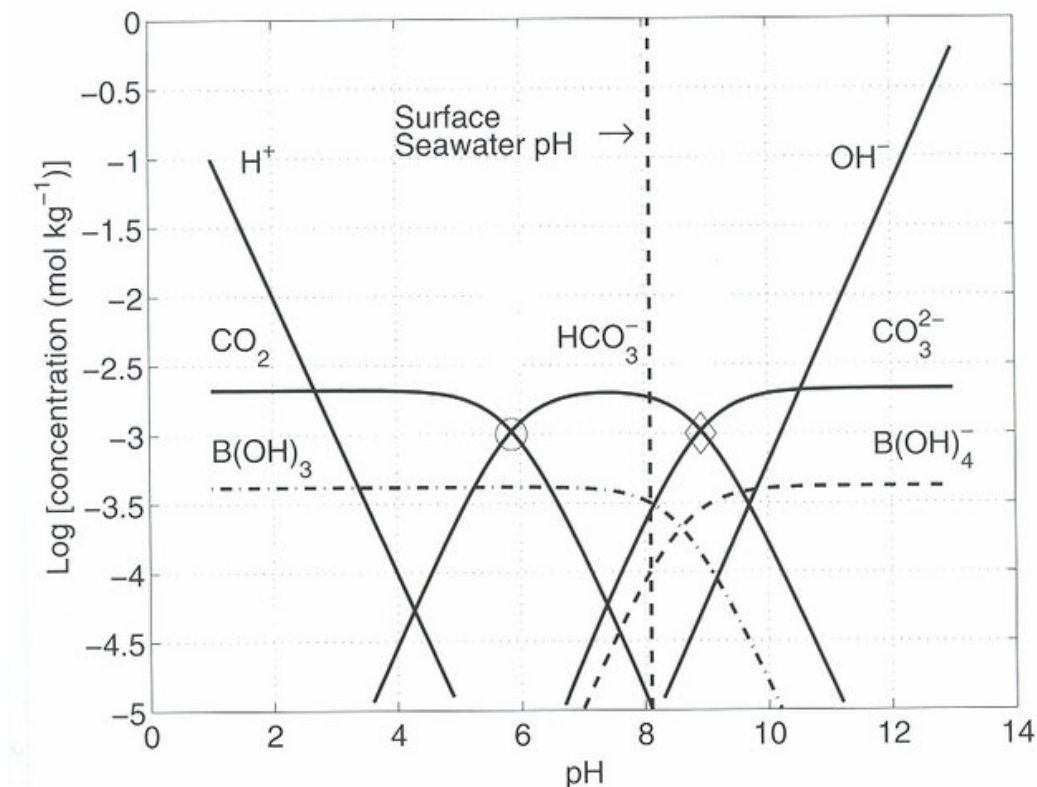


**Figure 3.6:** Bjerrum plot of carbonate system [125].

From the equation (3.13) and the distribution of concentrations in seawater, Table 3.2, it can be concluded that the carbonates have the major contribution to the alkalinity. Other chemical species have comparatively lower concentrations, and the hydrogen and hydroxide ions are not

that significant in the pH range in focus. Therefore, the alkalinity can be represented by the *carbonate alkalinity* comprised out of  $\text{HCO}_3^-$  and  $\text{CO}_3^{2-}$  alone, but for the waters having very high or very low levels of pH,  $\text{H}^+$  and  $\text{OH}^-$  concentrations can be included as well.

$$A_T = [\text{HCO}_3^-] + 2[\text{CO}_3^{2-}] + [\text{OH}^-] - [\text{H}^+] \quad (3.15)$$

Other weak acids in seawater, such as phosphoric, silicic, nitrous or boric acids, also contribute to the buffering capacity, but their influence is minor compared to carbonate species.

The buffering property of seawater opposes the change of pH when acid is added to it. Instead of lowering the pH values, as per equation (3.12), the  $\text{H}^+$  ions added to the solution in equilibrium shift the equilibrium reaction and the pH remains the same or changes in smaller proportions. Chemical species accounting for the alkalinity can react with  $\text{H}^+$  ions, thus preventing the pH change. This is one of the reasons why using seawater as scrubbing agent is beneficial.

With the overview of the alkalinity and the seawater properties discussed above, it can be concluded that in seawater scrubbing, pH represents the factor of strength and the alkalinity can be considered as a factor of capacity for buffering and  $\text{SO}_2$  absorption [126].

### 3.2.4 Seawater Chemical Model

The overview of seawater composition and its main characteristics indicated only the basic parameters that are commonly encountered in seawater modelling. In reality, seawater constituents are numerous, chemical reactions occurring in it are complex and intertwined, and the connection to biological processes and marine life forms is a topic of several scientific fields. However, since the focus of present work is on developing a comprehensive but robust model for  $\text{SO}_2$  absorption, a distinction between the pertinent and neglectable factors had to be done. Although the literature on complex processes in seawater is available, research and papers focused on developing models for technological applications are limited on a smaller number of influencing factors, such as alkalinity, salinity and acidity. Additional care has to be given to the abilities for seawater analysis in maritime or coastal applications: ships and power plants usually have limited time and equipment for determining seawater composition and properties. Thus, salinity and alkalinity have been accepted as major indicators for seawater quality, as they can describe the system in sufficient details and provide input data for modelling purposes.

Therefore, if the complete and detailed chemical system can be replaced with the simplified model containing only the significant parameters and chemical species without sacrificing the accuracy or robustness of the model, this would lead to easier implementation and use in practical applications.

As was described in previous section, the alkalinity is a major parameter in seawater buffering and reactions with hydronium ions, and for most seawater samples its substitution with the

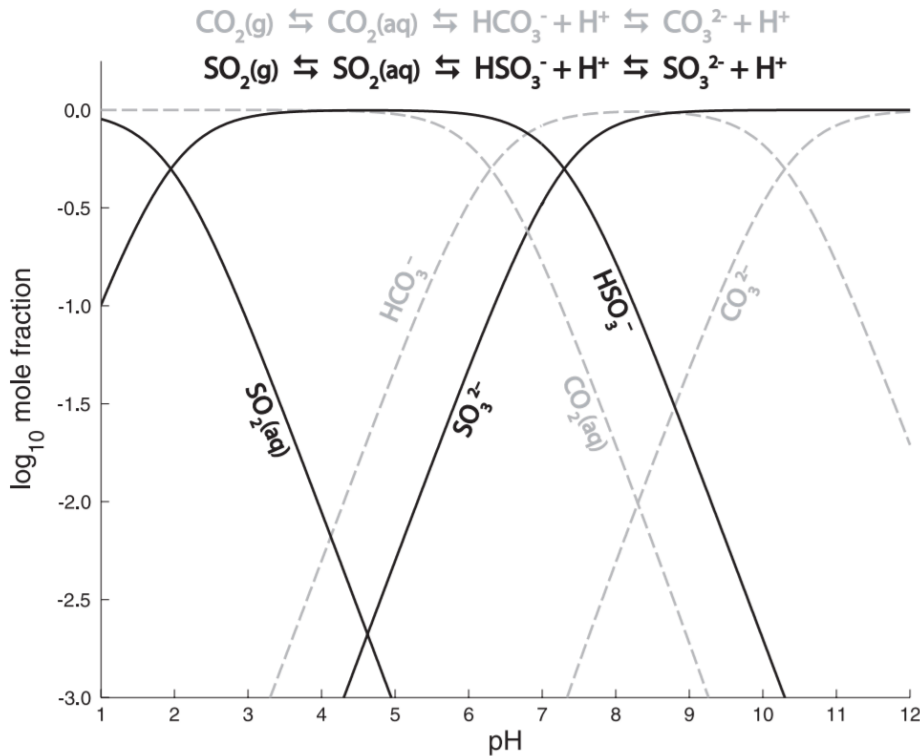


**Figure 3.7:** Bjerrum plot of  $\text{SO}_2$  and  $\text{CO}_2$  in aqueous solutions [127].

carbonate alkalinity is acceptable approximation and does not introduce noticeable errors.

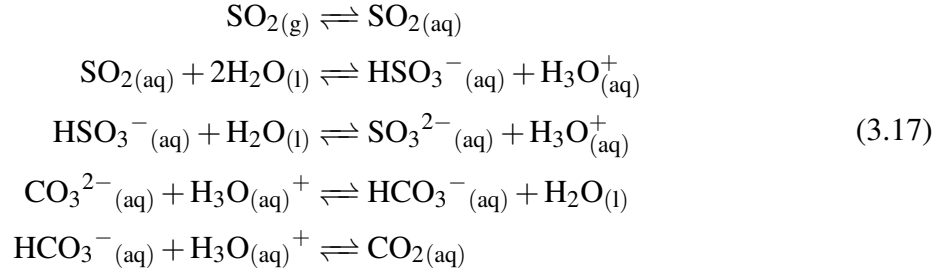
$$A_T = A_C = [\text{HCO}_3^-] + 2[\text{CO}_3^{2-}] \quad (3.16)$$

This way, the alkalinity represents species in seawater that influence the chemical reactions of  $\text{SO}_2$  in water. In the models reported in literature the carbonate alkalinity dominates and forms the major part of the system. The Fig. 3.6 shows the combined Bjerrum plots of  $\text{SO}_2$  and  $\text{CO}_2$  systems.

Acidity of solutions is often discussed in studies since it is an important parameter impacting the technological applications and marine life as effluent. However, even though the pH of a solution is used to define the conditions in chemical systems, it is a consequence of chemical reactions and concentration of hydronium ions, rather than the input parameter determining the system. The hydronium ions are coupled with both the  $\text{SO}_2$  and the  $\text{CO}_2$  systems, which is shown in Fig. 3.7.

The carbon system equilibrium from equation (3.14) shows the connection of carbonates to the  $\text{H}_3\text{O}^+$  ions in water solutions. The increased source of hydronium ions due to  $\text{SO}_2$  dissociation therefore interacts with the carbon system. Its balance is shifted and the buffer system opposes the change pH values. Differently stated, carbonate and bicarbonate ions comprising alkalinity react with  $\text{H}^+$  and produce  $\text{CO}_2$ , thus increasing the potential for  $\text{H}_3\text{O}^+$  production in the  $\text{SO}_2$  dissociation process. The consequence of this shift in  $\text{CO}_2$  system is the corresponding

shift in the sulfur equilibrium and the increased  $\text{SO}_2$  absorption capacity. The system in equation (3.17) also includes the carbonate species and the connection to the sulfur system via  $\text{H}_3\text{O}^+$  ions.



Additional issue is that the seawater is usually quantified, both in technological applications and modelling literature, by the overall alkalinity. Since the  $\text{HCO}_3^-$  has an overwhelming impact on the alkalinity, as can be seen both from values in Table 3.2 and the plot of concentrations for the pH range of interest in Fig. 3.7, the total alkalinity is approximated as the equivalent concentration of  $\text{HCO}_3^-$ .

For example, the work by Andreasen and Mayer [118], which has provided data for comparison of equilibrium models, lists the value of alkalinity at  $A_T = \text{HCO}_3^- = 2400 \mu\text{mol/kg}$ , which is a commonly used value that lies in the range of majority of seawater alkalinities. After the adoption of  $\text{HCO}_3^-$  approximating the total alkalinity, its equilibrium constant  $K_{alk}$  can be presented as:

$$K_{alk} = \frac{[\text{CO}_2(\text{aq})]}{[\text{HCO}_3^-][\text{H}_3\text{O}^+]}. \tag{3.18}$$

This is a reverse reaction of the first step of the equilibrium in equation (3.14), and has been comprehensively documented in the literature. Here, it is an inverse of the equilibrium constant of the alkalinity reaction,  $K_{CI} = K_{alk}^{-1}$ . The research by Roy et al. [128] focused on experimentally determining the carbonic acid dissociation constants in seawater under different temperatures and salinities. The empirical formula for the first dissociation constant extrapolated from the experimental data is temperature-dependant and shows great fit to the experimental data and other research.

$$\begin{aligned}
 \ln K_C &= 2.83655 - 2307.1266/T - 1.5529413 \cdot \ln T + \\
 &\left(-0.20760841 - 4.0484/T \cdot S^{1/2}\right) + 0.08468345 \cdot S - 0.00654208 \cdot S^{3/2}
 \end{aligned} \tag{3.19}$$

When the model presented for pure water is combined with the additional equations for the carbonate system, it accounts for the addition of alkalinity in seawater which increases the  $\text{SO}_2$  absorption capacity. Figure 3.8 displays the comparison of model results with the literature data for equilibrium concentration of total sulfur species in seawater. For the range of partial pressures up to 50 Pa, which roughly corresponds to 500 ppm under standard conditions, the

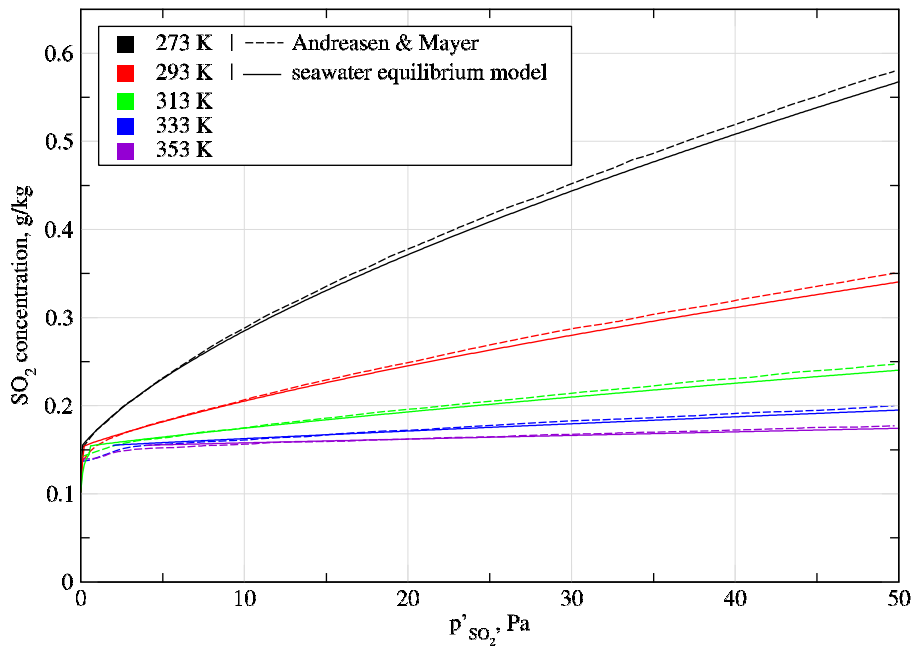


**Figure 3.8:**  $\text{SO}_2$  seawater equilibrium concentrations at different temperatures and partial pressures with  $S = 35 \text{‰}$  and  $A_T = 2400 \text{ }\mu\text{mol/kg}$ .

presented model shows good agreement with the literature data over different temperatures. The value of salinity was  $35 \text{‰}$ , while the alkalinity was the already reported value of  $2400 \text{ }\mu\text{mol/kg}$ . Compared to the Fig. 3.4, which was calculated for the pure water conditions, the inclusion of alkalinity in the seawater model increases the equilibrium concentrations and consequently the potential for  $\text{SO}_2$  absorption. Although the increase in absolute amounts is more prominent at low temperatures, the relative increases seen at high temperatures are more significant.

### 3.2.4.1 Ionic Strength

Seawater is a solution of salts that act as ionic compounds and dissociate when dissolved. These electrolytes form cation and anions in seawater, making the seawater electrically conducting, but without the applied electric potential, the bulk of the solution tends towards electroneutrality. In the idealised solutions reactions occur based on reactants' concentrations and according to the temperature-dependant equilibrium constants. However, due to dissolved ions, electrolyte solutions can deviate from ideality as electrostatic forces and repulsion between the ions with same charge can lead to an uneven distribution of ions that alters reaction rates. Thus the concept of effective concentration—activity  $a$ , was introduced, to account for these effects. The activity is proportional to concentration  $[c]$ , and the activity coefficient  $\gamma$  represents the



proportionality constant between them:

$$a = \gamma [c] . \quad (3.20)$$

Activity coefficients in an ideal solutions are equal to unity, and this approximation is applicable only for very dilute concentrations. In other cases, the correction should be applied for better agreement with reality.

The activity coefficients can be described through the ionic strength of the solution, where the ionic strength is a function of the concentration of all ions present in the solution. The ionic strength is calculated from the concentration of all dissolved ions, taking into account the property of an entire solution:

$$I = \frac{1}{2} \sum_{i=1}^n c_i z_i^2 , \quad (3.21)$$

where  $c_i$  represents the concentration of all anions and cations, and  $z_i$  stands for that ion's charge number. An approximated value commonly used for seawater is 0.72, which agrees well with the validation cases.

The Deby-Hückel theory explains the departure from ideality for electrolyte solutions, and connects the ionic strength to the activity coefficients, but it is also limited to lower concentrations. Davies equation represents its extension and somewhat relaxes the limit on the applicable concentration and temperature range.

$$-\log \gamma = A z_i^2 \left( \frac{\sqrt{I}}{I + \sqrt{I}} - 0.3I \right) \quad (3.22)$$

For 25 °C the model parameter  $A$  can be taken as  $1/2$ , but for other temperatures, the expression below is used, where  $\epsilon$  stands for dielectric constant of seawater:

$$A = 1.82 \times 10^6 (\epsilon T)^{-3/2} . \quad (3.23)$$

The calculated activity coefficients can be used for correcting the equations for equilibrium constants presented above. The equations (3.5), (3.7) and (3.18) are corrected with the corresponding activity coefficients, as can be seen on an example below for the second dissociation constant.

$$K_{II} = \frac{\gamma_{\text{SO}_3^{2-}} [\text{SO}_3^{2-}] \gamma_{\text{H}_3\text{O}^+} [\text{H}_3\text{O}^+]}{\gamma_{\text{HSO}_3^-} [\text{HSO}_3^-]} \quad (3.24)$$

The inclusion of ionic strength and activity coefficients alters the equilibrium constants, and in the case of  $\text{SO}_2$  absorption in seawater leads to increased equilibrium concentrations. The work by Andreasen and Mayer that has already been used for validation of chemical model again provides data for the modified activity coefficients. In Fig. 3.9 data sets from the literature and the previously presented model for the mentioned temperature and pressure ranges are

compared. The agreement between the curves is sufficiently good, with slight discrepancy at very low temperature. Additional factor to notice is the growth of equilibrium concentrations: contrary to the impact of alkalinity, the inclusion of ionic strength has a greater influence on the increase at lower temperatures, while the change at higher temperatures is not as great due to Davies equation and the dependency on temperature equation (3.23).

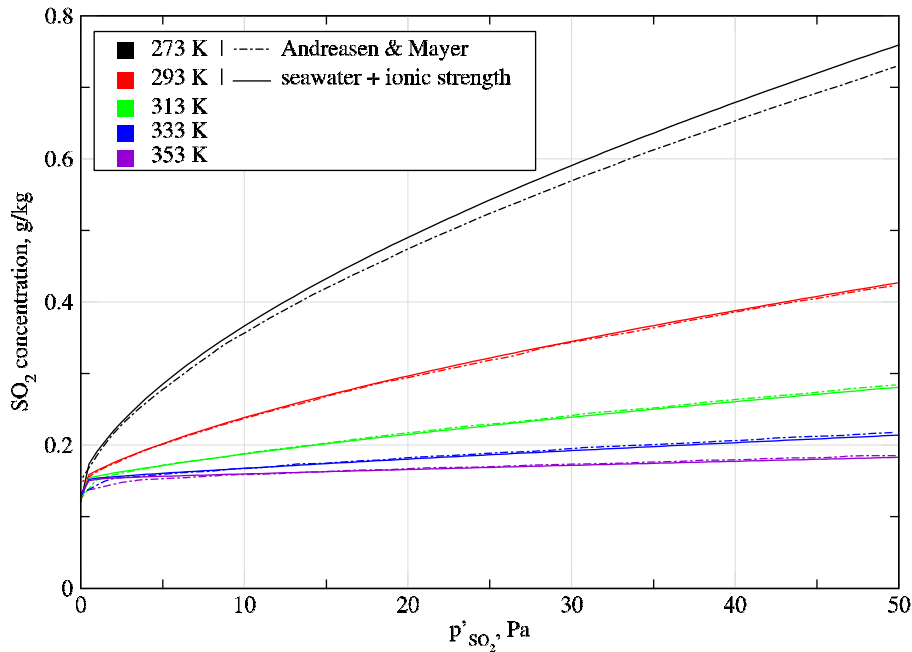


**Figure 3.9:**  $\text{SO}_2$  seawater equilibrium concentrations with the ionic strength included at different temperatures and partial pressures with  $S = 35\%$  and  $A_T = 2400 \mu\text{mol/kg}$ .

An additional source—a paper by Rodríguez-Sevilla et al. [108], focusing on the absorption equilibria of  $\text{SO}_2$  in seawater—provides more data for validation of chemical model for equilibrium conditions in both  $\text{SO}_2$ –pure water and  $\text{SO}_2$ –seawater systems. Their work shows the experimental investigation of equilibrium conditions in seawater over the range of parameters, but also provides the results of the experimental correlation for  $\text{SO}_2$  solubility in distilled water at  $25^\circ\text{C}$ . The range of  $\text{SO}_2$  partial pressures is higher than the previous case and reaches the  $1500 \text{ Pa}$ —which is higher even than the concentrations encountered in flue gases—but the results replicated by the chemical model are satisfying. Figure 3.10 presents the comparison between the developed pure water model and the results by expression derived from the experimental investigation, and the discrepancies are tolerable, especially as they are encountered at higher concentrations.

Secondly, the full seawater chemical model is compared to the experimental results for equilibrium concentrations of  $\text{SO}_2$  in seawater. The temperature of seawater was at  $25^\circ\text{C}$ , and

its properties were slightly different as well. The alkalinity is mostly due to bicarbonate ions, and has been calculated at  $3300 \mu\text{mol}/\text{kg}$ . The salinity of seawater, was  $36.87 \text{‰}$ , and the pH value was slightly higher than neutral at 7.79. The reported ionic strength of the solution was  $0.775 \text{ mol}/\text{kg}$ , which is a bit higher than in the last case, and on the edge of applicability of the Davies equation. The curve obtained by the equilibrium model does not deviate significantly from the data points, further solidifying the reliability of the model and validating it against the experimental data.

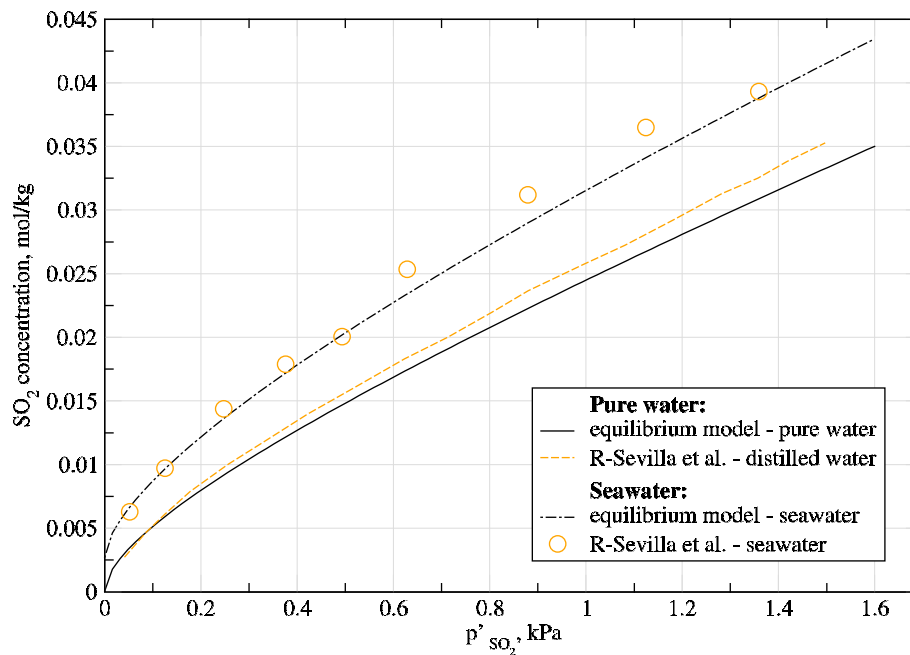


**Figure 3.10:** Comparison of the pure and seawater chemical model to experimental data [108].

### 3.2.4.2 Rate-approach Model

It has been shown that the presented models accurately predict equilibrium concentrations for sulfur dioxide absorption in both pure water and seawater. Furthermore, these types of chemical systems are prevalent in the available literature on equilibrium modelling, and mainly present systems of equations that are solved in order to calculate species concentrations. This approach is reasonable for the calculation of equilibrium conditions and concentrations in idealised bulk of liquid, or only once over some range of parameters. However, the aim of present work is to develop a model applicable in three-dimensional applications with description of absorption into full sprays. Considering that the number of droplets in the computational domain can be significant, the need for models to be as numerically efficient as possible is always present.

This requirement implies that alternative approach that avoids repeatedly solving a system of equations over a large number of equations would be preferable from the efficiency standpoint, if the model's accuracy is not disturbed. One of the simplifications commonly encountered is the disregarding the second dissociation constant of  $\text{SO}_2$  in water solutions, which can reduce the system of equations and enable the use of analytical solutions. Physically, this is a valid approximation, as the second dissociation constant is significantly smaller, and under most conditions the  $\text{SO}_3^{2-}$  concentrations can be neglected. However, this makes sense only for pure water, as in seawater models there are additional chemical reactions and equations which prevent the reduction of the model complexity.

With the aim of complexity reduction and the increase of efficiency and speed of chemical model, an alternative approach has been investigated. Commonly in literature and in technical applications alike, there is a lack of differentiation between the chemical species comprising the alkalinity, which has already been discussed. The accurate ultimate analysis of seawater is usually not available in seawater scrubbing applications on ships, but rather only parameters such as alkalinity and salinity are being monitored. Additionally, in engineering applications, the partitioning between the sulfur-containing species inside water droplets is not as important as the total sulfur uptake from the gas phase. Therefore, a rate-approach reaction model has been investigated, as it simplifies the calculation procedure and avoids the need for invoking the solver for systems of equations. In this approach, the alkalinity is represented as a single chemical species, similarly to the simple data values commonly encountered in literature for describing seawater. Additionally, all of the sulfur-containing chemical species are combined together under single term, and a global, rate-approach reaction model is applied. With this approach, the alkaline and sulfur species are tracked separately, and the resulting reaction term  $R_{Alk,SS}$  is calculated and added to both species' concentrations during the simulated reaction time. This approach is analogous to the one found in work by Caiazzo et al. [129], where the  $r$  is a kinetic constant representing the reaction rate, which approximates the nearly-instantaneous chemical equilibrium—a widely used assumption in flue gas desulfurisation modelling [130].

$$R_{Alk,SS} = -r \cdot c_{Alk} \cdot c_{SS} \quad (3.25)$$

With this approach, the sulfur species are increased by the interphase source of  $\text{SO}_2$ , which represents the absorption from the gas phase in Section 3.3.1. It is calculated for every droplet and at each time step in the mass transfer module, from the  $\text{SO}_2$  flux over the phase boundary. On the other hand, the reaction term  $R_{Alk,SS}$  represents the sink for both the alkaline and sulfur species, accounting for their consumption in chemical reactions.

$$\begin{aligned} c_{SS}^{new} &= c_{SS}^{old} + S_{\text{SO}_2} + R_{Alk,SS} \\ c_{Alk} &= c_{Alk}^{old} + R_{Alk,SS} \end{aligned} \quad (3.26)$$

This system presents a much streamlined solution for the chemical model, as it avoids solving a more complex system of equations and substitutes it for a rate based model dependent on the simplified species' concentrations. In the Fig. 3.11, a comparison between the literature results and the rate-approach model is given, and the achieved agreement is satisfyingly good. The results for full chemical model are in a better agreement with the literature data, but considering the significant approximation introduced, the discrepancies are rather small.

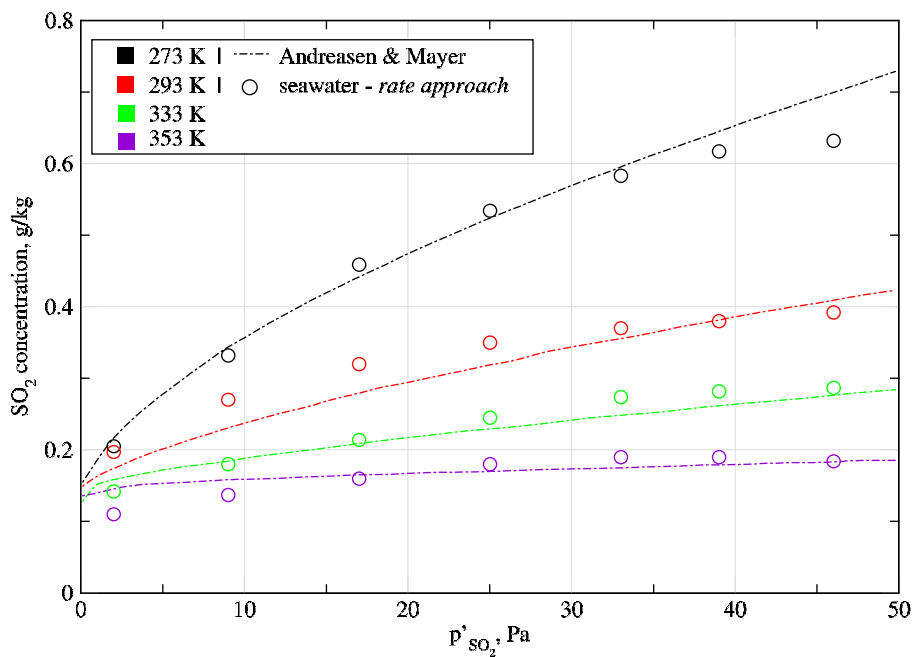


**Figure 3.11:** Comparison of the seawater rate-approach model to the literature data [118].

The additional validation of the rate approach will come in following sections, as a part of absorption dynamics modelling, but presently the validation over the presented range of temperatures and pressures indicates that the model is suitable for determining the equilibrium levels in the seawater under different conditions.

### 3.3 Mass Transfer Modelling for Flue Gas Desulfurisation

It was previously described that the absorption can be divided into two main sections that govern the entire process. Chemical reactions in the liquid phase were described in the Section 3.2, while this section will focus on modelling the mass transfer between the phases.

Modelling of mass transfer for different technical applications is an open topic of investigation for numerous researchers, as any improvements in the efficiency of processes or their managing lead to considerable savings. However, even though the interest in the topic of mass transfer is a long-lived one, some of the processes exhibit complexities that defy easy description or modelling.

The previously-presented chemical models and equilibrium concentrations are valid only for the static, equilibrium conditions between two phases, and represent the potential that can be achieved. However, in the contact between two real fluids, the dynamics of mass transfer depend on types and shapes of fluid, as well as on their properties. Thus, the potential for absorption, or the driving force described by the chemical models and equilibrium concentrations is limited and bounded by the dynamics of mass transfer.

For the spray scrubbing applications, the absorption of  $\text{SO}_2$  from flue gases to water droplets presents the main issue. Initially, the analysis of mass transfer for a single droplet will be shown, with comparison and validation against the available literature data. Afterwards, the model will be expanded on the entire sprays and the three-dimensional geometries.

### 3.3.1 Single Droplet Mass Transfer Modelling

In order to better understand the processes and the dynamics of absorption, the simplified model on a single droplet was initially implemented. Besides the fact that it facilitates the initial phases of implementation, another benefit of this approach is the possibility for easier validation of the model, as the experimental data is scarce, but still more available for absorption on a single-droplet level.

In the gas-liquid contactors, the goal is to obtain the greatest possible mass transfer, but the aim is also for it to be predictable and scalable over a range of conditions that occur in a scrubber. An overview of the main types of scrubbers was given previously in the Section 3.1.3, but the introduction in modelling of mass transfer is given below. Choosing the appropriate model for describing the mass transfer between the phases can be a complex issue, as it can be influenced by a number of complex phenomena. Depending on a type of scrubber, different conditions can occur in it, from film flows over complex geometries in the packed bed scrubbers; over the inverted approach in the bubbling columns and the liquid surrounding the rising gas bubbles; to the spray scrubbers, where falling droplets of water absorb pollutants from the stream of gases. In the spray scrubbers that are of interest in this work, the foundation of mass transfer is the absorption in droplets that form the spray, as they are the primary process of pollutant removal [131], while the additional liquid formations such as sheets, ligaments and wall film contribute to the absorption. Choosing the appropriate approach for modelling the mass transfer can present an issue because of the intricate fluid flow patterns present in the scrubber due to interactions of spray and gas, the complex physical phenomena in droplets occurring over small time and length scales [132], as well as for other physical occurrences present in spray scrubbers.

As a part of a developing field of fluid dynamics, detailed analytical approaches for resolving the internal distribution of pollutants absorbed in the droplet had been investigated over the last century. They provide a good overview of absorption dynamics and pollutants' mass propagation inside of droplets, but their application is limited to a cases with a narrowed range of conditions [111]. More recently, as the numerical methods gained more acceptance in the research communities and the computational capabilities increased significantly, the approaches that discretise the interior of the droplets accelerated the investigations [129]. However, although the advanced computational approaches can assist in analysing the absorption in spray scrubbers, the number of droplets in the scrubber that needs to be tracked and discretised makes this method prohibitively expensive from the computational standpoint. Therefore, the existing computational resources mandate the usage of approximations for in-droplet modelling in developing the tools for application in industrial cases.

A concentrated-parameter approach has been adopted as a modelling basis in present work. The properties of water droplets are assumed as evenly-distributed and constant over the entire droplet. In the applications such as modelling the full scale, three-dimensional sprays with a large number of droplets being introduced into domain, the utilisation of this approach benefits by significantly reducing the requirements on computational resources. However, as this approach stems from the previously mentioned discrete droplet method that is ubiquitous in spray modelling, the approximation of droplet properties as points with *lumped* parameters is just an extension of the common and validated model [73].

### 3.3.1.1 Two-film theory

Since the modelling of internal distribution of pollutants and other properties is avoided by applying the concentrated-parameter model and the DDM method (Section 2.4), the accurate assessment of the mass transfer becomes exceedingly important. Two-film theory is a widely-used approach for mass transfer modelling across the interface of two distinct phases. As a continuation of the Nernst's simple, single-film transfer model, this theory is based on the work by Whitman [107], and assumes the existence of two thin films on each side of the interface, where the resistance is located. The equilibrium of gas and liquid phase is assumed, and the gas solubility governed by the Henry's law constant is also fast.

The rate of mass transfer  $N_A$  is proportional to area  $a$  between the phases and driving force that causes the transfer process across the phase boundary. This proportionality is called the mass transfer coefficient, denoted as  $k$ , and it has the main impact on the overall mass transfer dynamics. The driving force is caused by the effective difference in concentrations of the component A in the bulk of gas phase  $C_{A,g}$  and bulk of liquid phase  $C_{A,l}$ .

$$N_A = k a \Delta C_A = k a (C_{A,g} - C_{A,l}) \quad (3.27)$$

The illustration of two film approach is presented in Fig. 3.12. In these stagnant films,

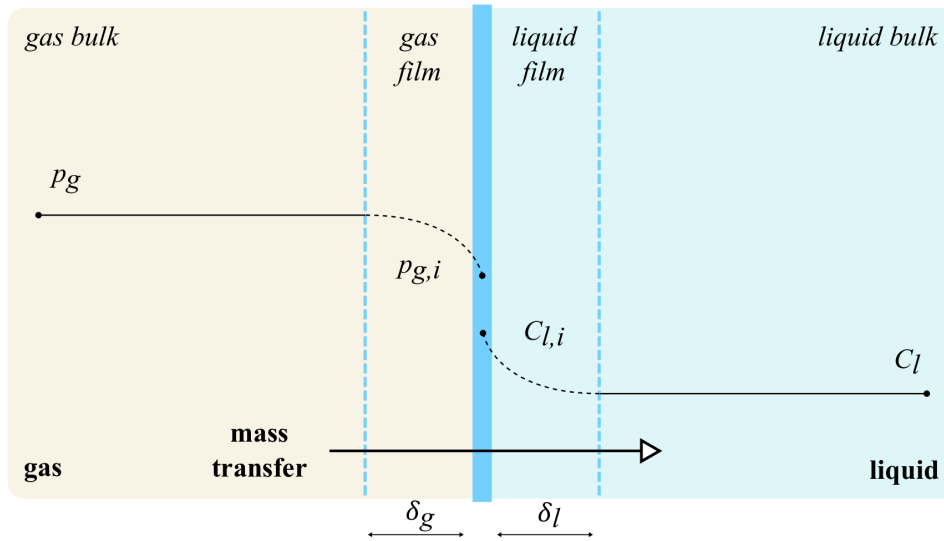


**Figure 3.12:** Illustration of the two film theory - concentrations at the gas-liquid interface.

neither the velocity profile, nor the exact concentration profile are known, and the mass transfer coefficients for both sides represent the concentration changes. For mass transfer across thin films the steady-state balance is valid, and the fluxes per unit of area  $J_A$  can be displayed as the differences between the bulk and the interface concentrations for each of the sides. On the gas side, the concentration is represented by the difference in partial pressures of species A:

$$J_A = \frac{N_A}{a} = k_g (p_g - p_{g,i}) = k_l (C_{l,i} - C_l) . \quad (3.28)$$

Since the concentrations at the interface cannot be directly measured, the concept of overall mass transfer coefficient is introduced. It is based on the concentration difference between the bulk of the phases, and takes both the gas side mass transfer coefficient  $k_g$  and the liquid side mass transfer coefficients  $k_l$  into account. After the introduction of Henry's Law (equation (3.1)) to relate the gas phase concentrations and the assumption of equilibrium conditions, the *total mass transfer coefficient*,  $K_{tot}$  is derived:

$$\frac{1}{K_{tot}} = \frac{1}{k_g} + \frac{H_{SO_2}}{E_{SO_2} k_l} . \quad (3.29)$$

In the equation (3.29), the total mass transfer coefficient is composed out of individual resistances for each phase, which are summed analogously to the serial resistances. The ratio between mass transfer coefficients indicate the phase's contribution to the overall resistance. The mass transfer can be liquid- or gas-side dominated, depending on the application. Although conflicting analyses for spray contactors could be found in the literature, stating both the liquid side and the gas side as dominant ones, the prevailing opinion is that  $SO_2$  absorption tends to be liquid-side dominated [133]. Initial tests in this work showed that the liquid side resistance



is higher for spray absorption. However, unlike the common assumption in available literature [134], the gas side mass transfer coefficient was not disregarded. Therefore both phases were modelled by the approaches presented below.

In the relation for the total mass transfer coefficient, an additional term  $E_{SO_2}$  is used to describe the influence of chemical reactions occurring in the system. This enhancement factor accounts for higher driving force compared to the absorption without chemical reactions [116].

The gas side mass transfer modelling generally receives less attention than the liquid side, and is almost universally modelled by the dimensionless correlations. Sherwood number represents the ratio of convective to diffusive mass transfer:

$$Sh = \frac{k}{D/L}, \quad (3.30)$$

and is analogous to Nusselt number in heat transfer operations. It is commonly expressed by the combination of Reynolds and Schmidt numbers in the modified Ranz-Marshall equation, derived for the flow around the sphere [116]:

$$Sh = \frac{k_g RT d}{D_{SO_2,g}} = 2 + 0.69 Re_l^{1/2} Sc^{1/3}, \quad (3.31)$$

and the Schmidt number is defined as:

$$Sc = \frac{\mu}{\rho D}. \quad (3.32)$$

The  $SO_2$  diffusivity in the gas phase around a droplet was obtained by the Fuller, Schettler, and Giddings's empirical relation, which was derived from an extensive set of experimental data and makes it advantageous in some cases over the kinetic theory approaches [135].

$$D_{SO_2,g} = \frac{10^{-3} T^{1.75} \left( \frac{1}{M_{SO_2}} + \frac{1}{M_{air}} \right)^{1/2} \cdot 1.013}{p \left[ (\sum v)_{SO_2}^{1/3} + (\sum v)_{air}^{1/3} \right]^2} \quad (3.33)$$

The liquid side mass transfer coefficient receives more attention in spray absorption modelling since it has proven to be a more trying task. The falling droplets in a turbulent flow field exhibit processes such as internal circulation, surface stretching and oscillations [136], which significantly impact the mass transfer [137]. Its dependence on flow and droplet conditions, such as turbulence, internal circulation, droplet oscillations and surface stretching has a greater impact on the mass transfer.

### 3.3.1.2 Film Theory

For film theory, it is assumed that the mass transfer across the film is governed by the molecular diffusion. Therefore, the Fick's law of diffusion can be used to describe the mass

transfer for each of the film regions. It states that the flux is proportional to concentration gradient, and the proportionality is described by the binary diffusion coefficient of component A in B, while the fraction  $\partial C_A / \partial x$  represents the concentration gradient in the direction of mass transfer. The negative sign ensures that the orientation of flux is opposite to the concentration gradient, i.e. from the higher concentration to the lower.

$$J_A = -D_{AB} \frac{\partial C_A}{\partial x_i} \quad (3.34)$$

Since the exact concentration profile across the film thickness is unknown, the film theory assumes the linear profile due to molecular diffusion and the constant diffusion coefficient  $D_{AB}$ . After the concentration change across the thin film, in the bulk of liquid the species' concentration is assumed uniform due to turbulent mixing. The concentration gradient is approximated as difference in concentrations over the film thickness, and with the assumption of steady-state and no accumulation in the stagnant film, the combination of previous formulas provides the following expression that depicts the linear concentration profile marked in Fig. 3.13.

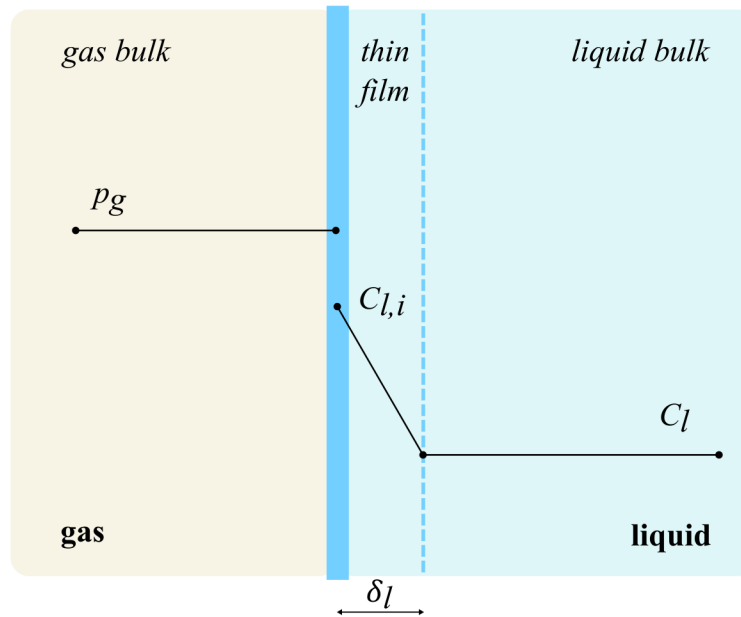


**Figure 3.13:** Illustration of film theory model.

$$J_A = -D_{AB} \frac{C_{l,i} - C_l}{\delta} \quad (3.35)$$

For the film theory, ratio of diffusion coefficient and film thickness defines the *mass transfer coefficient* for the liquid phase  $l$ . The  $k_l^{film}$  is linearly proportional to diffusion coefficient over the film thickness,

$$k_l^{film} \propto \frac{D_{SO_2,l}}{\delta}, \quad (3.36)$$

but this proportionality is somewhat modified for specific applications of mass transfer. The

exact film thickness is not known in advance and differs depending on the type of liquid. In case of absorption in liquid droplets, film theory is sometimes termed *long contact time approach* [138], and droplet diameter  $d$  is taken as a characteristic length together with the factor 10.

$$k_l^{film} = 10 \frac{D_{SO_2,l}}{d}, \quad (3.37)$$

Although in some applications—where droplets can be taken as stationary, if the steady state process can be assumed, or if mass transfer in liquid film over surface is diffusion-driven—film theory can provide good results, in reality it usually does not lead to accurate estimation of mass transfer coefficients. The actual concentration profile is non-linear and there are convective and turbulent processes inside liquid droplet that cannot be accounted for by film theory.

### 3.3.1.3 Penetration Theory

The penetration theory presents an upgrade to the film theory, as it includes transient behaviour of the mass transfer. Introduced by Higbie [139] in 1935, it is probably the most widely used approach for mass transfer calculation. It assumes the presence of internal circulation that enhances mass transfer rate compared to diffusion alone. Elements of liquid at the surface are replaced by the fresh liquid elements from the bulk of droplet [130]. Penetration theory introduces the unsteady transfer for the fresh parcels of liquid coming into contact with the boundary, where equilibrium conditions across the interface are assumed. The time that all fluid fragments spend in contact with gas phase before being swept back into solution and replaced by fresh liquid elements is constant, and called *contact time* [140]. This fluid circulation effectively introduces a thick film and combines diffusion across individual fluid elements with the convection process.

$$k_l^{P.T.} = 2 \sqrt{\frac{D_{SO_2,l}}{\pi t_{con}}} \quad (3.38)$$

While film theory displayed linear dependence on diffusivity of liquid phase, penetration theory is consistent with the experimental data that strongly suggest that the proportionality is non-linear, and that it scales according to  $k_l \propto D^{1/2}$  [134].

For penetration theory the contact time is generally an unknown parameter. For the mass transfer calculation in falling films, the contact time can be expressed as the ratio between the characteristic length and the velocity, but for droplets, similar detailed expressions were not available.

### 3.3.1.4 Surface Renewal Theory

Surface renewal theory is an additional expansion of the penetration theory that includes more detailed description of mixing between fresh and spent liquid. Developed by Danckwerts in 1955 [141], it assumes that all surface elements have an equal probability of being replaced by fresh liquid parcels, which accounts for the unpredictability of turbulent flow inside the droplet.

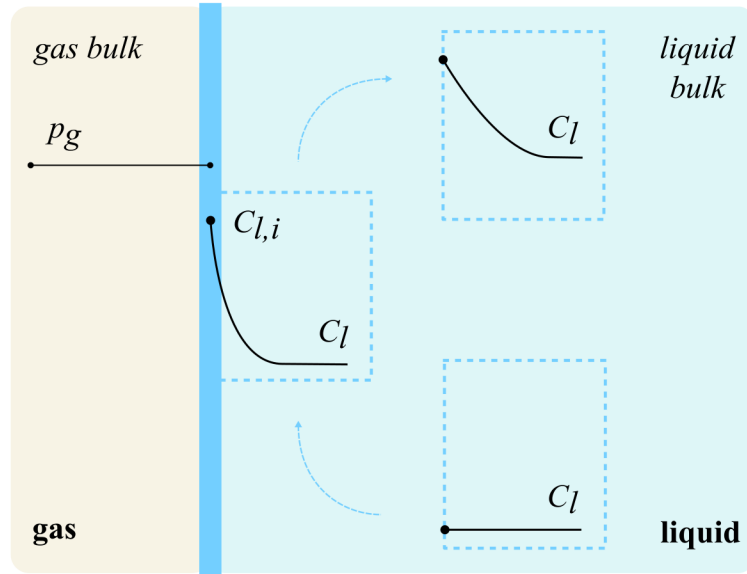


**Figure 3.14:** Illustration of penetration theory model.

Instead of the contact time concept, the element at the interface is renewed due to the effect of turbulence, and the mass transfer coefficient is expressed in terms of rate of surface renewal  $s$ , or the *production of fresh surface* [142]. With surface renewal theory, the thick film framework that is present in penetration theory is replaced by two regions that exchange mass, Fig. 3.15. As with the penetration theory, the mass transfer coefficient values scale proportionally to  $D^{1/2}$ .

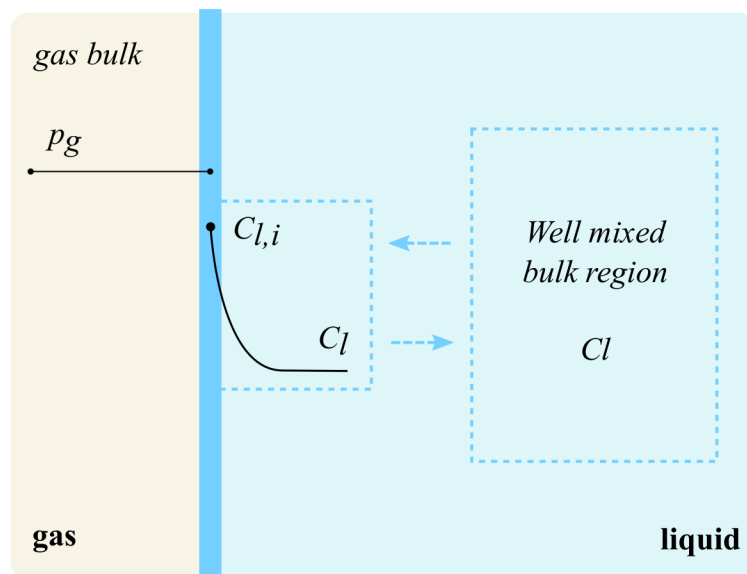


**Figure 3.15:** Illustration of surface renewal theory model.

$$k_l^{S.R.} = \sqrt{D_{SO_2,l}s} \quad (3.39)$$

Similar to previous theories that use parameters that are not known in advance, the surface renewal theory calculates the probability of particular element being replaced, and the average value is represented by the rate  $s$ . A modification of pure surface renewal theory presented in the work by Jajuee et al. simplifies the calculation with a more straightforward calculation for  $s$  [143].

$$k_l^{S.R.} = \left( \frac{4D_{SO_2,l}}{\pi} \sqrt{\frac{vg}{v}} \right)^{1/2} \quad (3.40)$$

Liquid phase diffusivity was universally used in previous equations as a main property influencing the mass transfer coefficient. The values of diffusivity were calculated with Stokes-Einstein equation, for which the constant was obtained from Perry's Chemical Engineers' Handbook [144].

$$\frac{D_{SO_2,l} \mu_{H_2O}}{T} = const. \quad (3.41)$$

In all previous models,  $D_{SO_2,l}$  is molecular diffusivity of  $SO_2$  in solution at infinite dilution, which in practice relates up to 5 % in solvent. Furthermore, although the constant value in equation (3.41) covers the temperature range around the reference value, this should be kept in mind when extrapolating to liquid phase temperatures above 80 °C.

### 3.3.1.5 Additional Mass Transfer Coefficient Models

Another expansion of the mass transfer calculation model is possible by including the influence of droplet oscillations and surface stretch. Angelo et al. [145] developed the model that also scales with  $D^{1/2}$ , includes the surface stretching via parameter  $\alpha$ , and models the oscillation time  $\tau$  by Lamb's model [146].

$$k_l^{Angelo} = 2 \sqrt{\frac{D_{SO_2,l}}{\pi\tau} \left( 1 + \alpha + \frac{3\alpha^2}{8} \right)} \quad (3.42)$$

$$\tau = \frac{\pi}{4} \sqrt{\frac{\rho_l d^3}{\sigma}}$$

Lastly, a model by Amokrane et al. [147] includes the interfacial velocity  $u_*$  and oscillation

frequency  $\omega$ , which relates shear stress with the mass transfer coefficient.

$$\begin{aligned} k_l^{Amokrane} &= \omega \sqrt{\frac{D_{SO_2,l} u_*}{d}} \\ u_* &= \sqrt{\frac{\tau}{\rho_l}} \end{aligned} \quad (3.43)$$

A large number of mass transfer models are available, such as Newman's model for stationary drops or Kronig–Brink model for creeping internal flows, but the models presented here are most common and more suitable for the application under consideration.

Total mass transfer coefficient is determined based on the equation (3.31) for the gas side, and one of the previously presented models for liquid side mass transfer model.

In the equations below, the molar flux  $N_{SO_2}$  over the droplet's surface is calculated as a product of driving potential between phases and the total mass transfer coefficient. The driving force is determined as a difference between the  $SO_2$  partial pressure in gas phase and the equilibrium concentration of the unreacted  $SO_2$  in the liquid phase. The equilibrium concentration is represented by the combination of Henry's constant and the concentration of unreacted  $SO_2$  in liquid phase. For each timestep, the  $SO_2$  source for a droplet is being calculated as a combination of droplet area, timestep size and molar flux, divided by the mass of a droplet.

$$\begin{aligned} N_{SO_2} &= K_{tot} (p_{SO_2} - H_{SO_2} C_{SO_2}) \\ S_{SO_2} &= \frac{N_{SO_2} A_d}{m_d} \end{aligned} \quad (3.44)$$

### 3.3.2 Validation of Mass Transfer Coefficient Models

The issue with modelling spray scrubbers is the difficulty in accurately predicting the overall mass transfer rates. Mass transfer highly depends on the droplet sizes, but other parameters such as internal recirculation, oscillations and pulsations can have significant influence. Different equations used for the liquid side mass transfer coefficient are expected to provide varied results and, as the liquid side has a larger influence on the total coefficient in this application, this choice has a critical effect on the overall mass transfer dynamics.

Another issue is the problem with scaling the model from comparisons on simplified cases to the full spray experiments. Overall, the experimental data on  $SO_2$  absorption in droplets and sprays is not abundant, and even the available cases are commonly presented with insufficient information on experimental set-ups and boundary conditions. When dealing with tests on individual droplets, further difficulties can be encountered in measuring quantities such as concentrations or internal state of a droplet, issues with obtaining droplet sizes, and duration of the contact time with the atmosphere.

Finally, even if comparisons between the model and available experimental data for single droplets do not show significant discrepancies, issues can arise in scaling the model to full three dimensional sprays, from using a model over wider distribution of droplet sizes.

The comparison of mass transfer coefficients by the presented approaches and the literature values has been made, and they differ significantly. This is expected since a single equation cannot cover a wide array of conditions for all the droplets in the spray. Here, the results of the models will be compared with three sets of data.

### 3.3.2.1 Single Falling Droplet Test: Walcek et al.

The first set of experimental data is obtained from Walcek et al. [112]. Their method included letting the pure water droplets fall through a roughly 30 m high rain shaft and then capturing them. Droplets were produced with hypodermic needle using distilled and deionised water, thus ensuring consistent droplet diameter of 300  $\mu\text{m}$ . Droplets falling in the shaft reached terminal velocity before entering the isolated compartment that contained  $\text{SO}_2$ -rich atmosphere. By varying the length of a compartment the exposure time was modified, and  $\text{SO}_2$  concentrations ranged between 1% to 100%. After falling to the shaft bottom, the droplets were collected and the absorbed  $\text{SO}_2$  was estimated by measuring the  $\text{HSO}_3^-$  concentrations.

The models presented previously were implemented in the MATLAB<sup>TM</sup> code that replicated the conditions reported in the paper. The mass transfer framework included only the changes of in-droplet species concentrations, as  $\text{SO}_2$  concentrations in gas phase were assumed constant for this situation. Besides the calculation of properties mentioned as part of absorption model, such as diffusivity, for other liquid and gas properties the Coolprop library was used [148].

When all of the models were used to replicate the literature results, only the film theory among the presented models produced results comparable to the experimental data. Other models universally displayed much faster absorption dynamics and are not shown in Fig. 3.16. The results obtained by film theory are in good agreement with the literature data, with more noticeable discrepancy at higher concentrations, where model assumptions are no longer valid.

### 3.3.2.2 Single Falling Droplet Tests: Saboni and Alexandrova

Another set of data is taken from the work of Saboni and Alexandrova [149], who presented experimental and numerical results for  $\text{SO}_2$  absorption on single droplet cases. The  $\text{SO}_2$  concentrations were comparatively lower at 97 ppm and 1.035 ppm and present the cases with weaker driving force. Droplet diameter was 2.88 mm with high exposure time, as the upward stream of gas maintained droplets suspended roughly at the same position and kept them exposed to polluted air.

Figures 3.17 and 3.18 display the implemented models compared to literature data. It can be noticed for the higher concentration case, Figure 3.17, that the absorption dynamics obtained by most of the models is quite similar and roughly matches the experimental data points, which are

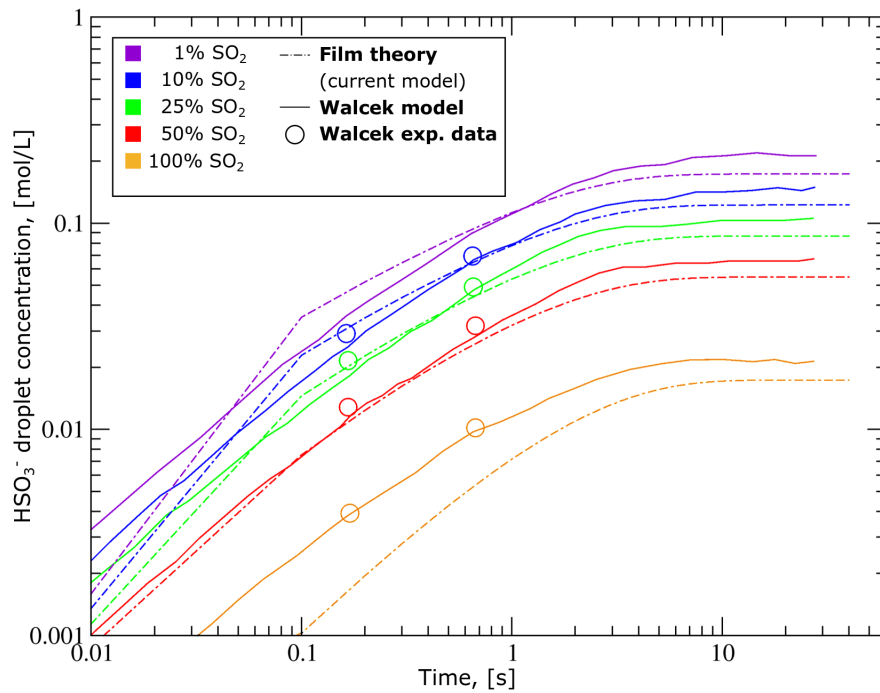


**Figure 3.16:** Comparison of film theory with literature data [112]. Single falling droplet,  $d = 300 \mu\text{m}$ ; 1%–100%  $\text{SO}_2$ ); film theory.

grouped in a narrow time range. The only outlier in this case is the film theory, which displays a significantly slower absorption rate.

For the second case, the  $\text{SO}_2$  concentration in air was 1.035 ppm and the effects of lower driving force were demonstrated in larger spread of absorption dynamics curves. Film theory again did not show agreement with literature data, while most of other models underpredicted the absorption. In this case, the surface renewal theory calculated the absorption dynamics that was closest to data reported by Saboni and Alexandrova.

Both the case by Walcek and by Saboni and Alexandrova represent borderline cases for application in spray scrubbers. In the first one, the residence time covers the short range usually encountered in scrubbers and the size of  $300 \mu\text{m}$  roughly matches the droplets in scrubbers. However, the concentrations of 1% and above are significantly higher than the  $\text{SO}_2$  concentrations in flue gases. This is the reason behind somewhat surprising film theory suitability—due to high concentrations, its usually slower absorption dynamics matched the literature data better than other, more sensitive models which were overshooting.

On the other hand, the results from Saboni and Alexandrova represent lower, but more reasonable concentration range, which causes film theory to fail. Among other models, penetration theory with the time parameter of 0.01 s and surface renewal achieve the best results. They differ between the 97 ppm and the 1.035 ppm case, where penetration theory is slightly more suitable for higher concentration case. Still, this literature source analyses droplets with diameter that is quite high for spray scrubbers, despite the coarse sprays encountered. Finally, the exposure time



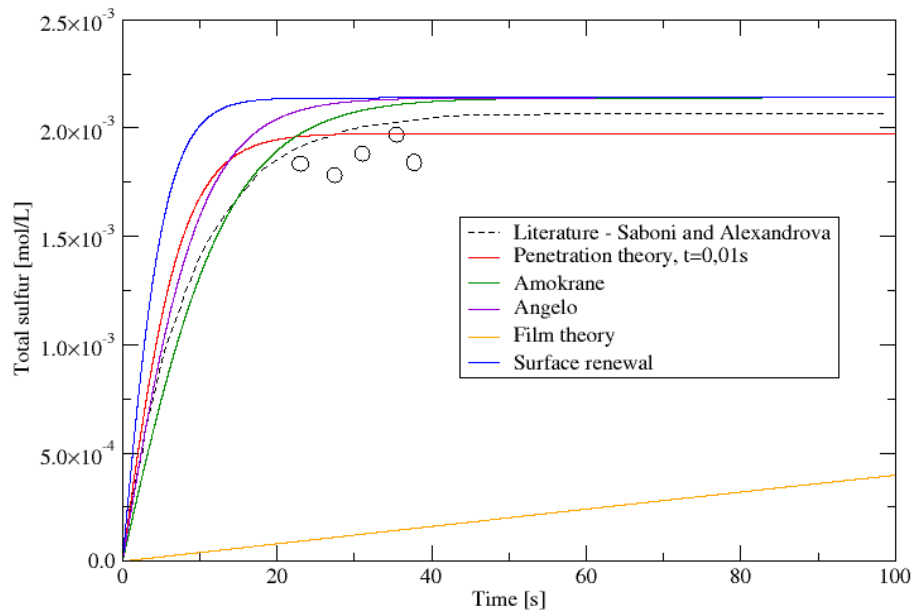


**Figure 3.17:** Comparison of mass transfer coefficient models with literature data [149]. Single falling droplet,  $d = 2.88$  mm;  $T = 12.5$  °C; 97 ppm  $\text{SO}_2$ .

is measured in tens of seconds, which is too high. Although these cases were not completely suitable for validation and selection of appropriate models, they provided some insight into models' behaviour.

### 3.3.2.3 Single Falling Droplet Tests: Kaji

The final set of data for a single droplet tests is obtained by Kaji [150]. Kaji performed measurements on free-falling pure water droplets with short exposure times to air mixed with  $\text{SO}_2$ . The concentrations were in the range pertinent for flue gas desulfurisation processes, and droplet diameters were 2.2 mm, which is a bit high, but still within the range of usually encountered operating conditions. The combination of mentioned parameters makes this case as the most suitable one for comparisons with real scrubber conditions.

Among the tested liquid side mass transfer coefficients, the penetration theory and surface renewal theory displayed the best agreement with literature results, and are shown in Fig. 3.19. Similarly to the previous two cases, surface renewal theory predicts higher absorption dynamics than the experimental data points, especially at higher concentrations. Meanwhile, the penetration theory slightly underestimates the absorbed  $\text{SO}_2$  in falling droplets.

The presented results were used for assessing the suitability of investigated models for accurately predicting the liquid side mass transfer coefficient. Although the used data sets did not most meticulously represent the conditions encountered in real industrial scrubbers, some conclusions about the models could be drawn nonetheless. Film theory was the least suitable model for mass transfer coefficient calculation, which confirmed the inherent limitations of the model. More complex models that included wider range of phenomena such as the models by

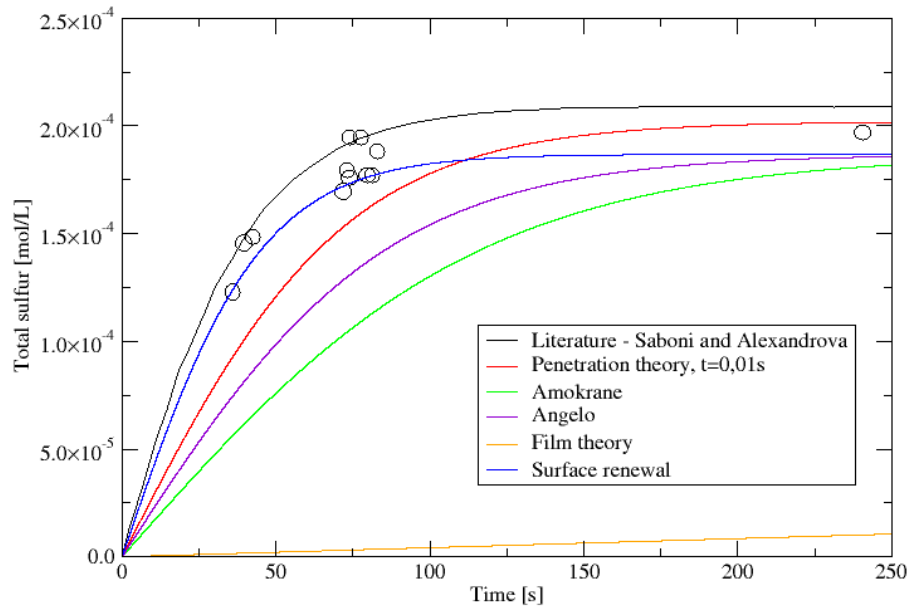


**Figure 3.18:** Comparison of mass transfer coefficient models with literature data [149]. Single falling droplet,  $d = 2.88$  mm;  $T = 10$  °C; 1.035 ppm  $\text{SO}_2$ .

Angelo and Amokrane were somewhat accurate in prediction of  $\text{SO}_2$  absorption, although they deviated more than penetration theory or surface renewal. These more detailed descriptions of underlying physics were lost due to rough description of boundary conditions, primarily droplets' properties. Therefore, it was concluded that the additional model complexity did not bring significant benefit.

Both surface renewal and penetration theory were close to literature data in predicting the absorption dynamics. The review of available literature suggests that the penetration theory is more commonly used approach, as was investigated in details in the group's previously published work [151]. Along with the performed test, this suggest that the penetration theory stands as a good solution for balance between the model's complexity and its accuracy, and will be used in further simulations. Finally, these results should be taken with some reservation, as scaling to full three dimensional sprays might introduce additional uncertainties. Yeh states that these single-droplet tests might have limited applicability to full sprays due to higher velocities in real scrubbers [152]. Still, the insight into absorption dynamics gained here has proven useful for the implementation and validation of three dimensional absorption model in AVL FIRE™.

### 3.4 $\text{SO}_2$ Absorption Modelling Results

In this section, the simulation results obtained by the absorption model will be presented. The sulfur dioxide absorption model described previously is implemented in the framework of computational fluid dynamics software AVL FIRE™ and coupled to the existing modules such

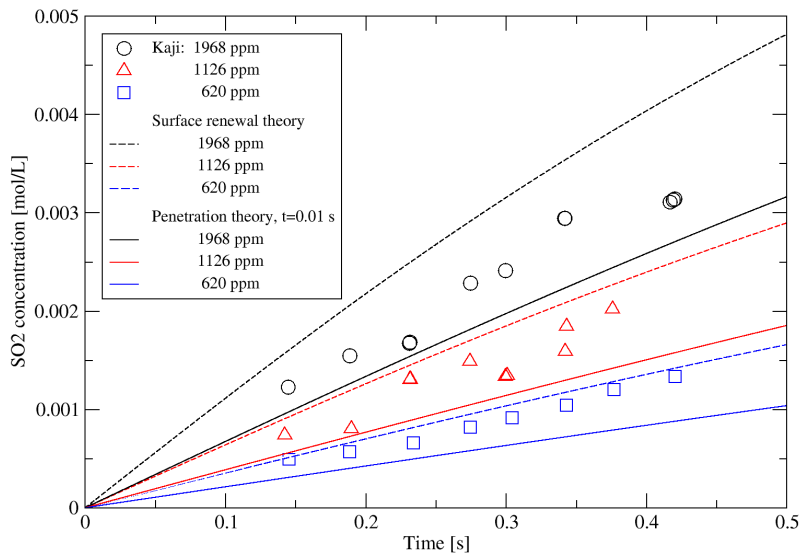


**Figure 3.19:** Comparison of mass transfer coefficient models with literature data [150]. Single falling droplet,  $d = 2.2$  mm;  $T = 20$  °C 620 ppm to 1968 ppm  $\text{SO}_2$ .

as heat, mass and species transport. The gas phase was described by the continuous phase, expressed numerically by the Euler flow field, while the main part of the implementation was done in spray module, following the Euler-Lagrangian formulation and the DDM approach presented in Section 2.4. The discrete phase was tracked through the domain as parcels, representing the collection of water droplets with similar properties. The concentrated-parameter approach was used in modelling the droplets, averaging the internal properties over the droplet volume. The Schiller-Naumann model was used for droplet drag calculation; interphase energy and mass exchange were taken into account by multi-component evaporation model, the particle-wall interaction model used was Walljet 0, and particle breakup and interaction models were not included in the simulations.

The absorption was coupled in one-way only, as the desorption process from droplets to gas was not included in the model. The turbulence was modelled by the standard  $k$ - $\epsilon$  turbulence model, as the initial simulations on simplified test geometries did not show discrepancies compared to the  $k$ - $\zeta$ - $f$  turbulence model. Programming was done in the FORTRAN language, by modifying the code provided through the collaboration with Advanced Simulation Technologies division of the AVL List GmbH.

The major issue for the validation of implemented models was the absence of available experimental data suitable for comparison. As the resources for performing the experimental research and obtaining the results were not available, the sources of data for model validation were found in the literature. Although the flue gas desulfurisation is not a novel topic, and despite the recent

growth of interest for the topic explained in the introductory sections (Section 3.1) extensive information about experimental research on pure and seawater absorption in spray scrubbers is not readily available. The majority of research has been done on packed bed scrubbers, while the spray scrubbers were not as represented. Additionally, the amount of research on seawater as a scrubbing agent is still limited compared to lime and limestone scrubbing.

Finally, there is an issue of reproducing the experimental research published by other authors. The results obtained from simulations and numerical models are highly-dependant on input data. For performing numerical simulations, the accurate knowledge of boundary conditions is an important condition. It is sometimes the case that experimenters do not anticipate that their work will be used as a basis for numerical simulations, and information about the set-up that is important for performing simulations is left out. In present case, this is especially important for spray modelling, as it is a major parameter influencing the mass transfer. These issues were encountered in this work as well, which additionally narrowed the list of available literature suitable for validation process. Still, despite these inevitable issues in numerical modelling, two of the cases that have been used are presented below.

### 3.4.1 1<sup>st</sup> Validation Case: Caiazzo et al.

The information about this case were obtained in the paper by Caiazzo et al. [153]. In their study, they performed experimental investigation of SO<sub>2</sub> absorption in pure and seawater sprays, measuring the removal efficiency of the process under the different liquid flow rates. The liquid was sprayed counter-currently in a stream of gas rising in the 1.88 m high and 0.18 m wide tube representing the scrubber, and the SO<sub>2</sub> concentrations were measured at the outlet on the top. Pollutant concentrations were varied between 500 ppm, 700 ppm and 900 ppm, and the gas temperature was 250 °C, representing flue gases entering the scrubber at the inlet at the bottom.

Spray parameters are crucial in influencing the absorption, since the mass transfer depends mostly on droplet diameter, contact surface area, droplet velocities and the spray geometry. Caiazzo et al. provided the spray analysis and the droplet distribution of the injector positioned at the scrubber outlet for the liquid flow rates ranging between 0.1 m<sup>3</sup>/h to 0.4 m<sup>3</sup>/h. The injector position was set at the top of scrubber, 20 mm in the domain from the outlet. Five nozzle holes were circularly arranged, on the rim of a 40 mm diameter circle. Nozzle holes had 2 mm radius, and produced spray with 60° angle. Droplet sizes were prescribed as a particle size distribution, according to the mean value, standard deviation and skewness factor provided by the authors of the experimental investigation. For the reproduction of droplet sizes useful for the modelling purposes, probability distributions were calculated from the provided experimental data. The skew-normal distribution was assumed for the droplet sizes, with the range between 0 mm to 2 mm, and the probability curves can be seen in Fig. 3.20, which are subsequently normalised during the injection calculation procedure.

The inlet boundary condition imitated flue gases from the marine engine, and was set as

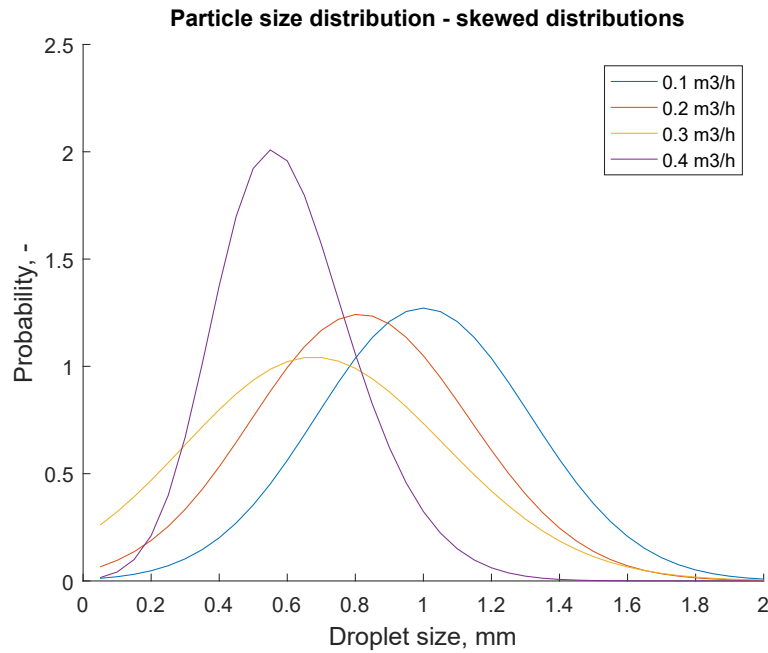


**Figure 3.20:** Particle size distribution for the injected droplets under different flow rates.

the normal velocity, with 0.437 m/s and gas temperature of 250 °C. Walls of the vessel were prescribed as constant boundary condition at 250 °C and no slip boundary condition. The outlet at the top of the scrubber was kept at the static pressure of 101 325 Pa, simulating the exhaust to the ambient atmosphere. The domain was uniformly initialised with the velocity and temperature from the inlet. The simulation time step was  $5 \times 10^{-4}$  s, and the spray started after the stationary conditions were achieved in the domain. Both the pure water and the seawater were used as scrubbing liquids, with the alkalinity of seawater set at the 0.0024 mol/kg. Overview of the numerical setup can be seen in Table 3.3.

The mesh representing the computational domain consists of 33 600 hexahedron cells, roughly 1 cm in size. Mesh independence calculation was performed on three meshes with different cell numbers and published as a part of separate work [154].

Although the source did not include information regarding the experimental measurements of fluid flow or temperatures that would facilitate model's validation, velocities, temperature profiles and the flow field data obtained at 15 s of simulation time show reasonable results in agreement with the expected physical behaviour. The left side of Fig. 3.21 shows the temperatures along the tube and in the droplets. The anticipated evaporative cooling can be observed in temperature profiles, which is essential for the determination of properties for the subsequent absorption modelling. Additionally, the evaporation influences the droplets sizes, gas phase composition and the SO<sub>2</sub> absorption.

On the right side of Fig. 3.21,b), the velocity field distribution and parcel velocities are presented for the flue gases flow of 40 m<sup>3</sup>/h and the pure water spray at 0.1 m<sup>3</sup>/h. The results show that the spray injection in the stream of continuously rising flue gases disrupts the fluid flow

**Table 3.3**  
Numerical settings for simulations of the Caiazza et al. [153] case.

<b>NUMERICAL SETTINGS</b>	
time step sizes	$5 \times 10^{-4}$ s, transient simulation
<b>FLOW</b>	
gas flow rate	40 m <sup>3</sup> /h
<b>SPRAY SETTINGS</b>	
liquid flow rate	0.1 m <sup>3</sup> /h–0.4 m <sup>3</sup> /h
injector position	axially, 20 mm downstream from the outlet
number of nozzles	5; radially arranged (40 mm circle radius)
angle between holes	72°
nozzle hole diameter	2 mm
cone angle	60°
particle size distribution	according to parameters in [153]; skew normal distribution assumed in Fig. 3.20
<b>SPRAY MODELS</b>	
drag law model	Schiller-Naumann
wall interaction model	Walljet 0
evaporation model	multi-component
<b>BOUNDARY CONDITIONS</b>	
inlet	normal velocity, 0.437 m/s; 250 °C 500 ppm–900 ppm SO <sub>2</sub> in air (N <sub>2</sub> /O <sub>2</sub> = 0.79/0.21)
<b>INITIAL CONDITIONS</b>	
velocity	uniform, upward direction 0.473 m/s
pressure	101 325 Pa
temperature	250 °C
chemical species	500 ppm–900 ppm SO <sub>2</sub> in air (N <sub>2</sub> /O <sub>2</sub> = 0.79/0.21)
<b>ASBSORPTION MODULE</b>	
liquid medium	pure water / seawater
absorption model	penetration theory; contact time = 0.1 s
seawater alkalinity	2400 μmol/kg

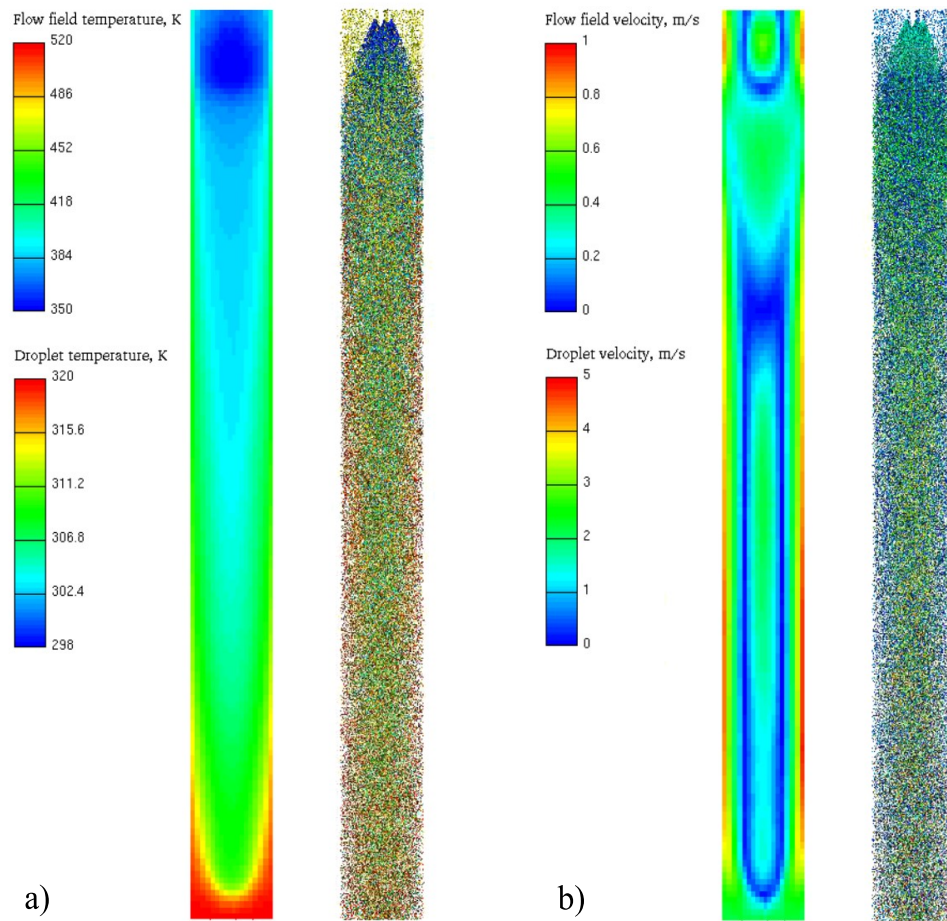


**Figure 3.21:** Fluid flow properties at cross-section, droplet properties: a) temperatures; b) velocities. Gas flow  $40 \text{ m}^3/\text{h}$ ; pure water flow  $0.1 \text{ m}^3/\text{h}$ , at 15 s.

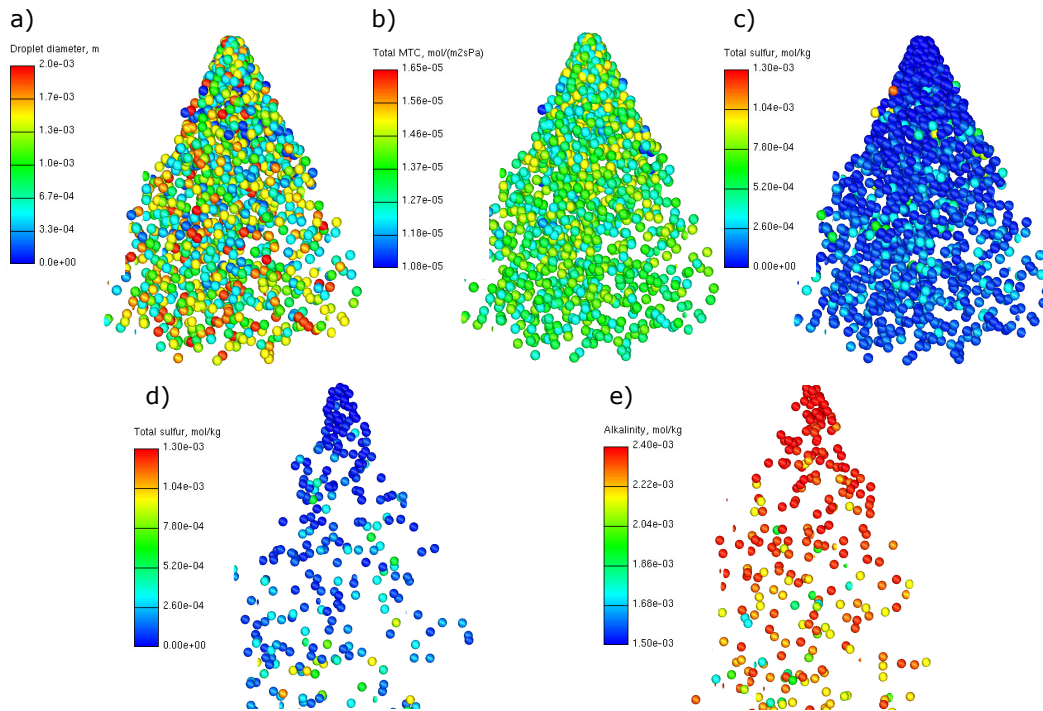


**Figure 3.22:** Physical values in spray droplets at the beginning of injection: a) droplet diameter; b) total mass transfer coefficient; c) total sulfur concentration for pure water; d) total sulfur concentration for seawater; e) seawater alkalinity.

significantly, leading to the vigorous mixing of the phases and highly turbulent flow. The initial velocity of the injected droplets is about 3 m/s, which is in agreement with the real industrial applications [155].

For the purpose of model verification and the illustration of physical properties changing in the absorbing droplets, Fig. 3.22 presents the selection of pertinent results. The figure shows properties in droplets at the beginning of the injection time for both pure water and the seawater. First, the droplet diameter shows the range according to the particle size distribution in Fig. 3.20 for the flow rate of  $0.1 \text{ m}^3/\text{h}$ . Following is the range of the overall mass transfer coefficients, combining the gas and the liquid side coefficients according to the equation (3.29). These values are consistent with the values reported in literature, and the liquid side had greater influence, although not a dominating one, as discussed in Section 3.3.1. The values at the beginning of injection are quite consistent, but the greater ranges are observed as the simulations proceeded due to different droplet parameters. Figure 3.22,c) and d) illustrate total concentration of sulfur-containing chemical species, which is an indicator that the  $\text{SO}_2$  removed from the gas phase is absorbed and converted to aqueous phase species. It can be noticed that the concentrations in seawater are somewhat higher, which is to be expected since seawater displays larger absorption capacity. Due to small time interval passed, the differences are not as big as in the overall results at the end of simulation. Finally, the alkalinity concentration is shown, and it can be seen that it is being spent as the droplet's lifetime increases and the chemical reactions take place in the



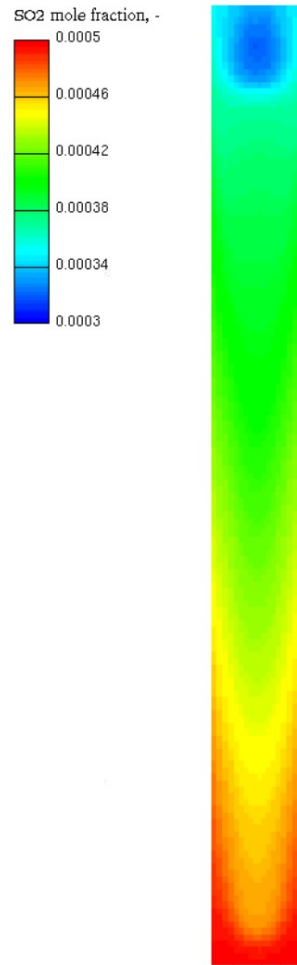


**Figure 3.23:** SO<sub>2</sub> concentration on the cross-section. Gas flow 40m<sup>3</sup>/h; pure water flow 0.1 m<sup>3</sup>/h.

liquid phase.

SO<sub>2</sub> concentrations in the gas phase are shown in Fig. 3.23. It can be noticed that the absorption in spray droplets occurs rapidly, as soon as droplets are introduced in the domain. Furthermore, the SO<sub>2</sub> concentration contour and the previous testing of the model indicate that the absorption is highly dependent on the spray and droplet characteristics. Smaller droplets display faster absorption due to higher surface-to-volume ratio, but the larger ones absorb a higher amount of pollutants.

The SO<sub>2</sub> removal efficiency is calculated as the ratio between the inlet concentration and the averaged concentration at the 15 s of the simulation time, 25 cm before the outlet as this distance was used for gas sampling in the experimental setup. The results for absorption of flue gases with 500 ppm–900 ppm SO<sub>2</sub> in the both pure and seawater were obtained by the spray absorption model. As the mass transfer to droplets was the main process in the simulations since the wall film was not investigated at this point, the whole process depended significantly on determination of mass transfer coefficient and the spray parameters. With all other parameters

such as injection pressure and nozzle diameter remaining unchanged, the droplet size distribution mainly depends on the liquid flow rate. Since limited information was available on the details of injection system, liquid flow rates combined with the replicated probability curves in Fig. 3.20 were used for setting up the spray. Overall, the replicated results for removal efficiencies across the concentrations, liquid flow rates and scrubbing liquid types displayed satisfying agreement with the experimental data.

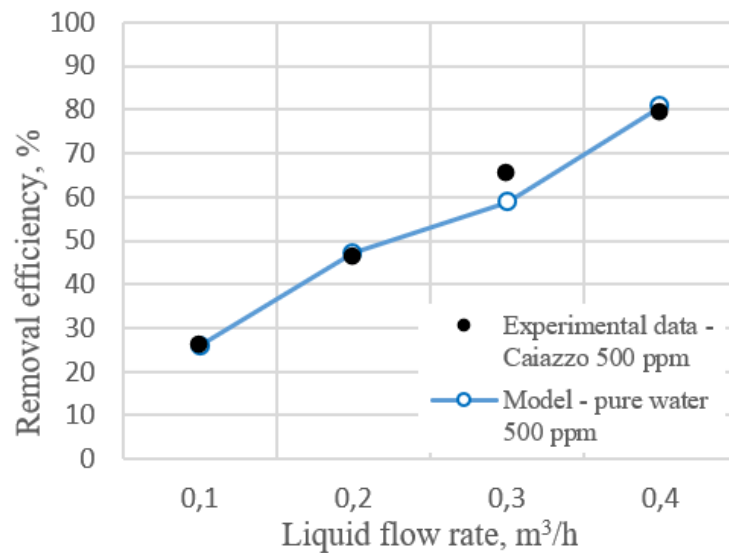


**Figure 3.24:** Removal efficiency for pure water absorption, 500 ppm – comparison with literature data.

It can be seen in Fig. 3.24 that for absorption of gases with SO<sub>2</sub> concentration of 500 ppm in pure water the results are replicated with high similarity to experimental data. The trend of increasing efficiency with higher liquid flow rates is accurately captured, displaying the model's sensitivity to droplet sizes and changing liquid-to-gas ratio. Slight deviation at 0.3 m<sup>3</sup>/h could be contributed to a number of factors, such as inaccurate droplet sizes, mass transfer calculation or wall film effects, but the increasing trend of efficiency with the rise of flow rates is still preserved.

For the second set of data points—removal of simulated flue gases with SO<sub>2</sub> concentration of 700 ppm with pure water—the obtained results shown in Fig. 3.25 are similar to the previous set. The sensitivity is reproduced here as well, keeping the calculated removal efficiency close to reported experimental values. The cause for disparities cannot be explicitly pinpointed to a single issue, as no clear pattern could be derived from the differences in results.

Next, the comparison of the model-obtained values with the experimental points is shown in Fig. 3.26. As in previous cases, the results are in good agreement with the literature data and the expected trend of increasing efficiency with rising liquid flow rate is conserved. If the resulting points are compared between the cases with different SO<sub>2</sub> concentrations, it can be

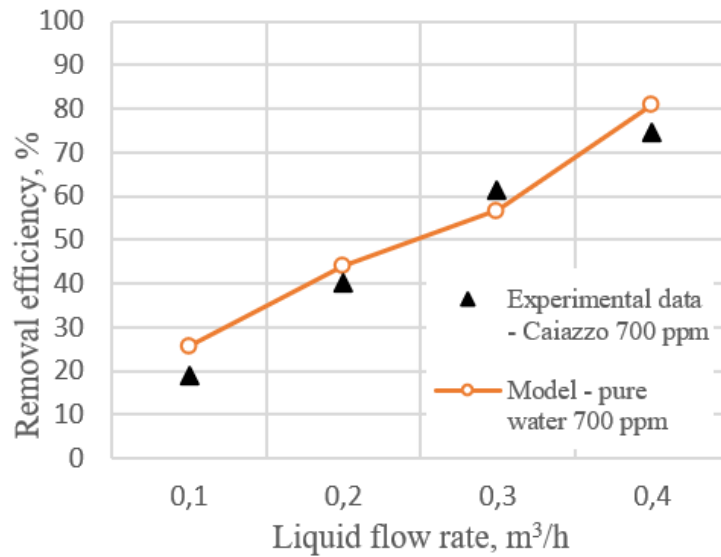


**Figure 3.25:** Removal efficiency for pure water absorption, 700 ppm – comparison with literature data.

seen that for 500 ppm the removal efficiencies are the highest, and they decrease with rising  $\text{SO}_2$  concentrations. The differences in removal efficiency reported by Caiazzo et al. are not quite significant as can be found in other literature sources, but the trend is noticeable. This indicates that resistance to absorption is not due to mass transfer, but due to absorbing capacity of the liquid used.

Relative errors are shown in Table 3.4, and indicate that the removal efficiency is satisfactorily reproduced, with somewhat higher relative errors at low liquid flow rates. This difference can be explained by the lower efficiencies in absolute terms causing the greater relative error, however, it may also indicate that the penetration theory might be less suitable for absorption in larger droplet sizes.

Finally, the results for 500 ppm flue gases absorption in seawater is shown in Fig. 3.27. The same trend and consistency with literature data can be found here as well, which indicates that the seawater chemistry model used is also valid for modelling flue gas desulfurisation process. Removal efficiency for seawater model shows the expected increase compared to pure water, which is in agreement with the real-life physics and chemistry. The experimental results are reproduced, with the deviation from the experimental data shown in the second part of Table 3.4, and they indicate the sensitivity to the liquid used.

### 3.4.2 2<sup>nd</sup> Validation Case: Chen et al.

Similar to the previous numerical setups, the literature case by Chen et al. [156] was used for further validation. In this research spray phenomena and operating conditions in large spray

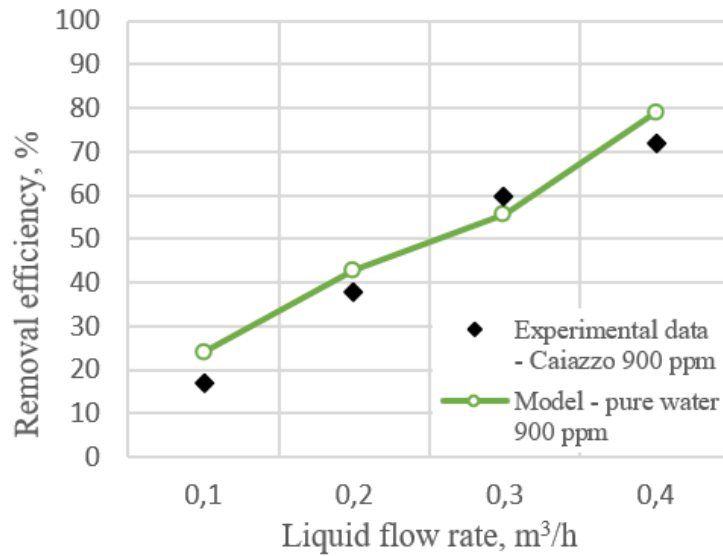


**Figure 3.26:** Removal efficiency for pure water absorption, 900 ppm – comparison with literature data.

scrubbers using limestone suspension was investigated. Although their research was not focused on the absorption itself, but rather on impact of deflectors on flow field inside the scrubber, data useful for comparison and validation can still be found.

The pilot plant was a cylindrical reactor with a diameter of 1.2 m and height of 4 m. The computational mesh consists out of 120 thousand dominantly hexahedral cells, Fig. 3.28. Gases entered from the inlet near the bottom, and the seawater was sprayed counter-currently from 72 spray nozzles distributed in three layers located 1.3 m, 1.5 m and 1.7 m from the gas inlet. The SO<sub>2</sub> concentration was 850 mg/m<sup>3</sup>, which corresponds to 300 ppm<sub>v</sub> in the simulated flue gases—pure dry air with temperature of 150 °C and inlet velocity of 0.8 m/s.

In their paper, Chen et al. did not provide accurate nozzle or spray description, making the

**Table 3.4**  
Relative errors for pure water simulations.

SO <sub>2</sub>	Relative error, %			
	0.1 m <sup>3</sup> /h	0.2 m <sup>3</sup> /h	0.3 m <sup>3</sup> /h	0.4 m <sup>3</sup> /h
<i>PURE WATER ABSORPTION</i>				
500 ppm	0.0%	−1.4%	−9.0%	2.4%
700 ppm	41.4%	10.1%	−8.5%	7.9%
900 ppm	40.9%	12.4%	−7.4%	9.9%
<i>SEAWATER ABSORPTION</i>				
500 ppm	−11.2%	3.5%	5.5%	5.5%

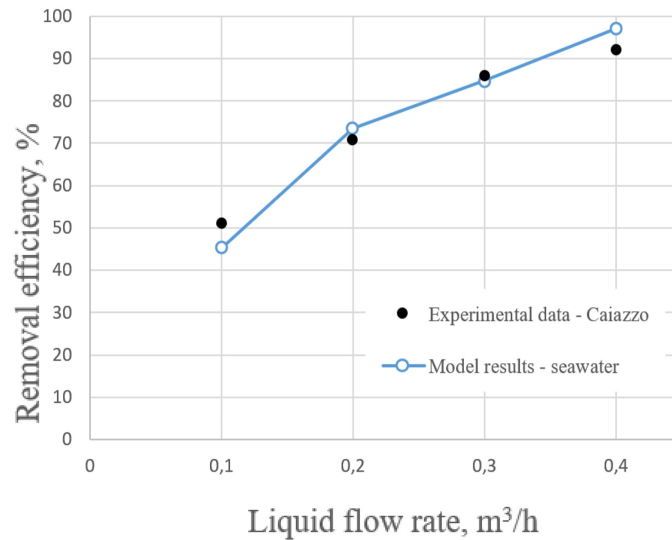


**Figure 3.27:** Removal efficiency for seawater absorption, 500 ppm – comparison with literature data.

validation significantly harder. In setting the simulation, the known parameters such as gas and liquid flow, spray angle, and liquid-to-gas ratio were combined with the assumed parameters, such as nozzle holes and particle size distribution common for scrubbing applications of these sizes, nozzle velocity, and alkalinity.

The vessel walls were set as thin walls at 80 °C—a boundary condition in FIRE<sup>TM</sup> that simulates the temperature across the wall—together with no-slip boundary condition. The outlet of the scrubber was at the upper end, replicating the counter-current flow in the scrubber. The outlet pressure was prescribed as constant static pressure with value of 101 325 Pa, and the scrubber was initialised with the inlet temperature and the average velocity calculated from the gas flow. The set simulation time step was  $5 \times 10^{-4}$  s, and the injection of seawater with the alkalinity of 0.0024 mol/kg was initiated after achieving stationary conditions. Overview of the numerical setup can be seen in Table 3.5.

Even though the complete description of experimental setup and the results was not reported, simulated velocities, temperature profiles and flow fields display reasonable agreement with the available data and the expected physical behavior. The magnitude of velocities in vertical direction varies up to 5 m/s, which is in agreement with the reported data from the literature, although the demister and the tray were not simulated as a part of the present work Fig. 3.29. Significant influence of spray injection on the flow field can be noticed, which is expected due to large amount of liquid phase. The injection velocity prescribed at 20 m/s causes strong recirculation in the spray zone, which is not rectified by the demister or the flow deflectors, as in experimental setup. Still, the velocity profiles are replicated with sufficient accuracy, when compared to the data provided by Chen et al.

**Table 3.5**  
Numerical settings for simulations of the Chen et al. [156] case.

<b><i>NUMERICAL SETTINGS</i></b>	
time step sizes	$5 \times 10^{-4}$ s, transient simulation
<b><i>FLOW</i></b>	
gas flow rate	7600 m <sup>3</sup> /h
<b><i>SPRAY SETTINGS</i></b>	
liquid flow rate	90 m <sup>3</sup> /h
injector position	three levels: 1.3 m, 1.5 m and 1.7 m from bottom
number of nozzles	24 per level; radially arranged (4 × d = 0.2m; 8 × d = 0.5m; 12 × d = 0.8m)
droplet diameter	probability distribution based on the reported nozzles
nozzle hole diameter	3 mm
injection velocity	20 m/s
cone angle	110°
L/G ratio	25 L/m <sup>3</sup>
<b><i>BOUNDARY CONDITIONS</i></b>	
wall	no slip, thin wall model: 80 °C
inlet	normal velocity, 0.8 m/s; 150 °C 300 ppm SO <sub>2</sub> in air (N <sub>2</sub> /O <sub>2</sub> = 0.79/0.21)
inlet	static pressure, 101 325 Pa zero gradient temperature
<b><i>INITIAL CONDITIONS</i></b>	
velocity	uniform, upward direction 0.8 m/s
pressure	101 325 Pa
temperature	150 °C
chemical species	300 ppm SO <sub>2</sub> in air (N <sub>2</sub> /O <sub>2</sub> = 0.79/0.21)
<b><i>ASBSORPTION MODULE</i></b>	
liquid medium	seawater
absorption model	penetration theory; contact time = 0.1 s
seawater alkalinity	0.0024 mol/kg

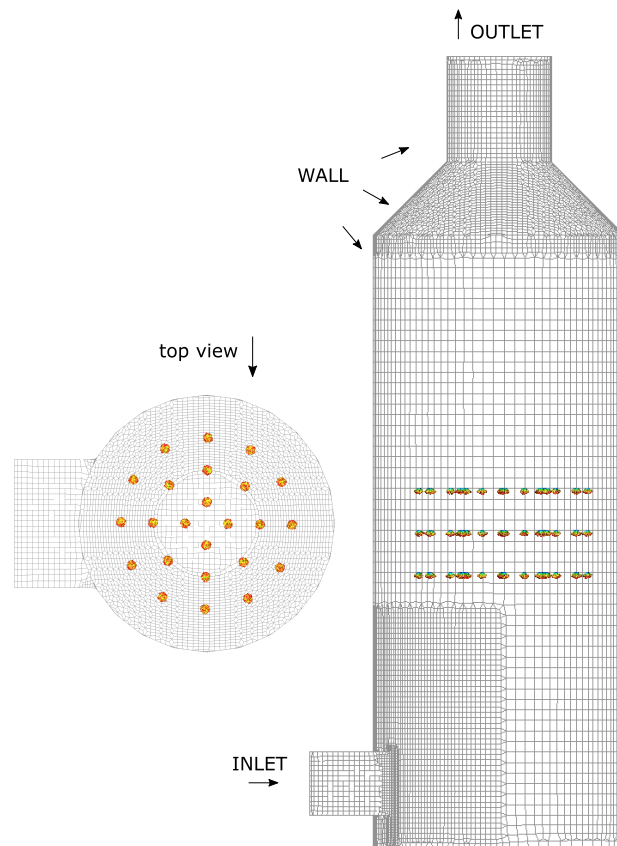


**Figure 3.28:** Computational mesh for the Chen case; side view and top view of mesh and nozzle position.

The temperature along the tube is in agreement with the expectations, since the plexiglass walls do not insulate the vessel good enough to maintain high temperature. Therefore, the wall film evaporative cooling effects are not so significant, and the wall temperatures are thus significantly lower. Flue gases entering the scrubber with heightened temperature are rapidly cooled by the falling droplets and the evaporative spray cooling, humidifying the gas during the process.

The  $\text{SO}_2$  distribution in the gas phase is highly dependent on the seawater spray characteristics. The large amount of seawater injected ensures the L/G ratio of approximately 25, and exposes fresh, unsaturated droplets with high alkalinity concentration to the polluted gas phase. Together with the intense mixing, achieving high removal efficiencies is possible. Initially, low  $\text{SO}_2$  concentration zone is formed below the spray injectors, which then propagates towards the outlet. After the quasi-stationary state is achieved, low concentrations in the upper part of the scrubber ensure uniform flow with no slippage.

In Fig. 3.30 the combined results for several properties are presented. First, the  $\text{SO}_2$  concentration at the start of injection and after achieving quasi-stationary state are shown. The large

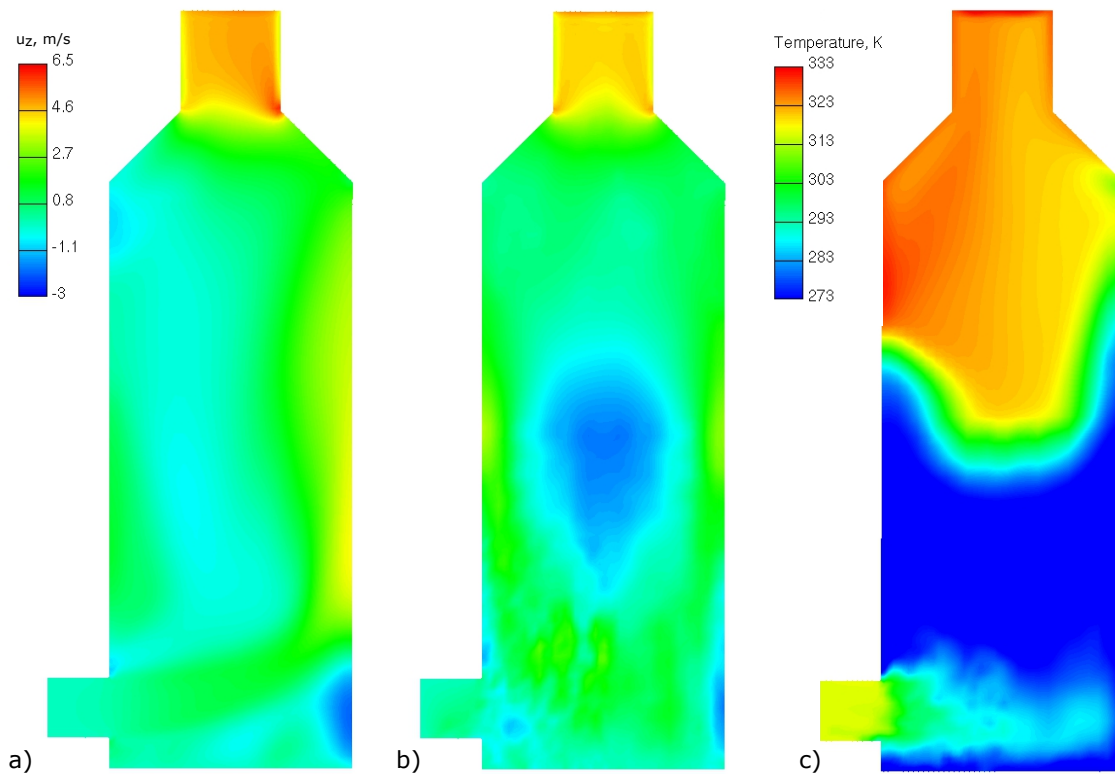


**Figure 3.29:** Physical values along the open spray scrubber height: a) gas flow; b) gas and spray; c) temperature profile.

number of nozzles causes the intricate spray pattern, but also ensures good mixing of the gas and the liquid phase. The total sulfur concentration is also shown, providing details about the absorption in droplets. Additionally, the liquid phase alkalinity was shown at the beginning of the injection. The reduction due to chemical reactions can be seen, and this behaviour continued as the simulation progressed. At the later stages, depletion of alkalinity could be observed in droplets with higher residence times, confirming the issue with seawater absorption capacity compared to other conventional alkaline scrubbers. Finally, the droplet Reynolds number values were shown, indicating the vigorous mixing, the turbulent conditions of the flow field, and the suitability of penetration theory compared to the purely diffusive film theory.

The removal efficiency is calculated as the ratio between the inlet concentration and the averaged concentration at the outlet after the quasi-stationary state has been achieved. For the inlet concentrations of 300 ppm, which correspond to  $850 \text{ mg/m}^3 \text{ SO}_2$ , the calculated seawater scrubbing removal efficiency was 87.6%. This value is near the range of 89% to 96% efficiency reported by Chen et al., which is in a good agreement considering significant differences and assumptions made while setting the simulation. Removal efficiency results, together with other physical values that are reproduced, indicate that the implemented seawater scrubbing model can be used as a foundation for simulating  $\text{SO}_2$  absorption in real industrial application, as well as for further model improvements.



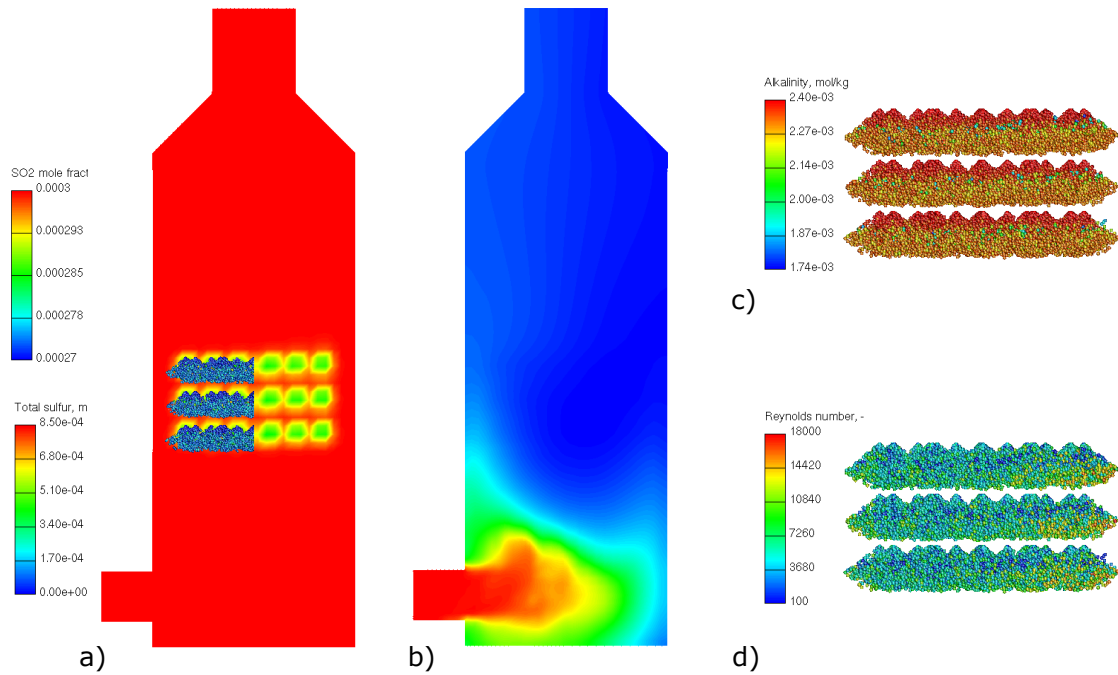


**Figure 3.30:** Simulation results for the Chen case: a) SO<sub>2</sub> concentration in gas phase and total sulfur in droplets at the beginning of spray injection; b) SO<sub>2</sub> concentration at the quasi-stationary state; c) alkalinity concentration in droplets; d) Reynolds number.

## 3.5 Wall Film Absorption

### 3.5.1 Overview of wall film absorption modelling

In numerical modelling of real-world processes, inevitably some approximations are introduced in the model. Besides the assumptions mentioned previously, the wall film formation and absorption of pollutants in it are commonly disregarded processes. Depending on the spray patterns, scrubber geometry and the flow field, the formation of liquid film on the scrubber walls can be more or less prominent, which has led to its contribution to SO<sub>x</sub> absorption being omitted from the models.

Still, the absorption of gases into falling liquid films is a widely-investigated topic, in the areas of thermodynamic and hydrodynamic research, mass transfer in contactors, process engineering and elsewhere.

The majority of the research on absorption into wetted walls was done for CO<sub>2</sub> removal. For example, Bishnoi and Rochelle investigated CO<sub>2</sub> absorption by organic solvents [157], essential for carbon capture processes. In principle, the liquid flowing in packed columns also forms a film over the packing material. However, due to complex geometry, they are usually modelled by volumetric discretisation along the scrubber height [131] or by using the porosity models [158]. Darake et al. [117] presented their numerical model for seawater spray absorber, which axially

discretises the scrubber and gave some information about the wall film formation from spray. In the CFD model of limestone scrubber, Marocco included only the droplet-wall interaction by using the approach by Weiss and Wieltch [159], but no wall film absorption. The experimental analysis of liquid film formation by Codolo showed that film formation in sodium hydroxide scrubber could reduce the droplet flow rate along the tower up to 30% of the total flow rate [79]. On the other hand, in the ammonia scrubber experimentally investigated by Javed et al. [102], about 25% of the total flow rate formed wall film. Finally, in an experimental section of their paper, Flagiello et al. [106] acknowledge the film formation in seawater spray and packed scrubbers but provide no experimental data, while in the numerical modelling section, they employ an approach similar to Darake.

Wall film formation and behaviour investigations had been developed as a part of fluid dynamics, and the overview of models and research is given in the review by Killion and Garimella [160]. A large number of parameters—such as fluid type, temperature, material roughness, gas-phase flow, and film thickness, to name a few—influence the wall film, and the exact behaviour is challenging to model. Detailed phenomena for different wall film processes can be modelled, but models suitable for the applications and with low computational intensity need to be selected. Although some work has been done on wall film modelling for scrubber applications, from the literature review, it is evident that no comprehensive model exists and that the experimental data does not conclusively assess the influence of wall film on the SO<sub>2</sub> absorption. The present work aims to fill the gap in the available models for SO<sub>2</sub> absorption in wall film of seawater spray scrubbers by improving previous research by the authors.

The absorption of pollutant gases in the liquid film forming on the walls of the scrubber is not a completely researched topic. The reason for this is mostly the dominance of absorption into spray over influence of the wall films. The exact figures are not reported and presumably vary depending on the conditions and the geometry, however, in the available research on the topic, different estimates are reported. For example, in the limestone spray scrubber modelling, Marocco [116] acknowledges the existence of the wall film, but does not model it; Flagiello et al. state that the influence of wall film on absorption is negligible [106]. In their experimental work on analysing the simplified spray scrubber, Caiazza et al. state that a fraction of the spray might create the film, but the estimation of the influence was not performed [153]. In the previously mentioned research by Darake et al. [117], the wall film was taken into consideration, and they state that, depending on the used nozzle, 30% to 50% of the liquid flow turns converted into the wall film. Similarly, depending on the nozzle type, the influence of wall film inclusion in the model can lead to discrepancies up to 20% compared to experimental results. However, the general modelling approach was not CFD-based, but employed the axial discretization of the scrubber, which does not allow for more detailed analysis of the flow, spray, or the geometry.

The research on falling film absorption was mainly focused on the simplified laminar flows, as the realistic phenomena is complex, coupled with heat transport, and difficult to model. However, the assumption of laminar film is not always justified, as the instabilities frequently

occur and disrupt the flow [160]. The hydrodynamics have a major impact on the absorption operation, namely wall thickness, turbulence, droplet-wall interaction, and wave formation. However, nearly all models are still based on the equilibrium assumption between the species' partial gas pressure and their concentration in wall film. Similarly to the considerations for falling droplets, the experimental tests on absorption into smooth, wetted walls found that mass transfer coefficient is proportional to  $D^{1/2}$ . Furthermore, for the application in scrubbers with high solubility of  $\text{SO}_2$  in water, the gas side mass transfer coefficient is often assumed negligible [134], with liquid side contributing to over 90% of resistance [161].

On the other hand, the theories for the mass transfer into highly-turbulent flows are usually based on the eddy diffusivity theory, and employing empirical or semi-empirical expressions for obtaining the concentration profile [162]. For example, Davies modified the existing theory and presented the model with a laminar film at the interface through which the transfer towards the bulk of the liquid occurs [163]. The eddies inside the film cause the surface to deform, and based on the balance between the internal dynamic thrust and the surface tension, the expression below was derived for the liquid side mass transfer in films. Possibly due to the model's dependency on the choice of characteristic velocity and because it does not account for eddies of different sizes, the predictions are lower than the experimental data.

### 3.5.2 Wall Film Absorption Modelling

Some of these deficiencies were recognised by Yih and Chen [164], as they concluded that damping of eddies is being caused by surface tension instead of viscosity, and that the waves on the free surface contribute to the increase of interfacial area by just a couple of percent. They modified the model by inclusion of expanded literature data set for long-wetted wall columns along their experiments on  $\text{CO}_2$  absorption. The resulting expressions for mass transfer coefficient are based on larger number of experimental points, include a wider range of conditions, temperatures, and absorbing gases. The film hydrodynamics develop with the increase of liquid flow rate and the surrounding parameters from the laminar flow, followed by the wavy-turbulent regime, and finally to the fully turbulent flow. In order to account for the variations in aggregated data from other sources, the resulting expression is represented through the dimensionless parameters. Therefore, the liquid side mass transfer coefficient is presented as a function of Schmidt number and Reynolds numbers between 1600 and 10500, with the parameters and the exponent empirically determined.

$$k_l^{Yih\&Chen} = 1.099 \times 10^{-2} Re^{0.3955} Sc^{1/2} \quad (3.45)$$

The variety of models in literature and experimental data sets for mass transfer coefficients complicated the choice of the appropriate approach, as the universal approach for laminar, wavy, turbulent flows and the absorption of different gases does not exist. Another approach based

on eddy diffusivity was presented by Fricke and Prasher [61]. It incorporates the Davies theory and is valid for thin wetted films up to 50 °C, and the correlation parameters were empirically derived from available experimental data. The eddy diffusivity is included in the model through the energy dissipation in liquid film,  $\varepsilon$ .

$$k_l^{Fricke\&Prasher} = \frac{0.0108}{\pi} \left(\frac{\rho}{\sigma}\right)^{1/2} \left(\frac{\delta^3 \varepsilon^3}{g\nu}\right)^{1/4} D^{1/2} \quad (3.46)$$

$$\varepsilon = 400^{1/5} \left(\frac{g\nu}{3}\right)^{1/3} \left(\frac{Re}{4}\right)^{7/15}$$

Although the previous two models were derived from the experimental data, they do not fully represent the conditions encountered in SO<sub>2</sub> scrubbers, as the experiments mostly monitored the absorption of CO<sub>2</sub> and other gases, with differences in geometries. The results obtained during the model's testing agreed with other literature values for  $k_l$ , such as the range of  $4 \times 10^{-5} < k_l < 1.5 \times 10^{-5}$  m/s reported by Zidar while measuring SO<sub>2</sub> absorption into NaOH solutions [165]. Furthermore, the presented models were tested against the work by Nielsen et al., in which they reported absorption rates in the internal pipe flow representing the wetted-wall column [166]. They also provided their expressions for the liquid phase Sherwood number, which they assumed depends also on the gas phase Reynolds number. The Fig. 3.31 shows the comparison between the models presented in this work and the data by Nielsen et al. The points represent their measurements, which they originally grouped according to the Reynolds numbers of the gas phase, and the lines are the expressions for the respective  $Re_g$ . Since the two presented models were constructed from the aggregated data and they did not assume the gas phase Reynolds number to influence the mass transfer, the expressions were compared to all data points by Nielsen et al. The resulting curves are in the envelope of the experimental data, with the expression by Fricke and Prasher better matching the points for lower gas Reynolds numbers, and the Yih and Chen capturing the higher gas flows. Although the differences between the models and the experimental results exist, such as using co-current scrubber by Nielsen et al., the results from Fig. 3.31 indicate that the models could be suitable for the intended applications in modelling absorption in wetted-wall scrubbers.

For the inclusion of the SO<sub>2</sub> absorption in wall film, only the liquid side mass transfer was taken into account, based on the presented literature overview. The rest of the absorption model follows the approach analogous to the absorption into spray droplets: calculation of the equilibrium conditions; determining the driving force as the difference between the actual concentrations and the equilibrium; calculation of interphase flux with regards to the resistance due to the liquid side mass transfer coefficient. Both of the presented absorption models were added to the existing wall film module in the AVL FIRE™ software, by modification of sources between the gas and the liquid phase. The resulting model was employed on the validation cases in order to examine the influence of wall film absorption on the overall SO<sub>2</sub> removal efficiency.

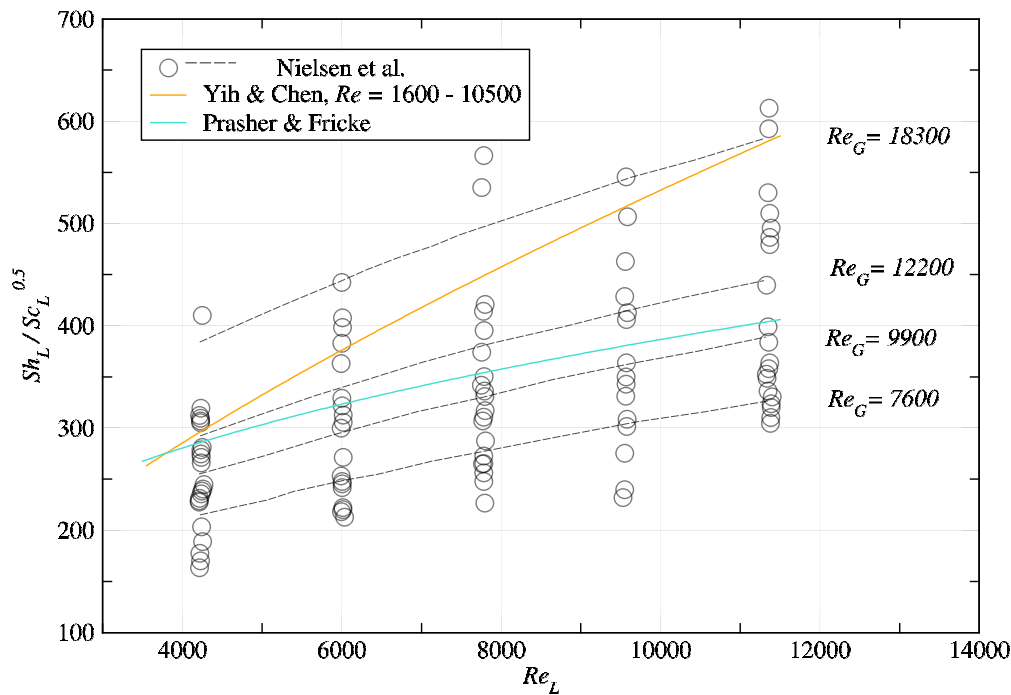


**Figure 3.31:** Comparison of liquid side mass transfer models with the experimental data from Nielsen et al. [166].

### 3.5.3 Numerical Simulations

#### 3.5.3.1 Initial Verification

An implemented model for wall film absorption equivalent to the spray absorption model was initially tested on a contrived case for purposes of model verification, while the wall film formation and behaviour were accounted for by the AVL FIRE<sup>TM</sup> wall film module [73]. The used mesh domain represented a section of gas around the wall that has liquid film forming on it. Side boundaries were treated as symmetry boundary conditions, while the bottom and the top domain boundaries simulated the upward motion of air polluted with 500 ppm SO<sub>2</sub> with velocity of 0.5 m/s. The wall was kept at constant temperature of 30 °C, thus preventing evaporation effects on the liquid film. The used domain contained 30 000 hexahedral cells and had dimensions of 50 × 50 × 25 cm, showed in Fig. 3.32.

The green area represents the feeder selection that is used for initialisation of wall film. In real scrubber simulations, the liquid film will be formed after the spray droplets impact the wall and the conditions are met for conversion from a droplet to liquid film. In order to have a more controlled conditions for wall film thickness, velocities, and other parameters during the

model testing phase, the introduction of wall film via the feeder was used. The selection had width and height of 42.5 and 3 cm, respectively. During these initial tests, the liquid flow rate introduced via the feeder was varied from 0.05 kg/s to 5 kg/s. With these flow rates the wetting of the surface below the feeder was complete, which is universally not the case for liquid films introduced by sprays, especially at the initial phases of the spray-wall interaction. Table 3.6 shows the development of the wall film for the liquid flow rate of 5 kg/s, and the film's thickness. It can be seen that a bulge is formed at the front where liquid film propagates down the wall. Eventually, a constant thickness profile is established along the wall, below the liquid inlet. This simplified case and the uniform wall film introduction method facilitated initial model testing and calibration.

The achieved velocity magnitudes in these cases ranged from 0.18 m/s to 0.82 m/s, which corresponded to the Reynolds numbers from 140 to 13 000, Table 3.7. This indicates that for the lowest flow rates the regime is laminar, that while at the flow of 1 kg/s the flow can be considered turbulent. Thickness is also proportional to the liquid flow rate, since due to surface tension larger amounts of liquid do not solely increase the wall film velocities. Film thickness at the lower end of presented liquid flow rates lies below the 1 mm, which is lower than the developed conditions in fully-wetted scrubbers. On the other hand, at higher flow rates, the liquid film thickness nearly reaches 2 cm, which represents another extreme that is difficult to achieve in realistic scrubbers even at high L/G ratios. In all of the cases, the Weber numbers are well below unity, meaning that the surface tension, or cohesion forces are high compared to inertia.

In Table 3.7 the results for mass transfer coefficients calculated by two different models are also represented. The values are quite similar, which was expected from the analysis of Fig. 3.31 and, as they lie within the expected range [165], suggest that the mass transfer calculation is valid. The matching liquid side mass transfer coefficients consequently cause almost non-existent differences in gas phase SO<sub>2</sub> concentrations between the calculation according to Yih and Chen, and Fricke and Prasher, equations (3.45) and (3.46). The results showed in Table 3.7 are calculated by the model by Yih and Chen.

Regarding the chemical side of the model, the expected behaviour can be noticed for alkalinity and total sulfur concentrations. Since the alkalinity is introduced at a constant concentration value in fresh seawater, it is being spent as the liquid film comes into contact with polluted air. Here, the lower mass of liquid causes the lower absorption potential, and the alkalinity is spent more rapidly for cases with lower flow rates. Inversely, the total sulfur is highest for lower mass flows, as it represents the absorbed sulfur concentration, which reaches the equilibrium values. Still, due to higher mass and thus higher absorption capacity, the high flow rate absorbs more SO<sub>2</sub> in absolute terms, thus increasing the removal efficiency. From these images it can be concluded that the resistance in system is not located in the chemical part. The chemical reactions are much faster compared to the physical absorption, making the process limited by mass transfer.

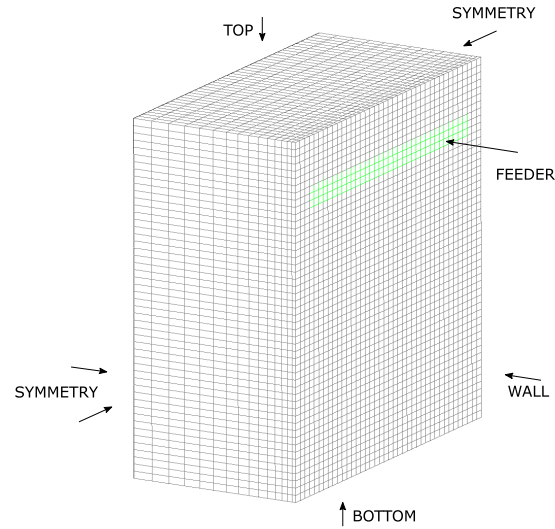
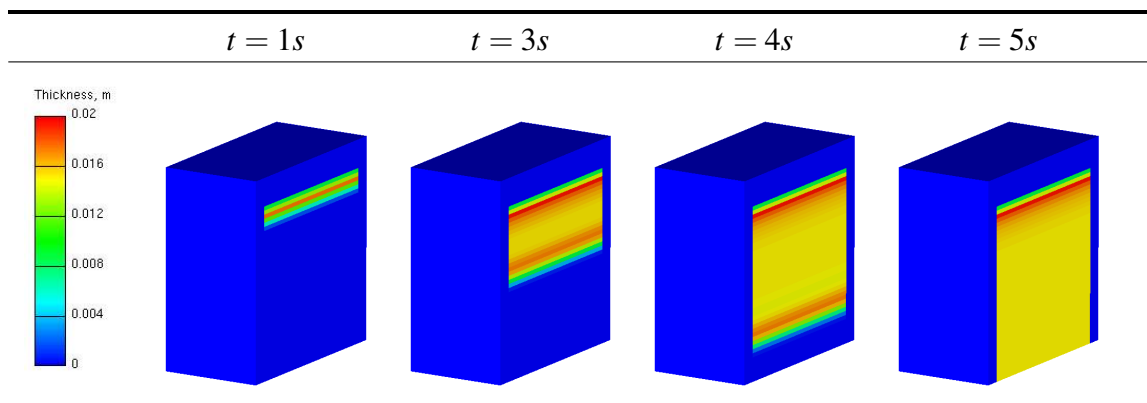


**Figure 3.32:** Used computational mesh for initial wall film absorption.

**Table 3.6**  
Wall film initialisation, liquid flow rate 5 kg/s.



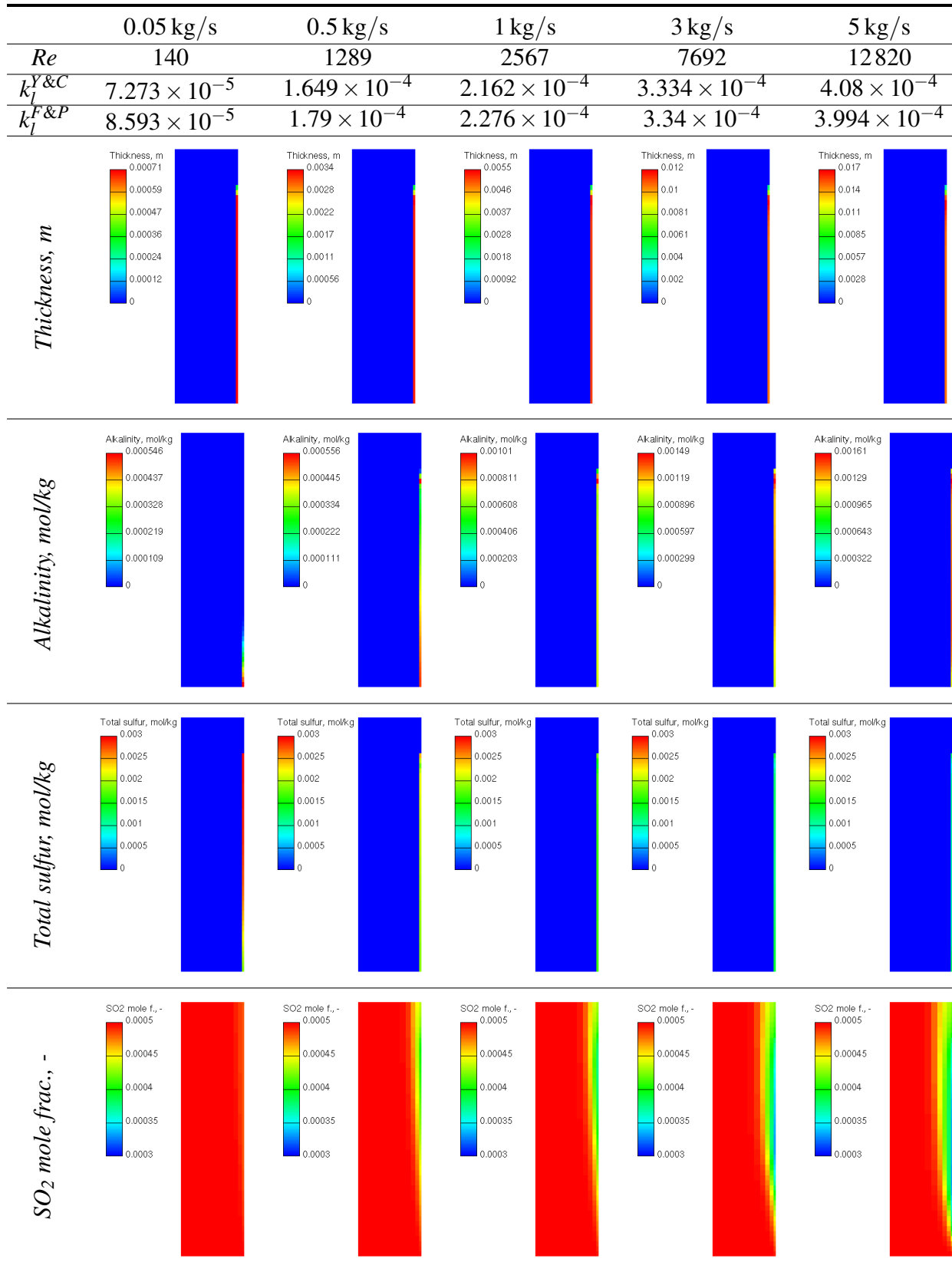
### 3.5.4 Wall Film Absorption Results

Previous chapters displayed the model and the results for the  $\text{SO}_2$  absorption in pure water and seawater sprays in experimental scrubbers with different fluid flows and pollutant concentrations in the gas phase. Although the fluid flow and spray conditions are complex even on the moderately simple geometries, approximations integrated in the model and the approach for calculating the mass transfer condition were accurate enough to ensure quite small errors [154]. However, only the absorption in spray droplets—modelled by penetration theory—was included, and the wall film formation was disregarded. The contact time parameter  $t_{con}$ , used in obtaining the liquid side mass transfer coefficient was tuned for the simulated case, but the absorption is highly dependent on it.

In order to test the influence of the implemented wall film absorption models with conditions

**Table 3.7**

Initial wall film verification results. Velocity, Reynolds number, liquid side mass transfer coefficient values and cross-sections of the domain representing wall film thickness, total sulfur concentration and  $SO_2$  mole fraction for different liquid flow rates.





reported in the literature, the same experimental case obtained from Caiazzo et al. was simulated.

The results did not indicate a significant change in the absorption efficiency with the wall film absorption model included. The absorption process was removing the SO<sub>2</sub> from the gas phase into the liquid, but the magnitude was too small to be noticeable compared to the spray absorption. One of the explanations was that the insulated walls kept at 250 °C prevented more intense wall film creation, which was supported by the average film thickness of approximately 0.2 mm and the average Reynolds number around 200. Furthermore, the high wall temperature influenced the Henry's constant and the SO<sub>2</sub> solubility in liquid phase, further preventing the absorption. As the literature source did not provide any data on wall film, additional conclusions could not be made, and the model was then tested on a previously-presented industrially-sized geometry obtained by Chen et al. [156].

For the larger case from Chen et al. that replicated industrial operating conditions, the simulation set-up was performed analogously to the spray-only absorption simulations in previous section, with the droplet contact time set to 0.1 s. The vessel walls were treated as thin walls at 80 °C, with the corresponding module activated. The inclusion of the model describing liquid film formation on the scrubber walls did not significantly alter the velocities or other flow field parameters inside the scrubber, making the previous comparisons valid for the present case as well.

Figure 3.33 shows the concentrations of sulfur-containing chemical species in the spray droplets soon after being injected from the first level of nozzles, as well as in the wall film after it develops. Initially, the driving force causing the absorption is high, but as the SO<sub>2</sub> is being removed, the low concentrations in the gas phase slow the absorption process. The increasing concentration of total sulfur in the liquid phase indicates that the SO<sub>2</sub> is being absorbed, but without taking into account the amount of liquid, this results are only indicative.

The liquid flow rate of 90 m<sup>3</sup>/h together with the L/G ratio of 25 ensure that the liquid film forms at the wall. The thickness of the wall film is approximately 10 mm. Higher values occurred at the bottom of the scrubber, as the bottom wall provided no outlet for them, thus impacting the average thickness and the Reynolds number. Presently, this issue could not be addressed, as it required modifications of the wall film model, but the increased film thickness at the bottom did not significantly impact the absorption. The Reynolds number ranged between 3000 and 6000, suggesting that the wall film flow is in the turbulent regime. These two results justify the use of the presented models for the calculation of mass transfer to wall film. The temperatures of the wall film were in the expected range, with the areas where film has formed undergoing cooling from the injected liquid. The wall temperature was set to 80 °C, and the red areas represent the numerically calculated temperature, although in these regions liquid film might not be present, or is extremely thin. Temperatures in the portion significant for the absorption process remained around 20 °C to 50 °C, which are the temperatures where chemical absorption still occurs.

Following is the comparison of SO<sub>2</sub> concentrations on the axial cut of the absorber. Figure 3.35 shows the concentrations for the absorption in spray only on the left side. As expected,

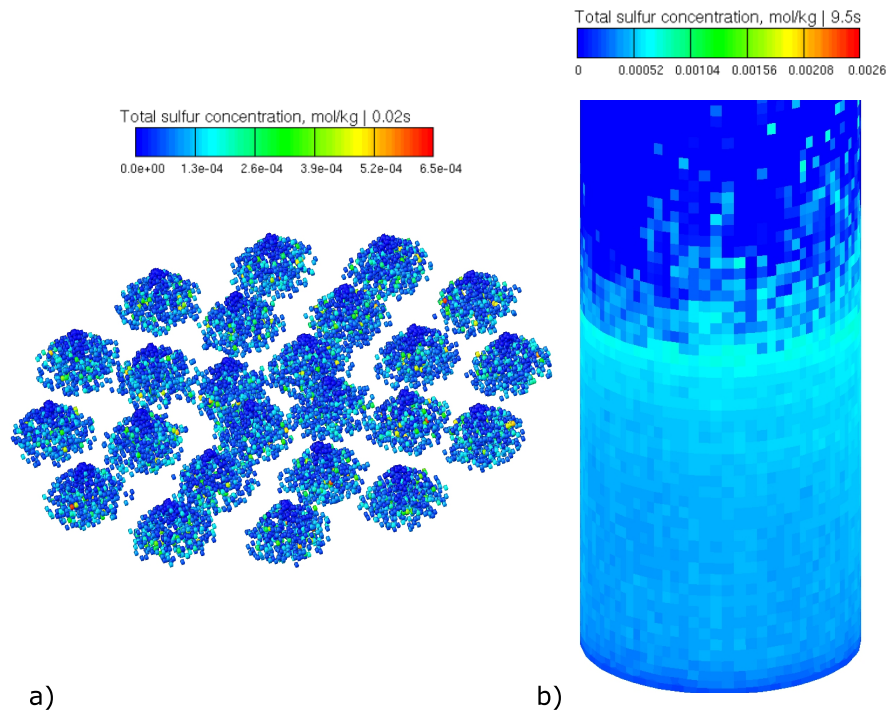


**Figure 3.33:** Concentrations of total sulfur absorbed in a) spray droplets; b) wall film.

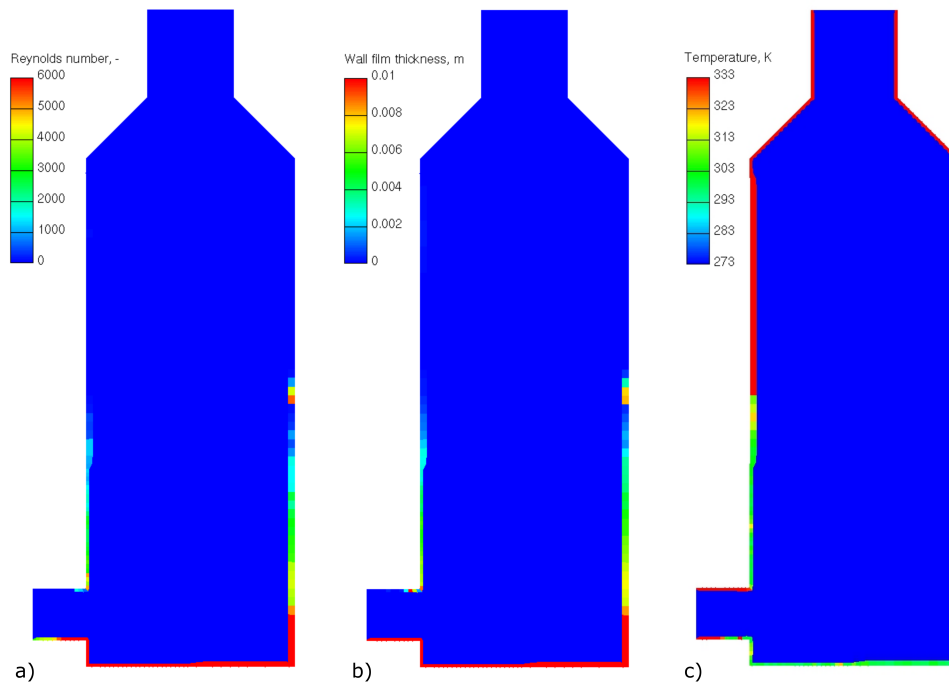


**Figure 3.34:** Wall film Reynolds number (a), thickness (b), and temperature (c) values on a large scrubber geometry.

the majority of droplets interacting with the gas flow below the three layers of nozzles form the zone with the lower  $\text{SO}_2$  concentration. As the quasi-stationary state between the flue gases entering the scrubber and the unpolluted seawater with high alkalinity is achieved, the  $\text{SO}_2$  outlet concentrations are also stabilised. When the wall film absorption was also enabled, namely the Yih and Chen model in Fig. 3.35, there was a noticeable decrease in the  $\text{SO}_2$  concentrations near the scrubber wall. At 2 s after the start of injection, on the back side wall the film was formed with thickness of approximately 0.3 mm, and the absorption is increased compared to the spray-only case.

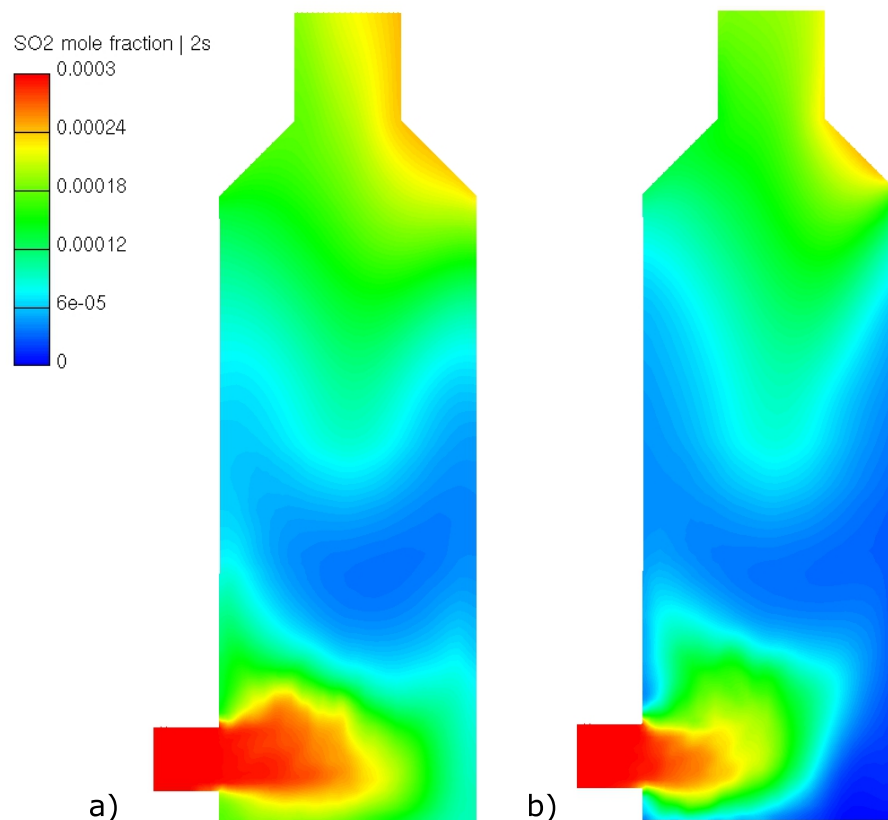


**Figure 3.35:** Comparison between the absorption in spray only (a), and the included wall film absorption – model by Yih and Chen (b).

The removal efficiency is calculated as the ratio between the inlet concentration and the averaged concentration at the outlet after the quasi-stationary state has been achieved. For the inlet concentrations of 300 ppm, which correspond to  $850 \text{ mg/m}^3 \text{ SO}_2$ , seawater scrubbing efficiency for absorption in spray only is 87.6%. Although the removal efficiency is high, even higher values usually reported for the seawater scrubbers could not be simulated with the set boundary conditions. By including the wall film absorption model, the removal efficiency was increased to 92.9% and 93%, for Yih and Chen and Fricke and Prasher models, respectively. These values are in range of 89% to 96% efficiency reported by Chen et al., which is good agreement considering significant differences and assumptions made while setting the simulation.

The difference between the applied mass transfer wall film models is quite small, and indicates that the approaches are applicable and that the mass transfer coefficients are correctly calculated. Additionally, it implies that the resistance is not the process-limiting step, at least in present application. Rather, either the amount of liquid on the wall, or the alkalinity—both representing the capacity for absorption—restrict the process. Finally, even though the present case does not represent all of the parameters, conditions and geometries of a scrubber, presented results give at least a rough estimate on the influence of wall film absorption compared to the absorption in a spray.

**Table 3.8**  
Removal efficiencies comparison with and without wall film absorption model.

	<i>Simulated efficiency, %</i>	<i>Efficiency increase, %</i>
Spray absorption only	87.6	-
Wall film absorption: Fricke & Prasher	93	6.16
Wall film absorption: Yih & Chen	92.9	6.05

This section presents the inclusion of a numerical model for simulating flue gas desulfurisation in liquid film forming on scrubber walls, as an expansion of the basic model implemented for absorption in spray droplets only. Similar to the initial approach, the identical assumptions regarding the sulfur chemistry and physical properties were applied. The lumped-parameter model was also used, but in a modified form that averages the properties across the wall film cell instead of the liquid droplet.

Two models for calculation of mass transfer coefficients in wall film are presented, and their analysis on both simplified cases and the real industrial case is shown. By replicating the available boundary conditions and parameters for large-scale scrubber from the literature, but using only the absorption into spray, the removal efficiency of 87% is achieved, which is lower than expected values.

By including the wall film absorption, the removal efficiency increased to 93%, for both cases. Since the dimensionless analysis showed the differences between the models are quite small, the almost identical results can probably be attributed to operating parameters not causing enough differences to show on the global level. The mass transfer coefficient calculation does not have high enough influence on the overall absorption compared to the wall film thickness representing the absorption capacity, or the chemical reactions, represented by the spending of the alkalinity species. For the case of a larger scrubber with realistic geometry and operating conditions used for simulations, the influence of wall film absorption to total removal efficiency was assessed at around 6%.

These result values can hardly be extrapolated and applied universally to other geometries and cases, as they represent specific conditions occurring in present scrubber. Although the operating parameters found in the paper by Chen et al. fall within the velocity, liquid-to-gas ratio

and temperature ranges usually reported for the spray scrubbers, the conditions such as scrubber dimensions and shape, spray pattern, number and type of spray nozzles used can significantly influence the droplet sizes and distribution, as well as wall film formation. Therefore, additional investigation on different scrubbers are needed, that will include wider set of conditions and test the model's flexibility under varying operating parameters. Unfortunately, at present time no additional geometries with accompanying data sufficient for modelling and replication of results were available. This was also a common issue encountered with other cases, where not enough detailed information was presented about the experimental set-ups. Besides the additional simulations on cases with more complete information about boundary conditions, the model itself can be improved in the future. The influence of high temperatures present due to hot flue gases can sometimes bring the system outside of temperature ranges that the Henry's constant parameters are calculated for. Additional issue is the inclusion of only the liquid side mass transfer coefficient. Although the literature sources indicate that the gas side mass transfer resistance can be neglected, its inclusion would lead to the more complete model. Finally, another improvement of the model can be done for the droplets and the wall film exiting the scrubber, in order to prevent unphysical behaviour in the sump at the bottom.

## 3.6 Conclusion

This chapter gave an overview of the development of sulfur dioxide removal in flue gas desulfurisation systems. The expansion of the model was presented, from the general calculations of equilibrium conditions in gas-liquid systems, over the initial mass transfer dynamics simulations on individual droplets and simplified cases, and finally to the full, three-dimensional simulations of available experimental and industrial cases.

Development and validation of chemical system modelling was shown, and the obtained results were analysed for pure water and seawater systems as well. Special attention was paid on the use of appropriate mass transfer modelling approach, as it was shown that this is a crucial part of SO<sub>2</sub> absorption systems. Finally, the model for describing absorption in wetted wall film was implemented, taking into account complex dependence of mass transfer coefficient on hydrodynamic properties.

Dimensionless analysis and initial investigation of the model on simplified cases provided great insight into the dynamics and behaviour of different physical and chemical properties relevant to absorption applications. Presented results for SO<sub>2</sub> absorption in spray droplets display very good agreement with literature data, validating the model for use in spray systems. The model's behaviour is in agreement with the expected trends when parameters such as droplet sizes, SO<sub>2</sub> concentrations or liquid-to-gas ratio are changed.

These results showed in this chapter indicate that the contribution of absorption in wall film to the overall removal efficiency can not be always disregarded. The initial results on

a simplified geometry that showed insignificant increases in SO<sub>2</sub> removal also prove that the increase obtained on the large scrubber case can not simply be extended to all cases. Still, the increase on the case replicating industrial conditions can be indicative of the relative importance of the wall film absorption. This can be especially important at higher efficiency ranges, where as accurate predictions as possible are needed for comparison between different technologies. From the obtained results, it can be concluded that the accurate prediction of desulfurisation efficiencies above 90% could not be performed without the wall film absorption taken into account.

The developed and implemented model can serve as a comprehensive tool for modelling SO<sub>2</sub> absorption in spray contactors, as it accounts for all major physical and chemical phenomena influencing the overall process. The combination of pure water and seawater chemistry, and absorption dynamics calculation for both spray droplets and liquid wall film, enable detailed and accurate prediction for SO<sub>2</sub> removal efficiency in spray scrubbers.

# Nitrogen Oxides Formation

## 4.1 Combustion systems overview

Despite the accelerating phase-out of coal as a fuel for electricity production and the tendency towards a greener and more sustainable technologies, the overview of global power generating capacities given in Section 1.2 indicate that the transition may not happen instantly. Therefore, additional research will still be needed in years to come in order to reduce the impact of existing power plants and minimise the pollution emissions. With that in mind, the aim of this chapter is to present a model for describing nitrogen oxides production from pulverised fuel combustion systems, that could aid in limiting pollutant emissions. The improvement of pollutant production models and the capability to have a greater insight in formation processes can be useful in designing combustion systems or modifying them to reduce the impact on the environment. As experimental investigations of new designs, suitability of different fuels or retrofits can be costly, numerical simulations of thermo-fluid properties can be a valuable tool when designing and managing the operation of more sustainable combustion and solid fuel utilization processes [167].

Among the solid fuel thermal utilisation technologies, three conventional approaches account for the majority of installed capacities. The first is fixed bed combustion, where fuel with coarser granulation is put on the grate, while preheated air rises through the bed and carries volatiles into the central section of the combustion chamber. The following is the fluidised bed, where the air stream from the bottom of combustion chamber suspends the solid fuel in the chamber volume, mixing the particulates, volatiles and oxidiser, achieving uniform temperature and good efficiency. Pulverised fuel combustion is the third one, and this work will focus on it. Finely-ground fuel entrained in the air stream is introduced in the combustion chamber, and a high specific surface area enables fast combustion reactions, steep heating rates and high temperatures. This approach offers flexibility in the combustion control, and high efficiencies for a variety of fuels, but suffers from slagging and higher costs due to solid fuel grinding and the need for more advanced collection equipment for fine ash particles.

In pulverised fuel combustion, coal was primarily used as a fuel, but biomass is also in-

investigated and used industrially. Either used exclusively or by co-firing with coal, it can lead to substantial CO<sub>2</sub> emissions reductions [168]. Still, though the biomass is established as a relevant mode for emissions reduction and achieving the set sustainability goals, its utilisation in the existing coal-fired plants may negatively influence the operation and performance of the boilers [169] due to composition of biomass, harmful chemical compounds and behaviour when combusted [170]. In present work, only the pulverised coal combustion will be investigated, but the developed approach and the model are suitable for application in thermal utilisation of biomass as well.

## 4.2 Pulverised Fuel Combustion

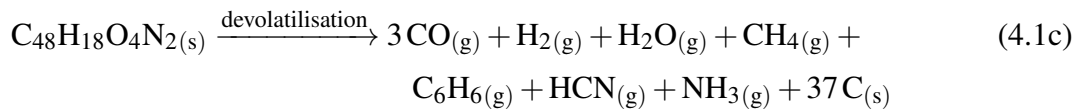
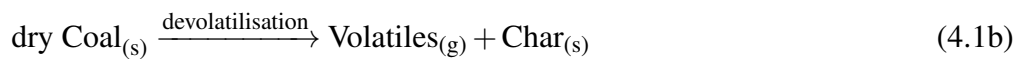
The main requirement for an accurate prediction of pollutant formation in pulverised fuel utilisation systems is the robust and detailed combustion model. Fine fuel particles are heated, exchange heat and mass with the surrounding gases, the emitted volatiles react in gas phase reactions, and the solid particles directly participate in heterogeneous combustion reactions. All of these processes must be considered, and the pulverised fuel combustion model previously implemented by Mikulčić et al. [171] in the AVL FIRE<sup>TM</sup> stands as a foundation for the development of additional models. The modelling of fuel particles lies on the Euler-Lagrangian premise and the DDM approach presented in Section 2.4 and used previously for modelling absorption in liquid droplets. The validity of the approach was substantiated by Yang et al. [172] and the investigation on the isothermal behaviour of single fuel particle below 200 μm.

Solid fuel particles undergo complex physico-chemical processes when entering the combustion chamber, usually divided into four distinctive phases: heating, drying, devolatilization and combustion of the volatile species and char [173]. In his work, Mikulčić has implemented pulverised solid fuel model where the particles' combustion is described by the mass exchange and the chemical reactions kinetics [174], providing additional sinks and sources for enthalpy and species equations in the gas phase.

The overview of the combustion model reactions is given in equation (4.1). While the fuel is heated, free moisture contained in it evaporates, leaving the dry coal particle. After the drying, the particle temperature increases, and the evolution of other volatile compounds initiates. This process reduces the particle mass and leaves char as a main constituent. The composition of emitted volatiles highly depends on fuel content and the conditions such as temperature, residence time, and air-fuel ratio. The main ones are taken into account by equation (4.1), and the dynamics of the reaction are modelled by kinetic rates and the Arrhenius-type expression. Simultaneously with the devolatilisation and pyrolysis process, the heterogeneous char oxidation occurs in particles, accounting for fuel particle size, porosity and temperature. The oxidation of char, which is modelled as carbon, forms the gaseous CO<sub>2</sub> and CO, further reducing the particle's mass until only the inert ash component remains.



Equations (4.1a) to (4.1e) are responsible for coupling the mass between solid particles and gas phase via the sources and sinks. They show the numerical representation of reactions and processes as they are implemented in the model. The rest of the homogeneous reactions are treated within the FIRE<sup>TM</sup> general gas phase reactions module, where volatile species taken into account are CO, CH<sub>4</sub>, H<sub>2</sub>, C<sub>6</sub>H<sub>6</sub>, NH<sub>3</sub> and HCN. Here, the nitrogen-containing species are a part of the general species transport model and chemical reactions system already present in FIRE<sup>TM</sup>, but the pollutant formation model in this work expands the complexity and introduces more details. In previously published work, the comparison between the general gas phase reactions model reactions and the fuel NO model was presented, showing that the former cannot be used in for accurate pollutant formation modelling in solid fuel combustion systems.



The pulverised fuel combustion model was validated in the referenced publications, and is suitable for modelling pyrolysis and combustion processes of coal and biomass, but also plastic materials and thermal decomposition of limestone for cement production. In this work, it will be used as a foundation for the development of models describing NO formation.

## 4.3 Formation Models

Understanding the pollutant production from conventional and alternative fuels is important due to their significance as future energy production and the reduction of the impact on the environment. Chemical reactions and the mechanism of the nitrogen oxides productions are complex and not entirely understood processes [175]. Attempts to estimate the pollutant concentrations based purely on the fuel composition do not provide satisfactory results [176] owing to their formation, which greatly depends upon the combustion conditions such as temperature, gas phase and fuel compositions, particle size and fuel to air ratio [177].

Detailed chemical models for describing the pollutant formation from combustion systems include hundreds of elementary reactions and species [178] and, at the present state of computer hardware, require unfeasible computational time for calculation. Therefore, the reduced models sufficiently simplify the chemical mechanisms for describing the formation of the nitrogen

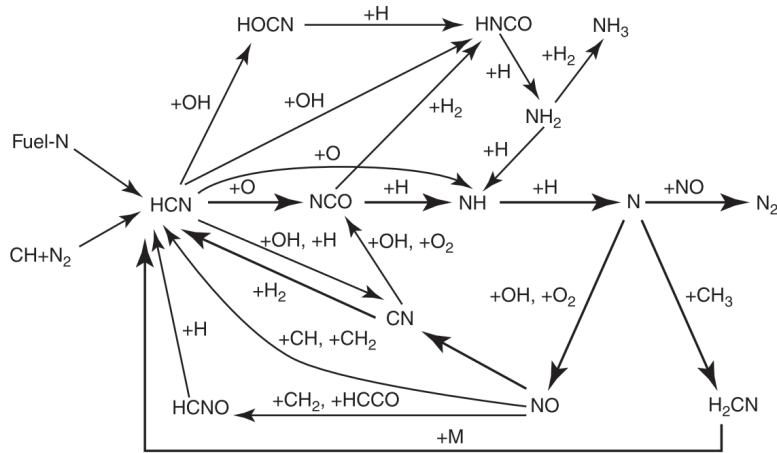


**Figure 4.1:** Detailed NO reaction mechanism scheme [41].

oxides and predicting their levels. Work done by Glaborg et al. [179] provides a comprehensive review of the commonly used models for the calculation of nitrogen oxides concentration in solid fuel fired systems, and other work has been focused on various related topics. For example, Molina et al. investigated nitrogen retained in char [180], functional forms of nitrogen were inspected by Kambara et al. [181], and Jones et al. modelled the coal devolatilization [182].

As the pollutant formation processes' complexity necessitates the application of simplified models, the one used in present work is based on coupling the introduced combustion system with the reduced chemical reaction mechanism [183]. Nitric oxide NO is considered as the most significant species, since it is dominant among the pollutants, accounting for up to 95% of the total emissions [184]. The rest of the compounds usually have a minor effect and will be neglected during the combustion process (Section 1.2.1).

Additional transport equations are introduced for pollutants and the intermediate chemical species, as shown in equation (2.11). Participation in chemical reactions is then numerically modelled as sources or sinks for the NO transport equation. This approach, decoupled from the main combustion and flow field calculations, is justified by the low NO concentrations that do not affect the flame structure or the fluid flow significantly [185]. Additionally, the timescales of the fast combustion reactions and the slower NO formation are different, which further justifies the approach.

The NO<sub>x</sub> formation is usually divided into three mechanisms: thermal, prompt and fuel nitrogen. Thermal NO forms under high temperatures by dissociation of the molecular nitrogen from the air and is described by the Zeldovich mechanism. Prompt NO<sub>x</sub> is described by the Fenimore's mechanism, which was additionally improved by De Soete by comparing it with experimental results. In this work, prompt mechanism will not be used, as its contribution is noticeable only in fuel-rich mixtures and at lower temperatures, below 1000 K [186]. Fuel NO<sub>x</sub> production and destruction is not yet entirely understood process, despite the extensive research on the topic. These models are described in details by the work of Vascellari [41], who presented

the comprehensive overview of the  $\text{NO}_x$  reactions modelling in combustion systems with the focus on coal, existing emissions control technologies,  $\text{NO}_x$  reaction paths, and chemical kinetics in turbulent flames.

### 4.3.1 Thermal NO Mechanism

Thermal NO forms at high temperatures by dissociation of the molecular nitrogen from the air and subsequent reactions of atomic nitrogen with oxygen. Due to the high energy needed for breaking the strong intermolecular nitrogen bonds, thermal NO is highly dependent on the temperature, nitrogen and oxygen concentrations, as well as the residence times. The following equations describe this process, commonly known as the extended Zeldovich mechanism. The experimentally determined reaction rates available in the literature [187] for reactions with nitrogen, oxygen and their radicals are included, and the extended Zeldovich mechanism additionally describes the atomic nitrogen reactions with hydroxyl radical, which have a significant impact in fuel-rich mixtures.



Using the quasi-steady-state assumption for the rate of production and depletion of the nitrogen radicals, the net rate of NO formation needed for the source calculation can be formulated as in equation (4.3), with  $k_{f,b}$  being the forward or backwards rate coefficients taken from the literature [188]. The necessary chemical species concentrations and temperature are taken from the calculated flow field results.

$$\frac{dc_{\text{NO}}}{dt} = 2k_{1f}c_{\text{O}}c_{\text{N}_2} \frac{1 - \frac{k_{1b}k_{2b}c_{\text{NO}}^2}{k_{1f}c_{\text{N}_2}k_{2f}c_{\text{O}_2}}}{1 + \frac{k_{1b}c_{\text{NO}}}{k_{2f}c_{\text{O}_2} + k_{3f}c_{\text{OH}}}} \quad (4.3)$$

### 4.3.2 Fuel NO Mechanism

Unlike the importance of thermal mechanism in the internal combustion engines or the gas-powered boilers, in solid fuel combustion systems the dominant mode of production of nitrogen oxides is the fuel mechanism [179]. This is especially true for the combustion temperatures below approximately 1500 K, at which the thermal mechanism is very weak. In solid fuels, nitrogen is usually contained as one of the functional groups—pyridinic, pyrrolic and quaternary in coal [181], and as amino acids and proteins (amine-N and protein-N) in biomass [189]. They break apart and react at different temperatures and conditions, and the general conclusions about

their behaviour and pollutant formation are hard to draw. Chemical mechanisms and pathways from solid fuel nitrogen to nitrogen oxides are not precisely known and depend on combustion conditions such as temperature, flow, air-fuel ratio, fuel type, particle sizes, residence times and type of combustion. During pyrolysis, tar and volatiles are emitted and subsequently form the intermediate species—hydrogen cyanide or ammonia—and nitrogen oxides are produced by their oxidation. The correct choice of the intermediate species between the fuel particle, volatiles and the final products is one of the most important parameters in fuel NO mechanism modelling, and also strongly depends on the combustion conditions [175]. Small quantities of nitrogen gas forming directly from pyrolysis can usually be neglected. Parallel to the production path from volatiles is the heterogeneous reaction of nitrogen retained in char that produces either intermediate species or nitrogen oxide directly. General approximations valid for all fuel types and combustion conditions are hard to make, and for this model, it is assumed that all the char nitrogen forms the intermediate species.

The solid fuel description is commonly given as ultimate and proximate analysis, providing only the elemental composition and the division according to the fuel's behaviour under thermogravimetric analysis [190]. This does not provide enough information to describe functional groups that nitrogen is contained in, which is the reason why detailed pathway choice depending on them is not commonly used in models developed for engineering purposes. Here, the mentioned HCN and NH<sub>3</sub> will be used as intermediate compounds, as they are the dominant ones in pulverised coal combustion, while other nitrogen-containing species such as HNCO are more significant in fluidised bed combustion [41].

The reactions of nitrogen-containing volatiles and char are modelled with the finite reaction rates, with sources and sinks of intermediate species contributing to their additional transport equations. Besides NO, the transport equations for HCN and NH<sub>3</sub> are introduced as well, and they are also decoupled from the general gas phase reactions. Therefore, in addition to thermal source, additional connections between the intermediate species and NO add up to the total sources of transport equation. Figure 4.2 depicts the scheme of the reaction mechanism and the pathways. This is a common approach in fuel NO modelling and accounts for several modes of nitrous oxide and intermediate species production. The coal particle can contribute to the formation of nitrogen-containing species either through the emitted volatiles or the heterogeneous char reactions. Although the NO can be formed directly by char oxidation, it is assumed that only the intermediate species are formed via this pathway [191].

Heterogeneous reactions of char forming the intermediate species are modelled according to Levy et al. [192], and equation (4.4) provides the expression for calculation of HCN or NH<sub>3</sub> source. Besides the influence of molar masses and volume,  $S_c$  stands for the char burnout rate, taken from the combustion model, and  $Y_{N,char}$  represents the fraction of nitrogen in char.

$$S_{\text{HCN/NH}_3,char} = \frac{S_c Y_{N,char} M_{\text{HCN/NH}_3}}{M_N V} \quad (4.4)$$

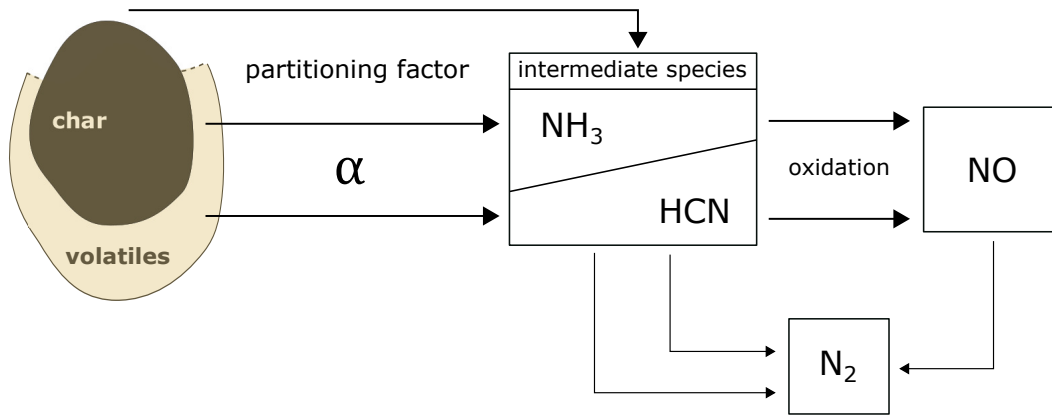


**Figure 4.2:** Fuel NO reaction mechanism scheme.

Volatiles evolved from the coal particles are the second major contributor of intermediate species. As the NO production via this pathway has been neglected, only HCN and NH<sub>3</sub> can be formed. Their sources are calculated by equation (4.5) and depend on several factors. One is the source of volatiles from the heating particle  $S_{vol}$ , which is a parameter obtained from the combustion model. Besides molar masses, the main parameter is the nitrogen fraction in emitted volatiles  $Y_{N,vol}$ .

$$S_{\text{HCN/NH}_3,\text{volatile}} = \frac{S_{vol} Y_{N,vol} M_{\text{HCN/NH}_3}}{M_N V} \quad (4.5)$$

Depletion of intermediate species occurs due to reacting with NO and forming N<sub>2</sub>. This sink  $S_{\text{HCN/NH}_3,\text{N}_2}$  is modelled by the finite reaction rate  $r_{\text{HCN/NH}_3}$  obtained from the literature and presented in equation (4.6).

$$S_{\text{HCN/NH}_3,\text{N}_2} = r_{\text{HCN/NH}_3} \frac{M_{\text{HCN/NH}_3} p}{RT} \quad (4.6)$$

In the fuel NO production model there are several simplifications made. The chemical mechanism used is reduced and consists of only two intermediate species, which are the most important ones. Heterogeneous reactions with char are also simplified and modelled as a rate reaction on a surface of the particle, while the surface area is defined as a specific area of solid fuel per unit mass. Additionally, the formation of tar and the evolution of species from it is neglected. Besides the Arrhenius-type reaction rates, this approach highly depends on the nitrogen content in char and volatiles. Additionally, the main issue that was skipped over is the contribution of different pathways and intermediate species, which can cause significant differences in modelling.

### 4.3.3 Impact of Turbulence on Pollutant Production

Combustion processes occur under highly-turbulent conditions that have a great impact on NO production. Using the averaged temperature field values in expressions for reaction rates and pollutant sources does not provide correct results since the temperature influence on the reaction rates is highly non-linear. The presumed probability density function (PDF) is used to model the effect of turbulent fluctuations on the NO kinetic rates, integrating the rates with respect to the temperature:

$$\overline{S_{\text{NO}}} = \int_0^1 P(T) S_{\text{NO}}(T) dT, \quad (4.7)$$

where  $P(T)$  is the probability density function of the normalised temperature field, and the  $S_{\text{NO}}$  presents the instant NO source. The *beta function* for the temperature probability density function is obtained from Vujanović et al., and the additional transport equation is introduced for the temperature variance [185]. This approach for the inclusion of temperature fluctuations due to turbulent flow field is extended both to thermal mechanism, and the NO production via the intermediate species.

## 4.4 Fuel Nitrogen Partitioning

In the previous section, the NO formation model has been presented, with the emphasis on fuel NO, as the main contributor to overall pollutant production in pulverised coal combustion systems. However, the variants of this model are known and commonly used, indicating that the model presents a good compromise between the complexity and computational intensity. Still, one of the main issues that is generally unknown for all combustion conditions is the influence of individual intermediate species. Conflicting information is reported in the literature about the dominant pathways, but the conclusion is that their importance is highly-dependant on parameters such as heating rate and temperatures, fuel and combustion chamber types, air to fuel ratio, secondary devolatilisation and particle sizes. This issue aggravates the modelling, making the development of simplified model for different conditions and fuels more difficult.

With the model set up as was previously displayed, the main issue is the partitioning of fuel nitrogen between the intermediate species, but also between the volatiles and the char. Although literature data on fuel partitioning exists, it is often limited for different coal types or combustion systems. With this question in mind, the experimental investigation was performed, aiming to obtain better insight into the division of fuel N between the pathways.

### 4.4.1 Experimental Determination of Fuel Nitrogen Partitioning

The experimental investigation was performed in the Fuel and Combustion Laboratory facilities at the Faculty of Mechanical Engineering, University of Belgrade. The coal samples were analysed in the coupled thermogravimetry and mass spectrometry (TG-MS) instrument by NETZSCH. The coupled system allows for the simultaneous thermogravimetric analysis and the mass spectrometry in the quadrupole mass analyser. The latter is more significant for the present analysis, as the mass spectrum of the gases evolved from the sample could provide more information about their composition.

The sample of bituminous coal, selected to match the one used in simulations and the referenced work [193], Table 4.2, was prepared by drying and the 10.45 g sample was analysed. The selected heating rate was 10 K/min, trying to replicate high heating rates of pulverised coal combustion systems in the available experimental setup. Two variations of experiments were performed in order to isolate the volatiles from heated coal particles. First, pure oxygen was selected as the carrier gas for connecting TG to the MS section via a transfer line. This was done to avoid the nitrogen from air to interfere with devolatilisation products. Secondly, the same process was conducted in the inert atmosphere of argon, in order to prevent the oxidation processes during pyrolysis. The gas flow rates were 20 mL/min and 70 mL/min, respectively.

The obtained mass spectrograms provide an incoherent image of all of the evolved species in the gas phase. Due to the large number of chemical compounds, this data is not applicable in the raw form, as overlapping signals for species with similar mass-to-charge ratio ( $m/z$ ) obfuscate the conclusions. Another issue is that the MS in this form is a qualitative method, not suitable for quantifying the amounts of species in gases, such as is the FTIR method. Therefore, the quantification method was devised for determining the absolute amounts of chemical species from the available data.

The signals were isolated for the pertinent species—HCN and  $\text{NH}_3$ . However, only the first one could be used for the analysis, as the  $\text{NH}_3$  signal, with the peak of  $m/z$  ratio at 17, overlapped with the  $\text{H}_2\text{O}$ . Therefore, the HCN was used as the initial step for determining the partitioning, and the values for  $\text{NH}_3$  were obtained by subtraction from the overall nitrogen content in fuel.

Figure 4.3 shows the processed signals for two cases, the first one with the  $\text{O}_2$  carrier gas, and the second with argon. The analysis was performed up to 1100 °C, with the heating rate of 10 K/min, and in the  $\text{O}_2$  atmosphere pyrolysis and char oxidation occurred. This procedure allowed obtaining the HCN signals for the overall process and the total evolution in volatiles and char alike. On the other hand, process in the inert atmosphere allowed the differentiation between the volatile evolution and the nitrogen remaining in char that account for the HCN formation. An additional assumption that HCN and  $\text{NH}_3$  are the only nitrogen-containing products from the fuel nitrogen allowed determination of the  $\text{NH}_3$  concentrations by considering total nitrogen content in fuel.

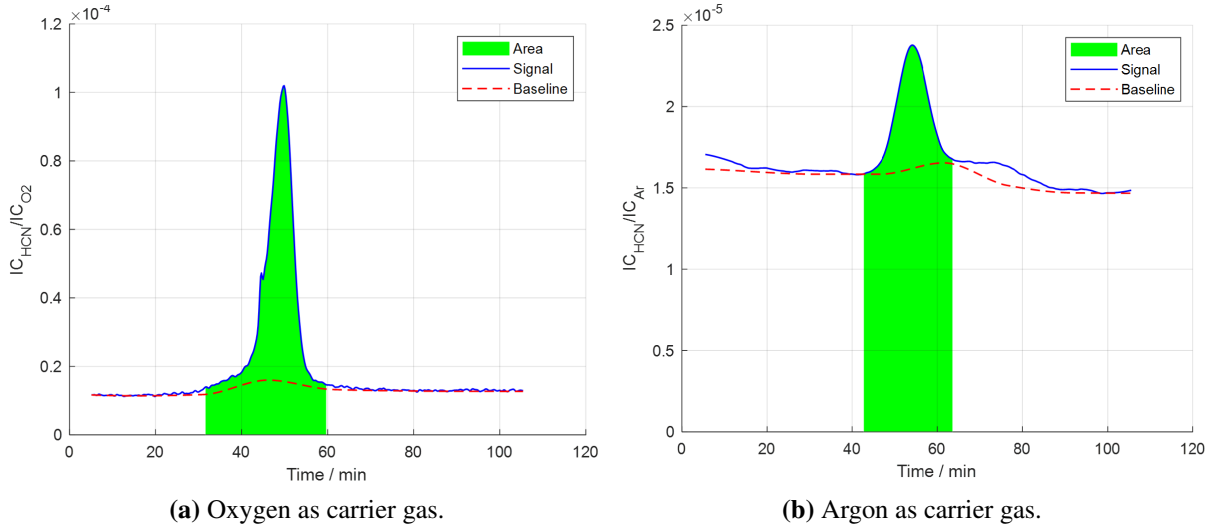


**Figure 4.3:** Mass spectrometry signals for HCN in oxygen and argon.

The fact that MS does not explicitly provide the quantitative analysis of the species' amounts was circumvented by equation (4.8). This equation presents the calculation of species concentration on the basis of fuel sample. In Fig. 4.3, it can be seen that the y-axis displays the relative ratio of analysed signal to the base one, measured as the ratio of their ion currents. To obtain the species' mass fraction in the fuel, the ratio of ion currents is translated into it by combination with the carrier gas flow rate and the mass of the sample. This calculation provides the mass fraction on the basis of the investigated fuel sample.

$$\begin{aligned}
 Y_{\text{HCN}} &= \frac{\text{IC}_{\text{HCN}}}{\text{IC}_{\text{carrier}}} \frac{q_{\text{carrier}}}{m_{\text{sample}}} \\
 &= \frac{\text{IC}_{\text{HCN}}}{\text{IC}_{\text{carrier}}} \frac{q_{v,\text{carrier}} \rho_{\text{carrier}} M_{\text{HCN}}}{m_{\text{sample}} \rho_{\text{HCN}} 22.4}
 \end{aligned} \tag{4.8}$$

The ratio of ionic currents in equation (4.8) is obtained by the numeric integration of HCN signal between the temperatures where devolatilisation and pyrolysis occurs, and the area is shown in green in Fig. 4.3.

After the data analysis and conversions, the partitioning of HCN and  $\text{NH}_3$  in solid fuel is obtained and presented in Table 4.1. These values are then used for improving the presented model for fuel nitrogen conversion, by introduction of weigh factors that influence the particular pathway.



**Table 4.1**  
Fuel nitrogen partitioning between species and the pathway type.

	total emissions, %	
Fuel nitrogen	HCN	NH <sub>3</sub>
	52.2	47.8
HCN	volatiles	char
	15.7	84.3

**Table 4.2**  
Coal characteristics [193].

<i>Proximate analysis</i>	<i>%wt</i>
Volatiles	37.6
Fixed carbon	58.8
Moisture	1.6
Ash	2.0
<i>Ultimate analysis</i>	<i>%wt</i>
Carbon	76.9
Hydrogen	5.1
Nitrogen	1.6
Sulfur	0.7
Oxygen	12.1
High heating value, MJ/kg	33.9
Low heating value, MJ/kg	32.7

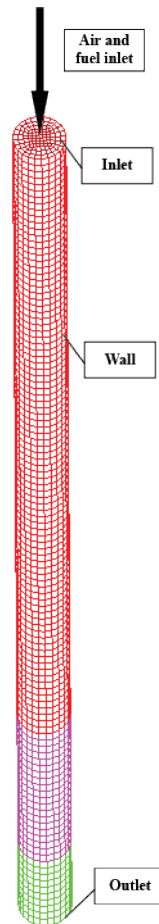


**Figure 4.4:** Computational mesh for the NO simulations with the selections.

## 4.5 Numerical Simulations

With the aim of numerically studying the solid fuel combustion, the formation of nitrogen oxides and other flow characteristics, a three-dimensional geometry of a drop tube has been used. Drop tube experiments are universally used in pyrolysis investigations, as they offer fine control over the operating conditions such as temperature, fuel and gas flow rates, but also reduce the influence of more complex geometries on flow and combustion process.

The simulation parameters for the combustion experiment conducted in an electrically heated drop tube are taken from the literature for coal experiments [193]. Figure 4.4 shows the boundary sections for the drop tube, which is a model of a 1200 mm long reaction tube, with the diameter being 38 mm. Wall temperatures are set to 1100 °C for the first 800 mm, and 900 mm and 300 mm for the subsequent 200 mm sections. The particle size distribution is provided by the authors of the experiment, with the average particle size of 29  $\mu\text{m}$ . The mesh consists out of 9600 cells, and the mesh dependency tests have already been performed during the combustion model development [194].

**Table 4.3**  
Coal pyrolysis simulation inlet boundary conditions.

	Tube diameter, mm	Temperature, °C	Velocity, m/s	Mass flow, g/h
Coal	38	80	0.19	25
Air		25		-

The transient simulation mode has been employed, with the timestep of  $2.5 \times 10^{-4}$  s. The MINMOD Relaxed differencing scheme was used for momentum, energy equations, and for turbulence and scalar equations, the Upwind scheme was employed [73].

The inlet parameters for the solid fuel and air are given in Table 4.3, the turbulence modelling is done by the standard  $k$ - $\epsilon$  model, and the radiative heat transfer and the influence of the particle radiation are taken into account by applying the P-1 radiation model.

The validation of pulverised fuel combustion model was performed in previously published research [195]. With the fuel injected from top of the tube, it is being heated by the surrounding gas and walls, and the devolatilisation and pyrolysis processes commence. Additionally, the char oxidation occurs in parallel with the particle burnout increasing along the tube length.

Simulation results are also shown in Fig. 4.5 for fluid flow and coal properties. Particle temperature rises rapidly as it enters the domain, initiating evaporation and devolatilisation processes. Extreme heating rates, characteristic for pulverised combustion systems, are considerably higher than the ones achieved in experimental TG tests, indicating that some caution is needed with the analysis of the results. The coal content represents the section of the particle that is being converted to volatiles. It can be seen that it matches the temperature profile of particles, and this exchange of mass is being used as an input for the source of volatiles in the fuel NO module. Lastly, the particles' char content is shown. It rises from the initial levels as the devolatilisation occurs, but subsequently drops as the char oxidation commences, and leaves ash as the main constituent of a particle.

The model for fuel NO that considers the partitioning of fuel nitrogen between the intermediate species and between evolution pathways into account is applied in the presented case. Parametric analysis with different values of partitioning factor  $\alpha$  was performed to test the sensitivity of the model. Factor  $\alpha$  was defined as the ratio of  $\text{NH}_3$  pathway to the HCN pathway and was varied between 0 and 1.0. In Fig. 4.6 it can be noticed that the change of concentrations along the drop tube height changes in the expected manner, increasing and decreasing as their relative importance changes. In Fig. 4.6a, the HCN concentrations fall with the increase of  $\alpha$ , and in Fig. 4.6b the opposite is true. The important thing to notice is the concentrations of individual species, where HCN rises up to several hundred parts per million, while  $\text{NH}_3$  concentrations are quite lower. While this can be substantiated by the literature sources that highlight the importance of HCN in pulverised combustion of bituminous coals [196], simulated  $\text{NH}_3$

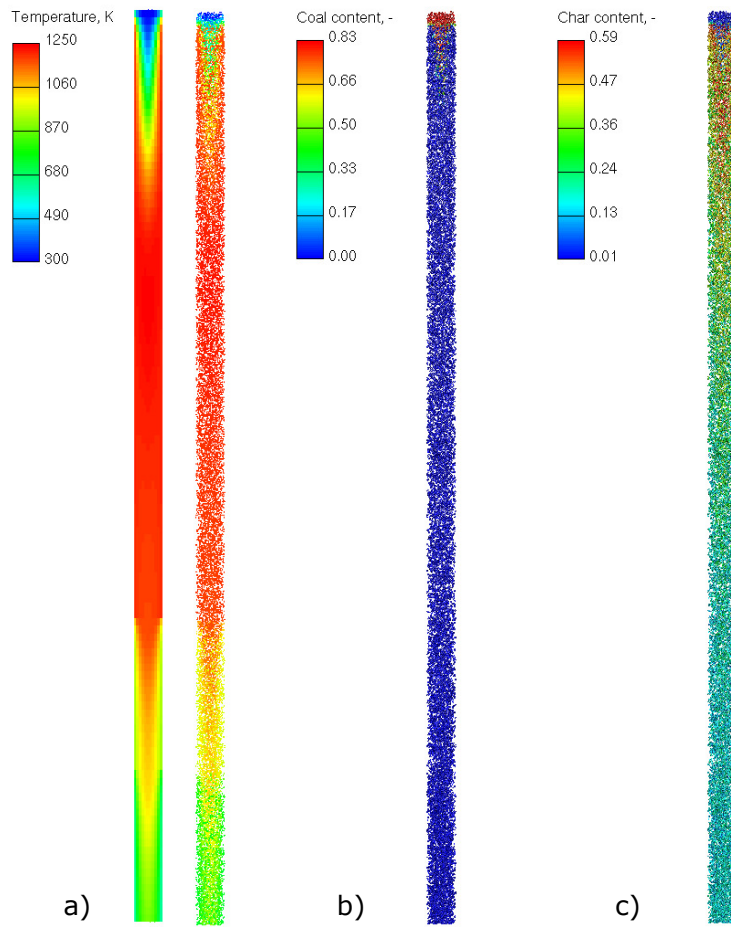
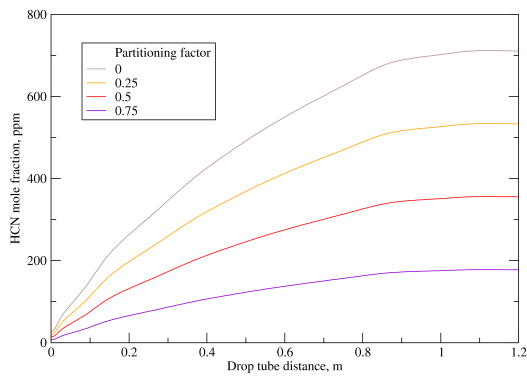
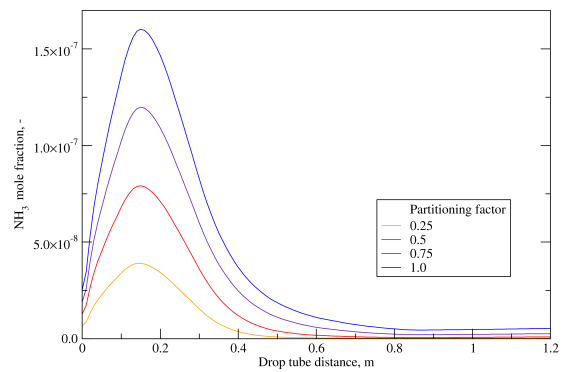


**Figure 4.5:** Temperatures (a) and particle composition (b) content of volatiles in coal; c) char content)) in drop tube simulations.



**(a)** HCN concentrations.



**(b)** NH<sub>3</sub> concentrations.

**Figure 4.6:** Intermediate species' concentrations depending on the partitioning factor used.

levels are quite low. This indicates that the HCN pathway and the reaction rates under present conditions contribute to the overall NO concentrations significantly more than the NH<sub>3</sub> pathway.

Next, the partitioning factor and the division between the char and volatiles obtained by the experimental investigation (Table 4.1) were used. For the simulated drop tube case, the resulting concentrations of NO and intermediate chemical species in fuel nitrogen pathway are shown. Firstly, in Fig. 4.7, the NO concentrations reach the levels of approximately 500 ppm as the solid fuel particles travel down the tube and react with the gas phase. The HCN concentrations are roughly at the same levels, which is expected, and NH<sub>3</sub> concentration is significantly lower. Additionally, these low concentrations further justify the approach for decoupling the pollutant formation model.

Routing of the production pathways has been previously reported in the literature [187], but an arbitrary partitioning factor was used for all simulations, without experimental determination and without the separation based on the choice between volatile or char pathway.

It can be seen in Fig. 4.7 that the NO concentration contour largely corresponds to the shape of HCN distribution. This is in agreement with the previous results from the parametric analysis. It can also be seen that the NH<sub>3</sub> concentration is higher at the drop tube entrance, as the particles devolatilise, but in absolute terms this is quite smaller than the HCN. On the other hand, the HCN evolution is stronger as the char oxidation occurs further down the tube. This is expected, as the char pathway is more pronounced, with 84% of HCN evolving this way Table 4.1.

Finally, Fig. 4.8 compares the NO concentrations along tube axis with the experimentally obtained concentrations reported by Wang et al. [193]. The partitioning factor used for simulations corresponded to values in Table 4.1 derived by the previously-described procedure. The experimental points for the sieved coal sampled reach the values of approximately 450 ppm after the introduction in drop tube, and remain level at the end of the tube. On the other hand, the simulated concentrations do reach concentrations comparable to the experimental ones, but the dynamic is somewhat slower. The discrepancy at the initial section of the tube indicates slower-than-expected conversion by the volatile pathway. This behaviour is in agreement with previous figures and graphs, and points out the direction of further model development.

The results obtained by applying the presented model on simulated case showed that the final levels of NO concentrations are replicated, and that the stationary state at the tube bottom is matched. After the conversion processes between intermediate chemical species shortly after initial devolatilisation and intense char oxidation diminish, the overall NO concentrations are stabilised and towards the end of the tube nearly constant concentrations are measured. The simulated results show discrepancy in the dynamics at the initial part of the drop tube, but the final levels are similarly matched, with 5.89% relative error after the conversion sources are depleted and stationary state is achieved.

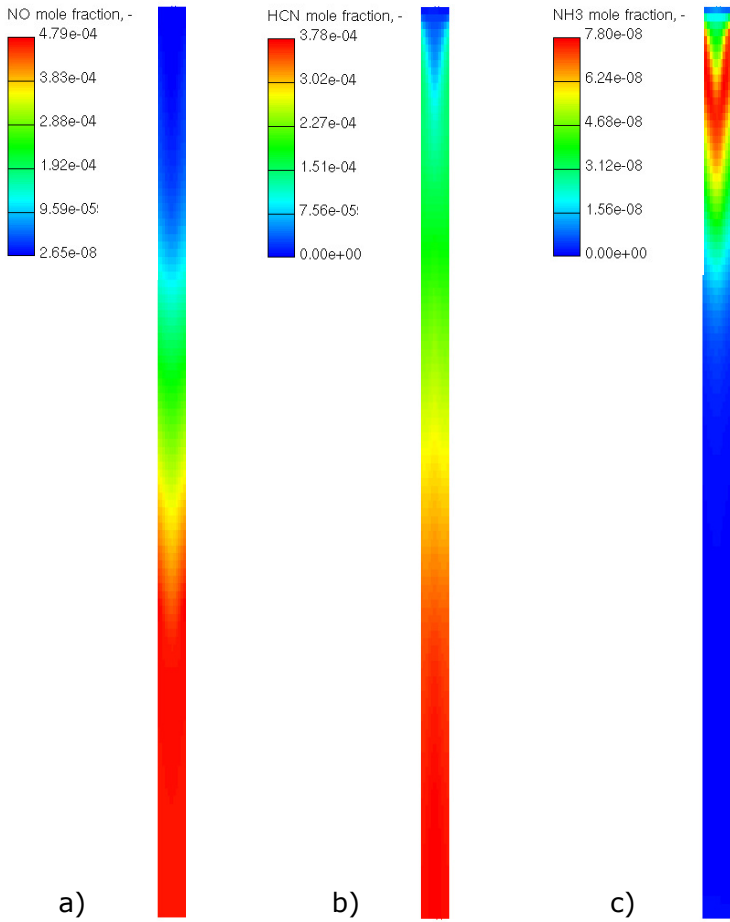


**Figure 4.7:** Pollutant mole fractions.

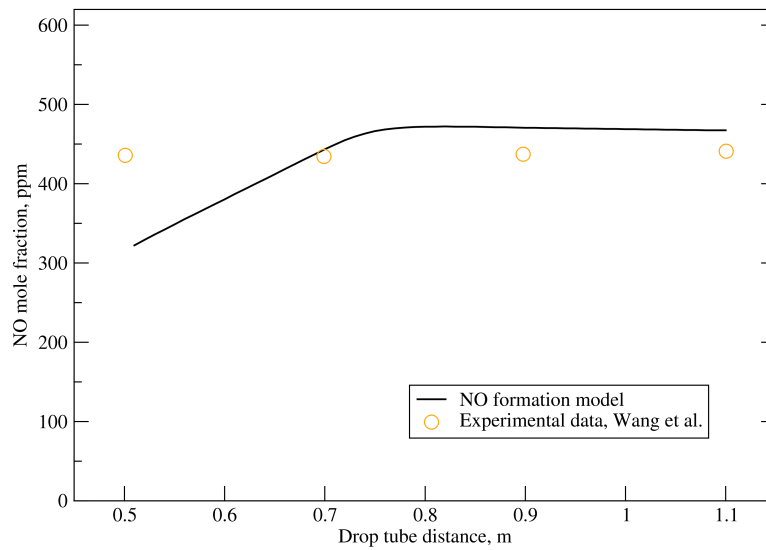


**Figure 4.8:** NO concentration profile along the drop tube axis.

## 4.6 Conclusion

In present chapter, combustion processes and formation of nitrogen-containing pollutants from solid fuels were investigated by numerically simulating the drop tube—a standard test case for evaluating the solid fuel properties and system operation. The AVL FIRE<sup>TM</sup> was used for simulating the three-dimensional geometry, temperature and turbulent flow fields, concentrations of the reactants, products and pollutants, as well as two-phase flow of solid fuel particles within the gas phase. Solid fuel reactions such as drying, devolatilization, gaseous species generation and char burnout are considered as well by the pulverised fuel combustion model.

A simplified numerical model for nitrogen oxides' formation in solid fuel combustion systems has been used, with thermal and fuel NO mechanisms and the effect of the temperature fluctuations taken into account. Furthermore, the fuel nitrogen partitioning between intermediate chemical species, and between evolution through char or volatiles has also been included in the model by a partitioning factor  $\alpha$ . Additionally, to obtain detailed characteristics specific for the fuel used, an experimental analysis of bituminous coal has been performed on a TG-MS system. The devised approach for spectrometry data analysis provided the information on fuel nitrogen partitioning required for the numerical simulations.

The simulation results were presented and analysed, indicating model's potential, but also pointing to the unrefined sections of the model as well. Parametric analysis showed that the partitioning factor influences the results as expected, but the comparison between intermediate species' pathways displayed HCN having significantly greater impact than  $\text{NH}_3$ . The discrep-

ancies at the top of the tube indicate that the formation mechanism is not fully tuned and that tests on additional cases and fuel types are needed. Possible culprit for the weaker  $\text{NH}_3$  influence might be found in differences in heating rates during the experimental investigation on TG-MS and the real drop tube. However, the need for additional modifications of the model is a more likely issue. Therefore, further development of the model is necessary, with additional simulations and the validation on a case with data on intermediate species concentrations.

The pollutant formation model, along with the procedure for determining fuel nitrogen partitioning, presents an integrated approach suitable for accurate modelling of pulverised combustion systems.



## CHAPTER 5

# Conclusions and Future Work

## 5.1 Conclusions

The work presented in this thesis focuses on both the formation and the removal side of pollutant modelling in combustion systems. The implemented models present an improvement compared to the currently used approaches, as they include additional physical or chemical processes into account when simulating the real systems.

The main section of this work revolved around modelling the absorption of  $\text{SO}_2$  in spray scrubbers. First step towards the comprehensive model was the implementation of equilibrium chemical models that essentially indicate the potential for absorption in a liquid. This was done for both pure water and seawater, with the description of chemical systems and relevant chemical species. The second major part of absorption modelling was the implementation of mass transfer between the phases. This is a complex topic due to large number of parameters influencing the transfer dynamics, and the analysed approaches were investigated and compared to available experimental data. Therefore, the model was in the end based on the Euler-Lagrangian approach for multiphase modelling, with DDM approach describing spray droplets. On a droplet level, concentrated parameter approach was utilised, and two different chemical models—for pure and for seawater—were implemented and validated. The two film theory is the basis of mass transfer modelling, with the penetration theory describing the dominating liquid side mass transfer coefficient.

These models were implemented and validated on simplified experimental cases with low influence of wall film, showing great agreement with literature data both for seawater and pure water absorption. Due to the fact that comparison with a case based on real industrial conditions showed greater discrepancy due to significant effect of wall film, the absorption model in wetted walls was also developed.

This model is based on analogous principles as the spray absorption, but differs in the approach for mass transfer calculation. As the hydrodynamic principles are different for liquid films on a wall compared to the droplet, the chosen approach was based on Sherwood number correlations in function of Reynolds number and other flow parameters. By application of

the model on a case with high liquid-to-gas ratio and influence of wall film, more accurate results were achieved, especially at high removal efficiencies above 90%. Good agreement with literature data in validation procedure implies that the model can be used in research and investigation of new desulfurisation technologies and designs.

The second major part of the thesis revolves around nitrogen oxides formation modelling in pulverised combustion systems. Although the conventional fossil fuel utilisation is quickly falling out of favour, the requirements for environmental impact reduction of a large number of currently installed fossil fuel-powered plants might lead to the use of pollutant formation models. The commonly used thermal and fuel nitrogen models were implemented in the Euler-Lagrangian framework of a computational fluid dynamics software. Then, the modification of the fuel NO mechanism was implemented, in order to account for the different influences of formation pathways and intermediate species on final NO production. After setting the framework that would allow weighted partitioning parameters for HCN or NH<sub>3</sub> intermediate species, or for defining the ratio between the formation pathway through the volatiles or char, the experimental investigation was performed.

The contribution of this work can be seen in the method for experimentally determining the fuel nitrogen partitioning in intermediate species by using the coupled TG - MS system, and later application of that data in numerical simulations for achieving better results. This method for the analysis of spectrometry data allows for the conversion between the qualitative MS results and quantification of different intermediate species and pathways. Data obtained for a bituminous coal sample showed comparable concentrations of HCN and NH<sub>3</sub> evolving during the coal heating process, but the HCN production pathway was strongly shifted towards the generation from char.

The obtained partitioning ratio was used in drop tube simulations and the parametric analysis was performed on the influence of different pathways. The simulation results indicated that the HCN dominated over the NH<sub>3</sub> pathway, which contributed weakly to the overall NO production. Finally, when compared to the experimental results, the model quite accurately predicted the final NO concentrations at the end of the tube, with more pronounced discrepancy at the initial parts.

Overall, the work presented here and validated against experimental measurements corresponding to industrial conditions proves the research hypothesis that the new and upgraded mathematical models will enable accurate and efficient calculation of complex physico-chemical processes of nitrogen oxides production during solid fuel combustion and of sulfur dioxide removal from flue gases by seawater absorption in spray droplets and wall film.

## 5.2 Proposals for Future Work

### 5.2.1 Future Work on Sulfur Dioxide Absorption Model

Although the intention during the model development was to include all relevant processes, assumptions were still made to reduce the model's complexity and numerical intensity. For example, SO<sub>2</sub> desorption was neglected during the model development, and it is conceivable that in some cases and applications it could be important. Additionally, the CO<sub>2</sub> chemistry in seawater could have an impact on the equilibrium concentrations in flue gases, so its inclusion might be beneficial.

For wall film, the mass transfer modelling could be improved upon by the addition of gas side mass transfer coefficient calculation, as well as by better handling of the unphysical behaviour in sump at the bottom of scrubbers. Additional topic that might be of interest is modelling of the acidification of sea when discarding the effluent water in maritime applications.

### 5.2.2 Future Work on Nitrogen Oxides Formation Model

Regarding the NO formation modelling from solid fuel combustion systems, one of the planned activities would be the expansion of the model and the fuel nitrogen partitioning characterisation to biomass and other fuel types. Some experimental work has already been done, but obtaining appropriate experimental data for drop tube-like test cases still needs to be performed. The inclusion of biomass could prove interesting considering the possibilities for co-burning and the potential for CO emissions reduction.

Additionally, it would be beneficial to validate the model results against the experimental case that provides data on evolution of individual intermediate species. This could further indicate whether the pathway selection approach is suitable for modelling pollutant formation from solid fuel combustion systems.

Finally, the idea is to expand the model from the current applications on test cases to full industrial combustion systems, and great burners with real operating conditions. This would ultimately prove that the approach is suitable for real-life use and beneficial in engineering applications for reduction of pollutant emissions.

# Bibliography

- [1] Cara A. Horowitz. „Paris Agreement”. In: *International Legal Materials* 55.4 (Aug. 2016), pp. 740–755. ISSN: 0020-7829. DOI: 10.1017/S0020782900004253.
- [2] Ed Dlugokenck and Pieter Tans. *NOAA/GML*. 2020. URL: [www.esrl.noaa.gov/gmd/ccgg/trends/](http://www.esrl.noaa.gov/gmd/ccgg/trends/).
- [3] International Energy Agency. *Global Energy & CO2 Status Report 2019*. Paris: IEA, 2019.
- [4] *World Energy Outlook 2019*. World Energy Outlook. OECD, 2019. ISBN: 9789264523272. DOI: 10.1787/caf32f3b-en.
- [5] ICAP. *Emission Trading Worldwide: Status Report 2020*. Tech. rep. Berlin: International Carbon Action Partnership, 2020, p. 160.
- [6] Craig Hart and M A Zhong. „China’s Regional Carbon Trading Experiments and the Development of a National Market: Lessons from China’s So 2 Trading Programme”. In: *Energy & Environment* 25.3-4 (Apr. 2014), pp. 577–592. ISSN: 0958-305X. DOI: 10.1260/0958-305X.25.3-4.577.
- [7] Hannah Ritchie and Max Roser. „CO2 and Greenhouse Gas Emissions”. In: *Our World in Data* (2017). <https://ourworldindata.org/co2-and-other-greenhouse-gas-emissions>.
- [8] European Environment Agency. *European Union emission inventory report 1990-2018*. Luxemburg: Publications Office of the European Union, 2020, p. 160. ISBN: 978-92-9480-237-8. DOI: 10.2800/233574.
- [9] European Environment Agency. *Emissions of primary PM2.5 and PM10 particulate matter (CSI 003)*. 2019. URL: <https://www.eea.europa.eu/data-and-maps/indicators/emissions-of-primary-particles-and-5> (visited on 08/17/2020).
- [10] European Environment Agency. *Air pollutant emissions data viewer*. URL: <https://www.eea.europa.eu/data-and-maps/dashboards/air-pollutant-emissions-data-viewer-3>.

- [11] Statista. *Transportation NOx emissions in the United States 1990-2019* Published by Ian Tiseo, Jul 30, 2020 Over the past three decades nitrogen oxide emissions in the United States have decreased significantly. By 2019 they had fallen to 4.9 million tons. In the Un. 2020. URL: <https://www.statista.com/statistics/860125/us-transportation-sector-nox-emissions/>.
- [12] US Environmental Protection Agency. *Clean Air Markets - Power Plant Emission Trends*. URL: <https://www.epa.gov/airmarkets/power-plant-emission-trends>.
- [13] European Environment Agency. *European Union emission inventory report 1990-2018*. Luxemburg: Publications Office of the European Union, 2020, p. 160. ISBN: 978-92-9480-237-8. DOI: 10.2800/233574.
- [14] „Directive 2010/75/EU of the European Parliament and of the Council of 24 November 2010 on industrial emissions (integrated pollution prevention and control) No 334/17”. In: *OJ L 334* (17.12.2010), pp. 17–119.
- [15] Health Effects Institute. *State of Global Air 2019*. Tech. rep. Boston, MA: Health Effects Institute, 2019.
- [16] Bo Zheng, Dan Tong, Meng Li, Fei Liu, Chaopeng Hong, Guannan Geng, Haiyan Li, Xin Li, Liqun Peng, Ji Qi, Liu Yan, Yuxuan Zhang, Hongyan Zhao, Yixuan Zheng, Kebin He, and Qiang Zhang. „Trends in China’s anthropogenic emissions since 2010 as the consequence of clean air actions”. In: *Atmospheric Chemistry and Physics* 18.19 (Oct. 2018), pp. 14095–14111. ISSN: 1680-7324. DOI: 10.5194/acp-18-14095-2018.
- [17] Greenpeace. *2017 China 365 Cities PM2.5 Concentration Ranking*. 2018. URL: <https://www.greenpeace.org.cn/air-pollution-2017-city-ranking/>.
- [18] Ling Tang, Jiabao Qu, Zhifu Mi, Xin Bo, Xiangyu Chang, Laura Diaz Anadon, Shouyang Wang, Xiaoda Xue, Shibe Li, Xin Wang, and Xiaohong Zhao. „Substantial emission reductions from Chinese power plants after the introduction of ultra-low emissions standards”. In: *Nature Energy* 4.11 (Nov. 2019), pp. 929–938. ISSN: 2058-7546. DOI: 10.1038/s41560-019-0468-1.
- [19] Valerie J. Karplus, Shuang Zhang, and Douglas Almond. „Quantifying coal power plant responses to tighter SO2 emissions standards in China”. In: *Proceedings of the National Academy of Sciences of the United States of America* 115.27 (2018), pp. 7004–7009. ISSN: 10916490. DOI: 10.1073/pnas.1800605115.
- [20] United Nations Conference on Trade and Development. *50 Years of Review of Maritime Transport, 1968-2018: Reflecting on the past, exploring the future*. Tech. rep. Geneva: United Nations, United Nations Conference on Trade and Development, 2018, p. 97.

- [21] United Nations Conference on Trade and Development. *UNCTAD Handbook of Statistics 2019*. Geneva: United Nations Publications, 2019, p. 104. ISBN: 978-92-1-112916-8. DOI: 10.1080/10426919008953291.
- [22] Naya Olmer, Bryan Comer, Biswajoy Roy, Xiaoli Mao, and Dan Rutherford. *Greenhouse Gas Emissions From Global Shipping, 2013-2015*. Tech. rep. Washington DC: International Council on Clean Transportation, 2017, p. 38.
- [23] International Maritime Organization. *Fourth IMO GHG Study 2020 – Final report*. Tech. rep. International Maritime Organization, 2020, p. 577.
- [24] International Maritime Organization. *Regulations for the Prevention of Air Pollution from Ships (Revised Annex VI of MARPOL 73/78)*. 2008.
- [25] Bilfinger Engineering & Technologies GmbH. *Exhaust Gas Cleaning For Maritime Applications*. URL: <https://www.bet.bilfinger.com/en/services/business-segments/exhaust-gas-cleaning-for-maritime-applications/legal-regulations/>.
- [26] „Directive (EU) 2016/802 of the European Parliament and of the Council of 11 May 2016 relating to a reduction in the sulphur content of certain liquid fuels”. In: *OJ L 135/58* (21.5.2016).
- [27] International Maritime Organization. *Sulfur monitoring for 2018, MEPC 74/5/3*. Tech. rep. London, UK: International Maritime Organization, 2019.
- [28] Jasper Faber, Saliha Ahdour, Maarten 't Hoen, Dagmar Nelissen, Anjani Singh, Petr Steiner, Sergio Rivera, Carlo Raucci, Tristan Smith, Eiichi Muraoka, Yakov Ruderman, Ivan Khomutov, and Shinichi Hanayama. *Assessment of fuel oil availability – final report*. Tech. rep. Delft: CE Delft, 2016, pp. 1–186.
- [29] Chris Le Fevre. *A review of demand prospects for LNG as a marine transport fuel*. Tech. rep. June. Oxford, United Kingdom: Oxford Institute for Energy Studies, June 2018, p. 35. DOI: 10.26889/9781784671143.
- [30] International Maritime Organization. *Studies on the feasibility and use of LNG as a fuel for shipping*. Tech. rep. London, UK: International Maritime Organization, 2016, p. 290.
- [31] International Maritime Organization. *Guidelines for exhaust gas cleaning systems - MEPC.259(68)*. 2015.
- [32] Gordon Rago. *Pollution "scrubbers" on ships keep the air cleaner — but they can make the water dirtier*. 2019. URL: [https://www.pilotonline.com/ask/article%7B%5C\\_%7D00f5842e-5bbb-11e9-9eb3-03b0075ca3bb.html](https://www.pilotonline.com/ask/article%7B%5C_%7D00f5842e-5bbb-11e9-9eb3-03b0075ca3bb.html).

- [33] Katsuo Oikawa, Chaturong Yongsirib, Kazuo Takeda, and Takayoshi Harimotoa. „Sea-water Flue Gas Desulfurization: Its Technical Implications and Performance Results”. In: *Environmental Progress* 22.1 (2003), pp. 67–73.
- [34] John B. Heywood and Emmanuel Kasseris. *Pollution Prevention and Response: Scrubber Environmental Impact Literature Review*. Tech. rep. MEPC 74/INF.10. International Maritime Organisation, 2019, p. 21.
- [35] Antoine Halff, Lara Younes, and Tim Boersma. „The likely implications of the new IMO standards on the shipping industry”. In: *Energy Policy* 126. April 2018 (Mar. 2019), pp. 277–286. ISSN: 03014215. DOI: 10.1016/j.enpol.2018.11.033.
- [36] Ship and Bunker News. *Number of Ships to be Equipped with Scrubbers Hits 4000: DNV GL*. 2020. URL: <https://shipandbunker.com/news/world/814936-number-of-ships-to-be-equipped-with-scrubbers-hits-4000-dnv-gl>.
- [37] R W Portmann, J S Daniel, and A R Ravishankara. „Stratospheric ozone depletion due to nitrous oxide: influences of other gases”. In: *Philosophical Transactions of the Royal Society B: Biological Sciences* 367.1593 (May 2012), pp. 1256–1264. ISSN: 0962-8436. DOI: 10.1098/rstb.2011.0377.
- [38] Steven S. Brown and Jochen Stutz. „Nighttime radical observations and chemistry”. In: *Chemical Society Reviews* 41.19 (2012), pp. 6405–6447. ISSN: 14604744. DOI: 10.1039/c2cs35181a.
- [39] Paul J Crutzen. „The Role of NO and NO<sub>2</sub> in the Chemistry of the Troposphere and Stratosphere”. In: *Annual Review of Earth and Planetary Sciences* 7.1 (May 1979), pp. 443–472. ISSN: 0084-6597. DOI: 10.1146/annurev.ea.07.050179.002303.
- [40] R Atkinson. „Atmospheric chemistry of VOCs and NO<sub>x</sub>”. In: *Atmospheric Environment* 34.12-14 (2000), pp. 2063–2101. ISSN: 13522310. DOI: 10.1016/S1352-2310(99)00460-4.
- [41] Michele Vascellari. „NO<sub>x</sub> Emission and Mitigation Technologies”. In: *Handbook of Clean Energy Systems* x (2015), pp. 1–23. DOI: 10.1002/9781118991978.hces118.
- [42] H. F. Johnstone. „Metallic Ions as Catalysts for the Removal of Sulfur Dioxide from Boiler Furnace Gases”. In: *Industrial and Engineering Chemistry* 23.5 (1931), pp. 559–561. ISSN: 00197866. DOI: 10.1021/ie50257a022.
- [43] G. M. Hidy and C. L. Blanchard. „The changing face of lower tropospheric sulfur oxides in the United States”. In: *Elementa* 4 (2016), pp. 1–20. ISSN: 23251026. DOI: 10.12952/journal.elementa.000138.

- [44] Paul R Robinson. „Sulfur Removal and Recovery”. In: *Carbon*. Ed. by Chang Samuel Hsu and Paul R. Robinson. Vol. 50. Springer Handbooks 5. Cham: Springer International Publishing, 2017, pp. 649–673. ISBN: 978-3-319-49345-9. DOI: 10.1007/978-3-319-49347-3\_20. arXiv: 0508657 [cond-mat].
- [45] A.N. Kolmogorov. „Dissipation of energy in the locally isotropic turbulence”. In: *Proceedings of the Royal Society of London. Series A: Mathematical and Physical Sciences* 434.1890 (July 1991), pp. 15–17. ISSN: 0962-8444. DOI: 10.1098/rspa.1991.0076.
- [46] F. Moukalled, L. Mangani, and M. Darwish. *The Finite Volume Method in Computational Fluid Dynamics*. Vol. 113. Fluid Mechanics and Its Applications. Cham: Springer International Publishing, 2016, p. 500. ISBN: 978-3-319-16873-9. DOI: 10.1007/978-3-319-16874-6.
- [47] Hung LE, Parviz Moin, and John Kim. „Direct numerical simulation of turbulent flow over a backward-facing step”. In: *Journal of Fluid Mechanics* 330. September 2000 (Jan. 1997), pp. 349–374. ISSN: 0022-1120. DOI: 10.1017/S0022112096003941.
- [48] J. Bardina, J. Ferziger, and W. Reynolds. „Improved subgrid-scale models for large-eddy simulation”. In: *13th Fluid and Plasma Dynamics Conference*. Reston, Virginia: American Institute of Aeronautics and Astronautics, July 1980. DOI: 10.2514/6.1980-1357.
- [49] Osborne Reynolds. „IV. On the dynamical theory of incompressible viscous fluids and the determination of the criterion”. In: *Philosophical Transactions of the Royal Society of London. (A.)* 186.1895 (Dec. 1895), pp. 123–164. ISSN: 0264-3820. DOI: 10.1098/rsta.1895.0004.
- [50] Ioannis Asproulias. „RANS Modelling for Compressible Turbulent Flows Involving Shock Wave Boundary Layer Interactions RANS Modelling for Compressible Turbulent Flows Involving Shock Wave Boundary Layer Interactions A thesis submitted to the University of Manchester”. PhD Thesis. The University of Manchester, 2016. DOI: 10.13140/RG.2.2.18091.23840.
- [51] Saskia Pattijn. „Non-linear, low-Reynolds, two-equation turbulence models”. PhD Thesis. Ghent University, 1999. DOI: 10.1007/978-94-015-8666-5\_3.
- [52] Alexandre J. A. Favre. „Formulation of the Statistical Equations of Turbulent Flows with Variable Density”. In: *Studies in Turbulence* (1992), pp. 324–341. DOI: 10.1007/978-1-4612-2792-2\_23.
- [53] François G. Schmitt. „About Boussinesq’s turbulent viscosity hypothesis: historical remarks and a direct evaluation of its validity”. In: *Comptes Rendus Mécanique* 335.9-10 (Sept. 2007), pp. 617–627. ISSN: 16310721. DOI: 10.1016/j.crme.2007.08.004.



- [54] Jiri Blazek. „Turbulence Modeling”. In: *Computational Fluid Dynamics: Principles and Applications*. Elsevier, 2015, pp. 213–252. ISBN: 9780080999951. DOI: 10.1016/B978-0-08-099995-1.00007-5.
- [55] John L. Lumley. „Computational Modeling of Turbulent Flows”. In: *Advances in Applied Mechanics*. Vol. 18. C. 1979, pp. 123–176. ISBN: 0120020181. DOI: 10.1016/S0065-2156(08)70266-7.
- [56] Peter A. Davidson, Yukio Kaneda, Keith Moffatt, and Katepalli R. Sreenivasan. *A Voyage Through Turbulence*. Ed. by Peter A. Davidson, Yukio Kaneda, Keith Moffatt, and Katepalli R. Sreenivasan. Cambridge: Cambridge University Press, 2011. ISBN: 9781139018241. DOI: 10.1017/CB09781139018241.
- [57] P. Y. Chou. „On velocity correlations and the solutions of the equations of turbulent fluctuation”. In: *Quarterly of Applied Mathematics* 3.1 (Apr. 1945), pp. 38–54. ISSN: 0033-569X. DOI: 10.1090/qam/11999.
- [58] B.E. Launder and D.B. Spalding. „The numerical computation of turbulent flows”. In: *Computer Methods in Applied Mechanics and Engineering* 3.2 (Mar. 1974), pp. 269–289. ISSN: 00457825. DOI: 10.1016/0045-7825(74)90029-2.
- [59] P. A. Durbin. „Near-wall turbulence closure modeling without "damping functions"”. In: *Theoretical and Computational Fluid Dynamics* 3.1 (1991), pp. 1–13. ISSN: 09354964. DOI: 10.1007/BF00271513.
- [60] R. Manceau, S. Parneix, and D. Laurence. „Turbulent heat transfer predictions using the  $v_2$ - $f$  model on unstructured meshes”. In: *International Journal of Heat and Fluid Flow* 21.3 (2000), pp. 320–328. ISSN: 0142727X. DOI: 10.1016/S0142-727X(00)00016-3.
- [61] K. Hanjalić, M. Popovac, and M. Hadžiabdić. „A robust near-wall elliptic-relaxation eddy-viscosity turbulence model for CFD”. In: *International Journal of Heat and Fluid Flow* 25.6 (Dec. 2004), pp. 1047–1051. ISSN: 0142727X. DOI: 10.1016/j.ijheatfluidflow.2004.07.005.
- [62] Branislav Basara. „Eddy Viscosity Transport Model Based on Elliptic Relaxation Approach”. In: *AIAA Journal* 44.7 (July 2006), pp. 1686–1690. ISSN: 0001-1452. DOI: 10.2514/1.20739.
- [63] P.A. Durbin. „On the  $k$ - $\epsilon$  stagnation point anomaly”. In: *International Journal of Heat and Fluid Flow* 17.1 (Feb. 1996), pp. 89–90. ISSN: 0142727X. DOI: 10.1016/0142-727X(95)00073-Y.
- [64] K. Ramadani, M. E. Kelterer, R. Pecnik, and W. Sanz. „Application of the zeta- $F$ -turbulence model to steady transitional flow”. In: *8th European Conference on Turbomachinery: Fluid Dynamics and Thermodynamics, ETC 2009 - Conference Proceedings August 2016* (2009), pp. 119–130. ISSN: 24104833.

- [65] M. Popovac and K. Hanjalic. „Compound wall treatment for RANS computation of complex turbulent flows and heat transfer”. In: *Flow, Turbulence and Combustion* 78.2 (2007), pp. 177–202. ISSN: 13866184. DOI: 10.1007/s10494-006-9067-x.
- [66] Günter P Merker, Christian Schwarz, and Rüdiger Teichmann. *Combustion Engines Development Mixture Formation, Combustion, Emissions and Simulation*. Berlin, Heidelberg: Springer Berlin Heidelberg, 2012. ISBN: 978-3-642-02951-6.
- [67] Zvonimir Petranović, Wilfried Edelbauer, Milan Vujanović, and Neven Duić. „Modelling of spray and combustion processes by using the Eulerian multiphase approach and detailed chemical kinetics”. In: *Fuel* 191 (Mar. 2017), pp. 25–35. ISSN: 00162361. DOI: 10.1016/j.fuel.2016.11.051.
- [68] F. V. Bracco. „Modeling of Engine Sprays”. In: *AIAA Journal*. Vol. 42. Heat and Mass Transfer 3. Berlin, Heidelberg: Springer Berlin Heidelberg, Feb. 1985, pp. 669–669. ISBN: 978-3-642-05629-1. DOI: 10.4271/850394.
- [69] Gunnar Stiesch. *Modeling Engine Spray and Combustion Processes*. Heat and Mass Transfer. Berlin, Heidelberg: Springer Berlin Heidelberg, 2003. ISBN: 978-3-642-05629-1. DOI: 10.1007/978-3-662-08790-9.
- [70] John K. Dukowicz. „A particle-fluid numerical model for liquid sprays”. In: *Journal of Computational Physics* 35.2 (Apr. 1980), pp. 229–253. ISSN: 00219991. DOI: 10.1016/0021-9991(80)90087-X.
- [71] Jose M Desantes, Jose M. Garcia-Oliver, Jose M. Pastor, and A. Pandal. „A Comparison of Diesel Sprays CFD Modeling Approaches: DDM Versus E-Y Eulerian Atomization Model”. In: *Atomization and Sprays* 26.7 (2016), pp. 713–737. ISSN: 1044-5110. DOI: 10.1615/AtomizSpr.2015013285.
- [72] S.M. Frolov, V.S. Ivanov, V.A. Smetanyuk, Branislav Basara, M. Suffa, and E. von Berg. „Spray penetration and vaporization in diesel engines: numerical simulation and experiments”. English. In: *Nonequilibrium Phenomena: Plasma, Combustion, Atmosphere*. Torus Press, 2009, pp. 324–331. ISBN: 978-5-94588-067-2.
- [73] *AVL FIRE Documentation*. Graz, 2017.
- [74] A D Gosman and E. Loannides. „Aspects of Computer Simulation of Liquid-Fueled Combustors”. In: *Journal of Energy* 7.6 (Nov. 1983), pp. 482–490. ISSN: 0146-0412. DOI: 10.2514/3.62687.
- [75] Yuan Xu. „Improvements in the Operation of SO<sub>2</sub> Scrubbers in China’s Coal Power Plants”. In: *Environmental Science & Technology* 45.2 (Jan. 2011), pp. 380–385. ISSN: 0013-936X. DOI: 10.1021/es1025678.
- [76] U.S. Department of Energy. *Electric Power Annual 2018*. Tech. rep. October 2019. Washington, DC 20585, 2019, p. 231.

- [77] *Assessment of Possible Impacts of Scrubber Water Discharges on the Marine Environment*. Miljøstyrelsen, 2012. ISBN: 9788792903303.
- [78] Jens Peter Hansen, Johan Kaltoft, Flemming Bak, Jens Gørtz, Michael Pedersen, and Chris Underwood. *Reduction of SO<sub>2</sub>, NO<sub>x</sub> and Particulate Matters from Ships with Diesel Engines*. Copenhagen: Miljøstyrelsen, 2014. ISBN: 978-87-93026-57-5.
- [79] Milene Costa Codolo and Waldir Antonio Bizzo. „Mass Transfer and Liquid-Film Formation in a Spray Tower for SO<sub>2</sub> Removal in Sodium Hydroxide Solution”. In: *Chemical Engineering & Technology* 39.10 (2016), pp. 1939–1945. ISSN: 09307516. DOI: 10.1002/ceat.201500389.
- [80] Ravi K. Srivastava, Wojciech Jozewicz, Carl Singer, and S O Reduction Program. „SO<sub>2</sub> scrubbing technologies: A review”. In: *Environmental Progress* 20.4 (2001), pp. 219–227. ISSN: 02784491. DOI: 10.1002/ep.670200410.
- [81] Antonio Gómez, Norberto Fueyo, and Alfredo Tomás. „Detailed modelling of a flue-gas desulfurisation plant”. In: *Computers and Chemical Engineering* 31.11 (2007), pp. 1419–1431. ISSN: 00981354. DOI: 10.1016/j.compchemeng.2006.12.004.
- [82] Min Kuang, Jinxin Wang, Xuehui Hu, and Guohua Yang. „Seawater/Seawater Cascade-Scrubbing Desulfurization Performance for Exhaust Gas of a 162-kW Marine Diesel Engine”. In: *Journal of Environmental Engineering* 146.1 (Jan. 2020), p. 04019090. ISSN: 0733-9372. DOI: 10.1061/(ASCE)EE.1943-7870.0001614.
- [83] Rui de Paula V. de Castro, José Luiz de Medeiros, Ofélia de Queiroz Fernandes Araújo, Matheus de Andrade Cruz, Gabriel Travagini Ribeiro, and Vanessa Reich de Oliveira. „Fluidized bed treatment of residues of semi-dry flue gas desulfurization units of coal-fired power plants for conversion of sulfites to sulfates”. In: *Energy Conversion and Management* 143 (July 2017), pp. 173–187. ISSN: 01968904. DOI: 10.1016/j.enconman.2017.03.078.
- [84] Barbara Toole-O’Neil and Ohio Coal Development Office, eds. *Dry Scrubbing Technologies for Flue Gas Desulfurization*. Boston, MA: Springer US, 1998. ISBN: 978-1-4613-7247-9. DOI: 10.1007/978-1-4615-4951-2.
- [85] D. Flagiello, A. Erto, A. Lancia, and F. Di Natale. „Experimental and modelling analysis of seawater scrubbers for sulphur dioxide removal from flue-gas”. In: *Fuel* 214.October 2017 (2018), pp. 254–263. ISSN: 00162361. DOI: 10.1016/j.fuel.2017.10.098.
- [86] U.S. Environmental Protection Agency. *EPA Air Pollution Control Cost Manual*. 6th Editio. January. Washington, D.C.: United States Environmental Protection Agency, 2002. ISBN: 1800553684.

- [87] Ma Shuangchen, Chai Jin, Chen Gongda, Yu Weijing, and Zhu Sijie. „Research on desulfurization wastewater evaporation: Present and future perspectives”. In: *Renewable and Sustainable Energy Reviews* 58 (2016), pp. 1143–1151. ISSN: 18790690. DOI: 10.1016/j.rser.2015.12.252.
- [88] L. E. Kallinikos, E. I. Farsari, D. N. Spartinos, and N. G. Papayannakos. „Simulation of the operation of an industrial wet flue gas desulfurization system”. In: *Fuel Processing Technology* 91.12 (2010), pp. 1794–1802. ISSN: 03783820. DOI: 10.1016/j.fuproc.2010.07.020.
- [89] Ricardo del Valle-Zermeño, Joan Formosa, and Josep Maria Chimeno. „Wet flue gas desulfurization using alkaline agents”. In: *Reviews in Chemical Engineering* 31.4 (Jan. 2015), pp. 303–327. ISSN: 2191-0235. DOI: 10.1515/revce-2015-0002.
- [90] B. Tilly, A. Griffiths, and E. Golland. „Flue Gas Desulphurisation at Longannet Power Station, Scotland; A Regulators View of the BPEO Assessment”. In: *The Institute of Energy's Second International Conference on Combustion & Emissions Control*. London: Elsevier, 1995, pp. 49–60. DOI: 10.1016/B978-0-902597-49-5.50008-1.
- [91] S. Ebrahimi, C. Picioreanu, R. Kleerebezem, J. J. Heijnen, and M. C.M. van Loosdrecht. „Rate-based modelling of SO<sub>2</sub> absorption into aqueous NaHCO<sub>3</sub>/Na<sub>2</sub>CO<sub>3</sub> solutions accompanied by the desorption of CO<sub>2</sub>”. In: *Chemical Engineering Science* 58.16 (2003), pp. 3589–3600. ISSN: 00092509. DOI: 10.1016/S0009-2509(03)00231-8.
- [92] K Diehl, S K Mitra, and H R Pruppacher. „A Laboratory and Theoretical Study on the Uptake of SO<sub>2</sub> Gas by Large and Small Water Drops Containing Heavy Metal Ions”. In: *Journal of Atmospheric Chemistry* 34 (2003), pp. 211–223.
- [93] Yusuf G. Adewuyi and Samuel O. Owusu. „Aqueous absorption and oxidation of nitric oxide with oxone for the treatment of tail gases: Process feasibility, stoichiometry, reaction pathways, and absorption rate”. In: *Industrial and Engineering Chemistry Research* 42.17 (2003), pp. 4084–4100. ISSN: 08885885. DOI: 10.1021/ie020709+.
- [94] Xiaoping Wang, Zhongjian Li, and Lecheng Lei. „Model study of sulfite oxidation in seawater flue gas desulfurization by cylindrical wetted-wall corona-streamer discharge”. In: *Chemical Engineering Science* 97 (2013), pp. 7–15. ISSN: 00092509. DOI: 10.1016/j.ces.2013.04.011.
- [95] Leroy A. Bromley. „Use of sea water to scrub sulfur dioxide from stack gases”. In: *International journal of sulfur chemistry: Part B* 7 (1972), pp. 77–84.
- [96] Wang Jin-gang, Zhang Shao-feng, Jing Rui-jing, and Li Wei-juan. „Flow Tray for Power Plant”. In: 20100226 (2012), pp. 1–4.

- [97] R. A. Pandey, R. Biswas, T. Chakrabarti, and S. Devotta. „Flue gas desulfurization: Physicochemical and biotechnological approaches”. In: *Critical Reviews in Environmental Science and Technology* 35.6 (2005), pp. 571–622. ISSN: 10643389. DOI: 10.1080/10643380500326374.
- [98] M. Radojević. „The use of seawater for flue gas desulphurisation”. In: *Environmental Technology Letters* 10.1 (1989), pp. 71–76. ISSN: 01432060. DOI: 10.1080/09593338909384719.
- [99] Rasmus Frimann Nielsen, Fredrik Haglind, and Ulrik Larsen. „Design and modeling of an advanced marine machinery system including waste heat recovery and removal of sulphur oxides”. In: *Energy Conversion and Management* 85.2014 (2014), pp. 687–693. ISSN: 01968904. DOI: 10.1016/j.enconman.2014.03.038.
- [100] Hongrui Ma, Koen Steernberg, Xavier Riera-Palou, and Nigel Tait. „Well-to-wake energy and greenhouse gas analysis of SOX abatement options for the marine industry”. In: *Transportation Research Part D: Transport and Environment* 17.4 (2012), pp. 301–308. ISSN: 13619209. DOI: 10.1016/j.trd.2012.01.005.
- [101] *Wet scrubber*. 2020. URL: [https://en.wikipedia.org/wiki/Wet%7B%5C\\_%7Dscrubber](https://en.wikipedia.org/wiki/Wet%7B%5C_%7Dscrubber).
- [102] K. H. Javed, T. Mahmud, and E. Purba. „Enhancement of mass transfer in a spray tower using swirling gas flow”. In: *Chemical Engineering Research and Design* 84.6 A (2006), pp. 465–477. ISSN: 02638762. DOI: 10.1205/cherd.05119.
- [103] W. F. Gohara T. W. Strock. „Experimental approach and techniques for the evaluation of wet flue gas desulfurization scrubber fluid mechanics”. In: *Chemical Engineering Science* 49.24 (1995), pp. 4667–4679.
- [104] Amitava Bandyopadhyay and Manindra Nath Biswas. „SO<sub>2</sub> scrubbing in a tapered bubble column scrubber”. In: *Chemical Engineering Communications* 193.12 (2006), pp. 1562–1580. ISSN: 00986445. DOI: 10.1080/00986440600584466.
- [105] *Spray tower*. 2019. URL: [https://en.wikipedia.org/wiki/Spray%7B%5C\\_%7Dtower](https://en.wikipedia.org/wiki/Spray%7B%5C_%7Dtower).
- [106] D. Flagiello, A. Parisi, A. Lancia, C. Carotenuto, A. Erto, and F. Di Natale. „Seawater desulphurization scrubbing in spray and packed columns for a 4.35 MW marine diesel engine”. In: *Chemical Engineering Research and Design* 148 (2019), pp. 56–67. ISSN: 02638762. DOI: 10.1016/j.cherd.2019.05.057.
- [107] Walter G. Whitman. „The two film theory of gas absorption”. In: *International Journal of Heat and Mass Transfer* 5.5 (May 1962), pp. 429–433. ISSN: 00179310. DOI: 10.1016/0017-9310(62)90032-7.

- [108] Juan Rodríguez-Sevilla, Manuel Álvarez, María C. Díaz, and María C. Marrero. „Absorption equilibria of dilute so<sub>2</sub> in seawater”. In: *Journal of Chemical and Engineering Data* 49.6 (2004), pp. 1710–1716. ISSN: 00219568. DOI: 10.1021/je0498331.
- [109] R Sander. „Compilation of Henry’s law constants (version 4.0) for water as solvent”. In: *Atmospheric Chemistry and Physics* 15.8 (2015), pp. 4399–4981. DOI: 10.5194/acp-15-4399-2015.
- [110] Allen E. Rabe and John F. Harris. „Vapor Liquid Equilibrium Data for the Binary System Sulfur Dioxide and Water.” In: *Journal of Chemical & Engineering Data* 8.3 (1963), pp. 333–336. ISSN: 0021-9568. DOI: 10.1021/je60018a017.
- [111] L. B. Baboolal, H. R. Pruppacher, and J. H. Topalian. „A Sensitivity Study of a Theoretical Model Of SO<sub>2</sub> Scavenging by Water Drops in Air”. In: *Journal of the Atmospheric Sciences* 38.4 (Apr. 1981), pp. 856–870. ISSN: 0022-4928. DOI: 10.1175/1520-0469(1981)038<0856:ASSOAT>2.0.CO;2.
- [112] C Walcek, P K Wang, J H Topalian, S K Mitra, and H R Pruppacher. „An Experimental Test of a Theoretical Model to Determine the Rate at which Freely Falling Water Drops Scavenge SO<sub>2</sub> in Air”. In: *Journal of the Atmospheric Sciences* 38.4 (Apr. 1981), pp. 871–876. ISSN: 0022-4928. DOI: 10.1175/1520-0469(1981)038<0871:AETOAT>2.0.CO;2.
- [113] John David Hem. *Study and Interpretation the Chemical of Natural of Characteristics Water*. 3rd. Alexandria, VA: U.S. Geological Survey, 1986, p. 272.
- [114] Frank J Millero, J. Beter Hershey, George Johnson, and Jia-Zhong Zhang. „The solubility of SO<sub>2</sub> and the dissociation of H<sub>2</sub>SO<sub>3</sub> in NaCl solutions”. In: *Journal of Atmospheric Chemistry* 8.4 (May 1989), pp. 377–389. ISSN: 0167-7764. DOI: 10.1007/BF00052711.
- [115] Andrei V. Bandura and Serguei N. Lvov. „The Ionization Constant of Water over Wide Ranges of Temperature and Density”. In: *Journal of Physical and Chemical Reference Data* 35.1 (Mar. 2006), pp. 15–30. ISSN: 0047-2689. DOI: 10.1063/1.1928231.
- [116] Luca Marocco and Fabio Inzoli. „Multiphase Euler-Lagrange CFD simulation applied to Wet Flue Gas Desulphurisation technology”. In: *International Journal of Multiphase Flow* 35.2 (2009), pp. 185–194. ISSN: 03019322. DOI: 10.1016/j.ijmultiphaseflow.2008.09.005.
- [117] Sh Darake, M. S. Hatamipour, A. Rahimi, and P. Hamzeloui. „SO<sub>2</sub> removal by seawater in a spray tower: Experimental study and mathematical modeling”. In: *Chemical Engineering Research and Design* 109 (2016), pp. 180–189. ISSN: 02638762. DOI: 10.1016/j.cherd.2015.11.027.

- [118] Anders Andreasen and Stefan Mayer. „Use of seawater scrubbing for SO<sub>2</sub> removal from marine engine exhaust gas”. In: *Energy and Fuels* 21.6 (2007), pp. 3274–3279. ISSN: 08870624. DOI: 10.1021/ef700359w.
- [119] Martin B Hocking and Graham W Lee. „Calculated Sulfur Dioxide Equilibria At Low Concentrations Between Air and Water”. In: 8 (1977), pp. 255–262.
- [120] Ida-Maja Karle and David Turner. *Seawater Scrubbing - reduction of SO<sub>x</sub> emissions from ship exhausts*. Tech. rep. Göteborg: Chalmers University of Technology, 2007.
- [121] Roy M. Harrison, ed. *Understanding our environment. An introduction to environmental chemistry and pollution*. Third. Cambridge: The Royal Society of Chemistry, 1999, p. 485. ISBN: 0854045848. DOI: 10.1016/0160-9327(93)90048-8.
- [122] DOE. *Handbook of methods for the analysis of the various parameters of the carbon dioxide system in sea water*. Ed. by Andrew G. Dickson and Catherine Goyet. Second. 1997, p. 187.
- [123] J. Peter and B. Williams. „The natural oceanic carbon and sulfur cycles: Implications for so<sub>2</sub> and CO<sub>2</sub> emissions from marine shipping”. In: *Underwater Technology* 29.1 (2010), pp. 5–19. ISSN: 01410814. DOI: 10.3723/ut.29.005.
- [124] Claude E. Boyd, Craig S. Tucker, and Benjaporn Somridhivej. „Alkalinity and Hardness: Critical but Elusive Concepts in Aquaculture”. In: *Journal of the World Aquaculture Society* 47.1 (2016), pp. 6–41. ISSN: 17497345. DOI: 10.1111/jwas.12241.
- [125] Richard Zeebe and Dieter Wolf-Gladrow. *CO<sub>2</sub> in seawater : equilibrium, kinetics, isotopes*. Amsterdam New York: Elsevier, 2001. ISBN: 0444505792.
- [126] Seung Ki Back, A. H.M. Mojammal, Hyeun Ho Jo, Jin Ho Kim, Min Jae Jeong, Yong Chil Seo, Hyun Tae Joung, and Seong Heon Kim. „Increasing seawater alkalinity using fly ash to restore the pH and the effect of temperature on seawater flue gas desulfurization”. In: *Journal of Material Cycles and Waste Management* 0.0 (2019), p. 0. ISSN: 16118227. DOI: 10.1007/s10163-019-00852-2.
- [127] I. Halevy, M. T. Zuber, and D. P. Schrag. „A Sulfur Dioxide Climate Feedback on Early Mars”. In: *Science* 318.5858 (Dec. 2007), pp. 1903–1907. ISSN: 0036-8075. DOI: 10.1126/science.1147039.
- [128] R N Roy, L N Roy, K M Vogel, C PorterMoore, T Pearson, C E Good, F J Millero, and D M Campbell. „The dissociation constants of carbonic acid in seawater at salinities 5 to 45 and temperatures to 45 degrees (vol 44, pg 249, 1996)”. In: *Marine Chemistry* 52.2 (1993), p. 183. DOI: 10.1016/0304-4203(93)90207-5.

- [129] Giuseppe Caiazzo, Antonio Di Nardo, Giuseppe Langella, and Fabrizio Scala. „Seawater scrubbing desulfurization: A model for SO<sub>2</sub> absorption in fall-down droplets”. In: *Environmental Progress and Sustainable Energy* 31.2 (July 2012), pp. 277–287. ISSN: 19447442. DOI: 10.1002/ep.10541.
- [130] Charlotte Brogren and Hans T. Karlsson. „Modeling the absorption of SO<sub>2</sub> in a spray scrubber using the penetration theory”. In: *Chemical Engineering Science* 52.18 (1997), pp. 3085–3099. ISSN: 00092509. DOI: 10.1016/S0009-2509(97)00126-7.
- [131] Shiva Darake, Amir Rahimi, Mohammad Sadegh Hatamipour, and Payam Hamzeloui. „SO<sub>2</sub> Removal by Seawater in a Packed-Bed Tower: Experimental Study and Mathematical Modeling”. In: *Separation Science and Technology (Philadelphia)* 49.7 (2014), pp. 988–998. ISSN: 15205754. DOI: 10.1080/01496395.2013.872660.
- [132] Akio Nishimura, Henry Weller, Hirokazu Maruoka, Masao Takayanagi, and Hideharu Ushiki. „Dynamics of a dry-rebounding drop: observations, simulations, and modeling”. In: *Open Physics* 16.1 (May 2018), pp. 271–284. ISSN: 2391-5471. DOI: 10.1515/phys-2018-0039.
- [133] Søren Kiil, Michael L. Michelsen, and Kim Dam-Johansen. „Experimental Investigation and Modeling of a Wet Flue Gas Desulfurization Pilot Plant”. In: *Industrial & Engineering Chemistry Research* 37.7 (2002), pp. 2792–2806. ISSN: 0888-5885. DOI: 10.1021/ie9709446.
- [134] Isabelle R. Horvath and Siddharth G. Chatterjee. „A surface renewal model for unsteady-state mass transfer using the generalized Danckwerts age distribution function”. In: *Royal Society Open Science* 5.5 (2018). ISSN: 20545703. DOI: 10.1098/rsos.172423.
- [135] James Welty, Charles E. Wicks, Robert E. Wilson, and Gregory L. Rorrer. *Fundamentals of momentum, heat and mass transfer*. Ed. by James Welty, Charles E. Wicks, Robert E. Wilson, and Gregory L. Rorrer. 5th. Wiley, 2007, p. 729. ISBN: 978-1-119-49541-3.
- [136] András Urbán, Matouš Zaremba, Milan Malý, Viktor Józsa, and Jan Jedelský. „Droplet dynamics and size characterization of high-velocity airblast atomization”. In: *International Journal of Multiphase Flow* 95 (Oct. 2017), pp. 1–11. ISSN: 03019322. DOI: 10.1016/j.ijmultiphaseflow.2017.02.001.
- [137] A. Kumar and S. Hartland. „Correlations for prediction of mass transfer coefficients in single drop systems and liquid-liquid extraction columns”. In: *Chemical Engineering Research and Design* 77.5 (1999), pp. 372–384. ISSN: 02638762. DOI: 10.1205/026387699526359.
- [138] Byron R. Bird, Warren E. Stewart, and Edwin N. Lightfoot. *Transport phenomena*. 2nd. Wiley, 2002, p. 914. ISBN: 0471410772. DOI: 10.1002/aic.690070245.



- [139] Ralph Higbie. „The rate of absorption of a pure gas into a still liquid during short periods of exposure”. In: *Trans. AIChE* 31 (1935), pp. 365–389.
- [140] David A. Glasscock and Gary T. Rochelle. „Numerical simulation of theories for gas absorption with chemical reaction”. In: *AIChE Journal* 35.8 (1989), pp. 1271–1281. ISSN: 15475905. DOI: 10.1002/aic.690350806.
- [141] Po V Danckwerts. „Gas absorption accompanied by chemical reaction”. In: *AIChE Journal* 1.4 (1955), pp. 456–463.
- [142] Badie I. Morsi and Omar M. Basha. „Mass Transfer in Multiphase Systems”. In: *Mass Transfer - Advancement in Process Modelling*. InTech, Oct. 2015. DOI: 10.5772/60516.
- [143] Babak Jajuee, Argyrios Margaritis, Dimitre Karamanev, and Maurice A. Bergougnou. „Application of surface-renewal-stretch model for interface mass transfer”. In: *Chemical Engineering Science* 61.12 (2006), pp. 3917–3929. ISSN: 00092509. DOI: 10.1016/j.ces.2006.01.026.
- [144] Bruce E. Poling, George H. Thomson, Daniel G. Friend, Richard L. Rowley, and W. Vincent Wilding. *Perry's Chemical Engineers' Handbook Section 2: Physical and Chemical Data*. 2007, pp. 1–517. ISBN: 0071542094. DOI: 10.1036/0071511253.
- [145] Jacob B. Angelo, Edwin N. Lightfoot, and David W. Howard. „Generalization of the penetration theory for surface stretch: Application to forming and oscillating drops”. In: *AIChE Journal* 12.4 (1966), pp. 751–760. ISSN: 15475905. DOI: 10.1002/aic.690120423.
- [146] Norman Kirk Yeh. „Liquid Phase Mass Transfer in Spray Contactors”. PhD thesis. The University of Texas at Austin, 2002.
- [147] H. Amokrane, A. Saboni, B. Caussade, Caussade B Amokrane H & Saboni A., H. Amokrane, A. Saboni, and B. Caussade. „Experimental study and parameterization of gas absorption by water drops”. In: *AIChE Journal* 40.12 (1994), pp. 1950–1960. ISSN: 15475905. DOI: 10.1002/aic.690401204.
- [148] Ian H. Bell, Jorrit Wronski, Sylvain Quoilin, and Vincent Lemort. „Pure and Pseudo-pure Fluid Thermophysical Property Evaluation and the Open-Source Thermophysical Property Library CoolProp”. In: *Industrial & Engineering Chemistry Research* 53.6 (2014), pp. 2498–2508. DOI: 10.1021/ie4033999. eprint: <http://pubs.acs.org/doi/pdf/10.1021/ie4033999>.
- [149] A. Saboni and S. Alexandrova. „Sulfur dioxide absorption and desorption by water drops”. In: *Chemical Engineering Journal* 84.3 (2001), pp. 577–580. ISSN: 13858947. DOI: 10.1016/S1385-8947(01)00172-3.

- [150] Ryuichi Kaji, Yukio Hishinuma, and Hiroshi Kuroda. „SO<sub>2</sub> absorption by water droplets.” In: *Journal of Chemical Engineering of Japan* 18.2 (1985), pp. 169–172. ISSN: 1881-1299. DOI: 10.1252/jcej.18.169.
- [151] Tibor Bešenić, Milan Vujanović, Jakov Baleta, Klaus Pachler, Niko Samec, and Matjaž Hriberšek. „Numerical analysis of sulfur dioxide absorption in water droplets”. In: *Open Physics* 18.1 (May 2020), pp. 104–111. ISSN: 2391-5471. DOI: 10.1515/phys-2020-0100.
- [152] Norman K. Yeh and Gary T. Rochelle. „Liquid-phase mass transfer in spray contactors”. In: *AIChE Journal* 49.9 (Sept. 2003), pp. 2363–2373. ISSN: 00011541. DOI: 10.1002/aic.690490912.
- [153] Giuseppe Caiazzo, Giuseppe Langella, Francesco Miccio, and Fabrizio Scala. „An experimental investigation on seawater SO<sub>2</sub> scrubbing for marine application”. In: *Environmental Progress & Sustainable Energy* 32.4 (Dec. 2013), pp. 1179–1186. ISSN: 19447442. DOI: 10.1002/ep.11723.
- [154] Tibor Bešenić, Jakov Baleta, Klaus Pachler, and Milan Vujanović. „Numerical modelling of sulfur dioxide absorption for spray scrubbing”. In: *Energy Conversion and Management* 217.May (Aug. 2020), p. 112762. ISSN: 01968904. DOI: 10.1016/j.enconman.2020.112762.
- [155] Milene C. Codolo and Waldir A. Bizzo. „Experimental study of the SO<sub>2</sub> removal efficiency and volumetric mass transfer coefficients in a pilot-scale multi-nozzle spray tower”. In: *International Journal of Heat and Mass Transfer* 66 (2013), pp. 80–89. ISSN: 00179310. DOI: 10.1016/j.ijheatmasstransfer.2013.07.011.
- [156] Zhen Chen, Haiming Wang, Jiankun Zhuo, and Changfu You. „Experimental and numerical study on effects of deflectors on flow field distribution and desulfurization efficiency in spray towers”. In: *Fuel Processing Technology* 162 (July 2017), pp. 1–12. ISSN: 03783820. DOI: 10.1016/j.fuproc.2017.03.024.
- [157] Sanjay Bishnoi and Gary T. Rochelle. „Absorption of carbon dioxide in aqueous piperazine/methyldiethanolamine”. In: *AIChE Journal* 48.12 (Dec. 2002), pp. 2788–2799. ISSN: 00011541. DOI: 10.1002/aic.690481208.
- [158] Dariusz Asendrych and Paweł Niegodajew. „Numerical Study of the CO<sub>2</sub> Absorber Performance Subjected to the Varying Amine Solvent and Flue Gas Loads”. In: *Chemical Engineering Communications* 204.5 (2017), pp. 580–590. ISSN: 15635201. DOI: 10.1080/00986445.2017.1292258.
- [159] C Weiss and U Wieltch. „Laser optical flow measurements and computational fluid dynamic calculation of spray tower hydrodynamics”. In: May (2005), pp. 492–507. DOI: 10.1205/cherd.04071.

- [160] Jesse D Killion and Srinivas Garimella. „A critical review of models of coupled heat and mass transfer in falling film absorption”. In: *International Journal of Refrigeration* 24 (2001).
- [161] Guojie Qi, Shujuan Wang, Zhicheng Xu, Bo Zhao, and Changhe Chen. „Mass transfer and kinetics study on combined CO<sub>2</sub> and SO<sub>2</sub> absorption using aqueous ammonia”. In: *International Journal of Greenhouse Gas Control* 41 (2015), pp. 60–67. ISSN: 17505836. DOI: 10.1016/j.ijggc.2015.06.023.
- [162] A. L. Fricke and Brahm D. Prasher. „Mass Transfer at a Free Gas-Liquid Interface in Turbulent Thin Films”. In: *Industrial and Engineering Chemistry Process Design and Development* 13.4 (1974), pp. 336–340. ISSN: 01964305. DOI: 10.1021/i260052a005.
- [163] J. T. Davies and S. T. Ting. „Mass transfer into turbulent jets”. In: *Chemical Engineering Science* 22.12 (1967), pp. 1539–1548. ISSN: 00092509. DOI: 10.1016/0009-2509(67)80192-1.
- [164] Siu Ming Yih and Khi Yune Chen. „Gas absorption into wavy and turbulent falling liquid films in a wetted-wall column”. In: *Chemical Engineering Communications* 17.1-6 (1982), pp. 123–136. ISSN: 15635201. DOI: 10.1080/00986448208911620.
- [165] Martin Zidar. „Gas-Liquid Equilibrium-Operational Diagram: Graphical Presentation of Absorption of SO<sub>2</sub> in the NaOH-SO<sub>2</sub>-H<sub>2</sub>O System Taking Place within a Laboratory Absorber”. In: *Industrial & Engineering Chemistry Research* 39.iv (2000), pp. 3042–3050. ISSN: 0888-5885. DOI: 10.1021/ie990711+.
- [166] Christian H.E. Nielsen, Søren Kiil, Henrik W. Thomsen, and Kim Dam-Johansen. „Mass transfer in wetted-wall columns: Correlations at high Reynolds numbers”. In: *Chemical Engineering Science* 53.3 (1998), pp. 495–503. ISSN: 00092509. DOI: 10.1016/S0009-2509(97)00320-5.
- [167] Hrvoje Mikulčić, Eberhard von Berg, Milan Vujanović, Xuebin Wang, Houzhang Tan, and Neven Duić. „Numerical evaluation of different pulverized coal and solid recovered fuel co-firing modes inside a large-scale cement calciner”. In: *Applied Energy* 184 (Dec. 2016), pp. 1292–1305. ISSN: 03062619. DOI: 10.1016/j.apenergy.2016.05.012.
- [168] Sandrina Pereira, Mário Costa, Maria da Graça Carvalho, and Abel Rodrigues. „Potential of poplar short rotation coppice cultivation for bioenergy in Southern Portugal”. In: *Energy Conversion and Management* 125 (2016), pp. 242–253. ISSN: 01968904. DOI: 10.1016/j.enconman.2016.03.068.
- [169] Hrvoje Mikulčić, Eberhard von Berg, Milan Vujanović, and Neven Duić. „Numerical study of co-firing pulverized coal and biomass inside a cement calciner.” In: *Waste management & research : the journal of the International Solid Wastes and Public Cleansing Association, ISWA* 32.June (2014), pp. 661–669. ISSN: 1399-3070. DOI: 10.1177/0734242X14538309.

- [170] Kenny Vanreppelen, Sonja Schreurs, Tom Kuppens, Theo Thewys, Robert Carleer, and Jan Yperman. „Activated carbon by co-pyrolysis and steam activation from particle board and melamine formaldehyde resin: production, adsorption properties and techno economic evaluation”. In: *Journal of Sustainable Development of Energy* 1.1 (2013), pp. 41–57. ISSN: 18489257. DOI: 10.13044/j.sdewes.2013.01.0004.
- [171] H. Mikulčić, E. von Berg, M. Vujanović, P. Priesching, L. Perković, R. Tatschl, and N. Duić. „Numerical modelling of calcination reaction mechanism for cement production”. In: *Chemical Engineering Science* 69.1 (2012). cited By 36, pp. 607–615. DOI: 10.1016/j.ces.2011.11.024.
- [172] Yao B. Yang, Vida N. Sharifi, Jim Swithenbank, Lin Ma, Leilani I. Darvell, Jenny M. Jones, Mohamed Pourkashanian, and Alan Williams. „Combustion of a Single Particle of Biomass”. In: *Energy & Fuels* 22.1 (Jan. 2008), pp. 306–316. ISSN: 0887-0624. DOI: 10.1021/ef700305r.
- [173] A. Williams, J.M. M. Jones, L. Ma, and M. Pourkashanian. „Pollutants from the combustion of solid biomass fuels”. In: *Progress in Energy and Combustion Science* 38.2 (Apr. 2012), pp. 113–137. ISSN: 03601285. DOI: 10.1016/j.pecs.2011.10.001.
- [174] Hrvoje Mikulčić. „Numerical modelling of thermo-chemical processes inside a cement calciner for a cleaner cement production, PhD Thesis”. PhD thesis. University of Zagreb, 2015.
- [175] E. Mura, O. Debono, A. Villot, and F. Paviet. „Pyrolysis of biomass in a semi-industrial scale reactor: Study of the fuel-nitrogen oxidation during combustion of volatiles”. In: *Biomass and Bioenergy* 59 (Dec. 2013), pp. 187–194. ISSN: 09619534. DOI: 10.1016/j.biombioe.2013.09.001.
- [176] Isabel Vermeulen, Chantal Block, and Carlo Vandecasteele. „Estimation of fuel-nitrogen oxide emissions from the element composition of the solid or waste fuel”. In: *Fuel* 94 (Apr. 2012), pp. 75–80. ISSN: 00162361. DOI: 10.1016/j.fuel.2011.11.071.
- [177] Jianguo Zhu, Ziqu Ouyang, and Qinggang Lu. „An Experimental Study on NO<sub>x</sub> Emissions in Combustion of Pulverized Coal Preheated in a Circulating Fluidized Bed”. In: *Energy & Fuels* 27.12 (Dec. 2013), pp. 7724–7729. ISSN: 0887-0624. DOI: 10.1021/ef402146w.
- [178] Olivier Mathieu and Eric L. Petersen. „Experimental and modeling study on the high-temperature oxidation of Ammonia and related NO<sub>x</sub> chemistry”. In: *Combustion and Flame* 162.3 (Mar. 2015), pp. 554–570. ISSN: 00102180. DOI: 10.1016/j.combustflame.2014.08.022.
- [179] P. Glarborg, A. D. Jensen, and J. E. Johnsson. „Fuel nitrogen conversion in solid fuel fired systems”. In: *Progress in Energy and Combustion Science* 29.2 (2003), pp. 89–113. ISSN: 03601285. DOI: 10.1016/S0360-1285(02)00031-X.

- [180] A Molina, E G Eddings, D W Pershing, and A F Sarofim. „Char nitrogen conversion : implications to emissions from coal-fired utility boilers”. In: 26 (2000), pp. 507–531.
- [181] Shinji Kambara, Takayuki Takarada, Masaru Toyoshima, and Kunio Kate. „Relation between functional nitrogen and NO<sub>x</sub> emissions coal combustion”. In: 74.9 (1995), pp. 1247–1253.
- [182] J M Jones, P M Patterson, M Pourkashanian, A Williams, A Arenillas, and F Rubiera. „Modelling NO<sub>x</sub> formation in coal particle combustion at high temperature : an investigation of the devolatilisation kinetic factors”. In: 78.x (1999), pp. 1171–1179.
- [183] S. C. Hill and L. Douglas Smoot. „Modeling of nitrogen oxides formation and destruction in combustion systems”. In: *Progress in Energy and Combustion Science* 26.4 (2000), pp. 417–458. ISSN: 03601285. DOI: 10.1016/S0360-1285(00)00011-3.
- [184] Shoaib Mehmood, Bale V. Reddy, and Marc A. Rosen. „Emissions and furnace gas temperature for electricity generation via co-firing of coal and biomass”. In: *Journal of Sustainable Development of Energy, Water and Environment Systems* 3.4 (2015), pp. 344–358. ISSN: 18489257. DOI: 10.13044/j.sdewes.2015.03.0026.
- [185] Milan Vujanović, Neven Duić, and Reinhard Tatschl. „Validation of reduced mechanisms for nitrogen chemistry in numerical simulation of a turbulent non-premixed flame”. In: *Reaction Kinetics and Catalysis Letters* 96.1 (2009), pp. 125–138. ISSN: 01331736. DOI: 10.1007/s11144-009-5463-2.
- [186] Luis I. Díez, Cristóbal Cortés, and Javier Pallarés. „Numerical investigation of NO<sub>x</sub> emissions from a tangentially-fired utility boiler under conventional and overfire air operation”. In: *Fuel* 87.7 (June 2008), pp. 1259–1269. ISSN: 00162361. DOI: 10.1016/j.fuel.2007.07.025.
- [187] Audai Hussein Al-Abbas and Jamal Naser. „Effect of Chemical Reaction Mechanisms and NO<sub>x</sub> Modeling on Air-Fired and Oxy-Fuel Combustion of Lignite in a 100-kW Furnace”. In: *Energy & Fuels* 26.6 (June 2012), pp. 3329–3348. ISSN: 0887-0624. DOI: 10.1021/ef300403a.
- [188] Ronald K Hanson and Siamak Salimian. „Survey of Rate Constants in the N/H/O System”. In: *Combustion Chemistry*. Ed. by William C Gardiner. New York, NY: Springer US, 1984, pp. 361–421. ISBN: 978-1-4684-0186-8. DOI: 10.1007/978-1-4684-0186-8\_6.
- [189] Xin Wang, Qiangqiang Ren, Linna Li, Shiyuan Li, and Qinggang Lu. „TG-MS analysis of nitrogen transformation during combustion of biomass with municipal sewage sludge”. In: *Journal of Thermal Analysis and Calorimetry* 123.3 (2016), pp. 2061–2068. ISSN: 15882926. DOI: 10.1007/s10973-015-4712-z.

- [190] Ewa Rostek and Krzysztof Biernat. „Thermogravimetry as a Research Method in the Transformation Processes of Waste Rubber and Plastic Products for Energy Carriers ( WtE and WtL Processes )”. In: *Sustainable Development of Energy, Water and Environment Systems* 1.2 (2013), pp. 163–171. ISSN: 18489257. DOI: 10.13044/j.sdewes.2013.01.0012.
- [191] L. Douglas Smoot and Philip J. Smith. „NO<sub>x</sub> Pollutant Formation in Turbulent Coal Systems”. In: *Coal Combustion and Gasification*. Boston, MA: Springer US, 1985, pp. 373–403. DOI: 10.1007/978-1-4757-9721-3\_15.
- [192] J.M. Levy, L.K. Chan, A.F. Sarofim, and J.M. Beér. „NO/char reactions at pulverized coal flame conditions”. In: *Symposium (International) on Combustion* 18.1 (1981), pp. 111–120. ISSN: 00820784. DOI: 10.1016/S0082-0784(81)80016-1.
- [193] Gongliang Wang, René Zander, and Mário Costa. „Oxy-fuel combustion characteristics of pulverized-coal in a drop tube furnace”. In: *Fuel* 115 (2014), pp. 452–460. ISSN: 00162361. DOI: 10.1016/j.fuel.2013.07.063.
- [194] Hrvoje Mikulčić, Eberhard Von Berg, Milan Vujanović, and Neven Duić. „CFD modelling of biomass combustion in an experimental drop tube furnace”. In: *Clean Air 2015*. Lisabon, 2015.
- [195] Tibor Bešenić, Hrvoje Mikulčić, Milan Vujanović, and Neven Duić. „Numerical modelling of emissions of nitrogen oxides in solid fuel combustion”. In: *Journal of Environmental Management* 215 (June 2018), pp. 177–184. ISSN: 0301-4797. DOI: 10.1016/J.JENVMAN.2018.03.014.
- [196] R. I. Backreedy, L. M. Fletcher, L. Ma, M. Pourkashanian, and A. Williams. „Modelling Pulverised Coal Combustion Using a Detailed Coal Combustion Model”. In: *Combustion Science and Technology* 178.4 (Apr. 2006), pp. 763–787. ISSN: 0010-2202. DOI: 10.1080/00102200500248532.

# Curriculum Vitae

Tibor Bešenić was born in Zagreb on 1 June 1991, Croatia. He finished the A.G. Matoš Science and Mathematics Program Secondary School in Zabok and enrolled in the Faculty of Mechanical Engineering and Naval Architecture at the University of Zagreb in 2009/2010. He completed his Master's degree in 2016, after which he enrolled in postgraduate doctoral study Power and energy engineering. He was employed at the Department of Energy, Power and Environmental Engineering as a research assistant and collaborated with the AVL List GmbH from Graz as a member of the *CFD Powerlab* group.

He published five scientific papers in journals indexed in the Web of Science Core Collection and six research papers at internationally recognized conferences. He served as a reviewer for nine scientific journals, including Journal of Environmental Management, Energy Conversion and Management, Fuel, Journal of Cleaner Production, Thermal Science, and Open Physics. As a member of the Local Organising Committee, he has been involved in the organization of four SDEWES conferences and the 8<sup>th</sup> European Combustion Meeting conference. He is a member of the International Centre for Sustainable Development of Energy, Water and Environment Systems and the Adria Section of the Combustion Institute.

He speaks and writes English.